EPFL

Thèse n° 10 219

Development of Advanced Methodologies for Monitoring and Modelling of Neutron Noise in Modern LWR Cores

Présentée le 16 septembre 2020

à la Faculté des sciences de base
Laboratoire de physique des réacteurs et de comportement des systèmes
Programme doctoral en énergie

pour l'obtention du grade de Docteur ès Sciences

par

Dionysios CHIONIS

Acceptée sur proposition du jury

Dr S.-R. Cherkaoui, président du jury
Prof. A. Pautz, A. Dokhane, directeurs de thèse
Prof. C. Demaziere, rapporteur
Prof. C. Montalvo, rapporteuse
Prof. H.-M. Prasser, rapporteur

École polytechnique fédérale de Lausanne

2020

To my beloved wife Vera
&
to my family Alkis, Irini, Angie, and Ira

"*Διωρισμένων δὲ τούτων ἐπισκεπτέον περὶ τῶν αἰτίων, ποῖά τε καὶ πόσα τὸν ἀριθμόν ἐστιν. ἐπεὶ γὰρ τοῦ εἰδέναι χάριν ἡ πραγματεία, εἰδέναι δ᾽ οὐ πρότερον οἰόμεθα ἕκαστον πρὶν ἂν λάβωμεν τὸ διὰ τί περὶ ἕκαστον, τοῦτο δ᾽ ἐστὶ τὸ λαβεῖν* ***τὴν πρώτην αἰτίαν****,…*"
Αριστοτέλης, Περί Φύσεως, Βιβλίο II.III, 194β, 16-21

"*We have next to consider in how many senses 'because' may answer the question 'why.' Knowledge is the object of our inquiry, and men do not think they know a thing till they have grasped of its 'why', which is to grasp its* ***primary cause****, …*"
Aristoteles, Physics, Book 2.3, 194b, 16-21

Acknowledgements

The current doctoral thesis summarizes my 5.5-years efforts in the research field of nuclear reactor physics. I will always characterize this period as a unique journey, during which I had the opportunity to improve my knowledge, and most importantly to interact with so many people who helped me, each one in her/his way. In these few lines, I would like sincerely to express my gratitude to those who accompanied me in this experience.

First and above all, I truly thank *Hamid Dokhane* for his tireless, continuous, and valuable support during this long period. Our discussions in our office and during all our scientific trips cannot be forgotten. You always guided me wisely allowing me at the same time to explore new paths. Your genially politeness and discretion are of highest value, which I hope that I will manage to carry them with me. I believe that our relationship has been grown over the years and has exceeded by far the simple supervisor-student interaction. I truly thank you for everything, none could have a better supervisor!

Hakim Ferroukhi and *Andreas Pautz* offered me an ideal place to work as a PhD student, giving me the privilege to work with exceptional colleagues at the LRS/LRT in PSI, having all the conveniences for an unperturbed research. You both supported me at every single stage of this work giving me the chance to attend conferences and meetings all over the world. Somehow in almost all decisions for my nuclear career you have played a role, and I thank you for that.

I would like also to thank *Prof. Prasser*, *Prof. Montalvo*, and *Prof. Demazière* for accepting participating in my jury committee and finding the time to go through this manuscript. Your comments and our discussion during the oral exam was a highlight for me. Thank you for your time and your feedback on my work. I also thank *Dr. Cherkaoui* for accepting the role of the jury president and organizing a smooth oral exam.

I received significant support from the Swiss nuclear industry during all stages of my doctoral studies. For that, I would like to express my gratitude to swiss*nuclear* for funding my project, and of course *Gaëtan Girardin*, *Lukas Meyer*, *Fabian Jatuff*, *Stefano Canepa* and *Rudi Meyer*, from KKG, for providing technical support, guidance and valuable suggestions and feedbacks over the last years. In addition, my thanks go also to *Carlos Aguirre* and *Roger Bieli*, from KKL, for their support and for providing plant data helping me to validate the advanced signal processing developed methodologies.

Sharing the office with people from different cultures and mindsets is not always trivial. However, in my case, I was so grateful to be in the same office (from just few months up to all the years of my presence at PSI) with *Hamid Dokhane*, *Roman Mukin*, *Omar Zerkak*, *Stefano Capena* and *Vasudha Verma*. Our interaction made so enjoyable my years at Villigen. You helped me multiple times solving technical issues, but most importantly, we had interesting discussions focusing on more attractive topics than reactor physics!

Many thanks from the bottom of my heart also to my dearest *Philippe Jacquemoud.* Clearly, without his technical support none of the results presented in this manuscript would be possible to be produced. But above all I want to thank you for our endless discussions covering every possible topic. It was such a privilege to meet you and spend time with you.

By being a member of LRS/LRT, I had the luck to interact with great scientists. All of you were available to help me and assist me on any question I had. Saying thousand thanks would not be enough. You always offered excellent support and great feedback.

In my PhD adventure I met *Petra Mala*, *Damar Wicaksono*, *Vladimir Brankov*, *Marianna Papadionysiou*, *Petros Papadopoulos* and *Boris Hombourger* who were doing or they are about to finish their PhDs at LRS/LRT. Sharing our experiences and helping each other was so relieving. Thank you for your kindness and I hope that somehow we will remain in touch.

My Greek friends *Giorgos*, *Stathis*, *Paris*, *Nikos* and *Giannis* are always giving me this extra push to chase my goals and to continue targeting higher. Your friendship over all these years is so important for me. Thank you for being next to me.

Andrea Mohr and *Ruth Ringele* offered always the best support on all these administrative issues appearing at the worst possible moment. Thank you so much for organizing everything so efficiently in LRS/LRT!

I had the honor (and the duty) to serve as the STARS/LRT coffee club president and the PSI volleyball coach. In both groups, I met countless interesting people and you all made my PSI-journey to be so enjoyable. Thank you for the memories.

Also I would like to acknowledge *Jan Krouthén*, *Tony Williams* and *Willy Kohlpainter* from Axpo Power AG for the flexibility that they showed during the last two years of my studies allowing me to finalize my thesis manuscript without any additional pressure.

This manuscript is also dedicated to the memory of *Kurt Hofer* who guided me wisely during my master studies and offered me generously so many advices. I truly thank you for all your support.

Όλα αυτά τα χρόνια, η οικογένεια μου πίσω στην Αθήνα με στηρίζει καθημερινά και με βοηθάει να κάνω κάθε φορά άλλο ένα βήμα μπροστά. Η ψυχολογική υποστήριξη και η αγάπη σας με συντροφεύουν όσα χρόνια και αν λείπω από το σπίτι. Πάντα θυμάμαι από που έρχομαι και τι μου μάθατε. *Μαμά*, *Μπαμπά*, *Άντζυ* και *Ήρα* είμαι τόσο τυχερός που σας έχω.

Last, but certainly not least, I would like to thank *Vera* with all my heart for her unbelievable patience and her endless support during all the stages of my PhD studies. Even if you don't want to believe it, without you it would be extremely difficult or even impossible to successfully reach this milestone. Σε ευχαριστώ Μπέκι μου που είσαι στη ζωή μου!

Διονύσης

26.06.2020

Abstract

Nuclear reactors are inherently stochastic systems, in which various neutronic and thermal-hydraulic parameters fluctuate over their mean values even during steady-state operating conditions. In addition, structural and mechanical components such as the fuel assemblies and the core barrel incessantly vibrate, in such conditions, because of the strong hydraulic forces originating from the upward flow of the core coolant. This stochasticity is the cause of the fluctuating behavior of the neutron population in the core, a phenomenon which is commonly referred as *neutron noise*.

The reactor detector signals, including the neutron noise levels, are continuously monitored in power reactors over their lifetime, as this information provides valuable knowledge of the core behavior and its dynamics. More importantly, the neutron noise monitoring could be used for the early detection of anomalies that might occur during the reactor operation. The neutron noise phenomenon has been an intensively-studied research topic for many decades, which laid the foundation for the development of numerous noise surveillance methods, signal processing techniques, and analytical solvers, utilized commonly to this day on a global scale. Nevertheless, an unexpected neutron noise level increase tendency, observed in the last decade in several European KWU pre-Konvoi PWR design reactors, triggered an increasing attention both in research and industry. This noise level increase trend is certainly not a safety related aspect. However, it has been causing undesirable costly operational consequences for the utilities since its appearance. The new observations revealed the need for an improved understanding of the neutron noise behavior in full power reactors, which is the main goal of this research.

In this context, the current doctoral research intends to systematically analyze the neutron noise phenomenon by developing innovative in-house PSI noise modelling methodologies and utilizing advanced signal processing techniques. The ultimate goal is to improve the noise modelling techniques in order to assist the in-depth understanding of the dynamic mechanisms taking part in any reactor core.

First, main attention is given to the identification of the neutron noise characteristics of the Swiss Gösgen nuclear reactor (KKG), representing a typical example of a KWU pre-Konvoi PWR design. KKG real plant data have been analyzed in detail in the time and frequency domains using traditional signal processing techniques. This systematic analysis revealed key aspects of the KKG neutron noise phenomenology, allowing the better characterization of the noise sources affecting the KKG dynamic behavior. Results showed a systematic neutron noise increase within-a-cycle and from cycle-to-cycle, whereas a tendency for higher noise levels towards the core-top axial level could be identified. More importantly, higher neutron noise amplitudes could be observed at the core-east side, which is a noise characteristic uniquely appeared in KKG. Moreover, the pronounced effect of three main noise sources has been identified by analyzing the KKG plant data in the frequency domain: the inlet coolant temperature fluctuations at low frequencies ($< 1\ Hz$), the fuel assembly vibration at around $2\ Hz$, and the core barrel pendular movement at $8\ Hz$.

Second, an in-house neutron noise modelling methodology has been developed, in this work, utilizing the advanced codes system CASMO-5/SIMULATE-3/SIMULATE-3K. These codes have been used to systematically model key noise sources (i.e. fuel assembly vibration, and inlet coolant temperature and flow fluctuations), and study their impact on the neutron noise phenomenology. In particular, the fuel lateral displacement can be modelled in the CASMO-5 code by modifying the lattice water side widths. The generated nuclear data are used in downstream 3D full core simulations utilizing the SIMULATE-3K code to model the fuel assembly

vibration by modifying the water gap widths between a selected bundle and its adjacent neighbors. The fuel assembly vibration modelling approach has been studied in detail and verified at a lattice level. Then, for the first time, the fuel assembly vibration model has been qualified at a 3D full core level through a series of simplified and complex scenarios. Key results showed that a vibrating fuel assembly affects mainly its adjacent neighbors, in the direction of vibration, resulting to higher noise levels. A temporal or static axial deformation (i.e. bow shape or vibration mode, respectively) is found to impact the axial noise distribution. Moreover, a tendency for higher noise amplitudes at the core-top could be identified because of the moderator density decrease. This detailed analysis, clearly, demonstrated the capabilities and the robustness of the newly developed PSI neutron noise methodology to successfully model key noise sources and reproduce neutron noise phenomena.

In addition, a comparative study has been carried out between the simulated results and the KKG measured data and revealed that the stochastic fluctuation of the inlet coolant temperature in combination with the fuel assembly vibration play a primary role on the KKG neutron noise behavior. Most importantly, it has been observed that the neutron noise increase trend observed in KKG could be explained, to some extent, by the introduction in the core of a newer fuel design which is more susceptible to lateral vibrations.

In parallel, the current thesis has significantly contributed to the establishment of a database of simulation results which has been extensively utilized by the consortium members of the Horizon-2020 CORTEX project. Simulated data generated by the PSI neutron noise modeling methodology have been systematically analyzed for developing and testing the performance of advanced signal analysis techniques using machine learning algorithms and deterministic solvers. The developed approaches have served as a solid basis for a growing network and promising further collaborations between PSI and international partners for future reactor physics research projects.

Last, a new in-house PSI methodology has been established serving as a supportive diagnostic tool for the detailed identification of signals connectivity patterns. To this aim, the PSI connectivity analysis methodology has been developed based on the causality analysis principles to help understanding the cause-and-effect interactions between nuclear reactor signals. The nuclear reactor core is analyzed utilizing the most eminent causality analysis techniques in the frequency domain, namely the rPDC and the DTF measures. The rPDC measure indicates the direct signals connections, whereas the DTF estimates how the information is transferred from a noise source to the rest of a multivariate system. Combined results from both the rPDC and the DTF measures indicate the root-cause of simulated or measured disturbances. The current research is the first-ever application of causality analysis techniques on the field of nuclear reactor data analysis. The applicability of the PSI methodology is demonstrated using analytical examples, simulated systems, and even against challenging real plant data. Results show that the developed methodology successfully indicates both all causal interconnections in analytical examples with predefined connectivity patterns, and the perturbation root-cause, which is a priori known, in a simulated reactor system. Most importantly, the application of the connectivity analysis methodology on real plant data has identified valuable information with respect to the measured plant disturbance and its involved connectivity patterns.

Keywords: *neutron noise, fuel assembly vibration modelling, causality analysis*

Zusammenfassung

Kernreaktoren sind von Natur aus stochastische Systeme, in denen die kontinuierliche Fluktuation der neutronischen und thermohydraulischen Parameter auch unter stationären Betriebsbedingungen über ihre Mittelwerte überwacht werden kann. Zudem vibrieren strukturelle und mechanische Komponenten wie die Brennelemente und der Kernbehälter ununterbrochen aufgrund der starken hydraulischen Kräfte, die durch die nach oben gerichteten Strömungen des Kernkühlmittels entstehen. Diese Stochastizität ist die Ursache für das fluktuierende Verhalten der Neutronenpopulation im Kern; ein Phänomen, das allgemein als Neutronenflussrauschen bezeichnet wird.

Die Reaktordetektorsignale, einschliesslich des Neutronenrauschniveaus, werden in Kernreaktoren während ihrer Lebensdauer kontinuierlich überwacht, da diese Informationen wertvolle Erkenntnisse über das Kernverhalten und seine Dynamik liefern können. Insbesondere kann die Überwachung des Neutronenrauschens zur Früherkennung von Anomalien genutzt werden, die während des Reaktorbetriebs auftreten können. Neutronenflussrauschen ist seit vielen Jahrzehnten ein intensiv untersuchtes Forschungsthema, das den Grundstein für die Entwicklung zahlreicher Rauschüberwachungsmethoden, Signalverarbeitungstechniken und analytischen Lösungen gelegt hat, die bis heute auf globaler Ebene gebräuchlich sind. Trotzdem hat eine unerwartete Tendenz zum Neutronenflussrauschen, wie sie in letzter Zeit in mehreren europäischen Kernreaktoren beobachtet wurde, sowohl in der Forschungsgemeinschaft als auch in der Industrie eine gesteigerte Aufmerksamkeit ausgelöst. Die Erhöhung des Neutronenrauschens ist sicherlich kein sicherheitsrelevanter Aspekt, allerdings bewirkt sie unerwünschte und teure Betriebsfolgen für die Betreiber. Die neuen Beobachtungen zeigen die Notwendigkeit eines besseren Verständnisses des Neutronenrauschverhaltens in Kernreaktoren, was das Hauptziel dieser Forschung ist.

Vor diesem Hintergrund versucht die vorliegende Doktorarbeit, das Neutronenrausch-Phänomen durch die Entwicklung innovativer Rauschmodellierungsmethoden systematisch zu analysieren. Das übergeordnete Ziel ist die Verbesserung der Rauschmodellierungstechniken, um ein tieferes Verständnis der dynamischen Mechanismen zu erlangen, die an jedem Reaktorkern beteiligt sind.

Zuerst wird das Hauptaugenmerk auf die Identifizierung der Neutronenrauschcharakteristiken des schweizerischen Kernreaktors Gösgen (KKG) gelegt, der ein typisches Beispiel für eine KWU-vor-Konvoi DWR Anlage darstellt. Die realen KKG-Daten wurden im Zeit- und Frequenzbereich mit traditionellen Signalverarbeitungstechniken detailliert analysiert. Diese systematische Analyse deckte Schlüsselaspekte der Neutronenrauschphänomenologie des KKG auf und ermöglichte eine bessere Charakterisierung der Rauschquellen, die das dynamische Verhalten des KKG beeinflussen. Die Ergebnisse zeigten eine systematische Zunahme des Neutronenrauschens innerhalb eines Zyklus und von Zyklus zu Zyklus, wobei eine Tendenz zu höheren Rauschniveaus in Richtung des axialen, oberen Bereichs des Kerns festgestellt werden konnte. Noch wichtiger ist, dass höhere Neutronenrauschamplituden auf der Kern-Ost-Seite beobachtet werden konnten; eine Rauschcharakteristik, die bei KKG einzigartig ist. Darüber hinaus weist die Rauschspektralanalyse auf den starken Einfluss von drei Hauptgeräuschquellen bezüglich der Neutronenrauschphänomenologie hin: die Temperaturschwankungen des Kühlmitteleintritts bei niedriger Frequenz (< $1\ Hz$), die Brennelementvibrationen bei etwa $2\ Hz$ und die Pendelbewegung des Kernrohrs bei $8\ Hz$.

Weiterhin wurde in dieser Arbeit eine Methode zur Modellierung von Neutronenrauschen entwickelt, wobei das fortschrittliche Codesystem CASMO-5/SIMULATE-3/SIMULATE-3K verwendet wurde. Diese Codes wurden zur systematischen Modellierung der Hauptgeräuschquellen (d.h. Brennelementvibrationen, Temperatur- und Strömungsschwankungen des Kühlmitteleintritts) und zur Untersuchung ihrer Auswirkungen auf die Phänomenologie des Neutronenrauschens verwendet. Insbesondere die laterale Brennstoffverschiebung kann im CASMO-5-Code durch die Modifizierung der Gitterwasserseitenbreiten modelliert werden. Danach werden die generierten nuklearen Daten in nachfolgenden 3D-Vollkernsimulationen unter Nutzung des SIMULATE-3K-Codes verwendet, um die Brennelementschwingung durch Modifizierung der Wasserspaltbreiten zwischen einem ausgewählten Bündel und seinen angrenzenden Nachbarn zu modellieren. Der Ansatz zur Modellierung der Brennelementschwingungen wurde detailliert untersucht und auf Gitterebene verifiziert. Im Zuge dessen wurde erstmalig das Brennelementschwingungsmodell systematisch untersucht und durch eine Reihe von vereinfachten und komplexen Szenarien auf einem 3D-Vollkernniveau qualifiziert. Die wichtigsten Ergebnisse zeigten, dass ein vibrierendes Brennelement hauptsächlich seine benachbarten Nachbarn in Vibrationsrichtung beeinflusst, was zu höheren Geräuschniveaus führt. Es wurde festgestellt, dass eine zeitliche oder statische axiale Verformung (d. h. eine Bogenform bzw. ein Schwingungsmodus) die axiale Geräuschverteilung beeinflusst. Darüber hinaus konnte eine Tendenz zu höheren Geräuschamplituden an der Oberseite des Kerns festgestellt werden, die auf die Abnahme des Moderator Temperaturkoeffizienten zurückzuführen ist. Diese detaillierte Analyse zeigt deutlich die Fähigkeiten und die Robustheit der neu entwickelten PSI-Neutronenrauschmethodik zur erfolgreichen Modellierung von Schlüsselrauschquellen und zur Reproduktion von Neutronenrauschphänomenen.

Des Weiteren wurde eine Vergleichsstudie zwischen den simulierten Ergebnissen und den KKG-Messdaten durchgeführt und ergab, dass die stochastische Schwankung der Kühlmitteleintrittstemperatur in Kombination mit der Brennelementvibration eine Hauptrolle für das Neutronenrauschverhalten des KKG spielt. Am wichtigsten ist die Erkenntnis, dass der bei KKG beobachtete Trend bezüglich der Zunahme des Neutronenrauschens bis zu einem gewissen Grad durch die Einführung einer neueren Brennstoffauslegung im Kern erklärt werden kann, die anfälliger für laterale Schwingungen ist.

Parallel dazu hat die Dissertation wesentlich zum Aufbau einer Datenbank mit Simulationsergebnissen beigetragen, die von den Konsortiumsmitgliedern des CORTEX-Projekts Horizon-2020 intensiv genutzt wurde. Die mit der PSI-Neutronenrausch-Modellierungsmethodik erzeugten simulierten Daten wurden systematisch analysiert, um die Leistung fortschrittlicher Signalanalyseverfahren unter Verwendung von Algorithmen des maschinellen Lernens und deterministischer Solvern zu entwickeln und zu testen. Die erarbeiteten Ansätze dienen als solide Grundlage für ein wachsendes Netzwerk und vielversprechende weitere Zusammenarbeit zwischen dem PSI und internationalen Partnern für künftige Forschungsprojekte in der Reaktorphysik.

Darüber hinaus wurde eine neue interne Methodik eingeführt, die als unterstützendes Diagnosetool für die detaillierte Identifizierung der Verbindungsmuster von Signalen verwendet wird. Zu diesem Zweck wurde die PSI-Methodik der Konnektivitätsanalyse auf der Grundlage der Prinzipien der Kausalitätsanalyse entwickelt, um die Ursache- und Wirkungsinteraktionen zwischen Kernreaktorsignalen aufzuzeigen. Der Reaktorkern wird unter Verwendung der bekanntesten Kausalitätsanalyse-Techniken im Frequenzbereich, nämlich der rPDC- und der DTF-Messungen, analysiert. Das rPDC-Mass zeigt die direkten Verbindungen der Signale an, während das DTF-Mass schätzt, wie die Information von einer Rauschquelle auf den Rest eines multivariaten Systems übertragen wird. Kombinierte Ergebnisse sowohl des rPDC- als auch des DTF-Kausalitätsmasses weisen auf die Ursache der simulierten oder gemessenen Störungen hin. Die vorliegende Arbeit ist die erste Anwendung von Kausalitätsanalyse-Techniken auf Kernreaktordaten. Die Anwendbarkeit der PSI-Methodik der

Konnektivitätsanalyse wird anhand analytischer Beispiele, simulierter Systeme und sogar anhand anspruchsvoller realer Anlagendaten demonstriert. Die Ergebnisse zeigen, dass die entwickelte Methodik erfolgreich sowohl alle kausalen Zusammenhänge in analytischen Beispielen mit vordefinierten Konnektivitätsmustern als auch die a priori bekannte Störungsursache in einem simulierten Reaktorsystem aufzeigt. Am wichtigsten ist, dass die Anwendung der Methodik der Konnektivitätsanalyse auf reale Anlagendaten wertvolle Informationen in Bezug auf die gemessene Anlagenstörung und die damit verbundenen Konnektivitätsmuster identifiziert hat.

Schlüsselwörter: *Neutronenflussrauschen, Kausalitätsanalyse, Brennelementvibrationsmodellierung*

Περίληψη

Οι πυρηνικοί αντιδραστήρες σχάσεως είναι εκ φύσεως στοχαστικά συστήματα, στους οποίους νετρονικοί και θερμοϋδραυλικοί παράμετροι παρατηρείται διακύμανση ως προς τις μέσες τιμές τους ακόμα και υπό συνθήκες κανονικής λειτουργίας. Επιπλέον, κατασκευαστικά και μηχανικά μέρη του πυρήνα του αντιδραστήρα, όπως οι δέσμες πυρηνικού καυσίμου και ο κύλινδρος συγκράτησης του πυρηνικού καυσίμου, δονούνται ακατάπαυστα λόγω των ισχυρών υδραυλικών δυνάμεων, οι οποίες πηγάζουν από τη κυκλοφορία του ψυκτικού υγρού. Αυτή η στοχαστικότητα είναι η αιτία της διακυμαίνουσας συμπεριφοράς του νετρονικού πληθυσμού στον πυρήνα του αντιδραστήρα· ένα φαινόμενο το οποίο ονομάζεται νετρονικός θόρυβος.

Η ανάλυση σημάτων ενός πυρηνικού αντιδραστήρα προσφέρει σημαντική πληροφόρηση ως προς την εις βάθος κατανόηση της λειτουργίας του. Συνεπώς, τα σήματα ενός αντιδραστήρα, συμπεριλαμβανομένων των επιπέδων του νετρονικού θορύβου, παρακολουθούνται και ερευνώνται συνεχώς καθ' όλη τη διάρκεια λειτουργίας ενός πυρήνα. Επιπλέον, η ανάλυση του νετρονικού θορύβου μπορεί να χρησιμοποιηθεί για την έγκαιρη διάγνωση πιθανής δυσλειτουργίας του αντιδραστήρα. Ο νετρονικός θόρυβος έχει εκτενώς μελετηθεί στο παρελθόν, θέτοντας τις βάσεις για την ανάπτυξη αρκετών μεθόδων παρακολούθησης, ανάλυσης και μοντελοποίησης του φαινομένου, οι οποίες χρησιμοποιούνται μέχρι και σήμερα. Ωστόσο, προσφάτως αρκετοί ευρωπαϊκοί πυρηνικοί αντιδραστήρες (του γερμανικού μοντέλου KWU pre-Konvoi PWR) παρουσίασαν μία απροσδόκητη αυξάνουσα τάση του νετρονικού θορύβου. Λόγω αυτής της συμπεριφοράς, η ερευνητική κοινότητα και η βιομηχανία έστρεψαν ξανά την προσοχή τους στη μελέτη του νετρονικού θορύβου. Πρέπει να σημειωθεί ότι η αυξάνουσα τάση του νετρονικού θορύβου δεν σχετίζεται επουδενί με την ασφάλεια του πυρηνικού αντιδραστήρα, έχει, ωστόσο, κοστοβόρες επιπτώσεις για τις διαχειρίστριες εταιρίες. Τα νέα δεδομένα καταδεικνύουν την ανάγκη για εμβάθυνση της κατανόησης του νετρονικού θορύβου. Ως εκ τούτου, κύριος στόχος της παρούσας διδακτορικής διατριβής είναι η συστηματική και ενδελεχής έρευνα του φαινομένου του νετρονικού θορύβου αναπτύσσοντας καινοτόμες μεθόδους μοντελοποίησης και ανάλυσης του.

Στο πλαίσιο αυτό, έμφαση δίνεται πρώτα στην ταυτοποίηση των χαρακτηριστικών του νετρονικού θορύβου του ελβετικού πυρηνικού αντιδραστήρα ισχύος Γκέσγκεν (KKG). Ο KKG, όντας ένα KWU pre-Konvoi PWR μοντέλο, έχει παρουσιάσει μία διαρκή αύξηση των επιπέδων νετρονικού θορύβου κατά την τελευταία δεκαετία. Στην παρούσα διατριβή, σήματα και δεδομένα από τον KKG αναλύονται λεπτομερώς τόσο στο πεδίο του χρόνου όσο και σε αυτό των συχνοτήτων χρησιμοποιώντας συμβατικές μεθόδους ανάλυσης σημάτων. Κύριες εκφάνσεις της μορφολογίας του νετρονικού θορύβου του υπό ανάλυση αντιδραστήρα μπόρεσαν να ταυτοποιηθούν μέσω της ενδελεχούς ανάλυσης σημάτων, βοηθώντας στην κατανόηση των μορφών και πηγών θορύβου, οι οποίες επηρεάζουν τη δυναμική λειτουργία του KKG. Πιο συγκεκριμένα, τα επίπεδα του νετρονικού θορύβου αποδείχθηκαν να έχουν συστημική αυξάνουσα τάση τόσο κατά τη διάρκεια ενός κύκλου λειτουργίας όσο και μεταξύ διαδοχικών κύκλων λειτουργίας του KKG. Επίσης, υψηλότερα επίπεδα θορύβου παρατηρούνται στο άνω τμήμα του αντιδραστήρα, καθώς και στην ανατολική πλευρά του πυρήνα (ένα χαρακτηριστικό που δεν έχει αναφερθεί στην βιβλιογραφία για κάποιον άλλο αντιδραστήρα έως τώρα). Επιπρόσθετα, τρεις πηγές θορύβου μπόρεσαν να ταυτοποιηθούν μέσω της φασματικής ανάλυσης του νετρονικού θορύβου· πρώτον, η διακύμανση του ψυκτικού υγρού στην είσοδο του πυρήνα με χαμηλές συχνότητες ($< 1\ Hz$), δεύτερον, η δόνηση των δεσμών πυρηνικού καυσίμου σε συχνότητα περί τα $2\ Hz$, και τέλος, η εκκρεμής κίνηση του κυλίνδρου συγκράτησης του πυρήνα σε συχνότητας $8\ Hz$.

Εν συνεχεία, οι προηγμένοι υπολογιστικοί κώδικες CASMO-5, SIMULATE-3 και SIMULATE-3K χρησιμοποιήθηκαν στην παρούσα διατριβή για την ανάπτυξη μίας νέας μεθόδου μοντελοποίησης του νετρονικού θορύβου και της διάδοσης του στο σύνολο του πυρήνα. Η μέθοδος αυτή επιτρέπει την συστηματική μοντελοποίηση των σημαντικότερων πηγών θορύβου (όπως επισημάνθηκαν ανωτέρω), καθώς και την ανάλυση των επιπτώσεων τους στη φαινομενολογία του νετρονικού θορύβου. Πιο συγκεκριμένα, η πλευρική στατική μετατόπιση του πυρηνικού καυσίμου μπορεί να προσομοιωθεί μέσω του κώδικα CASMO-5 τροποποιώντας την ποσότητα επιβραδυντή (νερό) που αντιστοιχεί σε κάθε δέσμη καυσίμου. Έπειτα, τα παραγόμενα νετρονικά δεδομένα χρησιμοποιούνται από τον τρισδιάστατο υπολογιστικό κώδικα SIMULATE-3K για την μοντελοποίηση της πλευρικής δόνησης των πυρηνικών δεσμών τροποποιώντας την ποσότητα επιβραδυντή μεταξύ της δονούμενης και των δύο πλευρικών δεσμών. Οι δυνατότητες των χρησιμοποιούμενων κωδίκων προσομοίωσης καθώς και η απόδοση της αναπτυγμένης τεχνικής, ως σύνολο, επαληθεύονται εκτενώς ως προς αποτελέσματα αναφοράς και σε σύγκριση με διάφορα σενάρια προσομοίωσης. Τα σημαντικότερα ευρήματα επισημαίνουν υψηλότερα επίπεδα νετρονικού θορύβου εκατέρωθεν μίας δονούμενης δέσμης καυσίμου. Ακόμα, η χρονική ή και στατική παραμόρφωση της αξονικής γεωμετρίας μίας δέσμης βρέθηκε να επηρεάζει την αξονική κατανομή του νετρονικού θορύβου. Υψηλότερες τιμές θορύβου παρατηρούνται, επιπλέον, στο άνω τμήμα του πυρήνα λόγω της αντίστοιχης μείωσης της πυκνότητας του επιβραδυντή. Η παρούσα ενδελεχής ανάλυση κατάφερε να παρουσιάσει τις δυνατότητες και την αποτελεσματικότητα της νέας μεθοδολογίας για την μοντελοποίηση του φαινομένου του νετρονικού θορύβου.

Παράλληλα, η σημασία τόσο της διακύμανσής του ψυκτικού υγρού όσο και των δονούμενων πυρηνικών δεσμών αποδείχθηκε μέσω της σύγκρισης των υπολογιστικών αποτελεσμάτων και των μετρήσιμων δεδομένων από τον KKG. Ακόμα, διαπιστώθηκε ότι η αυξάνουσα τάση του νετρονικού θορύβου στον KKG μπορεί να αποδοθεί στη χρησιμοποίηση ενός νέου τύπου πυρηνικού καυσίμου, το οποίο δονείται πλευρικά με μεγαλύτερη ευκολία ακόμα και υπό κανονικές συνθήκες λειτουργίας.

Περαιτέρω, η παρούσα διδακτορική διατριβή συνείσφερε σημαντικά στη δημιουργίας μίας βάσης υπολογιστικών δεδομένων, η οποία έχει χρησιμοποιηθεί εκτενώς από τα μέλη της κοινοπραξίας του ευρωπαϊκού ερευνητικού προγράμματος Horizon- 2020 CORTEX. Προσομοιωμένα δεδομένα μέσω της μεθοδολογίας μοντελοποίησης νετρονικού θορύβου του PSI έχουν μελετηθεί και αναλυθεί από τους συνεργάτες του ερευνητικού προγράμματος με στόχο την ανάπτυξη και τον έλεγχο επίδοσης διάφορων προηγμένων μεθόδων αναλύσεως σημάτων χρησιμοποιώντας αλγορίθμους μηχανικής μάθησης και ντετερμινιστικούς κώδικες. Οι αναπτυγμένες μέθοδοί συνείσφεραν στην βελτίωση της δικτύωσης και στη μελλοντική συνεργασία μεταξύ του PSI και τον διεθνών συνεργατών σε ερευνητικά προγράμματα πυρηνικής φυσικής του αντιδραστήρα.

Τέλος, μία νέα μεθοδολογία αναπτύχθηκε για την ενδελεχή μελέτη και κατανόηση των μοτίβων συνδεσιμότητας μεταξύ σημάτων. Η μέθοδος αυτή μπορεί να χρησιμοποιηθεί ως υποστηρικτικό διαγνωστικό εργαλείο για εφαρμογές πυρηνικής τεχνολογίας και βασίζεται πάνω στις αρχές της ανάλυσης αιτιότητας με στόχο να ερευνήσει τις σχέσεις αιτίας και αιτιότητας μεταξύ σημάτων του αντιδραστήρα. Ως εκ τούτου, οι τεχνικές αιτιότητας rPDC και DTF, οι οποίες είναι οι πιο διαδεδομένες τεχνικές στο πεδίο των συχνοτήτων με βάση τη βιβλιογραφία, χρησιμοποιούνται στην παρούσα εργασία. Η πρώτη υπολογίζει τα επίπεδα απευθείας συνδεσιμότητας μεταξύ σημάτων, ενώ η δεύτερη καταδεικνύει πως ένα σήμα μπορεί να μεταφερθεί από μία πηγή στο υπόλοιπο σύστημα. Τα αποτελέσματα και των δύο τεχνικών μπορούν να χρησιμοποιηθούν για την εύρεση του βασικού αιτίου μίας προσομοιωμένης ή μίας μετρήσιμης διαταραχής του συστήματος. Η αποτελεσματικότητα των αρχών της ανάλυσης αιτιότητας σε πυρηνικά συστήματα παρουσιάζεται μέσω

αναλυτικών εφαρμογών, προσομοιωμένων συστημάτων, καθώς και μέσω πολύπλοκων μετρήσιμων δεδομένων. Οι εφαρμογές αυτές δείχνουν ότι η παρούσα μέθοδος μπορεί να υπολογίσει αποτελεσματικά όλες τις συσχετίσεις αιτιότητας σε αναλυτικά μοντέλα με προκαθορισμένες αλληλεπιδράσεις σημάτων, αλλά και να αποφανθεί ορθώς ως προς την a priori κύρια αιτία μίας προσομοιωμένης διαταραχής. Σημαντικότερα, η εφαρμογή της ανάλυσης αιτιότητας σε μετρήσιμα δεδομένα μπόρεσε να προσφέρει πολύτιμες πληροφορίες σχετικά με πραγματικές διαταραχές στη λειτουργία ενός πυρηνικού αντιδραστήρα.

Λέξεις κλειδιά: *νετρονικός θόρυβος, ανάλυση αιτιότητας, μοντελοποίηση δόνησης δεσμίδων πυρηνικού καυσίμου*

Content

List of Figures

List of Tables

Chapter 1: Introduction

This chapter introduces the reader to the so-called neutron noise phenomenon, which is the central topic of research that the current doctoral thesis deals with. To this aim, a brief literature review is provided about the importance of the neutron noise phenomenon on monitoring the normal operation of nuclear reactors and on detecting abnormal behaviors. In addition, a general overview is given about the main achievements in neutron noise analysis and modelling, which have significantly assist in the understanding of the reactor operation. The limitations and shortcomings of the existing techniques are also discussed, and therefore, the area of application of the current thesis is then defined. Furthermore, the main motives and objectives of the present doctoral research are described then, followed by a short description of the original contributions that have been achieved throughout this work. Finally, in the end of this chapter the thesis structure and the main highlights of each chapter are presented.

1.1. Background

In a rapidly developing world with a significant increase of the electricity demand, nuclear power plants (NPP) provide a reliable solution for the worldwide base-load electricity mix and contribute to lowering the carbon dioxide (CO_2) footprint. The industrial full scale application of nuclear power started in 1956 at Calder Hall in the United Kingdom, where the very first commercial nuclear reactor for electricity production was commissioned. Since then, the nuclear industry and research institutes have intensively worked on enhancing the understanding of the nuclear reactors operation and on developing more advanced reactor designs, focusing on the safety of the population and the environment. Nuclear power provides nowadays about 10% of the worldwide electricity through the operation of 450 nuclear reactors in 30 countries [1]. In addition, about 225 research and experimental reactors operate currently in more than 50 countries for promoting education and improving operators training, as well as, for the production of medical and industrial isotopes [1].

A nuclear reactor, independently of its type and design, is a rather complex system, utilizing a series of processes in order to generate electricity based on the nuclear fission reaction within the nuclear fuel. The reactor core is the most important and crucial component of a nuclear reactor, since it hosts the nuclear fuel, and allows the fission reactions to occur and the energy to be released into the coolant. The steadily and reliably electricity production is directly related to the controlled process of the nuclear fission reactions within the core. This can be achieved by designing the reactor operation (e.g. core loading pattern, cycle depletion process, energy utilization plan, etc.) to be fully compatible with all the international and national safety requirements and by preserving all the thermal margins during normal and transient conditions. The reactor operation is designed using advanced simulation tools, which intend to model with high precision the neutron diffusion within the reactor core. These reactor simulation tools can predict the reactor operation at every depletion step of the cycle and their precision is periodically compared against plant measurements. The latter are performed using a continuous monitoring system that exists in every nuclear reactor.

The monitoring system is of key importance for the reactor operation, since it provides to the reactor control system all the data about the status of the reactor sub-systems. Consequently, the operators have all the needed information in hand in order to operate safely the reactor and to perform with confidence any planned or unplanned manoeuver. The reactor monitoring system collects data at short time steps from all key processes taking place in the reactor. Of highest importance are the neutron detector signals, for monitoring

the neutron flux at various locations of the core; the fuel temperature responses, for screening the maximum temperature at the top of the fuel assemblies; the coolant flow and temperature signals, for tracking the coolant flow properties at the core inlet; the reactor pressure gauges, for monitoring the maximum pressure within the reactor pressure vessel; and others. Ordinarily, under normal operating conditions, the reactor signals have a steady-state behavior. However, under transient events the reactor signals automatically activate all the necessary control systems (e.g. SCRAM system, safety relief valves, etc.), which preserve and ensure the safe status of the reactor. Most importantly, the continuous monitoring and analysis of the reactor signals with traditional and advanced signal analysis techniques can provide, on the one hand, valuable information of the physical phenomena taking place under normal reactor operation, and can contribute, on the other hand, to the identification of the processes, which led to abnormal conditions.

1.1.1. Reactor signals processing

Historically, both the nuclear industry and the research institutes have been actively involved in the development and utilization of various signal analysis techniques for extracting important information about the reactor operation from the reactor signals [2]. These signal analysis techniques can be categorized in two groups: the traditional/standard and the advanced techniques. The former group is based on the evaluation of the statistical characteristics of the reactors signals, e.g. mean value, standard deviation, signal to noise ratio, peak to peak amplitude, etc.; and on their analysis in the time and frequency domains, without any need of high computational power ([3], [4]). The statistical analysis, in the traditional approach, can give a quick and rough estimation of the signals quality and a prompt assessment about the normal reactor operation. The reactor signals can be studied using the correlation function in the time domain, and the coherence and phase difference functions in the frequency domain, in order to estimate any pairwise dependency pattern and the level of synchronization between the analyzed signals. In addition, the signal spectral representation reveals the frequency components of importance, and therefore, valuable information about the signals nature can be extracted without high computational power. All these signal characteristics are commonly monitored at different depletion steps and their tendency over the cycles is periodically estimated. A modification in the core operation or the core design strategy could result into an alternation of the signals characteristics. In case of an abnormal event, the traditional analysis techniques are used, to some extent, in order to identify, which signal pairs are highly correlated to each other, and therefore, a basic assessment of those processes that might lead to this excitation of the reactor operation can be made.

At PSI, the STARS project[1], within the activities of the Laboratory of Reactor Physics and Thermal-Hydraulics (LRT), has a long and proven experience on the systematic analysis of nuclear plant data for all the Swiss nuclear reactors. In this context, a Time Signal Analysis methodology for Reactors (PSI-TSAR) has been developed at STARS by utilizing various statistical tools in the time- and the frequency-domain. In addition, the PSI-TSAR methodology has been already successfully utilized for estimating the stability characteristics of the Swiss boiling water reactor (BWR), Leibstadt (KKL), for all stability tests performed at various cycles; and for analyzing a stability event that took place during the start-up of cycle 24 ([5], [6]).

The continuous enhancement of instrumentation and monitoring devices (e.g. increased number of simultaneously recorded signals, higher sampling frequency, improved signals filters, etc.) and the improvements in computational power allowed the development of more advanced signal processing

[1] STARS project: Steady-state and Transient Analysis Research for the Swiss reactors (https://www.psi.ch/en/stars, accessed on 26.06.2020).

techniques. These techniques analyze simultaneously the interdependency patterns between multiple signals, and therefore, a more reliable and detailed characterization of the interconnectivity relationships between the system processes could be achieved. For example, already in the early '$80s$, the signal transmission path (STP) method has been utilized widely in nuclear reactor applications for identifying the feedback mechanisms among reactor signals [7]. The STP method introduced a significant improvement in the signal processing approach, since it allows the analyst to estimate the direction of influence between two signals, and consequently, a better understanding of the system behavior could be performed. The STP method has been already applied, at PSI/LRT, in the analysis of the signals interconnectivity direction for KKL measured data [8]. Other examples of highly promising techniques for estimating faulty mechanisms are based on pattern recognition and on artificial neural networks methods. The former method focuses on identifying the system anomalies based on symbolic feature extraction and the associated pattern classification, whereas the latter method emphasizes on unfolding, de-noising and reconstructing the signals with the goal to localize and characterize any perturbation source using deep neural network architectures. First successful applications of these advanced signal processing techniques on nuclear reactor data have been already demonstrated in ([9], [10]).

The continuous developments and enhancements in signal processing methods indicate the importance of the estimation of the leading role of the key processes within an analyzed system. The key processes drive the response of other signals and therefore, the identification of causal interdependencies between signals can indicate the excitation source of the system. The identification of causal interdependencies is equally important for normal operation (i.e. for understanding the information flow paths between signals) and for transient events (i.e. for estimating the root-cause of a perturbation). Several researchers have identified the important role of causation between signals and in this context many methods and techniques have been developed in order to identify the *cause-and-effect* relationships within a system. The most eminent techniques are based on the so-called *Granger causality* concept, which simply states that *if the past of one signal significantly improves the prediction of the future of a second signal, then the former is said to be the cause of the latter* [11]. Causality techniques have been widely applied in many research areas, such as in econometrics, climatology, biology, process engineering, etc., and have demonstrated their capabilities in identifying the causal structure of highly complicated and complex systems.

As it will be presented in the next paragraphs and the following chapters, this doctoral thesis intends to bridge the gap between advanced signal processing techniques and nuclear reactor applications. To this aim, the most eminent causality techniques are applied on nuclear reactor measured and simulated data, and a new approach for assessing the reactor status is proposed. Emphasis is given to the systematic study on the *neutron noise* phenomenon, briefly introduced in the next section.

1.1.2. Neutron noise phenomenon

One of the nuclear reactor phenomena that significantly strengthen the utilization and development of signal analysis techniques in nuclear reactor applications is the *neutron noise* phenomenon. Neutron noise analysis provides a profound mean of understanding the fundamental mechanisms driving the operation of a nuclear reactor, and therefore, its analysis can be used for identifying the feedback relationships, defining the complex nature of the reactor core and its sub-systems. In this sub-section, the neutron noise phenomenon is introduced and in the following chapters a detailed description of its nature and its importance is given in detail.

As already mentioned in the previous sub-section, all nuclear reactors are equipped with neutron detectors in order to measure the time-dependent response of neutron population at various locations inside and outside the reactor core, i.e. in-core and ex-core detectors, respectively. The estimation of the reactor power is based on the neutron detectors response, commonly observed to have a stochastic nature. This stochasticity or randomness depends on the inherent comportment of several neutronic and thermal-hydraulic parameters that are randomly fluctuating over their mean values, even at steady-state conditions. In addition, structural and fuel components of the core are incessantly vibrating due to the strong hydraulic forces originating from the coolant flow. All these perturbation and fluctuation sources are affecting the neutrons transport rate and consequently, the neutron detectors indicate a fluctuating response, frequently referred as the *neutron noise*. The neutron noise is commonly estimated as the amplitude of neutron detectors fluctuations (i.e. standard deviation) over their mean value. Fig. 1 represents schematically some examples of various types of parameters (e.g. fission yield, vibration of core barrel, fluctuation on inlet temperature, etc.) that affect the neutron balance locally or even globally, and consequently, drive the stochastic fluctuation of neutron flux in the time domain.

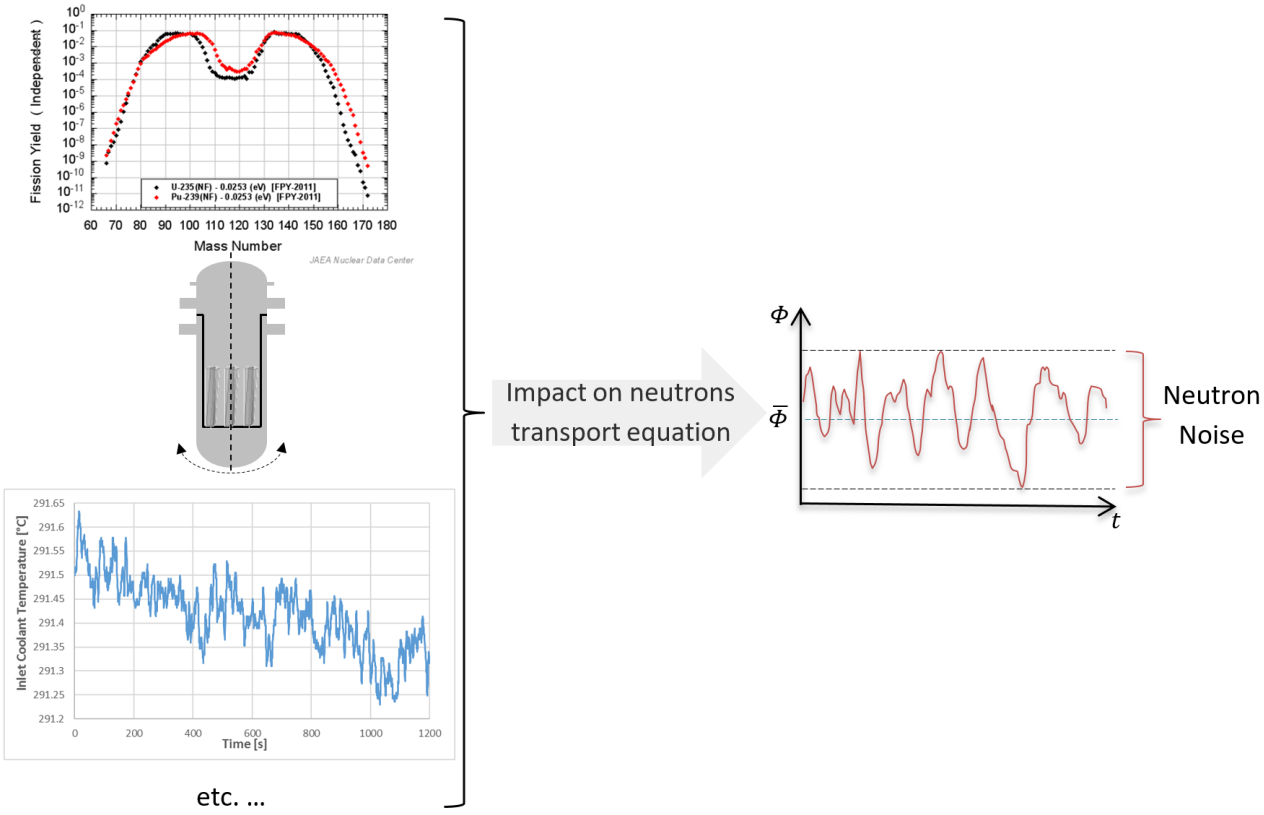

Fig. 1: Dependency of neutron noise on various stochastic perturbations.

The significant role of neutron noise in nuclear reactor applications was identified early enough due to its important role in estimating the reactor behavior and identifying the reactor characteristics that can lead to possible malfunctions ([12], [13]). The neutron detector signals are periodically analyzed in both the time and the frequency domains and their responses can be used for assessing the reactor behavior under various operating conditions (e.g. depletion steps, reactor power and flow, control rod density, etc.) and core designs (e.g. change of fuel design, uprate in reactor power, longer operational cycles, etc.). A typical shape of the neutron detector response in the frequency domain over different operational cycles for a German pressurized water reactor (PWR) is presented in the Fig. 2. The systematic analysis of the detector responses identifies the

reactor-specific characteristics, called also neutron noise signatures, which correspond to the individual neutron noise features. Extensive measuring campaigns are commonly performed at many nuclear reactors in order to identify the perturbation sources that affect the neutron noise phenomenology. Noise sources that typically appear in LWRs (Fig. 2) include, among others, the lateral vibration of the fuel assemblies in the frequency range of 1-5 Hz, the core barrel motion of various modes at around 8 Hz and 20 Hz, the inlet coolant temperature and flow fluctuation at the low frequency range below 5 Hz, and others [14]. The deep and detailed knowledge of the plant-specific noise signatures is of paramount importance since any possible deviation from normal operating conditions can be reflected into the neutron detectors responses, and consequently, it can be promptly identified. Clearly, the early identification of possible malfunctions depends on the quality of the measured signals and the utilized signal processing techniques.

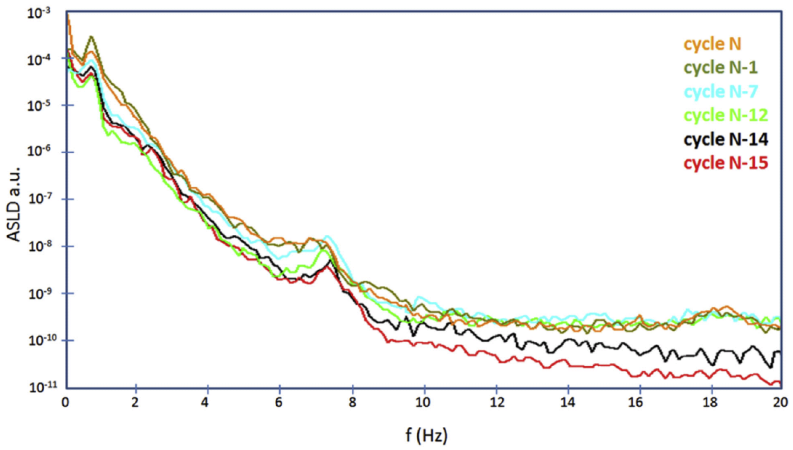

Fig. 2: Neutron detector spectrum for a German PWR at different operational cycles [14].

1.1.3. Neutron noise modelling

In parallel to the signal processing of measured neutron detectors signals, attention is also given to the modelling of noise sources using advanced simulation tools in order to understand in-depth the mechanisms involved in the neutron noise phenomenon. The significant increase in computer power over the last decades allowed significant improvements and enhancements of the reactor physics and thermal-hydraulics codes. Among other developments, several deterministic and probabilistic codes are now able to model, in high detail, a large variety of noise sources and assess their impact on the neutron noise phenomenology. Most of the deterministic solvers (e.g. SIMULATE-3K, DYN3D, APOLLO3, PARCS, etc.) perturb the macroscopic cross-sections or the coolant properties in the time domain in order to simulate the fuel pin/assembly lateral vibration or the inlet coolant flow/temperature fluctuation, respectively, and consequently, to estimate the neutron flux response by solving the neutron transport/diffusion equation. Other probabilistic codes solve the transport equation in the time (i.e. Serpent-2) or the frequency domain (i.e. TRIPOLI-4) and allow the perturbation of the macroscopic cross sections for modelling the fuel vibration, too. The most eminent code for neutron noise modelling is CORE SIM, a dedicated neutron noise solver in the frequency domain, which has been validated against plant data and has been extensively used for modelling various types of noise sources (e.g. control rod vibration, core barrel oscillation, travelling perturbations, etc.) [15]. It should be noted that, only few codes (e.g. CORE SIM and the noise modules of APOLLO3 and TRIPOLI-4) have been verified for noise application. Modelling of neutron noise phenomena has an important role on the identification of specific neutron noise characteristics by performing a direct comparison against real plant data. It is recalled that, the nuclear reactor is a rather complex system, and consequently, several sources are

simultaneously influencing the neutron noise phenomenology. Clearly, the advanced simulation tools can be used in order to model individually the most important sources and asses their separate impact on the neutron noise behavior. The latter would be relatively difficult to be achieved by utilizing only signal processing techniques, since it is practically impossible to isolate individual noise sources (e.g. fuel assembly vibration, coolant properties fluctuation, etc.) and study their impact on the detectors response. In a nutshell, the neutron noise modelling can be used as a supportive tool for enhancing the nuclear reactor monitoring and surveillance.

The profound advantages of the neutron noise modelling on the understanding of the reactor behavior triggered in 2015 the preparation of a concentrated effort for developing innovative methods and techniques for the neutron noise phenomenon study in order to enhance the reactor safety [16]. These efforts led to the European Union-funded research project CORTEX (i.e. CORe monitoring Techniques and EXperimental validation and demonstration), launched its activities in 2017 by bringing on board 20 European and oversees partners with long experience in reactor diagnostics and reactor physics modelling. The CORTEX project focuses on the utilization of neutron noise modelling combined with machine learning techniques in order to detect and identify possible anomalies appeared in a nuclear reactor by analyzing the measured neutron detector responses. PSI is an active member of the CORTEX project providing, among other duties, simulated neutron noise data to the consortium partners. The PSI contribution in the CORTEX project will be described in more details the next paragraphs.

1.2. Thesis motivation

Neutron noise phenomena have been studied in Europe already since the ‘$80s$ when KWU (i.e. the predecessor of SIEMENS) introduced in the market a new type of PWRs, namely the pre-Konvoi reactors. These reactors were constructed in Germany, Switzerland and Spain, among others, and they have experienced small but not negligible neutron noise amplitudes since the beginning of their operation. As mentioned earlier, the neutron noise phenomenon corresponds to the fluctuation of the neutron detectors signal over their mean value. In the case of the KWU pre-Konvoi PWRs, the neutron noise levels were significantly larger, already from their commissioning, compared to other reactor types. The neutron noise characteristics during the first operational cycles of the KWU pre-Konvoi PWRs were able to be identified using traditional/standard signal processing techniques. Therefore, the reactor-specific noise characteristics were determined for each reactor. However, a trend in which an unexpected increase of the neutron noise amplitude has been observed in the KWU pre-Konvoi PWRs in the last two decades. These abnormally high neutron noise levels have been found to be unrelated to any safety issue, however, in many cases they have caused undesirable costly operational consequences (e.g. activation of the SCRAM system, modification of the reactor operation by restricting the maximum power output, etc.). An example on the characteristic of the neutron noise level increase over the reactor depletion in many cycles is presented in Fig. 3 for a German KWU pre-Konvoi PWR.

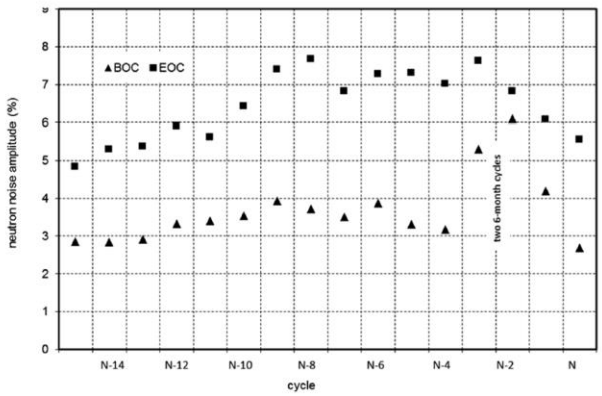

Fig. 3: Neutron noise level increase trend in a German KWU pre-Konvoi PWR [14].

The Swiss Gösgen power plant (KKG) is a KWU pre-Konvoi PWRs that exhibited similar increase of neutron noise levels since 2007 (i.e. operating cycle 28). The neutron noise level increase trend in KKG is monitored over the last decade by dedicated measuring campaigns using both in-core and ex-core neutron detectors. The occurrence of this trend triggered some preliminary in-house investigations in order to identify the root-cause of this behavior. Since no significant modification occurred either on the plant structure or on the reactor operation conditions before and after the appearance of the trend, a possible explanation of this phenomenon can be attributed to the introduction of a new type of fuel design, in the core, which coincided with the appearance of the noise level increase trend. Based on the long-standing collaboration of PSI/LRT with the Swiss nuclear industry and the well-established experience of the STARS project in reactor signal analysis, the current doctoral research was established in order to study in high detail the observed neutron noise level increase trend in KKG and to assist in better and deeper understanding of the underlying phenomena.

Therefore, the *main motive* and starting point of this doctoral thesis originated from this undesirable high neutron noise level increase trend, observed in the KKG core for more than a decade. This work intents to perform a deeper investigation on the neutron noise phenomena by systematically analyzing the reactor signals from KKG and by unfolding those noise characteristics that could be responsible for the observed behavior. Advanced signal processing techniques and state-of-the-art modelling tools are used, in this framework, for analyzing the phenomena of interest. By carrying such task, the PSI reactor signal techniques can be further developed and enhanced in order to investigate and study more efficiently and systematically the neutron noise phenomena. Therefore, the PSI-TSAR will become a consolidated methodology for analyzing nuclear reactor signals.

1.3. Thesis goals and objectives

The analysis of the neutron noise phenomenon is triggered by the ambition to understand in-depth the fundamental behavior and the underlying mechanisms contributing into the stochastic operation of nuclear reactors. It should be emphasized that, neutron noise is an inherent characteristic of any nuclear reactor type, and therefore, the systematic study of neutron noise behavior indicates key feature signatures of the analyzed core. More importantly, neutron noise analysis can contribute in the early detection of deviations from normal operation due to possible malfunctions, as mentioned earlier. Therefore, research centers and nuclear utilities are constantly monitoring and studying the neutron noise trends and characteristics. To this aim, signal analysis techniques have been developed over the years in order to estimate the key neutron noise characteristics and to indicate or even identify the impact of various perturbation sources on the measured

neutron noise behavior. Historically, these signal post-processing techniques focus on estimating the degree of similarity between signals in the time and in the frequency domains using the correlation and coherence functions, respectively. It is important to note that, the correlation and coherence functions can analyze the interdependency between only two signals at a time (i.e. bivariate systems). Consequently, it is practically impossible to identify the root-cause of a perturbation within a multi-variate system when traditional signal analysis techniques are used. Since a nuclear reactor is a rather complex system, including tight interconnections between neutronic and thermal-hydraulic parameters, it is self-evident that advanced signal analysis techniques are needed in order to systematically investigate the information flow paths between the various reactor processes.

Therefore, the *first main goal* of this doctoral thesis is to *implement advanced signal analysis techniques* in order to consolidate the existing signal analysis methodology of PSI/LRT, by further enhancing the in-house signal post-processing methods in extracting valuable signals signatures and characteristics from real plant data. To this aim, a methodology is developed, based on the so-called *causality signal analysis techniques* in order to study and analyze the cause-and-effect problem in nuclear reactor systems. Causality analysis techniques have been developed, originally, in the field of econometrics and successfully applied in neuroscience, mainly, for studying the complex structure of the human brain. An analogy between the human brain and a nuclear reactor core is performed, in the context of this study, with the intention to use causality analysis for studying the cause-and-effect interconnections between different signals and ultimately determine the root-causes of the encountered anomalies. To the author knowledge, this work is the first attempt to implement the most eminent Granger causality analysis techniques in the field of nuclear reactors, and most importantly, it introduces to the nuclear community an advanced complementary signal post-processing method for neutron noise analysis.

As stated previously, signal analysis techniques are useful tools for studying the signals characteristics. However, the comprehensive analysis of neutron noise phenomena requires the modelling of the stochastic perturbations with the state-of-the-art simulation tools, which were not available in the past due to the high computational cost. Key element of neutron noise analysis is the systematic modeling of neutron noise phenomena using deterministic and probabilistic methods with the ultimate goal to reproduce the plant measurements and extract the importance of different perturbation sources on the neutron noise behavior.

The *second main goal* of this doctoral thesis is to *develop advanced deterministic models* for simulating the impact of neutronic and thermal-hydraulic perturbations and mechanical and structural vibrations on neutron noise phenomenology. To this aim, the code system CASMO-5/SIMULATE-3/SIMULATE-3K, developed by Studsvik Scandpower (SSP), has been extensively used in this thesis for modelling such stochastic phenomena, after contributing in new developments that have been introduced recently in SIMULATE-3K. This doctoral research is one of the first attempts to utilize state-of-the-art time-dependent neutronic solvers for the comprehensive and systematic analysis of neutron noise behavior.

In a nutshell, the *proposed strategy* of the present doctoral thesis is to systematically analyze the neutron noise phenomena and to examine the stochastic behavior of a nuclear reactor with a twofold approach (Fig. 4); first, by *improving and implementing the signal analysis techniques in nuclear reactor analyses*. Second, by *developing deterministic models and reactor core simulation methods for reproducing the trends and signatures, observed in plant measurements,* which will allow a better understanding of the key characteristics of neutron noise phenomena.

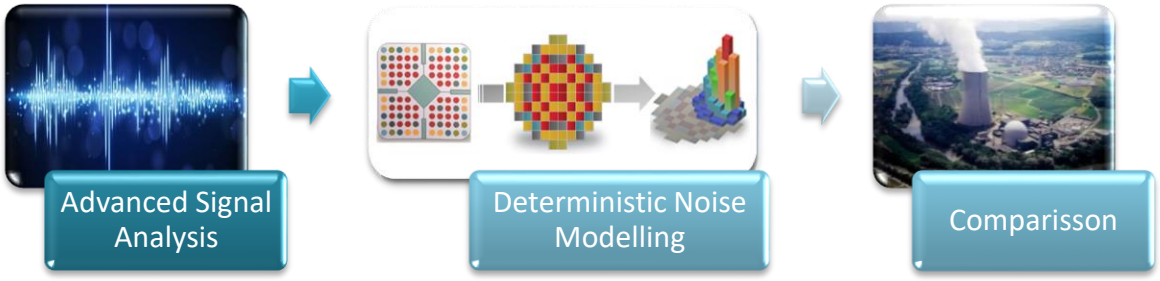

Fig. 4: Thesis roadmap.

The performance of the proposed methodology can be ultimately compared against plant data and measured neutron noise characteristics from the Swiss power plants. On the one hand, the causality measures are applied on real plant data and the resulted causal interconnectivity patterns are assessed based on the reactor engineering judgment and experience. On the other hand, the modeling of single or combined noise sources using advanced simulation tools will produce simulated neutron noise behavior, which is then directly compared against the measured neutron noise phenomenology, based on the KKG data. Therefore, the identification of the individual neutron noise characteristics can be achieved and the understanding of the neutron noise phenomenon can be further enhanced.

1.4. Thesis achievements

Based on the obtained thesis results, a series of original contributions have been achieved within this doctoral research. All the achievements are briefly listed below, however, a more elaborated description is presented in the final chapter, i.e. *chapter 7*.

- A connectivity analysis toolbox, dedicated to nuclear reactor applications has been developed and implemented in the PSI-TSAR methodology. This connectivity toolbox utilizes the most eminent Granger causality measures and serves as a supportive tool for identifying plant anomalies. With the help of causality measures, it is possible to identify cause-and-effect interdependencies between signals of the same system. To the author's knowledge, the current research is the first application of connectivity analysis using causality techniques in the nuclear reactor field.
- For the first time, the best-estimate code system CASMO-5/SIMULATE-3/SIMULATE-3K has been used for a systematic and comprehensive modelling and analysis of the neutron noise phenomena. In particular, a methodology has been developed for the study of fuel assembly vibration modelling with SIMULATE-3K code and its impact on the neutron noise phenomenology. The extensive and systematic analysis of fuel assembly vibrations, and the verification and qualification of the codes' modules, through a tight collaboration with SSP, resulted in the enhancement of the capabilities of SIMULATE-3K to model the fuel assembly vibrations.
- A platform for generating neutron noise simulated data using the SIMULATE-3K code in the framework of the CORTEX project is established. This platform simplifies the process for generating neutron noise data in a user-friendly manner. This development allows new opportunities for strong and long term collaboration between PSI and other national and international partners from both the industry and the academia.

The research and developments that have been performed throughout this doctoral thesis have been documented in several publications (i.e. journal papers and PSI internal technical reports) and have been presented in multiple international conferences and technical workshops. It is to note that, a list of all the relevant produced publications is given at the beginning of each chapter in order to guide the reader with respect to the thesis achievements.

1.5. Thesis structure

This doctoral thesis is organized in five chapters and its structure is illustrated in Fig. 5 by indicating the utilized methodology, the associated application area, and of course, the obtained results. The reader is introduced to the field of the reactor neutron noise phenomenon, then to the main motives and the key objectives of this research in the present chapter, i.e. *chapter 1*. The main investigations and developments are presented and discussed in detail in *chapters 2-6*, leading to deeper understanding of the neutron noise phenomena. The developments and the analyses, performed in this thesis, focus on updating, improving and extending the capabilities of the PSI methodologies for studying nuclear reactor systems.

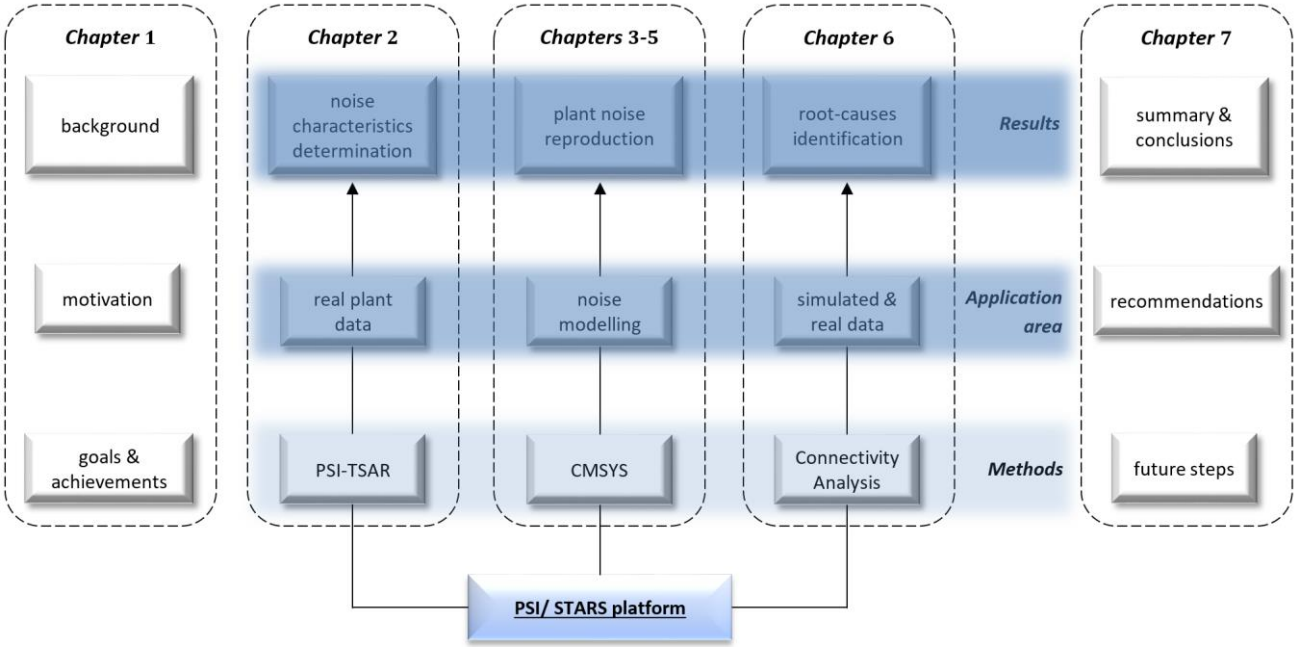

Fig. 5: Thesis structure and its main chapters.

First, the traditional (standard) signal analysis methodologies, used for nuclear reactor applications, are presented in *chapter 2*. The reader is introduced to the principles, advantages, and limitations of the traditional signal analysis techniques being used in nuclear reactor applications for decades. Particular emphasis is given to the detailed description of the PSI-TSAR methodology for the analysis of the Swiss LWRs reactor signals. The PSI-TSAR capabilities are discussed and the most notable examples of its application on the Swiss LWRs data are described. The *chapter 2* mainly focuses on the analysis of KKG plant data using the PSI-TSAR methodology in order to identify the neutron flux spectrum signature. A broad overview of the neutron noise characteristics in KKG is given, and the main conclusions about the KKG neutron noise phenomenology are identified. The analysis of the KKG neutron noise pattern is of key importance for this doctoral thesis, since the individual neutron noise characteristics (i.e. separate effects) based on the plant data are attempted to be explained using advanced neutron noise modelling techniques, in *chapter 5*.

The neutron noise modelling is the main goal in *chapters 3-5*. First, in *chapter 3*, some theoretical considerations about neutron noise are presented, then a brief description of the techniques, developed since the '70s for modelling and analyzing neutron noise phenomena is given. In addition, the PSI modelling approach for simulating stochastic perturbations by utilizing state-of-the-art deterministic solvers is presented. The verification of the proposed methodology against 2D lattice and 3D nodal simulations is extensively discussed in *chapter 4*, and the qualification of the CMSYS codes for the modelling of neutron noise phenomena is assessed. Furthermore, a systematic modelling of various stochastic perturbations is presented in *chapter 5*, and key observations, supporting the understanding of the key mechanisms behind the neutron noise phenomena, are assessed. Finally, an attempt to identify and determine the root-cause behind the neutron noise level increase trend, observed in KKG, is also given in *chapter 5*, by modelling real core loadings and simulating relevant stochastic perturbations as a function of time (i.e. over an operational cycle and over cycles).

Chapter 6 provides a detailed description of the advanced signal analysis techniques that have been extensively used in the literature for extracting the key characteristics of an analyzed system. Emphasis is given to the concept of causality and a discussion about the transition from the philosophical notion to the mathematical formulation is presented. Causality analysis intents to identify the information flow paths between processes within a system, and to indicate possible root-causes of an observed perturbation. The modelling of the analyzed system using multi-variate modelling approach has a key impact on the application success of causality analysis techniques. Therefore, an extensive description of the modelling process of multi-variate systems is given, followed by a comparison of the most important causality analysis techniques. The capabilities and limitations of the causality measures are demonstrated through a set of analytical examples. Then, the most eminent causality analysis measures are implemented in the PSI connectivity analysis methodology for analyzing data sets provided from both nuclear reactor simulated systems and real nuclear plants. The capability of the PSI connectivity methodology for indicating and identifying the root-cause of various stochastic perturbations is demonstrated with the help of simulated and measured nuclear reactor data.

The main findings and the original contributions and accomplishments of this doctoral research are discussed in detail in *chapter 7*. The impact of the various utilized techniques on advancing the study of neutron noise phenomena is assessed in detail. In addition, recommendations for future research activities are proposed.

Chapter 2: KKG Data Signal Analysis using the PSI Standard TSAR Methodology

The present chapter aims for the signal analysis of Gösgen nuclear reactor (KKG) data to identify trends and characteristics of its neutron noise phenomenology. The KKG noise phenomenology is attempted to be explained, in chapter 5, using neutron noise simulated results. The detailed signal analysis of the KKG data, performed in this chapter, employs traditional signal analysis techniques, commonly used in nuclear reactor applications. The nuclear reactor signals, comprising neutron detector responses and process signals, are simultaneously recorded by the online monitoring systems and are post-processed and analyzed in the time- and frequency-domain in order to extract the key signals characteristics, which can give valuable information about the operational status of the analyzed reactor. PSI has been extensively involved in the systematic signal analysis of the Swiss nuclear reactors, and therefore, it has developed, along the years, its in-house methodology for Time Series Analysis for Reactors (PSI-TSAR). The PSI-TSAR methodology is briefly described in this chapter and then applied on real plant data, originating from KKG, measured during operational cycles that showed increasing neutron noise levels. Last, the neutron noise phenomenology based on KKG data is compared against German and Spanish plants data to identify not only similar trends but also differences in the noise behavior, attributed to the specificities of the individual reactor.

The content of this chapter is based on the analyses performed in the following peer reviewed papers and PSI internal reports:

- D. Chionis, A. Dokhane, H. Ferroukhi, A. Pautz, "*PWR neutron noise phenomenology: Part II – Qualitative comparison against plant data*", Proceedings of the 2018 International Conference on the Reactor Physics (Physor '18), Cancun, Mexico (2018) [17].
- A. Dokhane, D. Chionis, H. Ferroukhi, "*Towards systematic and continuous tracking of neutron and process noise signatures during LWR operation*", Proceedings of the 2018 International Conference on the Reactor Physics (Physor '18), Cancun, Mexico (2018) [18].
- D. Chionis, "*Neutron noise analysis of KKG measured data (cycle 30 to 37)*", PSI internal report TM-014-14-003 [19].
- D. Chionis, A. Dokhane, "*ENSI On-call – Causality analysis of KKL Cycle 33 – Start-up measurements from February 2017*", PSI internal technical report AN-41-18-01 (2018) [20].

2.1. Introduction

From a pure intuitive perspective, the term *noise* has an unwanted nature since it is expected to deteriorate and disturb the quality of the information within an analyzed process. Various techniques have been developed over the years in the fields of acoustics, image processing, pattern recognition, etc., in order to overcome the disturbing character of noise and to significantly improve the signals quality. However, the important role of noise and in particular of *neutron noise* in nuclear power applications has been identified already from the mid-20^{th} century ([2], [13]). The systematic study of neutron noise using signal processing techniques in both the time- and frequency-domain is beneficial in extracting key information about the reactor dynamics and the interconnection between different reactor processes. More importantly, the continuous monitoring of the neutron noise phenomenon is used for obtaining the reactor specific signatures (characteristics) and therefore, helping the early detection of possible malfunctions. To this aim, research

institutes and nuclear industry have been investing on the continuous development of signal processing techniques and on the improvement of the signal monitoring and acquisition systems. In the following paragraphs a brief introduction is given on the traditional, called also standard, techniques being used for investigating neutron noise phenomena.

Historically, the neutron noise phenomenon has been studied in experimental zero-power reactors using neutron detector signals in pulse mode measurements. The kinetic parameters (e.g. delayed neutron fractions, prompt neutron lifetime, etc.) could be extracted from the zero-power noise using the so-called *Rossi-alpha* and *Feynman-alpha* methods [21]. In addition, the interconnectivity between different neutron detectors could be estimated in the time-domain using the *auto-* and *cross-correlation* functions [2]. Further information about the neutron detector signal quality could be estimated with the so-called *signal-to-noise ratio* (SNR) [2]. The SNR is defined in the time-domain and estimates the signal strength with respect to the noise level. The continuous research developments and the improvements of signal acquisition devices has led to a rapid increase of interest in the research and industrial communities on the neutron noise phenomena for studying the reactor dynamic behavior. Therefore, signal analysis techniques have started to be applied not only on zero-power reactors but also on power reactors by analyzing both detector and process signals [22]. Neutron noise analysis faced its golden era from 1975 to 1995 during which a series of symposiums were organized with a special focus on reactor surveillance and signals diagnostics ([23]–[29]). Furthermore, the transformation of the neutron detectors signals in the frequency domain revealed the oscillatory nature of neutron noise. To this aim, extensive core monitoring programs were organized worldwide (e.g. USA, Germany, the Netherlands, Italy, etc.) and key characteristics related to the fuel assemblies motion, vessel internals vibration, control rod anomalies, and boiling instabilities were able to be identified ([30]–[36]). In addition, accelerometers, displacement sensors, pressure gauges, and ex-core neutron detectors have been utilized for estimating the core barrel motion ([32], [34], [37]), and therefore, to deeper identify the neutron noise signatures in the high frequency range. Moreover, more advanced signal analysis techniques have been proposed in the early $80s'$ for identifying cause-and-effect relationships between measured signals in both qualitative and quantitative manner [7]. The so-called *signal transmission path* (STP) method has been widely applied in nuclear reactor systems for identifying the noise propagation within the analyzed processes ([38]–[41]). More recently, the signals from in-core neutron detectors and temperature thermocouples at the core-top axial level were used in order to estimate, with high confidence, the moderator temperature coefficient (MTC), which is an important safety parameter in PWRs [42].

This brief overview of the neutron noise applications shows the important nature of the analyzed phenomenon by investigating and extracting valuable information about the reactor behavior. A detailed theoretical description of neutron noise phenomena and an overview of neutron noise applications has been already provided in the literature ([2], [21], [43], [44]). The neutron noise phenomena started to become again an appealing and attractive research topic at the beginning of the 21^{st} century when a specific design of PWRs started to exhibit a neutron noise level increase trend over successive cycles [14]. Therefore, standard signal analysis techniques have been utilized for studying this neutron noise trend. In addition, more advanced signal processing techniques have been proposed to be used in order to better understand the observed trends and to thoroughly understand its main features and its root-cause [16]. In the following sections, standard signal analysis methods are utilized for studying the neutron noise phenomenology of the Swiss KKG reactor, which is a typical example of a KWU pre-Konvoi PWR, experiencing an increase of neutron noise levels over the last decade.

2.2. PSI Signal analysis methodology

PSI has a long and proven experience in the systematic analysis of nuclear reactor signals as a result of the close collaboration with the national regulatory authority (ENSI) and the Swiss utilities. Nuclear reactor signals are analyzed at PSI using the so-called *PSI Time Series Analysis Methodology for Reactors* (PSI-TSAR), which has been initially developed for screening the operation of BWRs and for evaluating, with high degree of accuracy, BWR stability parameters (i.e. decay ratio and resonance frequency) [5]. The PSI-TSAR consists of several calculation steps (i.e. blocks), developed all in the MATLAB environment. The first three main analysis blocks were already developed in the initial versions of the PSI-TSAR. These are the *time domain analysis*, the *frequency domain analysis*, and finally the *stability analysis*. In the framework of this doctoral thesis, the PSI-TSAR was further improved, automatized and extended to include two additional important analysis blocks, namely the *signature monitoring analysis* and the *connectivity analysis* (highlighted in Fig. 6). The main features of the PSI-TSAR are presented in Fig. 6 and they are further described in the following sections.

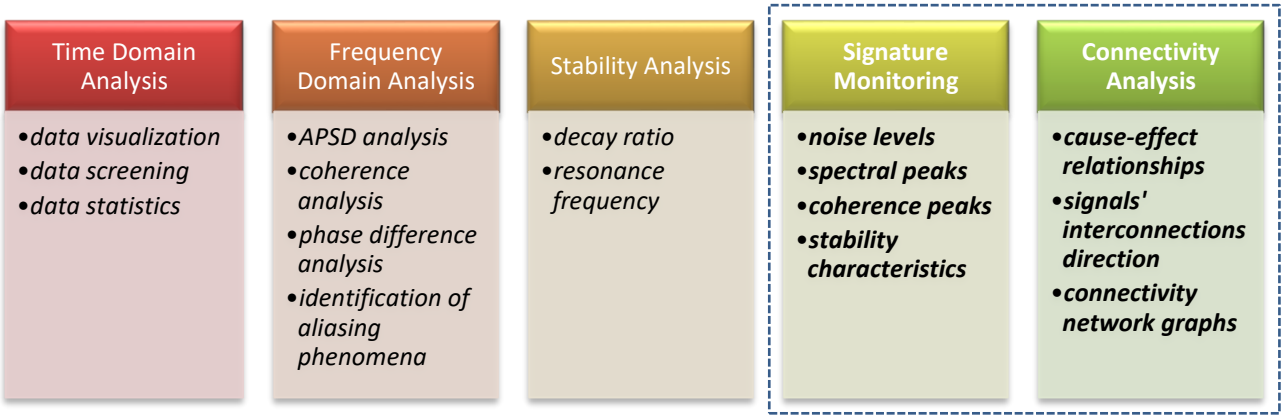

Fig. 6: Main analysis blocks of the PSI-TSAR.

2.2.1. Time domain analysis

First, all the available signals, i.e. neutron flux and process signals[2], are analyzed in the time domain. A data set of simultaneously recorded time signals, using a specific monitoring and acquisition system, describes the time evolution of different parameters of the analyzed system. The data set contains the raw information that can be examined with various means of analytical tools. The reactor time signals are post-processed in the following three steps:

- *Visual screening* of the signals in order to verify the stationary properties of the time series. In case of non-stationary signal, it is first segmented into smaller stationary intervals and the various analysis blocks of PSI-TSAR will be applied only on stationary segments with sufficient number of data points, ensuring the statistical significance of the results. In addition, erroneous or corrupted signals are identified and removed from the next steps of the analysis, since they can lead to wrong assessments. Corrupted signals appear due to a damaged or a wrongly calibrated detector, and due to a failure of the monitoring system.
- *Detrending* of the time signals is performed in order to subtract the mean value and any linear trend of the analyzed data set. Detrending is beneficial since it focuses on the real fluctuations of the signals and not on any linear trend that erroneously distorts the signals behavior.

[2] Process signals correspond to coolant temperature signals, pressure signals, valve opening positions, etc.

- *Standardizing* of the time signals is performed by normalizing every signal with respect to its standard deviation value. Standardization is a beneficial normalization method, commonly utilized when the dependency between signals is investigated and these signals are measured at different scales (e.g. neutron fluxes and coolant temperature signals)[3].

Preliminary characteristics of the signals can be identified by visualizing the time-dependent behavior of the signals and by estimating their main statistical quantities (e.g. signal mean value and standard deviation, signal-to-noise ratio, deviation from signal minimum/maximum to mean value, signal variance, etc.). The main focus is given, in this work, to the estimation of the neutron noise levels as they are recorded by the in- and ex-core neutron detectors, at several axial levels and azimuthal locations of a nuclear reactor. To this aim, the statistical quantity, called the coefficient of variation (CV), is utilized for calculating the neutron noise level[4]. The CV indicates the signal variation around its mean value and allows the comparison between different detectors at different operational conditions (e.g. cycle characteristics and different burnups). Therefore, a reliable comparison of the neutron noise levels can be achieved, and both the time evolution and the spatial dependency of neutron noise can be assessed. The CV is defined in Eq. 1, where μ and σ are the signal mean value and standard deviation, respectively. The higher is the CV, the higher is the neutron noise level of the corresponding neutron detector.

$$CV = 100\frac{\sigma}{\mu} \quad \text{Eq. 1}$$

2.2.2. Frequency-domain analysis

Time domain analysis is an absolutely necessary step for estimating quickly and efficiently the main characteristics of the analyzed data set. In addition, frequency domain techniques have gained great importance as soon as the measuring techniques were improved, allowing the signals to be recorded at higher sampling frequencies. Frequency domain techniques can estimate the frequency content of a measured signal [4], and therefore, additional information about the signals structure and their interdependencies can be extracted. The transition from the time to the frequency domain is performed using the well-known *Fourier transformation*, stating that any time signal can be decomposed into a sum of a set of sinusoid waves with different frequencies, amplitudes and phases [4]. It is important to note that the transformation from the time to the frequency domain is taking place without losing any information from the signal. The frequency domain analysis in PSI-TSAR focuses on the estimation of the auto-power spectral density (APSD) of each signal, and the evaluation of the coherence function and the phase difference function between pairs of signals.

The APSD (Eq. 2) of a signal is defined as the Fourier transformation of the signals autocorrelation function:

$$P_{xx}(f) = \sum_{m=-\infty}^{\infty} R_{xx}(m) \cdot e^{-jfm} \quad \text{Eq. 2}$$

[3] Signal standardization is not applied in the KKG data analysis, since all analyzed signals are of the same type; in-core detectors. However, it is to note that, standardization is a key post-processing tool in the connectivity analysis, in which cause-and-effect interdependencies are identified between signals of different origins (e.g. neutron detectors, pressure signals, thermocouples responses, etc.).

[4] It should be mentioned that, many different ways for evaluating the neutron noise level exist in the literature. For example, in [14] the neutron noise level corresponds to three times the standard deviation of the signal (3σ), and in [50] the neutron noise corresponds to the normalized root mean square of the signal (NRMS).

where, the autocorrelation function (Eq. 3) is the cross-correlation of a signal with itself at different points in time:

$$R_{xx}(\tau) = \frac{1}{N}\sum_{t=1}^{N} x(t) \cdot x(\tau - t) \quad \text{Eq. 3}$$

The APSD is estimated in the PSI-TSAR using the *cpsd function*[5] in MATLAB, which is based on the Welch method, as described in [45].

One of the most important steps of any signal analysis methodology is the estimation of the dependency between signals. In other words, signal analysis techniques should have the capability to examine if any similarity between signals exists, and consequently to investigate if a change in the behavior of one signal could affect the behavior of another signal. This analysis is commonly performed using the coherence function, which is the equivalent measure of the correlation function in the frequency domain. The complex dimensionless coherence function can be estimated according to the following expression:

$$FCoh_{xy}(f) = \frac{P_{xy}(f)}{\sqrt{P_{xx}(f)} \cdot \sqrt{P_{yy}(f)}} \quad \text{Eq. 4}$$

The magnitude squared coherence is used for estimating the level of similarity between pairs of signals and it is defined as (Eq. 5):

$$Coh_{xy}(f) = \frac{\left|P_{xy}(f)\right|^2}{P_{xx}(f) \cdot P_{yy}(f)} \quad \text{Eq. 5}$$

The magnitude squared coherence between any pair of simultaneously recorded signals is estimated in the PSI-TSAR using the *mscohere function*[6], in MATLAB.

The coherence function between a pair of signals corresponds to a complex number, characterized by its phase and modulus. The former determines the phase difference between the two analyzed signals, while the latter corresponds to the signals connection (similarity) strength, in the frequency domain. The magnitude squared coherence is a normalized expression, as presented by Eq. 5, and therefore, its value lies between 0 (absence of coherence) and 1 (complete coherence). Coherence function is a powerful tool as it can estimate very fast and without a lot of computation power if there is a strong dependency between two signals by quantifying the strength of the link between their oscillatory components [46]. However, the coherence function is defined only for bivariate systems (i.e. system with only two signals). Therefore, it is practically impossible to distinguish direct from indirect dependencies within a multivariate system, neither it is possible to estimate the direction of the interaction (i.e. if signal x drives the behavior of signal y, or vice-versa). In order to

[5] https://ch.mathworks.com/help/signal/ref/cpsd.html, accessed on 26.06.2020.
[6] https://ch.mathworks.com/help/signal/ref/mscohere.html, accessed on 26.06.2020.

overcome this limitation, advanced signal analysis techniques based on the causality analysis measures are utilized, as briefly described in Sec. 2.2.5 and in more depth in *chapter 6*.

In addition, the frequency-domain analysis includes the evaluation of the phase difference between pairs of signals in order to estimate in-phase ($0°$) or out-of-phase ($180°$) dependencies. The phase difference function is calculated based on the following expression (Eq. 6):

$$Phase_{xy}(f) = \tan^{-1}\left[\frac{Im\{FCoh_{xy}(f)\}}{Re\{FCoh_{xy}(f)\}}\right] \quad \text{Eq. 6}$$

The phase difference function between a pair of signals is estimated in PSI-TSAR using the absolute value of the *angle function*[7] in MATLAB.

An in-phase relationship between two signals can be intuitively estimated in case of the synchronous evolution of the two signals in the time domain. The out-of-phase relationship indicates that, on the one hand, two signals are strongly coherent, but on the other hand, they have a time shift corresponding to a 180 degree (i.e. when the first signal reaches its highest value, the second signal simultaneously reaches its lowest value and vice versa).

Last, the frequency domain analysis assists in assessing if the utilized sampling frequency of a measurement is adequate enough to capture the individual spectral characteristics of the analyzed signals. The sampling frequency of a measurement should be at least two times higher compared to the highest frequency component of interest of any of the recorded signals, based on the *Nyquist theorem*. The Nyquist sampling theorem states that in order to sufficiently capture all the information of a signal, the sampling rate should be at least two times higher than the highest frequency component of the measured signal [4]. Otherwise, when the sampling frequency is too low, false (alias) frequency components are generated along with the correct ones, and therefore, *aliasing effects* can cause different signals to become indistinguishable during the frequency sampling [4]. Aliasing phenomena can affect both the evaluated statistical characteristics of the analyzed signals, and their frequency domain estimators (e.g. APSD, coherence function, and phase difference function).

2.2.3. Stability analysis

An innovative and robust module is included in the PSI-TSAR for the evaluation of the stability characteristics, i.e. decay ratio and resonance frequency, of a BWR [5]. This methodology is using a parametric univariate auto-regressive moving average (ARMA) modelling of the neutron flux signals by assuming a correlation between the measured neutron flux signals and white noise ([5], [8]). Therefore, every neutron flux signal $y(k)$ is fitted to a univariate ARMA model (Eq. 7) using a white signal $e(k)$ and a set of ARMA model coefficients (a_1, …, a_{na}, c_1, …, c_{nc}).

$$y(k) + a_1 y(k-1) + \cdots + a_{na} y(k-na) = e(k) + c_1 e(k-1) + \cdots + c_{nc} e(k-nc) \quad \text{Eq. 7}$$

Key component of this analysis is the optimized evaluation of the model orders na and nc, representing the best-estimate number of backward time-steps of the neutron flux signal $y(k)$ and the white noise signal $e(k)$,

[7] https://ch.mathworks.com/help/signal/ref/angle.html, accessed on 26.06.2020.

respectively. The best-estimate selection of the model orders will ensure the optimal fitting of the ARMA model and consequently the prediction error will be minimized and the number of free parameters, needed for representing adequately the measured system, will be the minimum [5]. Three model-order optimization methods are integrated in the PSI methodology; the Plateau method, the Akaike Information Criterion, and the Rissanen minimum description length. All the three methods are described in detail in [5]. The selection of the best-estimate model-order method is performed through the HPTSAC code [47] of the stability analysis module of the PSI-TSAR. Given the optimal model orders na and nc the next step is to evaluate the ARMA model coefficients by minimizing the expected prediction error. This minimization is also performed through the HPTSAC code [47]. This procedure estimates the transfer function of the system, and therefore, the stability characteristics can be evaluated.

The stability analysis methodology has been validated against plant measurements at KKL and has been extensively utilized for estimating the dynamic behavior of KKL during the occurrence of stability transient scenarios, as presented in the Sec. 2.2.6

2.2.4. Signature monitoring analysis

In the framework of this doctoral thesis, the PSI-TSAR methodology has been further enhanced, through the introduction of an automatisation scheme and the extension to include new features in its structure. First, a time-dependent evolution of the key signal characteristics (signatures) is estimated using the *signature monitoring* block of the PSI TSAR. Plant signals can be analyzed regularly at various burnup steps (i.e. BOC, MOC, EOFP) within a cycle and over successive cycles, and therefore, the main signal characteristics can be compared whether within a cycle or between cycles in order to follow the evolution of any signature. More importantly, unexpected change in any signal behavior can be easily monitored during this analysis. The deviation of the signal signatures from their normal behavior can be an indication of a reactor malfunction. Some of the most important signal signatures that can be estimated via the signature monitoring block are:

- the signal noise level evolution (time domain),
- the signal strongest spectral peaks and the corresponding frequencies (frequency domain),
- the magnitude of the strongest coherence peak between signal pairs and the associated frequency, and
- the decay ratio and resonance frequency evolution of the neutron flux signals.

2.2.5. Connectivity analysis

The *connectivity analysis* block is the second enhancement introduced into the PSI-TSAR, in the framework of this thesis. This module extends the PSI-TSAR methodology capabilities to identify the level of interconnection between signals within a multivariate system. The developed connectivity analysis module includes a set of advanced statistical measures, called causality measures, based on the representation of a measured signals data-set via a multi-variate autoregressive model (MVAR). The causality measures can be used for identifying the cause-and-effect interdependencies between simultaneously recorded signals. In addition, the causality measures can estimate the strength of interaction and, most importantly, the direction of interconnection between the analyzed signals. Therefore, it is possible to study how the information is transmitted within the analyzed signals and consequently to indicate possible deviation from normal trends, which might be related to potential anomalies of the reactor operation.

The connectivity analysis module corresponds to one of the key activities and main developments that have been performed during this doctoral thesis, and therefore, it is further presented and implemented in *chapter 6*.

2.2.6. Previous work at PSI/STARS

The PSI-TSAR methodology was initially developed with the intention to be a generic platform for the systematic post-processing signal analysis of any nuclear power plant. However, most applications, so far, were carried out for BWRs, more specifically for the Swiss BWR at Leibstadt (KKL), by emphasizing on the estimation of the core stability characteristics.

First, the PSI-TSAR was developed for the analysis of the stability measurement tests that were performed at the beginning of cycle 19 (BOC 19) at KKL, with the main aim to study the impact of the power upgrade on the core stability characteristics [3]. This state-of-the-art methodology has evaluated, with high accuracy, the core stability characteristics including their uncertainty range, and showed that the core is stable at all the investigated stability tests. In addition, the systematic post-processing analysis of the plant measured data has indicated possible enhancements and consequently few recommendations were proposed in order to improve the process of future stability measurements. That clearly indicates the tight collaboration of PSI/STARS with the Swiss nuclear industry and the direct contribution of the PSI-TSAR methodology on key operational applications of the Swiss reactors.

Furthermore, the PSI-TSAR methodology was then extended to analyses the stability tests that were performed at the beginning of cycles 10 and 13, at KKL ([48], [49]). These analyses aimed on further verification and validation of the PSI-TSAR methodology for stability tests, corresponding to various operating state-points in the BWR power/core flow map. These investigations showed that the KKL core remains stable under all the analyzed operational points. In addition, the stability analysis results of BOC 10 obtained from the PSI-TSAR methodology were compared against validated fuel vendor results and showed very good agreement. It should be noted that, the experience gained from the stability analyses of the three cycles (i.e. cycles 10, 13, and 19) indicated some global characteristics and trends (i.e. stability signatures) of the KKL core, but it also identified some phenomena that could be correlated to the reactor cycle specific operation (e.g. the stability characteristics dependency on the power upgrade which took place in cycle 19).

A challenging stability event occurred during the start-up of cycle 24, at KKL, has been studied with PSI-TSAR aiming to identify the root-causes [6]. The online monitoring system of KKL has indicated, unexpectedly, high decay ratios with corresponding large values of the resonance frequencies, at low power and low flow rates, where the core is expected to be very stable. The PSI-TSAR analysis was performed for all available in-core neutron detector and process signals, which were simultaneously recorded over a period of one hour. The systematic analysis was able to confirm the very high decay ratios and to estimate the evolution of the resonance frequency during the occurrence of the stability event. Most importantly, this analysis has indicated the strong correlation between the neutron flux signals and the main process signals (i.e. steam and core flow, pressure signals). However, it was identified that the capabilities of PSI-TSAR[8] were not mature enough to estimate the root-cause of the stability event.

[8] The analysis of the KKL stability event in cycle 24 [6] was performed using earlier PSI-TSAR version that did not include the connectivity analysis block.

The stability event at KKL has clearly indicated that the root-cause identification of the perturbation sources is of key importance and a challenge for any signal analysis method. Therefore, it was decided, at PSI-STARS, to further invest in the development of new signal analysis techniques in order to have the capability to analyze the reactor signals from a different perspective and unveil the root-cause of such complex behaviors. To this aim, a series of the so-called "*causality techniques*" have been studied and applied to nuclear reactor studies.

First, a novel continuous and structural model based on the autoregressive moving average (CSARMA) parametric signal analysis technique has been utilized for the analysis of the KKL data from the stability event of cycle 24 [8]. The time domain based CSARMA approach concept is based on deriving canonical models of a given multivariate model in order to achieve a unique characterization of the system dynamics, and therefore, to extract quantitative information about the cause-and-effect interaction between the physical properties of the system [8]. This modelling approach was able to estimate that the plant system disturbance had a key role in the KKL stability event compared to core instabilities. However, the CSARMA approach did not give more insights on the specific parameter or a system component that triggered the stability event.

In parallel, an extensive literature review of advanced signal analysis methods in the frequency domain has revealed the robustness of the signal transmission path (STP) method [7] to investigate the feedback mechanisms among time signals and to study the noise propagation paths within dynamic systems. The main advantage of the STP method, compared to the traditional coherence function analysis, which is already implemented in the PSI-TSAR, is its capability to estimate the direction of interaction between two signals (i.e. whether one signal is triggering the behavior of a second signal or vice versa). The STP method was applied then on the KKL plant data, recorded during the stability event of cycle 24 in order to examine its capabilities and limitations. This method has confirmed the CSARMA findings, by indicating that the instabilities were caused by the pressure control system disturbances and not due to core perturbations [8]. However, it was identified that the STP method is able to analyze the causal interactions between only pairs of signals (i.e. bi-variate models) and it does not yet have a mature formulation for multivariate modelling. This was a significant limitation of the STP method, especially when it is applied to a complex dynamical system, like a nuclear reactor, since it is of key importance to distinguish direct from indirect interactions and consequently to identify the real root-cause of a perturbation within multivariate systems.

The limitations of the CSARMA and STP methods had led the PSI-STARS to initiate a research proposal, which is an important component of the current doctoral research thesis, focusing on the development and implementation, into the PSI-TSAR, of state-of-the-art signal analysis techniques for the estimation of the signal causal interdependencies within multivariate systems. This is one of the main topics to be tackled in this work, presented in details in *chapter 6*.

Finally, the final enhanced version of the PSI-TSAR, as presented in Fig. 6, has been employed for the systematic analysis of the KKL plant data during an entire cycle [18]. PSI has launched this project in 2015 in collaboration with KKL and ENSI, with the goal to estimate the signature characteristics of the measured plant data, and therefore, to identify patterns that are associated to specific operating conditions (e.g. start-up maneuvers, hot full power conditions, normal operation, transients, shut-down, etc.) and their impact on possible fuel malfunctions. The PSI-TSAR methodology has been already applied to the KKL plant data for cycles 33 and 34, for supporting monitoring and diagnostic purposes. The comparison of the signal characteristics (i.e. noise levels, stability parameters, coherence amplitude between pair of signals, spectral

behavior, etc.) over a range of measuring points (i.e. at different burnup steps over many cycles) should be beneficial for the early identification of a possible malfunction or deviation from normal operation regime.

2.3. Extensive signal analysis of KKG plant data

As stated in *chapter 1*, the motivation of the current doctoral thesis is the systematic investigation of the neutron noise level increase trend that has been observed over more than a decade, in several European KWU-PWRs. The first step of this work is emphasizing on the extensive analysis of plant measured data. This is a key step for this doctoral study, because the post-processing analysis of the real plant data should indicate the specific characteristics and trends of the neutron noise. The importance of the noise signatures is twofold: *first*, the better and deeper understanding of the neutron noise phenomenology based on plant measurements; and *second*, a comparison could be performed between the simulated results, using advanced deterministic solvers, and the measured neutron noise phenomenology. As a result, the separate noise signatures could hence be identified (*chapter 5*).

The Swiss KKG has been monitoring the neutron noise trend over the years by continuously recording the in- and ex-core neutron detectors signals. A large set of measured plant data has been provided to PSI, in the framework of this doctoral thesis [19]. Therefore, the state-of-the-art PSI-TSAR methodology has been applied on the KKG data and the key neutron noise characteristics are presented in the following sections.

2.3.1. Description of the KKG reactor

Kraftwerk Union AG (KWU), the predecessor of SIEMENS Nuclear Power GmbH (SIEMENS), introduced world-widely (e.g. Germany, Switzerland, Spain, Iran, Brazil, etc.) a new PWR design, the so-called *KWU pre-Konvoi PWR*, during the mid-$70s$, then an updated version, the so-called *KWU Konvoi PWR*, during mid-$80s$. The KKG is a typical KWU pre-Konvoi PWR, located in the northwest part of Switzerland. The construction of the KKG has been started in 1973 and it was commissioned in 1979. KKG designed to have an electrical output of $970\ MW_e$, which was gradually upgraded to the present electrical output of $1'060\ MW_e$ (i.e. $3'002\ MW_{th}$).

The KKG core contains 177 fuel assemblies with an active length of $352\ cm$ (almost half a meter shorter active height compared to a typical KWU pre-Konvoi PWRs). The core has a $15x15$ fuel assembly layout in a quarter symmetry, as presented in Fig. 7. In addition, KKG has three cooling circuits with three steam generators and one pressurizer. The KKG core is monitored online by both in- and ex-core neutron detectors. In-core instrumentation tubes are positioned at the middle of six fuel assemblies, located at the positions N08, J06, J14, G02, G10, and C08, as presented in Fig. 7. Every in-core instrumentation tube contains six self-powered neutron detectors (SPNDs) using Co^{59} as an emitter material. The in-core detectors are axially distributed over the active core height, and therefore, the neutron flux can be monitored in adequate detail. The ex-core detectors are ionization chambers and are located at four different azimuthal locations (e.g. S1, S2, S3, and S4, see Fig. 7) outside the RPV at a $3.5\ m$ distance from the core-center. In each azimuthal location there is one instrumentation tube hosting five detectors at five different axial positions: two at the upper part of the core, one in middle, and two at the lower part of the core. The two upper and two lower detectors are used continuously, whereas the middle detector is used only during transient operating conditions. The azimuthal locations of the in-core and ex-core neutron detectors are represented by the red squares and the green circles, respectively, in Fig. 7. Moreover, Fig. 7 shows the exact location of the 48 control rods (i.e. black circles) which are inserted in the core for controlling the reactivity, and the azimuthal location of the inlet and outlet cooling loops orifices (i.e. inlet/outlet loop 1, 2, 3).

It is important to note that, the control rod pattern does not follow a quarter symmetry, as it would be theoretically expected. A quarter symmetric pattern implies that control rods should be also located at core-locations K2 (west core-side) and B10 (south core-side). However, control rods are not located in these two positions. Instead, control rods can be found in core-locations K4 and D10, and therefore, the symmetry of the control rod pattern is distorted, as illustrated in Fig. 7. Last, it is to mention that, the steam generators in KKG do not contain the feedwater preheaters, and the core design includes a dedicated flow distribution structure right below the core-bottom in the RPV. The purpose of this structure is to homogenize the flow distribution spatially across the fuel assemblies inlet positions. All these characteristics make the KKG design different from the typical pre-Konvoi/Konvoi PWR cores, whose neutron noise phenomenology has been recently studied in the literature ([14], [50]–[52]). Therefore, the analysis performed in this doctoral thesis, intents to indicate the neutron noise phenomenology particularities, associated to KKG core design.

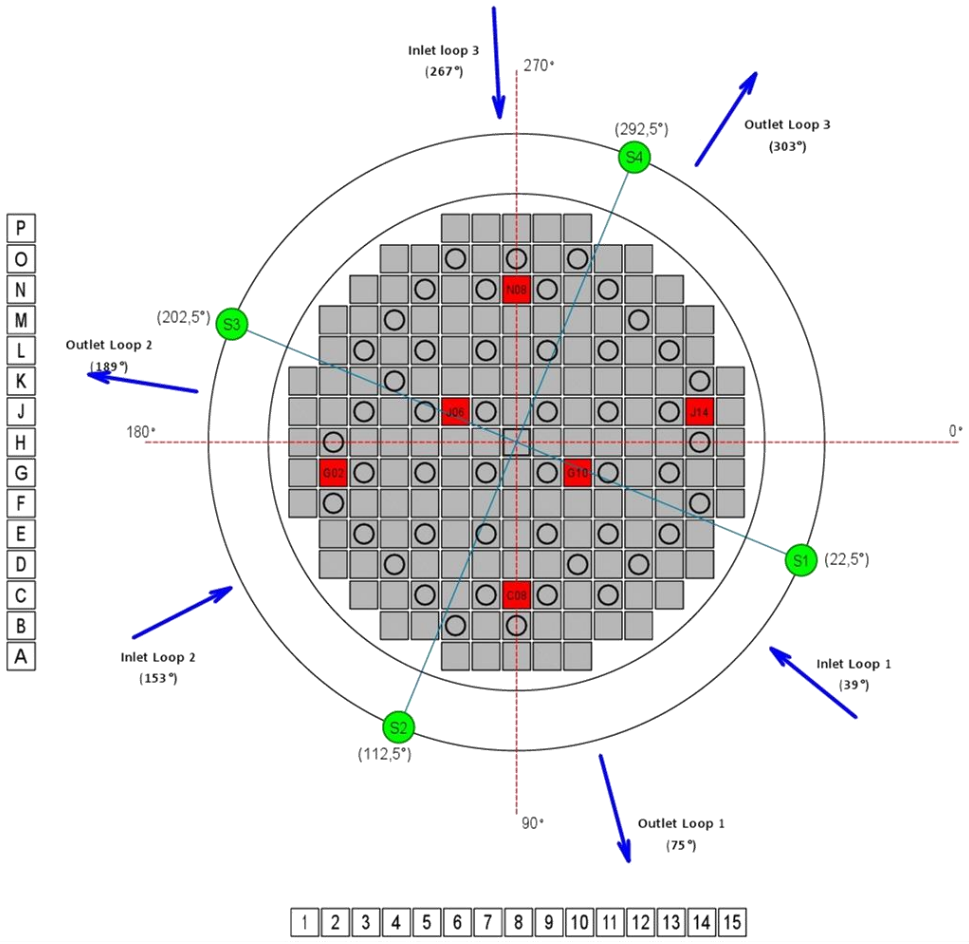

Fig. 7: Radial view of KKG core.

2.3.2. Signal analysis of KKG data

As stated earlier, a neutron noise level increase trend has been identified in KKG using the in-core and ex-core neutron detectors since cycle 28. KKG has provided to PSI a wide range of plant data from cycle 30 to cycle 37, in the framework of this research. These data-sets contain, mainly, in-core and ex-core neutron detector signals, which were simultaneously recorded with sampling frequencies that vary from 2 to 100 Hz, depending on the measurement campaign. The PSI-TSAR is applied to the KKG data and the main neutron noise characteristics (i.e. noise levels spatial distribution, noise evolution, spectral characteristics) are extracted and

described in the next Sec. 2.3.2.1 – 2.3.2.3. The following table summarizes all the provided data for analysis. The datasets which are analyzed in the current thesis are presented in bold font.

Table 1: Analyzed KKG data-sets.

Data set	Cycle	Burnup [EFPD]	Sampling Frequency	Measured Signals
1	30	90	$2\ Hz$	• In-core detector signals (at 6 azimuthal locations and at 6 axial levels). • Ex-core detector signals (at 4 azimuthal locations and 2 axial levels). • Thermocouple responses at core-top axial level at the locations N08, J14, G02, G10, and C08. • Pressure signals at the inlet of the recirculation pumps, and the inlet and outlet of the RPV for all 3 loops. • Temperature signals at the inlet of the RPV for all 3 loops. • Thermal power level signal. • Boron concentration signal. • Pressure signal at the steam generators outlet for all 3 loops.
2	30	150		
3	31	20		
4	31	90		
5	31	150		
6	31	270		
8	32	20		
9	32	90		
10	32	150		
11	32	270		
12	33	20		
13	33	90		
14	33	150		
15	34	20		
16	35	20		
17	35	90		
18	35	150		
19	36	20		
20	37	20		
21	37	90		
22	31	242	$100\ Hz$	• In-core detector signals at core axial level 5 at the locations J14 and N08. • Ex-core detector signals at azimuthal location S1 at the core-top and core-bottom axial level.
23	31	326	$10\ Hz$	• In-core detector signals at core axial level 1 and 5 at locations N08 and G10.
24	31	326	$100\ Hz$	• In-core detector signals at core axial level 1 and 5 at locations N08 and G10.
25	33	228	$100\ Hz$	• Most of the in-core and all ex-core detector signals.
26	33	318	$10\ Hz$	• Most of the in-core detector signals.
27	33	318	$10\ Hz$	• In-core detector signals at core axial levels 3 and 5. • All the ex-core detector signals.
28	34	87	$10\ Hz$	• Most of the in-core and all ex-core detector signals.
29	34	87	$100\ Hz$	• Most of the in-core and all ex-core detector signals.

2.3.2.1. Neutron noise levels

As stated previously, the neutron noise levels can be estimated at every neutron detector location based on the statistical measure, coefficient of variation (CV), defined in Eq. 1. The CV is a normalized version of the standard deviation and it is used to compare the spread of time-signals with different units and/or different means [53]. Therefore, by evaluating the CV of neutron detector signals, it is possible to compare the neutron noise levels between in-core and ex-core neutron detectors, having different units, due to the different utilized measuring principles[9]. In addition, the CV expression can be used for performing a reliable comparison of the neutron noise evolution within an operation cycle (i.e. at different burnup-steps) and over the cycles during which the operating conditions might be varied. The neutron noise levels based on the in- and ex-core neutron detectors are presented in the following figures and the key observations are discussed.

The in-core spatial distribution of neutron noise levels over a cycle is assessed based on four data-sets obtained by the KKG monitoring system at four burnup steps: at 20, 90, 150 and 270 equivalent full power days ($EFPD$), for the operational cycle 31 and a sampling frequency of $2\ Hz$. According to the PSI-TSAR, the data-sets are first screened in the time-domain for assessing their stationarity and for possible identification of corrupted signals. Then, the CV of each signal is estimated over a sufficiently wide segment[10]. The neutron noise levels at different axial (i.e. from core-bottom to core-top) and radial levels over a cycle, are presented in Fig. 8. The plots of Fig. 8 contain a small core-map in which the azimuthal location of the in-core instrumentation tubes are indicated in order to assist the interpretation of the spatial neutron noise distribution results.

It is clearly observed in Fig. 8 that, the in-core detectors located at the azimuthal location J14 (i.e. east core-side) exhibit the highest neutron noise levels at all the axial levels. The J14 detectors have almost twice as high neutron noise level compared to all the other azimuthal locations. This behavior is observed in all provided datasets, as presented in [19]. It is to note that, according to the literature, this is a unique characteristic of KKG, as no other KWU pre-Konvoi PWR has reported to have such an inhomogeneous spatial noise distribution ([14], [50], [51]). In addition, the central and east core-location (i.e. J06, G10, and G02, respectively) tend to show lower noise levels, systematically, at the bottom part of the core. Moreover, a slight swift of higher noise levels from core-top to core-bottom axial levels is observed as the burnup increases (i.e. from 20 to 270 $EFPD$). All these observations indicate that KKG has a strong inhomogeneous neutron noise phenomenology. Therefore, local phenomena shall affect the spatial behavior of neutron noise for the KKG core.

A more detailed analysis of the neutron noise evolution over a time-span of eight cycles is presented in Fig. 9. The neutron detectors at the core east-side J14 are used as a representative example[11] for demonstrating the neutron noise evolution. Each plot in Fig. 9 shows the noise level evolution, at a different axial level (i.e. Lv1: core-bottom, and Lv6: core-top). Note that, no results are presented for J14 at axial level 5, since it was not recorded. It should be noted also that, the measuring campaigns performed at KKG from cycles 30 to 37 were mainly focused at the BOC and MOC. Most of the data sets were recorded at one (i.e. 20 $EFPD$), three (i.e. 90

[9] It recalled that, SPNDs are used for in-core monitoring of the neutron flux in KKG, whereas ionization chambers are utilized for the ex-core detection. The two detectors types result to different signals amplitudes, and therefore, the use of CV is needed for the meaningful comparison of their neutron noise levels.

[10] This segment depends on the measurement duration and the measuring sampling frequency. In this analysis, a segment of $3'000$-$6'000$ data point is used for estimating the statistical quantities of the time signals.

[11] The neutron noise patterns according to the other five azimuthal locations (i.e. N08, J06, G02, G10, and C08) are following similar trends like those for J14, and therefore, they are not further analyzed in the current thesis.

$EFPD$), or five months (i.e. $150\ EFPD$) after the BOC, which indicates the strong interest of the operators on the start-up conditions of the core after the new core loading. Consequently, there is a lack of data sets at the EOC conditions, and therefore, although a clear increase of the noise level from cycles 31 to 33 is observed, no definite conclusions can be made about the reported increase[12] of the neutron noise amplitude during each cycle and from cycle to cycle.

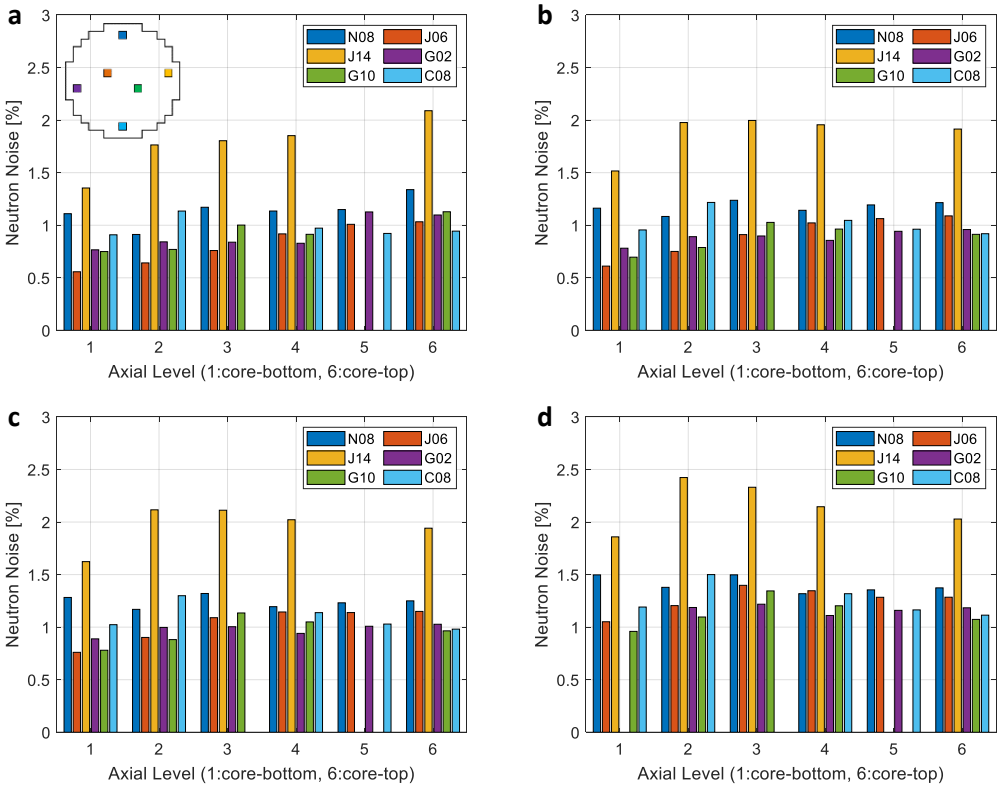

Fig. 8: Axial and radial neutron noise distribution during KKG cycle **31** at **20** (a), **90** (b), **150** (c), and **270** (d) EFPDs.

A clear neutron noise increase within cycles 31, 32 and 33 is observed for all the axial levels (Fig. 9). The *within-the-cycle neutron noise increase* is a well-studied phenomenon and it is directly related to the increase of magnitude of the moderator temperature coefficient due, mainly, to the decrease of boron concentration, during the cycle. The highest value of boron concentration is at the BOC; therefore, the macroscopic absorption cross-section in the coolant is high too. The neutrons are restricted within the core and consequently the neutron noise levels are lower throughout the core. However, at the EOC the boron concentration is approximately zero and the absorption cross section of the coolant is much lower compared to the initial state of the cycle. Therefore, at EOC the neutrons can diffuse more freely in the core, and consequently, the neutron noise is expected to increase.

Moreover, the *cycle-to-cycle neutron noise increase* is more pronounced at the EOC state points, especially for cycles 31 to 33 during which the neutron noise increases linearly (Fig. 9). However, the noise level evolution at the BOC state points does not have a clear increasing behavior, as it would be expected (i.e. decrease from BOC 30 to BOC 31; increase from BOC 31 to BOC 32; decrease from BOC 32 to BOC 33, etc.). This is most probably due to different operating conditions at BOC between different cycles, especially the boron

[12] The KKG neutron noise increase trend has been reported for the first time in [140].

concentration, found to be an important parameter affecting the noise level. It was found[13] that, the neutron noise levels are inversely proportional to the boron concentration (e.g. decrease of boron concentration from BOC 33 to BOC 34 leads to a corresponding increase of noise levels, as shown in Fig. 10) indicating the importance of the operating conditions on the neutron noise levels.

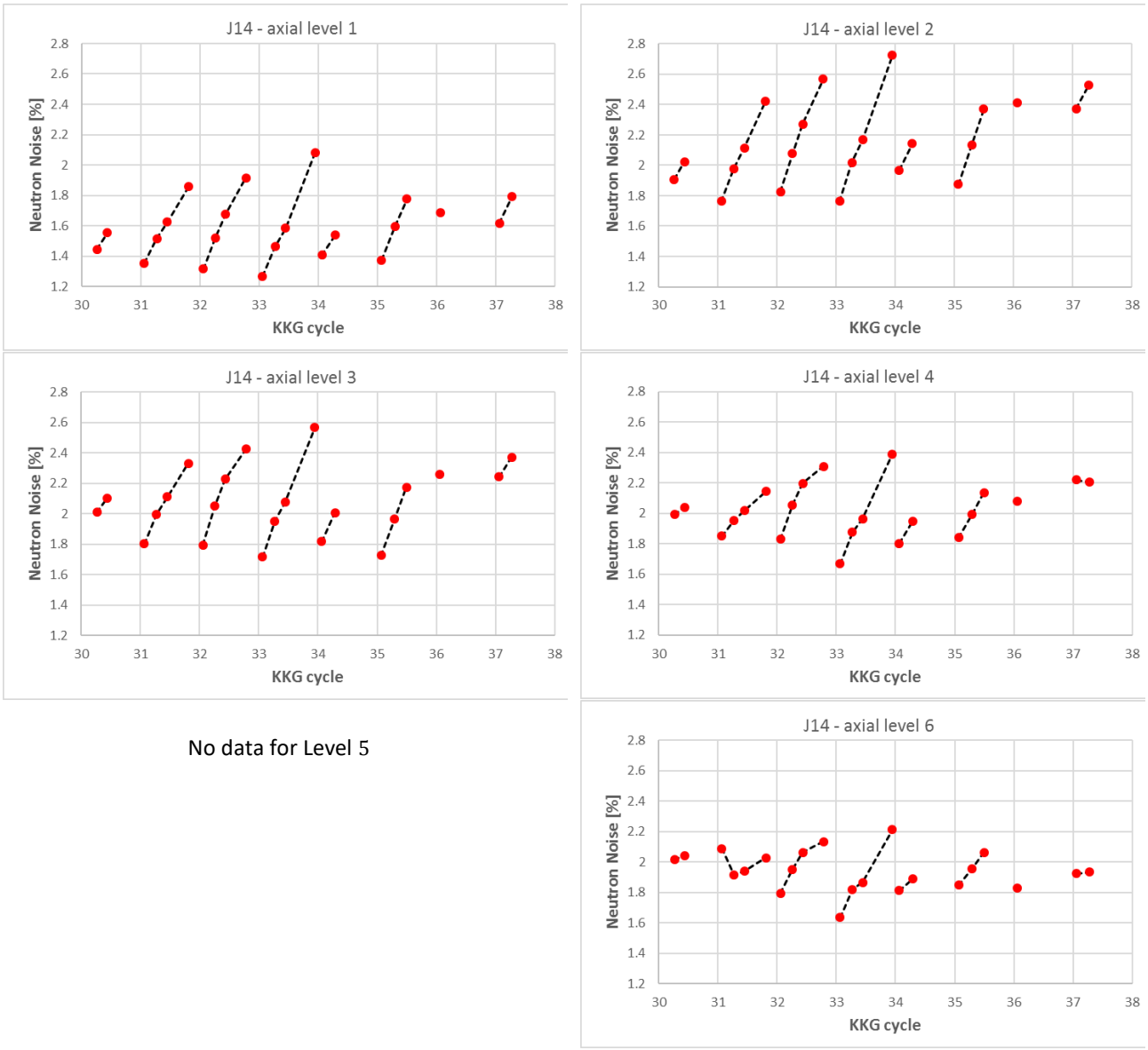

Fig. 9: Neutron noise evolution from cycles 30 to 37 for the in-core neutron detectors located at the azimuthal east core-position J14 (only available measured pointes are presented).

[13] More information can be found in [19] under request (https://www.psi.ch/stars/). The KKG operating conditions (e.g. power, flow, core pattern, boron concentration, etc.) are confidential information, and therefore, their open-public release and distribution is prohibited.

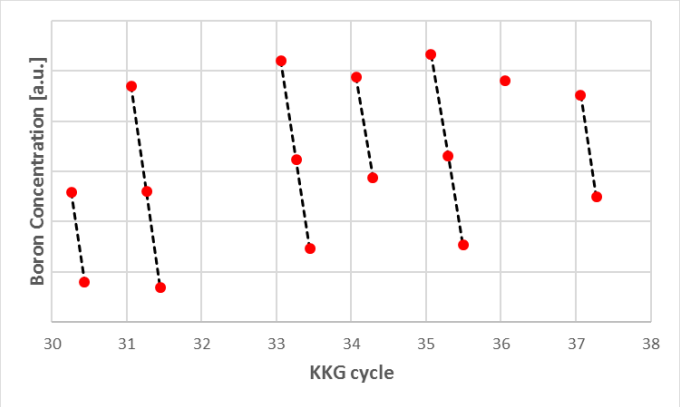

Fig. 10: Boron concentration evolution for KKG cycles **30** to **37** (only available measured points are presented).

This section is concluded with the presentation of Fig. 11 representing the neutron noise evolution, recorded by the ex-core neutron detectors, at the four azimuthal locations (i.e. S1, S2, S3, and S4). The *cycle-to-cycle neutron noise increase* due to the increase of the magnitude of the negative moderator temperature coefficient is clearly observed for all the four ex-core detectors. Moreover, it is found that the S1 and S4 ex-core detectors exhibit significantly higher neutron noise levels compared to the S2 and S3 positions. It should be noted that, both S1 and the S4 ex-core detectors are located at the east half-part of the core (Fig. 7). This shows that both the in- and the ex-core detectors show similar behavior.

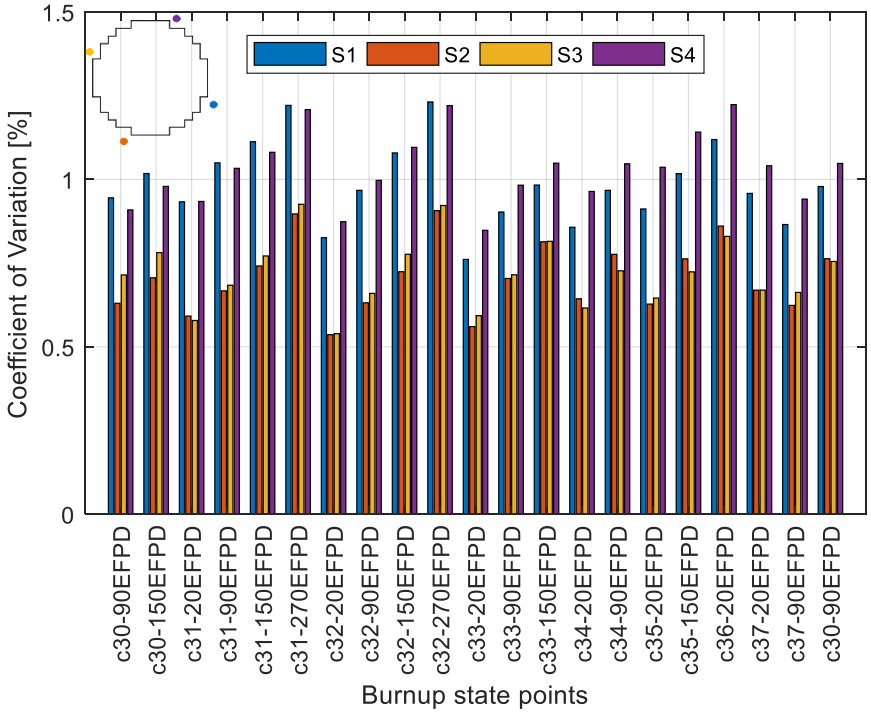

Fig. 11: Neutron noise levels based on the four ex-core detectors over the cycles **30** to **37**.

2.3.2.2. Neutron noise spectral analysis

The systematic analysis of the neutron noise phenomenology and the study of its main characteristics require complementary analysis in the frequency-domain. The frequency-domain analysis intends to identify the spectral characteristics of neutron noise by focusing on the estimation of the signal APSD and the signal-pairs coherence function and phase difference function, using the PSI-TSAR.

The neutron noise spectral characteristics are demonstrated in this section using a representative measured dataset, with high sampling frequency of f_s=100 Hz, recorded at BOC 34 of KKG. The selection of a high-sampled data-set is of key importance in the frequency-domain analysis, since the successful identification of the signals characteristics require that all the frequency components of the analyzed signals have to be included within half of the sampling frequency range (i.e. 0-$f_s/2$), according to the Nyquist sampling theorem [4]. Otherwise, when the sampling rate is lower, some of the highest frequency components of the signals will not be represented correctly and erroneous and misleading results may be obtained from the frequency-domain analysis, due to aliasing[14]. Literature suggests that the neutron noise of a PWR has a strong spectrum in the frequency range of 0-30 Hz, due to both reactivity perturbations and mechanical components vibrations [2]. Therefore, it is expected that any dataset, which is sampled with a sampling frequency above 60 Hz could reliably capture the neutron noise spectral components.

First, the APSD of the in-core neutron detectors at the core-bottom and core-top axial elevations are presented in Fig. 12, in the frequency range of 1-10 Hz, in which the strongest spectral characteristics of neutron noise are contained in the case of the KKG data. The spectral shape of neutron noise in KKG is similar to previously analyzed KWU pre-Konvoi PWRs in Germany, according to the literature ([14], [51]). It is observed that all the available in-core detector signals have similar behavior, characterized by a strong spectrum in the low frequency range (0 - 6 Hz), then followed by a several order of magnitude reduction of the spectral components. Two spectral peaks at 1.8-2 Hz and at 8 Hz are observed. The former peak is related to the fuel assembly vibration first mode [54], whereas the latter is associated to the core-barrel classical beam mode of vibration (i.e. pendular movement of the core barrel) [37]. Interesting enough, the spectral peak at 8 Hz is more pronounced at the core-top axial level compared to that at the bottom part (i.e. Fig. 12, right plot). Possible reasons for this behavior might be the higher neutron noise amplitude at the core-top elevation, and the turbulent character of the coolant at the core-bottom which could mitigate the response of the detectors to the core-barrel vibrations. It should be noted that, recent analyses have indicated that the 8 Hz beam mode spectral peak could embed a double-peak; the first at a frequency about 7 Hz, corresponding to the actual core-barrel lateral movement, while the second peak, at a frequency around 8 Hz, is related to the flow induced vibrations of individual bundles [55]. This clearly illustrates the richness and the high complexity hidden in the spectral components of neutron noise. In other words, local perturbations of various origins (e.g. stochastic nature of neutronic parameters, mechanical and structural components vibrations, thermo-hydraulic parameters fluctuations, etc.) are overlapping, and consequently, the extraction of the individual noise components (separate effects) becomes a challenging task when traditional signal analysis techniques are utilized.

[14] The impact of the so-called *aliasing phenomenon* on the interpretation of neutron noise phenomenology in the frequency-domain is briefly assessed in the Sec. 2.3.2.3.

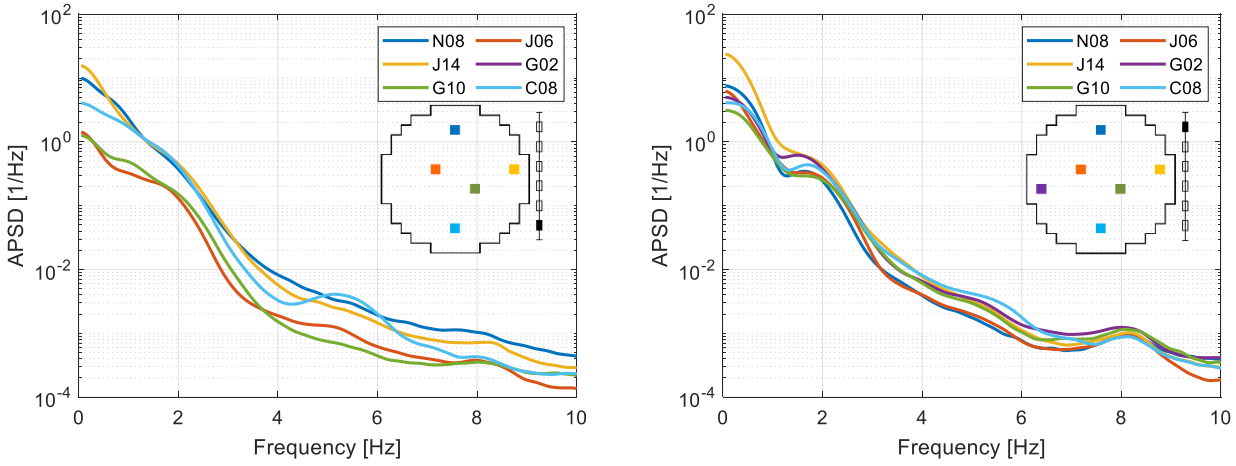

Fig. 12: In-core neutron detectors APSDs at KKG BOC **34** at core-bottom (left plot) and core-top (right plot) axial levels.

Valuable information about the interdependencies between the in-core neutron detector signals can be extracted by estimating the coherence and the phase difference functions between detectors pairs, according to Eq. 5 and Eq. 6, respectively. The radial phenomenology at both core-bottom and core-top axial levels are presented first in Fig. 13 and Fig. 14, using as reference the detector J14, located at the azimuthally core-east part, and the detector J06, located at the azimuthally core-central part, respectively, highlighted in black color.

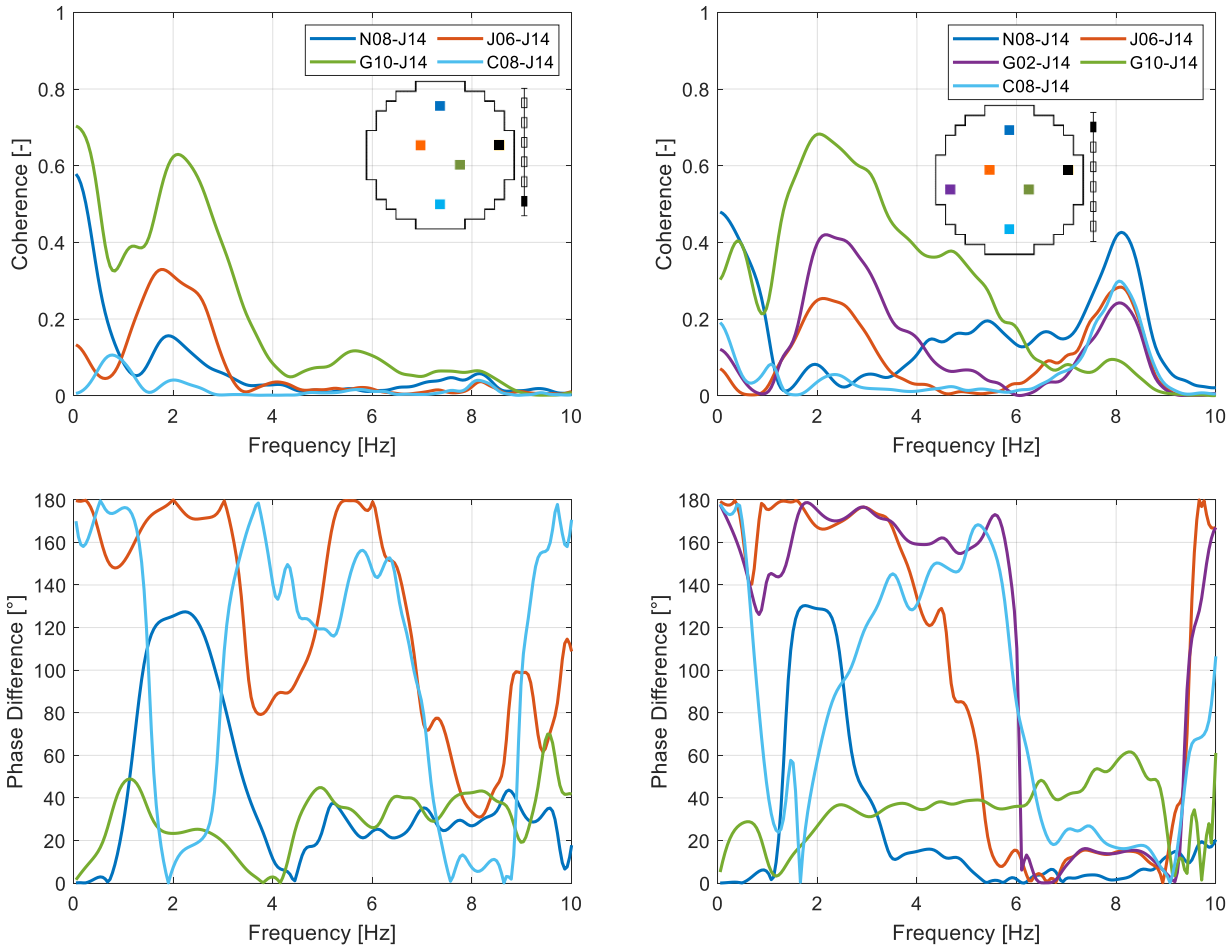

Fig. 13: Radial coherence (top plots) and phase difference (bottom plots) between measured in-core detector signals at core-bottom (left plots) and core-top (right plots) axial levels using as reference the azimuthally east in-core detector J14 (black square).

Strong coherence is observed at the frequency about $2\ Hz$ between the detector pairs J14/G10, and J14/J06 at both bottom and top axial levels, and between J14/G02 at top axial level (i.e. Fig. 13). Also, all detectors seem to be highly coherent with J06 at $2\ Hz$ at both top and bottom axial levels, as presented in Fig. 14. This behavior can be related to the fuel assembly vibration first mode in the x-y-direction perpendicular to a symmetry line splitting the core in two halves; one including the C08, J14, and G10 detectors, and the second including the J06, G02, and N08 detectors. The hypothesis of the fuel assemblies vibration in the x-y-direction is also supported by the fact that the phase-difference at same frequency indicates a rather synchronized interconnection between detector pairs J14/G10, J14/C08, J06/N08 and J06/G02, and an out-of-phase relationship between the detector pairs J14/J06, J14/N08, J14/G02, J06/C08, and J06/G10 (i.e. Fig. 13 and Fig. 14, bottom plots).

Moreover, most of the detectors seem to be highly coherent and in-phase at the frequency of $8\ Hz$, which is an illustration of the global character of the core barrel pendular movement. It should be emphasized that, the pair-wise coherence at $8\ Hz$ is more pronounced at the core-top compared to the core-bottom axial elevation (i.e. top right and top left plots in both Fig. 13 and Fig. 14, respectively), which is in agreement with the previous observation on the distinct spectral nature of the core barrel beam mode at the top region of the core (Fig. 12, right plot).

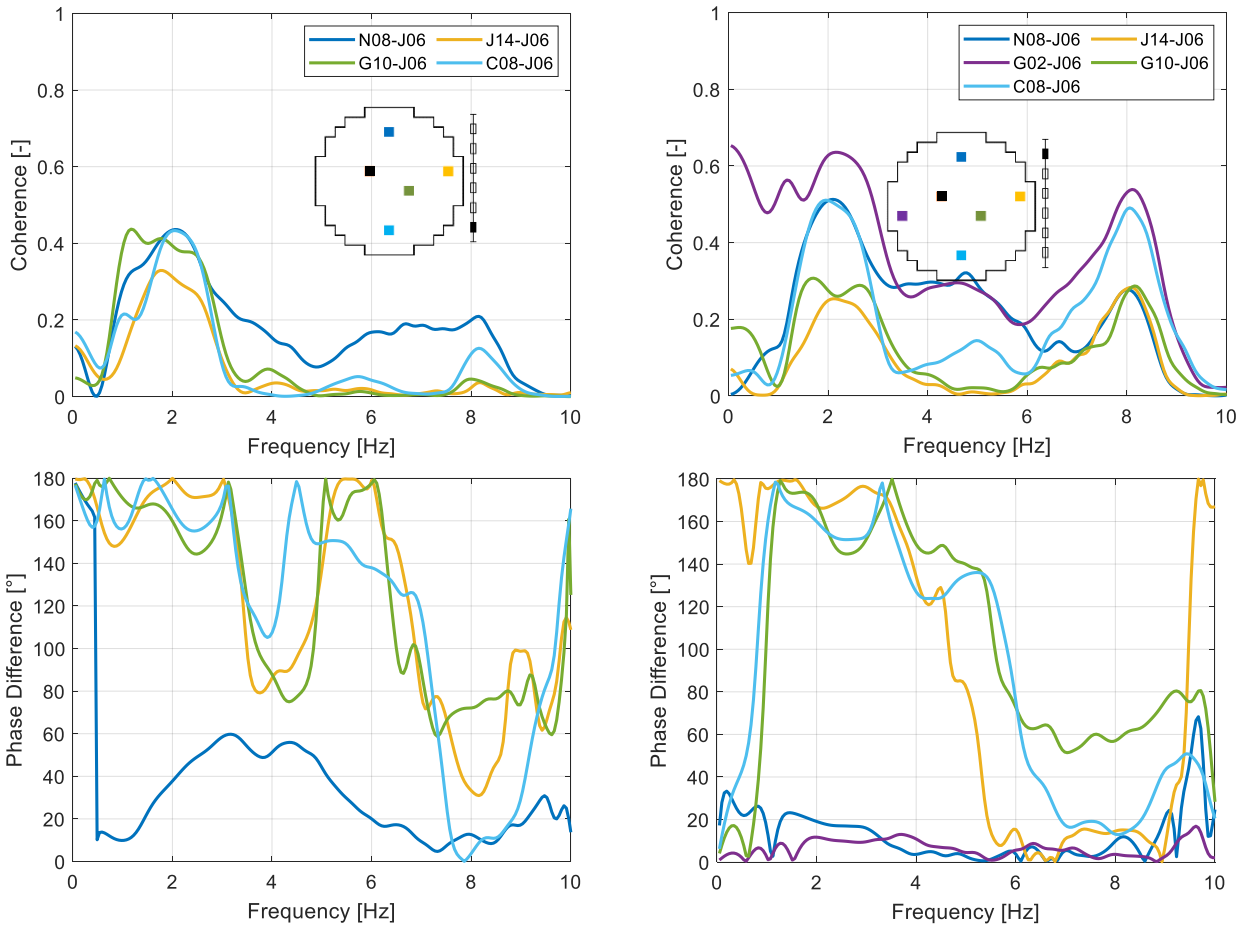

Fig. 14: Radial coherence (top plots) and phase difference (bottom plots) between measured in-core detector signals at core-bottom (left plots) and core-top (right plots) axial levels using as reference the azimuthally central in-core detector J06 (black square).

The propagation of the information flow from the core-bottom towards to the core-top parts can be investigated by focusing on the axial phenomenology of neutron noise. Once more the east-core (J14) and

central-core (J06) azimuthal locations are selected as reference points. The coherence and the phase difference functions focus on the pairwise relationship between the core-bottom, core-middle, and core-top axial levels in Fig. 15 and Fig. 16.

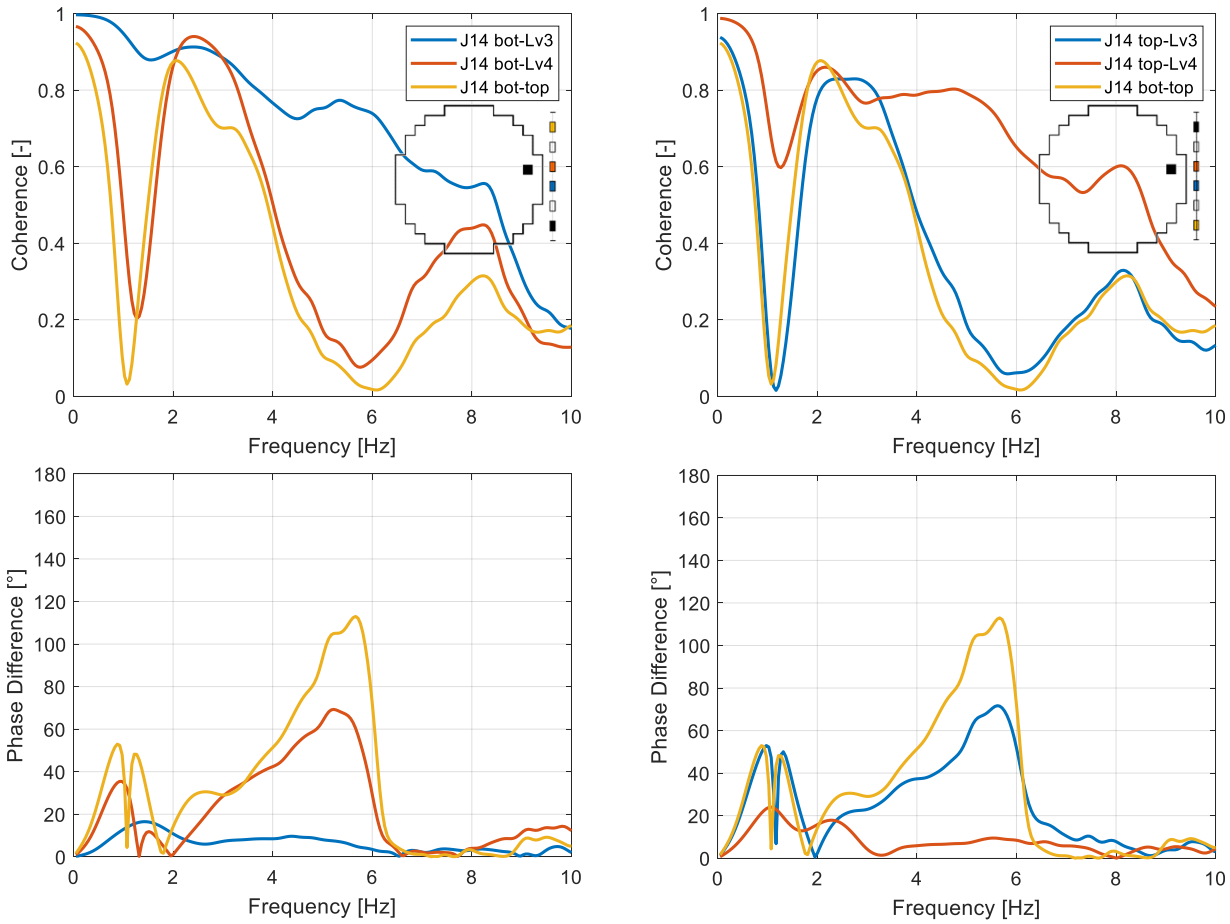

Fig. 15: Coherence (top) and phase difference (bottom) between measured in-core detector signals at east-core azimuthal location J14 (black square) using as reference the core-bottom in-core detector (left plots) and the core-top in-core detector (right plots).

The behavior of the in-core detectors at azimuthal locations J14 shows a very strong decrease of the axial coherence at $1\ Hz$, which reaches almost zero value in some cases (i.e. Fig. 15 top plots). The axial coherence decrease at $1\ Hz$ becomes more intense as the distance between the analyzed detector pairs increases too. The rapid axial coherence decrease at $1\ Hz$ has been observed and reported already in the literature and it is commonly referred as "*sink frequency*", which corresponds to the transit time, i.e. the time needed for the coolant temperature fluctuations to be transported from the core-bottom to the core-top ([33], [51]). Moreover, there is a second drop in axial coherence at a frequency of $6\ Hz$, which, to the author' knowledge, has never been reported in the literature. Concerning the beam mode frequency (i.e. $8\ Hz$), all the detector pairs show high coherence, justifying again the global character of the core-barrel pendular movement. The bottom plots in Fig. 15 present the phase difference between the J14 detectors, located at different axial levels. As can be observed, the axially neighboring detectors have an in-phase behavior across the entire spectrum. It is noted that, the J14 detectors have in-phase behavior even at $1\ Hz$, despite the very low coherence which is observed at that specific frequency ("sink frequency"). In addition, the phase difference behavior exhibits a jump at $1\ Hz$ related to the coolant temperature transit time. Moreover, the phase difference increases between the axially farthest detectors at the frequency range of 2.5-$6\ Hz$. This increasing behavior of the phase difference from $2.5\ Hz$ to $6\ Hz$ between the in-core detectors that belong to the same

radial instrumentation tube is observed for all the azimuthal locations, as presented in more detail in [19]. This is a very interesting observation since such pattern has not been reported to occur in the other KWU pre-Konvoi PWRs. Last, at $8\ Hz$ all the detector pairs show a perfect synchronized behavior due to the core-barrel movement.

The behavior of the in-core detectors at azimuthal locations J06 shows that the axially neighboring detectors are more coherent between each other compared to the axially furthest detectors (i.e. top plots in Fig. 16). Moreover, the coherence decreases rapidly at $1\ Hz$, and even more intensively at $6\ Hz$. As the distance between the analyzed detectors increases, the decrease of the two coherence dips is more noticeable. At the beam mode frequency, the neighboring detectors are more coherent compared to the axially furthest J06 detectors. It is to note that, the azimuthally central in-core detectors at locations G02 and G10 exhibit a very similar behavior like J06, as it is presented in Appendix i. This observation shows that the azimuthally central-west part of the core behaves similarly concerning to the axial coherence phenomenology. It should be noted that, the coherence dip at $1\ Hz$ is more pronounced for the detectors located at locations J14 and N08 as compared to the other core-locations. This coherence dip is related to the coolant temperature transit time, and it would be expected that all detector would exhibit the same axial phenomenology at $1\ Hz$. No clear conclusion can be made about this differentiation, however, a plausible hypothesis could be that the detectors with considerably higher noise (i.e. J14 and N08) could enhance the amplitude of the sink frequency at the characteristic frequency of $1\ Hz$.

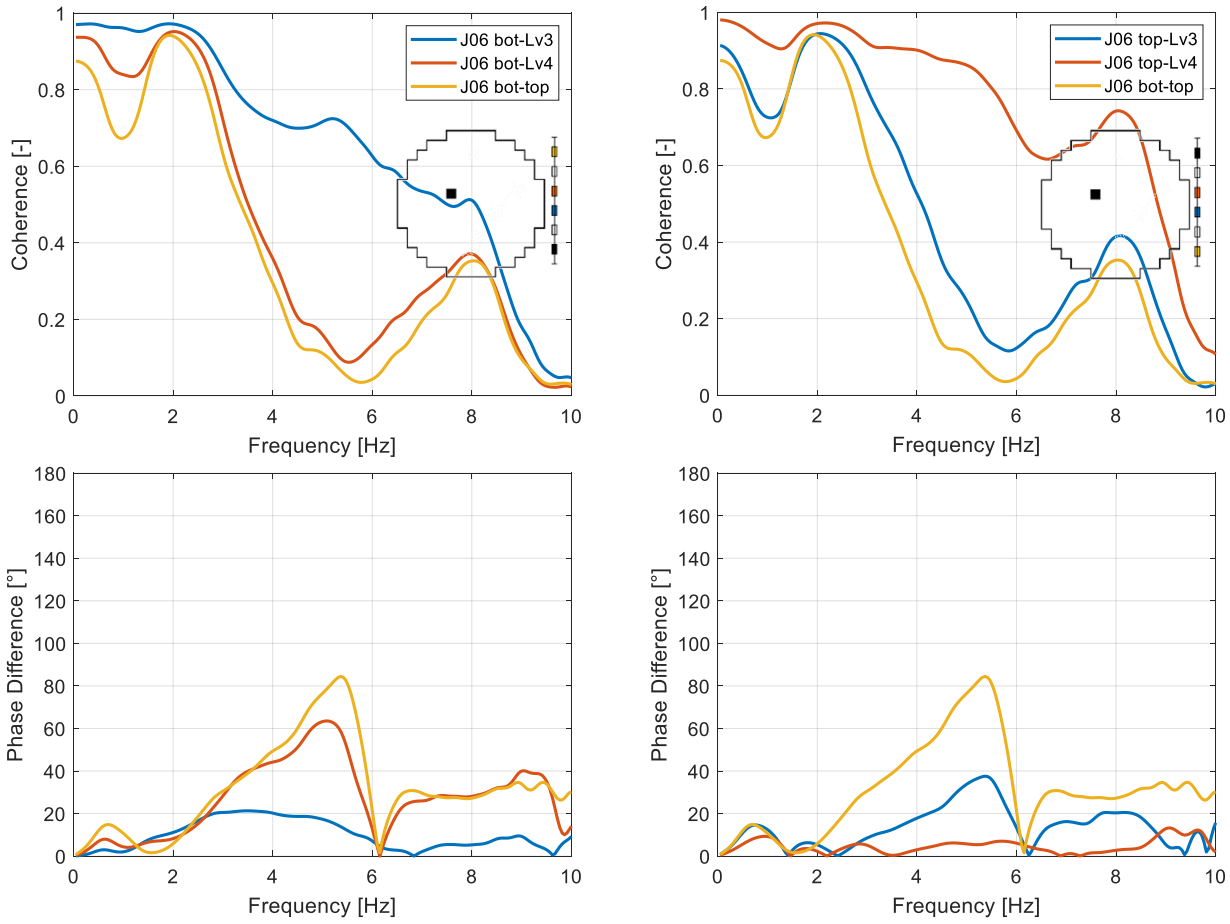

Fig. 16: Coherence (top plots) and phase difference (bottom plots) between measured in-core detector signals at central-core azimuthal location J06 (black square) using as reference the core-bottom in-core detector (left plots) and the core-top in-core detector (right plots).

In addition, the bottom plots in Fig. 16 show the axial phase-difference between the in-core detectors that are located at the azimuthally central side of the core (i.e. J06). The J06 detectors have a relative in-phase relationship between each other at the frequency ranges of 1-3 Hz, and of 6.5-10 Hz. In the intermediate range of 3-6.5 Hz the phase difference of the relative axial furthest detectors increases as the distance increases too.

2.3.2.3. Importance of suitable sampling frequency on neutron noise analysis

As mentioned in the previous sections, the signal analysis techniques in both the time- and the frequency-domains are highly depending on the sampling frequency. It is recalled that, in signal processing techniques the measurements sampling frequency should be at least twice the highest frequency component of interest contained in the system, according to the Nyquist sampling theorem. Otherwise, false frequency components are erroneously generated along with the correct ones if the sampling frequency is too small [4]. The aliasing phenomenon is commonly observed in signal processing analyses and can be the cause of wrong interpretation of the signal characteristics. The impact of aliasing phenomenon on neutron noise analysis (i.e. noise levels and frequency-domain estimators) is intended to be estimated in the current section. To this aim, two datasets from KKG are analyzed. Both datasets include the same four in-core neutron detector signals (i.e. N08 and G10 at axial levels 2 and 6). The two datasets have been simultaneously recorded, however, the first has been sampled with a low sampling frequency of 10 Hz and the second with a higher sampling frequency of 100 Hz. Therefore, these two datasets serve as a good example for examining the importance of measurement sampling frequency on the neutron noise phenomenology.

First, the impact of the sampling frequency on neutron noise levels is demonstrated in Fig. 17. The blue bars correspond to the noise levels of the data set with 10 Hz sampling frequency, whereas the orange bars show the noise levels of the data set with 100 Hz sampling frequency for the four simultaneously recorded in-core neutron detector signals. This comparison shows that the noise levels are systematically higher, up to almost 9%, for the 10 Hz sampled data compared to the 100 Hz sampled data. This observation indicates that the neutron noise levels tend to be overestimated if a low sampling frequency is erroneously utilized for the signals recording.

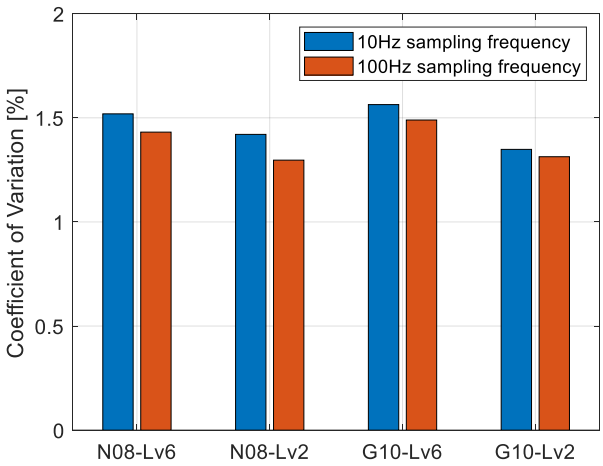

Fig. 17: Difference in neutron noise levels between the **10 Hz** and **100 Hz** sampled data.

The impact of sampling frequency on neutron noise becomes more evident when emphasis is given to the frequency-domain estimators (i.e. APSD, pairwise coherence and phase difference functions). Fig. 18 presents the signals APSDs for the two analyzed sampling frequencies. The spectral representation of the simultaneously recorded signals shows a clear impact of the aliasing phenomenon, in the case of the $10\ Hz$ sampled signals (Fig. 18, left plot); strong peaks appear at $4\ Hz$ and $5\ Hz$ even though it is not expected to observe these noise characteristics in the low frequency range, as was shown in Fig. 12. In fact, these two peaks are related to the strong spectral peaks at the higher frequency range of the $100\ Hz$ sampled data (Fig. 18, right plot). The latter set of spectral peaks in the range of $30\ Hz$ to $35\ Hz$ are artificially made by a pulse generator during the measuring campaign in order to examine the proper functionality of the measuring system. Therefore, due to the aliasing phenomenon, the strong spectral characteristics of the measured signals, which correspond to the high frequency range (i.e. above the $5\ Hz$) are folded back and appear in erroneous (alias) spectral locations. Consequently, incorrect interpretation of the neutron noise phenomenology might take place if insufficiently low sampling frequency is selected in a measurement. It should be noted that, aliasing phenomena could have been prevented if anti-aliasing filters had been used during sampling. However, that was not the case in the low sampled datasets in KKG, as clearly shown in Fig. 18.

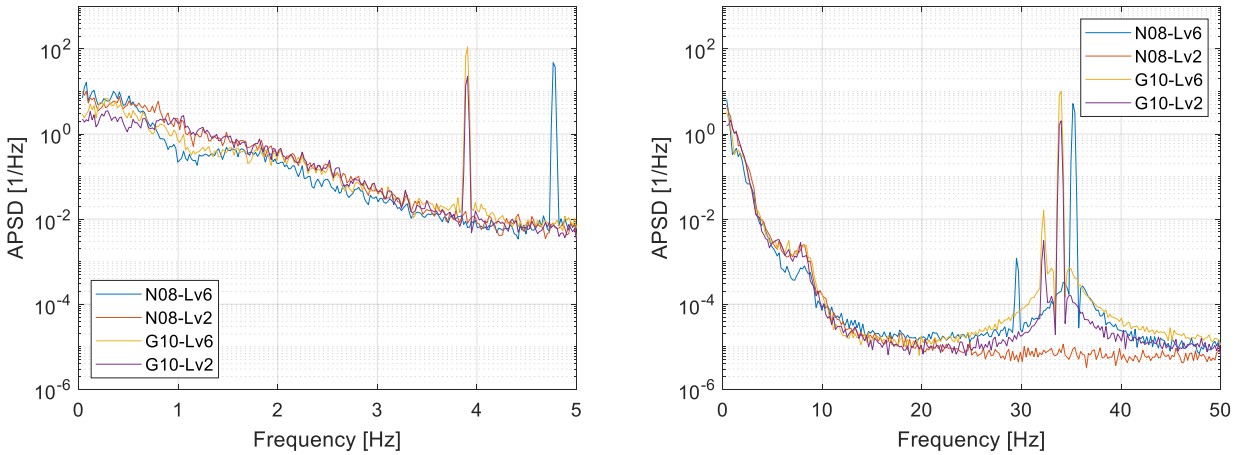

Fig. 18: Demonstration of aliasing phenomenon on signal APSD based on a $\mathbf{10\ Hz}$ (left plot) and $\mathbf{100\ Hz}$ (right plot) sampling frequency.

A representative demonstration of the pairwise coherence function dependency on the sampling frequency is showed in Fig. 19. The blue lines of both plots, in Fig. 19, indicate the coherence function between in-core detectors, located in the same azimuthal location (i.e. G10 at Lv6 and Lv2), whereas the orange lines show the coherence function between two detectors which are located at the same axial level but at different azimuthal position (i.e. N08 and G10 at Lv6). The comparison of the two plots shows that the coherence function plots in the low frequency range of $0\text{-}5Hz$ are very similar between the $10\ Hz$ and $100\ Hz$ sampled data-sets. However, an erroneous coherence peak at $3.9\ Hz$ is observed at the low sampled dataset between the G10 detectors. This coherence peak is clearly a result of the aliasing phenomenon, as it corresponds to the coherence and spectral peak at $35\ Hz$ of the G10 detectors in the high sampled dataset (i.e. Fig. 19 and Fig. 18, right plots, respectively). This is an indication that the coherence function can be affected by aliasing phenomena.

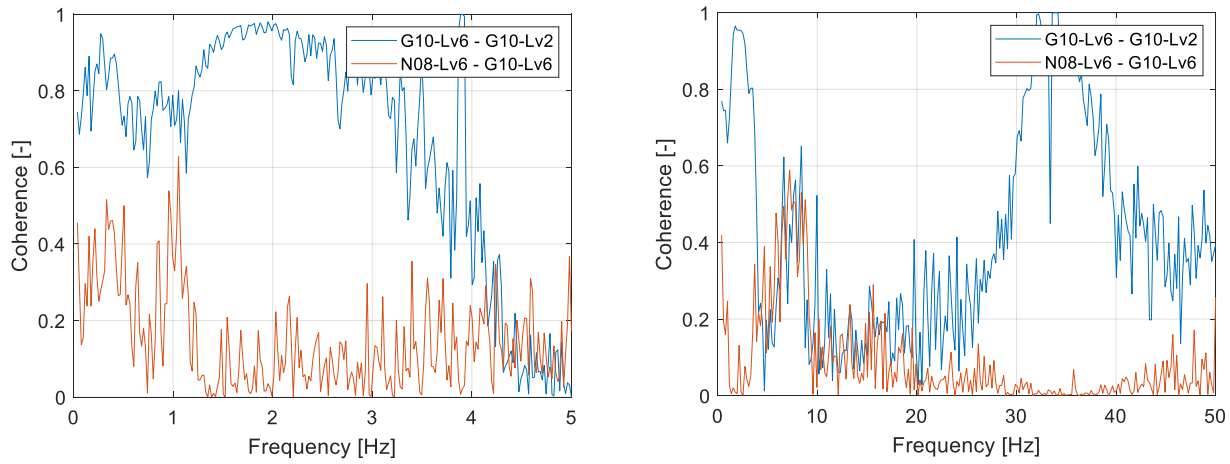

Fig. 19: Demonstration of aliasing phenomenon on signal pairwise coherence function based on a $\mathbf{10\ Hz}$ (left plot) and $\mathbf{100\ Hz}$ (right plot) sampling frequency.

Last, the following Fig. 20 shows the pairwise phase difference between various in-core neutron detectors signals for the $10\ Hz$ (left plot) and $100\ Hz$ (right plot) sampled data-sets. Contrary to the coherence function results, the different sampling frequency seems to have minor effect on the phase difference function results. First, the phase behavior seems to have the same trend in both cases. In addition, the phase values are systematically slightly lower in the case of the $10\ Hz$ compared to $100\ Hz$. It is also observed that the phase difference between detectors that are located in the same azimuthal location (i.e. N08 at Lv6 and Lv2) is relatively small, indicating that there is a linear increase of the phase due to the delay in the flow transport, especially at the low frequency range (<$5Hz$). The phase difference results between the signals that do not belong at the same azimuthal location (i.e. N08 and G10 at Lv6) show higher values of phase difference in almost across the entire spectrum.

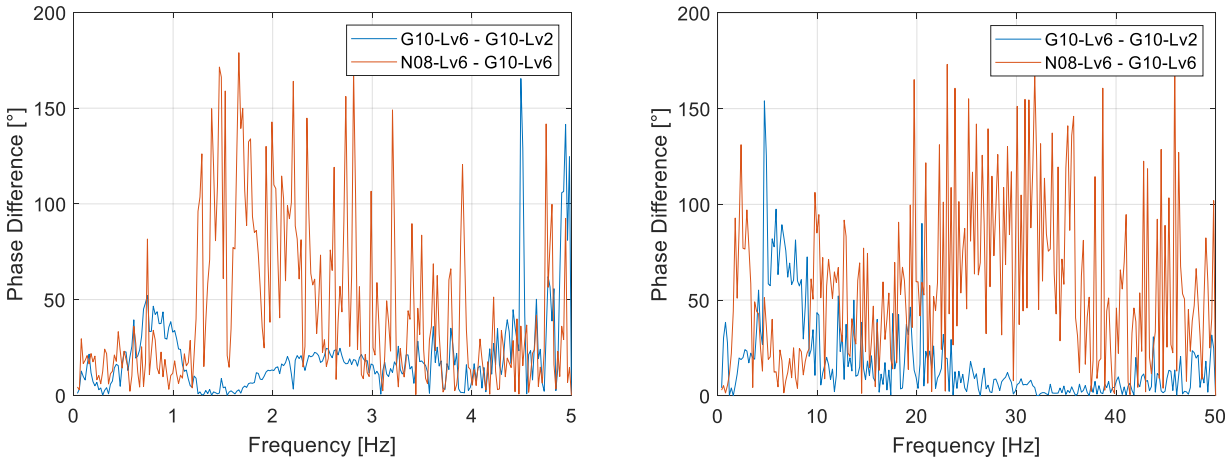

Fig. 20: Demonstration of aliasing phenomenon on signal pairwise phase difference function based on a $\mathbf{10Hz}$ (left plot) and $\mathbf{100\ Hz}$ (right plot) sampling frequency.

2.3.3. Comparison between KKG and other plants neutron noise phenomenology

The previous sections attempted to perform a complete assessment of the neutron noise phenomenology, resulted from the KKG plant data. It has been already mentioned that each reactor has its individually inherent stochastic behavior (signature), and consequently, some neutron noise characteristics reflect the plant

exclusiveness. The current section presents in brief a comparison between the KKG noise characteristics and the neutron noise phenomenology that has been recently reported in the literature for other KWU pre-Konvoi and Konvoi reactors. First, common trends are presented, followed by a brief description of the differences.

First, experience from German reactors indicates a similar noise spectral behavior like in KKG, which is determined by strong content in the low frequency range with a $1/f^2$ shape and distinct spectral peaks at around $1\ Hz$ and 7-8 Hz ([14], [51]). In addition, a neutron noise trend analysis in German KWU pre-Konvoi and Konvoi PWRs shows increasing noise levels within the cycles (i.e. from BOC to EOC) and from cycle to cycle over the first analyzed cycles [14]. In the case of a KWU pre-Konvoi design the noise levels almost doubled over 15 years, whereas the noise amplitude quadrupled within 20 years for a Konvoi design. Moreover, the radial neutron noise distribution in both a German and a Spanish KWU pre-Konvoi PWRs exhibits lower noise levels at the core center, similarly to KKG ([50], [51]). Last, concerning the coherence and phase difference analyses, the reported experience in ([14], [51]) focuses mainly on the very low frequency range between 0-2 Hz. In all analyzed plants, an out-of-phase behavior between detectors from opposite core halves and an almost in-phase relationship between detectors located at the same radial position have been reported.

Despite these similarities, the KKG signal analysis results in noticeable differences compared to other analyzed reactors. The German KWU analysis showed that the neutron noise level exhibits a decreasing trend over the last analyzed cycles in both pre-Konvoi and Konvoi designs [14]. This behavior has not yet been fully understood and has not been observed in KKG signal analysis. Moreover, the KKG phenomenology revealed very high noise levels at the core-east side, which is almost double compared to the rest of the core. However, no other plant has reported to have such higher noise level heterogeneity, as observed in KKG. In addition, the Spanish KWU pre-Konvoi PWR showed a significant heterogeneity related to the axial noise distribution, i.e. higher noise level at the core-bottom level in one core-half, whereas the other core-half exhibits a tendency for higher noise level at the core top level [50]. It is important to note though that, the analysis of the Spanish plant was focused on a single operating point, in contrast to the study of the KKG data, which covered the noise distribution over the cycle in Sec. 2.3.2.1, and indicated a tendency for higher noise levels towards the core-bottom towards the end of the cycle. Concerning the coherence and phase difference analyses, the German plants showed very strong coherence between neighboring detectors, which however, was not observed in the KKG data. In addition, the KKG analysis indicated strong coherence dips at $1\ Hz$ and $6\ Hz$, a noise characteristic which has not reported in ([14], [51]).

2.4. Conclusions and recommendations

In the current chapter, the standard signal analysis techniques, commonly utilized in the nuclear industry and research for monitoring and studying the neutron noise phenomena, have been introduced. These techniques focus on the time- and frequency-domain analysis of the in- and ex-core neutron detectors. Similar techniques have been implemented in the PSI-TSAR methodology for signal analysis of the Swiss reactors. The main emphasis has been given in this chapter to the systematic analysis of the neutron noise phenomenology of the Swiss KKG, which represents a typical KWU pre-Konvoi PWR, in order to identify different characteristics and signatures. The PSI-TSAR has been applied on KKG plant data and the following key neutron noise characteristics have been identified:

- The neutron noise levels found to be increasing within all the analyzed operational cycles. This is a well understood phenomenon, related to the decrease of boron concentration and consequently the increase of the magnitude of the negative moderator temperature coefficient as the burnup increases.

- A relative increase of neutron noise from cycle to cycle is observed. This increase is more pronounced at the EOC state-points.
- The east-core region systematically exhibits the highest neutron noise amplitudes at all axial levels. Additionally, the ex-core detectors located at the east half-part outside of the core show also higher neutron noise levels compared to the west ex-core half-part. This observation suggests the existence of an inhomogeneous spatial (i.e. asymmetric or local perturbation) behavior of neutron noise in KKG, indicating that local phenomena have stronger impact compared to global phenomena.
- Higher neutron noise amplitudes are observed at the core-top axial level during BOC, while a slight shift of higher noise levels towards the core-bottom could be noticed during the cycle.
- All the in-core neutron detectors have a similar spectral behavior, characterized by the very strong spectrum in the lower frequency range (<$5Hz$) and two distinct high spectral peaks at 1.5-$2\ Hz$ and $8\ Hz$. The first peak is believed to be related to the fuel assembly lateral vibration, whereas the second peak corresponds to the well-studied core-barrel pendular motion.
- Azimuthally neighboring in-core neutron detectors have stronger coherent behavior and exhibit an in-phase relationship.
- A relative out-of-phase relationship has been observed between the two halves of the core, which reveals the inhomogeneous behavior of the neutron noise across the core.
- In-core detectors belonging to the same instrumentation tube exhibit high coherence and a linear increase of the phase over the entire low frequency range except at frequencies around $1\ Hz$ and $6\ Hz$ (coherence dips).
- Coherence dips at $1\ Hz$ and $6\ Hz$ are observed in the axial coherence phenomenology. The first dip corresponds to the transit time of the inlet coolant temperature, whereas the second dip has not been fully explained. The coherence at $1\ Hz$ gets lower values at the J14 and N08 detectors, which have the highest neutron noise levels among the other core-positions.

The last part of this chapter has focused on the importance of highly sampled data to perform reliable neutron noise analysis. More specifically, two data sets including the same in-core neutron detector signals but having different sampling frequencies (i.e. $10\ Hz$ and $100\ Hz$) have been analyzed. This comparison showed that the lower sampled data are consistently overestimating the neutron noise levels. Moreover, the frequency representation of the lower sampled data shows erroneous spectral behavior, due to the aliasing phenomenon, revealing that for the reliable investigation of the neutron noise phenomenology, it is crucial to use higher enough sampled data.

The time series analysis of the KKG plant data revealed many specificities and new localized neutron noise characteristics (e.g. the axial phase shift between in-core detectors that belong to the same radial location, inhomogeneous radial neutron noise distribution, etc.) that have not been reported in many other KWU pre-Konvoi PWRs, to the author's knowledge. Therefore, the continuation of the systematic monitoring of neutron detector signals with high sampling frequency is highly recommended. In addition, valuable information can be further extracted if additional process signals are also recorded at high sampling frequency, since the interdependencies between neutronic and thermal-hydraulic parameters would be possible to be studied in a more detailed manner.

Chapter 3: PSI Neutron Noise Methodology: Modelling and Developments

The current chapter introduces the principles of neutron noise modelling with advanced simulation tools. First, a brief theoretical background about the spatial and time-dependent expression of the neutron scalar flux, based on the two-group diffusion theory, is given. Based on a literature review, various types of noise sources are then listed and described. These noise sources can be modelled by perturbing stochastically the time-dependent terms of the diffusion equation (i.e. macroscopic cross-sections, diffusion coefficients, etc.). Therefore, the theoretical background of the diffusion theory and the neutron noise phenomena are used to describe the neutron noise modelling procedure followed in the present doctoral thesis, using the transient nodal code SIMULATE-3K, and in other research activities, which have used other advanced deterministic or probabilistic simulators in the time and the frequency domain (e.g. CORE SIM, DYN3D, PARCS, APOLLO3, and TRIPOLI4). Emphasis is given in this chapter to the description of the neutron noise modelling using the SIMULATE-3K code. To the author's knowledge, this is the first systematic and extensive use of SIMULATE-3K code to model different types of stochastic fluctuations (i.e. lateral vibration of fuel assemblies, fluctuation of thermal-hydraulic parameters) and their impact on the neutron noise temporal and spatial phenomenology. The familiarization with the SIMULATE-3K code and the extended use of its capabilities result in the development of the PSI neutron noise modelling methodology for generating a large range of simulating scenarios in an automatized manner and in a user-friendly environment. Performing such simulations assists in the identification of the neutron noise characteristics, resulted from specific perturbation types, and can be compared to the real plant data noise phenomenology, described in chapter 2. In addition to that, the PSI neutron noise platform is used to provide simulated neutron noise data to the consortium partners of the European Union funded research project "CORTEX", aiming for the development of innovative core monitoring techniques for the detection of reactor anomalies [16].

This chapter is based on the researches performed in the following papers:

- D. Chionis, A. Dokhane, L. Belblidia, G. Girardin, H. Ferroukhi, A. Pautz, "*Development and verification of a methodology for neutron noise response to fuel assembly vibrations*", accepted to be published in Annals of Nuclear Energy, (2020) [56].
- D. Chionis, A. Dokhane, M. Pecchia, G. Girardin, H. Ferroukhi, A. Pautz, "*SIMULATE-3K analyses of neutron noise response to fuel assembly vibrations and thermal-hydraulics parameters fluctuations*", Proceedings of the 2017 International Conference on Mathematics & Computational methods applied to nuclear science and engineering (M&C '17), Jeju, Korea, (2017) [57].

3.1. Introduction

A plethora of measuring campaigns have been performed across the world in both commercial and experimental reactors since the early 70's, for the identification of different types of stochastic phenomena (e.g. control rods and fuel assembly vibrations, coolant flow fluctuations, etc.), found to considerably influence the neutron noise behavior [2]. It is recalled that, one of the main goals of this doctoral thesis is the utilization of advanced simulation tools to model various types of noise sources and to estimate their impact on the neutron noise phenomenology. PSI has a long experience with the CMS platform codes, developed by SSP (i.e. CASMO-5/SIMULATE-3/SIMULATE-3K [58]), therefore, it was a natural decision to utilize the same tools in the

current work for modelling the neutron noise phenomena. The 3D solvers SIMULATE-3 and SIMULATE-3K are based on the neutron diffusion theory, simpler approximation of the neutron transport equation, describing the spatial and temporal neutron distribution throughout the core. In the following paragraphs, the neutron transport and diffusion equations are introduced. Next, a short description of the neutron noise terms is given in order to establish the theoretical background of the underlined mechanisms. Then, a literature review of various types of stochastic perturbations is presented in Sec. 3.2. For completeness, a brief introduction to the modelling techniques, employed by other research institutions, is given in Sec. 3.3. Finally, the neutron noise modelling methodology, developed in the framework of this thesis, is presented in detail in the remaining sections of this chapter.

The study of the neutron noise phenomenon shall start with a brief description of the transport of neutrons and their interaction with matter in space. To this aim, it is fundamental to discuss how the neutron flux depends on space ($\boldsymbol{r}$: position vector, and $\boldsymbol{\Omega}$: unit vector in the direction of motion), energy (E), and time (t) in the analyzed system, i.e. the reactor core. The accurate and precise modelling of neutrons behavior throughout the core is of key importance for reactor physics applications, since it can be used for analyzing the reactor state in steady-state (e.g. eigenvalue and power distribution, burnup estimation, etc.) and transient (e.g. 3D time-dependent reactor power, xenon concentration, etc.) conditions.

The neutrons movement in the system is described by the so-called *neutron transport equation,* having a similar expression as the Boltzmann formulation of the kinetic theory of gases. The time-dependent form of the neutron transport equation is described in Eq. 8 ([44], [59]).

$$\frac{1}{v(E)}\frac{\partial}{\partial t}\psi(\boldsymbol{r},\boldsymbol{\Omega},E,t)+\boldsymbol{\Omega}\cdot\nabla\psi(\boldsymbol{r},\boldsymbol{\Omega},E,t)+\Sigma_t(\boldsymbol{r},E,t)\psi(\boldsymbol{r},\boldsymbol{\Omega},E,t)$$
$$=\int_0^\infty\int_{4\pi}\Sigma_s(\boldsymbol{r},\boldsymbol{\Omega}'\rightarrow\boldsymbol{\Omega},E'\rightarrow E,t)\psi(\boldsymbol{r},\boldsymbol{\Omega}',E',t)d\Omega'dE' \qquad \text{Eq. 8}$$
$$+\frac{\chi^p(E)}{4\pi}\int_0^\infty\int_{4\pi}\nu(\boldsymbol{r},E')\,\Sigma_f(\boldsymbol{r},E',t)\psi(\boldsymbol{r},\boldsymbol{\Omega}',E',t)d\Omega'dE'+\sum_{i=1}^{N^d}\frac{\chi^{d,i}(E)}{4\pi}\lambda_i C_i(\boldsymbol{r},t)+q(\boldsymbol{r},\boldsymbol{\Omega},E,t)$$

where, ψ is the angular neutron flux, v is the neutrons velocity vector, χ^p is the prompt neutrons fission spectrum, ν is the prompt and delayed neutrons fission yield, $\chi^{d,i}$ is the delayed neutrons spectrum, λ_i is the delayed neutron decay constant, and C_i is the precursor density in the i^{th} delayed neutron precursor group. The macroscopic total (i.e. sum of absorption and scattering), scattering, and fission cross-sections are expressed by the terms Σ_t, Σ_s, and Σ_f, respectively. The left and right sides of Eq. 8 describe the neutron balance between the losses and production rate terms, respectively. More specifically, Eq. 8 can be translated as the neutron balance between the:

rate of change of neutron density **+** *rate of loss due to neutron leakage* **+** *rate of loss due to collisions*

=

rate of gain due to in-scattering **+** *rate of gain due to prompt fissions*

+ *rate of gain due to delayed neutrons* **+** *rate of gain due to an external neutron source*

In addition, the delayed neutron behavior is expressed by the delayed neutron precursor concentration equation:

$$\frac{\partial}{\partial t}C_i(\boldsymbol{r},t)+\lambda_i C_i(\boldsymbol{r},t)=\int_0^{\infty}\int_{4\pi}\nu(\boldsymbol{r},E')\,\Sigma_f(\boldsymbol{r},E',t)\psi(\boldsymbol{r},\boldsymbol{\Omega}',E',t)d\Omega' dE' \quad , \quad i=1,2,\dots,N^d \qquad \text{Eq. 9}$$

The neutron transport equation has an integro-differential formulation in which the angular neutron flux has a spatial, time, and energy dependency on the analyzed system. Due to this complexity, the neutron transport equation has an analytical exact solution only for very simple problems (e.g. 1D geometries with mono-energetic neutrons, or 2D/3D geometries with multi-energetic groups in homogeneous medium, etc.), describing systems far from a realistic reactor core. Several methods have been employed in the literature for approximating the neutron transport equation by handling either the angular dependency (e.g. spherical harmonics P_N methods, discrete ordinates S_N methods, methods of characteristics, and collision probabilities method, etc.), or the energy dependency (e.g. multi-group approximation, etc.), or the space dependency (e.g. fine-mesh finite differences, nodal methods, finite elements, etc.), or the time dependence (e.g. forward difference scheme, backward difference scheme, etc.). The interested reader can find detailed description of various approximation methods in nuclear reactor physics textbooks and monographs ([44], [59]). The so-called *neutron diffusion theory,* developed and widely employed in assembly-homogenized core codes such as the SIMULATE-3 and SIMULATE-3K nodal codes, is a simpler approximation of neutron transport equation, by eliminating the angular dependency and assuming isotropic scattering in the laboratory reference system. To this aim, two variables have to be defined: *first*, the scalar flux (φ), which expresses the integral of the total number of neutrons over all angles (Eq. 10); and *second*, the angular net current (J), which describes the total number of neutrons crossing a differential area (Eq. 11).

$$\varphi(\boldsymbol{r},E,t)=\int_0^{4\pi}\psi(\boldsymbol{r},\boldsymbol{\Omega},E,t)d\boldsymbol{\Omega} \qquad \text{Eq. 10}$$

$$\boldsymbol{J}(\boldsymbol{r},E,t)=\int_0^{4\pi}\psi(\boldsymbol{r},\boldsymbol{\Omega},E,t)\boldsymbol{\Omega}d\boldsymbol{\Omega} \qquad \text{Eq. 11}$$

Therefore, the integration of the transport equation over angle and the introduction of Eq. 10 and Eq. 11 into Eq. 8 results in the so-called *continuity equation* (Eq. 12):

$$\frac{1}{v(E)}\frac{\partial}{\partial t}\varphi(\boldsymbol{r},E,t)+\nabla\cdot\boldsymbol{J}(\boldsymbol{r},E,t)+\Sigma_t(\boldsymbol{r},E,t)\varphi(\boldsymbol{r},E,t)=\int_0^{\infty}\Sigma_s(\boldsymbol{r},E'\to E,t)\varphi(\boldsymbol{r},E',t)dE'$$
$$+\frac{\chi^p(E)}{4\pi}\int_0^{\infty}\nu(\boldsymbol{r},E')\Sigma_f(\boldsymbol{r},E',t)\varphi(\boldsymbol{r},E',t)dE'+\sum_{i=1}^{N^d}\frac{\chi^{d,i}(E)}{4\pi}\lambda_i C_i(\boldsymbol{r},t)+Q(\boldsymbol{r},E,t) \qquad \text{Eq. 12}$$

The scalar flux and the net current are the two unknowns in the continuity equation, therefore, a link between these two variables is needed in order to reach a solution of this expression. This link can be achieved by using the so-called *Fick's law*, originally describing the diffusion in liquids and gases, and under certain conditions, can be used in the neutron diffusion theory for providing a relationship between the scalar flux and the net current. These assumptions are: *i)* the scattering is assumed isotropic in the laboratory coordinate system (i.e. weak directional dependence of the angular flux), *ii)* the neutron absorption is assumed to be weak, *iii)* an infinite medium is assumed to exist, and *iv)* the scalar flux is assumed to be a slowly varying function of $\boldsymbol{r}$. Under these conditions, the Fick's law for neutrons describes the proportional behavior between the net current and the negative gradient of the scalar neutron flux (Eq. 13) by introducing the so-called diffusion coefficient D as the proportionality constant.

$$\boldsymbol{J}(\boldsymbol{r},E,t) = -D(\boldsymbol{r},E,t)\nabla\varphi(\boldsymbol{r},E,t) \qquad \text{Eq. 13}$$

The diffusion coefficient is commonly expressed as a function of the macroscopic transport cross-section, as presented in Eq. 14. The transport cross-section is used in order to correct the anisotropic scattering effects and can be estimated by various methods, such as the in-scatter and out-scatter methods [60].

$$D(\boldsymbol{r},E,t) = \frac{1}{3\Sigma_{tr}(\boldsymbol{r},E,t)} \qquad \text{Eq. 14}$$

Finally, the introduction of Eq. 13 into Eq. 12 results into the diffusion approximation of the neutron transport equation (Eq. 15) and the delayed neutron precursor concentration equation (Eq. 16).

$$\begin{aligned}&\frac{1}{v(E)}\frac{\partial}{\partial t}\varphi(\boldsymbol{r},E,t) - \nabla\cdot D(\boldsymbol{r},E,t)\nabla\varphi(\boldsymbol{r},E,t) + \Sigma_t(\boldsymbol{r},E,t)\varphi(\boldsymbol{r},E,t)\\ &= \int_0^\infty \Sigma_s(\boldsymbol{r},E'\to E,t)\varphi(\boldsymbol{r},E',t)dE' + \frac{\chi^p(E)}{4\pi}\int_0^\infty \nu(\boldsymbol{r},E')\Sigma_f(\boldsymbol{r},E',t)\varphi(\boldsymbol{r},E',t)dE'\\ &\quad + \sum_{i=1}^{N^d}\frac{\chi^{d,i}(E)}{4\pi}\lambda_i C_i(\boldsymbol{r},t) + Q(\boldsymbol{r},E,t)\end{aligned} \qquad \text{Eq. 15}$$

$$\frac{\partial}{\partial t}C_i(\boldsymbol{r},t) + \lambda_i C_i(\boldsymbol{r},t) = \int_0^\infty \nu(\boldsymbol{r},E')\Sigma_f(\boldsymbol{r},E',t)\varphi(\boldsymbol{r},E',t)dE' \quad , \quad i = 1,2,\dots,N^d \qquad \text{Eq. 16}$$

The diffusion equation is commonly employed by simulation codes in order to estimate the flux distribution across the reactor core. Clearly, the solution of the diffusion equation in a very fine mesh over the entire core requires enormous amount of computational resources due to the complexity of the material structure and the core dimensions. This limitation can be overcome by utilizing adequate spatial and energetic discretization schemes. Commonly, the core is divided in rectangular cuboid shape volumes (i.e. nodes) with a radial size of

one or ¼ of a fuel assembly and a height about 10-20 cm in order to reduce the complexity of the system. In addition, two energy groups are used by most nodal codes for solving the diffusion equation; one for the fast and one for the thermal energy spectrum. In addition, the reaction rates have to be preserved during the simplification of the discretization scheme. This is a complicated task, which requires the use of specific modelling methods and algorithms. The description of the algorithms and methods which are used in the simulation codes for the numerical solution of the diffusion equation is beyond the scope of the current doctoral thesis. However, the interested reader can refer to [61] for a detailed presentation of the main aspects of the diffusion equation solution as they are implemented in the most frequent utilized commercial codes (e.g. SIMULATE-3, SIMULATE-5, POLCA-7, PRESTO-2, MICROBURN-2, etc.).

The modelling of neutron noise phenomena using the diffusion equation is achieved by introducing temporal perturbations of the time-dependent terms in Eq. 15. Small variations of the cross-sections, the diffusion coefficients, and the precursor concentrations will lead to a spatial and temporal modifications of the scalar flux. Commonly, these perturbations are defined as *noise sources*, whereas the scalar flux fluctuations are addressed as *neutron noise*. Consequently, all the time-dependent terms of the diffusion equation (i.e. $X(\boldsymbol{r},t)$) can be expressed as a function of their mean value (i.e. $X_0(\boldsymbol{r})$) and their fluctuating part (i.e. $\delta X(\boldsymbol{r},t)$) [62]. Therefore, the scalar flux and an example of a noise source (e.g. cross-section) can be expressed by equations Eq. 17 and Eq. 18, respectively.

$$\varphi(\boldsymbol{r},E,t) = \varphi_0(\boldsymbol{r},E) + \delta\varphi(\boldsymbol{r},E,t) \qquad \text{Eq. 17}$$

$$\Sigma(\boldsymbol{r},E,t) = \Sigma_0(\boldsymbol{r},E) + \delta\Sigma(\boldsymbol{r},E,t) \qquad \text{Eq. 18}$$

Neutron noise sources are inherently present in all nuclear reactors and characterized by fluctuations of neutronic parameters (e.g. cross-sections, number of neutrons per fission, neutron flight path, etc.), mechanical components vibrations (e.g. core barrel oscillation, fuel assembly vibrations, etc.), and thermal-hydraulic parameters fluctuations (e.g. coolant inlet temperature, coolant inlet flow, etc.). Moreover, neutron noise strongly depends on the type of the reactor (e.g. PWR, BWR, etc.) and its characteristic features (e.g. fuel assembly mechanical designs, number of coolant loops, existence or not of preheaters in the steam generator, etc.). The next section, Sec. 3.2, describes in more details the different types of noise sources as they are reported in the literature. Then, the various modelling approaches for simulating realistic stochastic perturbations using state-of-the-art computational codes in the time and the frequency domains based on the previously described diffusion theory approximation are introduced in Sec. 3.3. Last, the PSI methodology for modelling neutron noise phenomena using the SIMULATE-3K transient nodal code is presented in detail in Sec. 3.4, while its qualification is described in *chapter 4*, and a systematic study of the simulated noise phenomenology is given in *chapter 5*.

3.2. Literature review of neutron noise sources

Historically, research institutes and the nuclear industry have focused on the development of special monitoring techniques for neutron noise surveillance during the normal operation of nuclear reactors. To do so, a large variety of detectors can be used, such as neutron flux detectors, strain gauges, accelerometers,

velocity and pressure sensors, acoustic detectors, ultrasonic sensors, and others ([12], [36]). Their goal is to extract reliable information about the moving structural core components and the stochastically fluctuating thermal-hydraulic properties of the coolant flow. These properties have been identified as key sources, affecting the neutron noise characteristics in reactors. Therefore, the neutron noise on-line monitoring assists in insuring the normal operation of the core, and more importantly, detects and indicates possible malfunctions or abnormalities. The deviation from normal operation can be inferred by the observation of an unexpected phenomenology of the noise characteristics (i.e. patterns of APSD, amplitude, coherence and phase difference, etc.). It is to note that, the systematic surveillance of the reactor operation, using the neutron noise phenomenology, assisted repeatedly in the past in identifying the malfunction sources that prevent the normal and economical operation of reactors [6]. Typical neutron noise spectra based on on-line neutron detectors are presented in Fig. 21, for different PWRs worldwide. It can be easily observed that, all the spectra share similar shapes, i.e. stronger spectrum at the lower frequency range (<5 Hz), followed by a series of spectral peaks at specific frequencies. The following paragraphs give a short description of the knowledge, gained until nowadays, on identifying individual noise sources characteristics using on-line monitoring techniques.

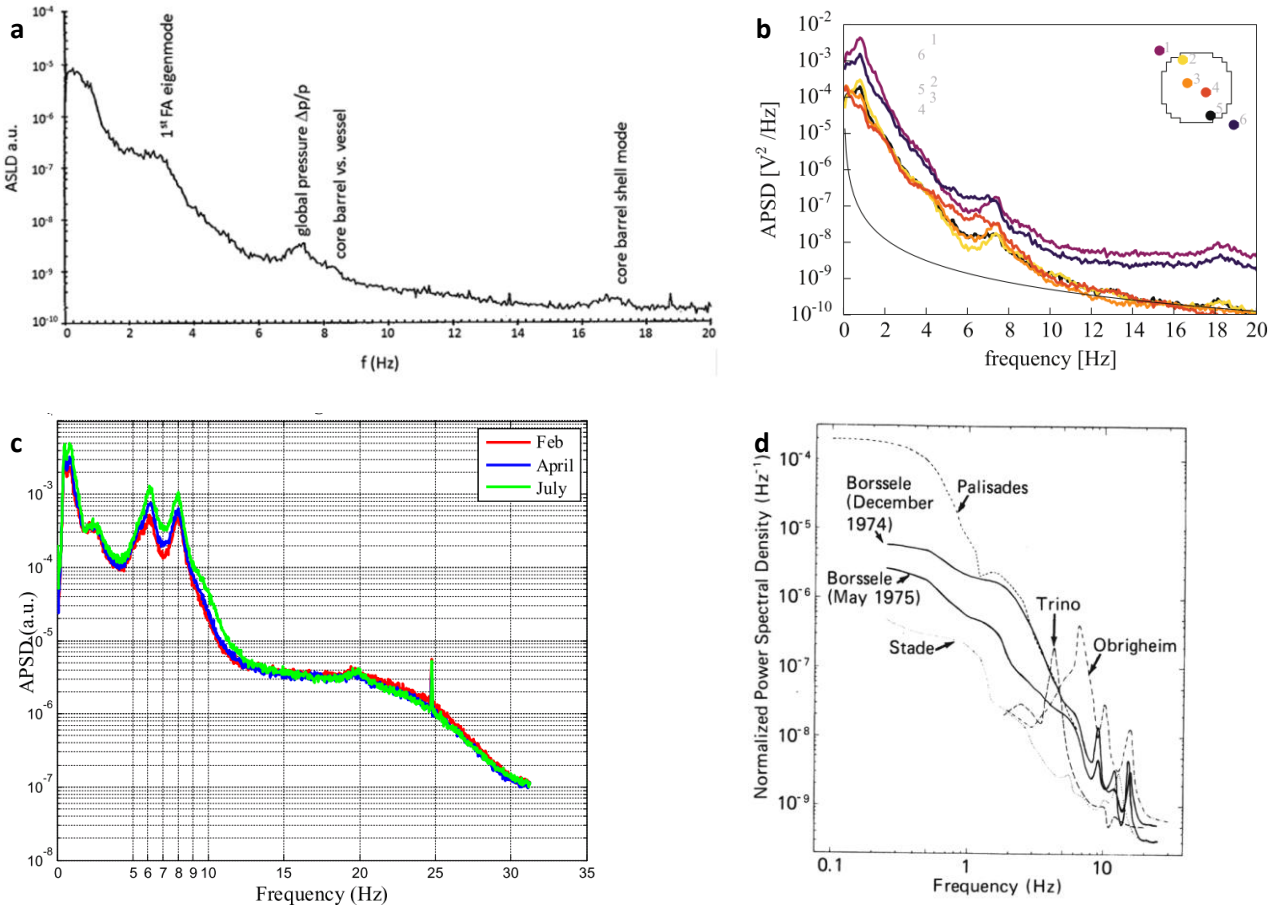

Fig. 21: Typical neutron noise spectrum based on in/ex-core neutron detectors in German (a & b, [14], [63]), Swedish (c, [64]), and other international PWRs (d, [12]).

Special attention has been given, by many researchers, to the understanding of the fuel assembly vibrational behavior due to the strong hydraulic forces, originating from the upward flow of the coolant ([12], [14], [33], [34], [36], [54]). Fuel vendors perform, systematically, extensive structural and dynamic examinations during the development and licensing of their fuel type designs. The fuel bundle vibrational modes either due to hydraulic forces from the coolant, or due to the motion excitation originating from the vibration of the core

support plate, can be studied in dedicated single channel thermal-hydraulic loops. Typically, three vibrational modes are reported in the literature: the first mode, at 0.6-$2\ Hz$, describes a clamped free assembly, fixed at the core-bottom; and the second and third modes at 0.8-$4\ Hz$ and 5-$10\ Hz$, respectively, corresponding to a perfectly fixed bundle at core-top and core-bottom levels with a C- and S-axial shape, respectively, as shown in Fig. 22 ([12], [33]). The fuel assembly motion is monitored during the normal operation using any type of neutron detectors. The core geometry is locally or globally modified due to the lateral vibration of the fuel bundles, and consequently, neutron flux gradients are expected to be observed in the vicinity of the noise source. The in-core neutron detectors can be used for indicating the location of a single or cluster of vibrating fuel assemblies, whereas the ex-core detectors are utilized for detecting the global motion of the peripheral fuel assemblies.

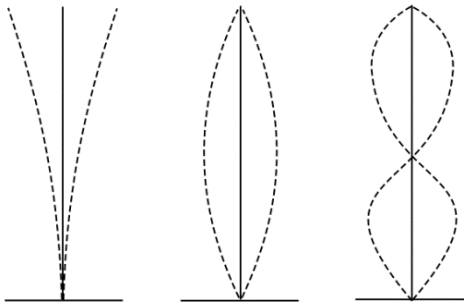

Fig. 22: First (left), second (center), and third (left) beam modes of fuel assembly vibration.

Another important structural component that affects significantly the neutron noise phenomenology is the motion of the core barrel, located inside the reactor pressure vessel. The coolant flows through the coolant loops, and enters the RPV from the side inlet orifices. Then the coolant flows downwards through the downcomer before it reaches the core lower plenum. The high turbulent inlet flow of the coolant results in strong pressure fluctuations impacting the core barrel, which in turn will start to vibrate in the sub-millimeter range ([33], [44]). Accelerometers and pressure sensors have been used for identifying two key vibrational modes of the core barrel; namely the *beam* and *shell* modes. The first corresponds to the pendular movement of the core barrel at the frequency of $8\ Hz$, whereas the latter describes the shape distorting vibration (i.e. changing circumferential shape) at the frequency of 20-$25\ Hz$, as shown in Fig. 23 ([36], [37], [65]). The monitoring of the core barrel vibrational behavior can be achieved by analyzing mainly the ex-core neutron detectors in the frequency domain and estimating their spectrum and the pairwise coherence and phase difference relationships at the frequencies of interest. More recently, indications of another core barrel mode, namely the *tilting* mode, have been presented in [64]. This mode describes the periodic tilting vibration of the core barrel around a horizontal, diagonal pivot direction, at the core half height at a frequency about $6\ Hz$, and it is possible to be identified when ex-core detectors at different azimuthal and axial levels are simultaneously analyzed.

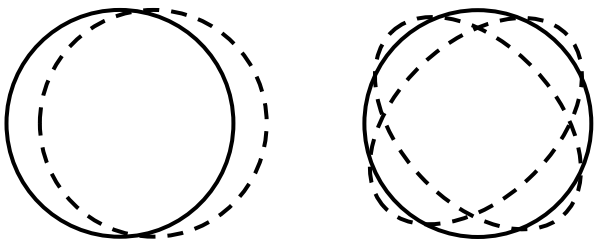

Fig. 23: Beam (left) and shell (left) modes of core barrel vibration.

Moreover, more challenging is the monitoring of the location of the vibration of control rods in PWRs. The amplitude of the control rods vibration is very small, and consequently, an in-core neutron detector has to be in the vicinity of the perturbation in order to detect this noise source. Their surveillance is rather important since their excessive vibrational behavior, due to the turbulent coolant flow, can lead to their damage [66]. In this unwanted scenario, the insertion of damaged control rods inside the fuel assemblies might be challenging or even impossible, and consequently, the safe operation of the reactor might be jeopardized. The control rod oscillatory movement is characterized in low frequency range (<5 Hz) due to the turbulent coolant flow [12]. In addition, partially inserted control rod will result to an unexpected neutron flux gradient, as measured by the in-core neutron detectors [12].

The vibration of permanently installed instrumentation tubes in BWRs has been extensively studied in the literature [43]. The vertical instrumentation tubes host the in-core neutron detectors for monitoring the neutron flux throughout the core. These tubes are typically located between four fuel assembly channels in BWRs. The turbulent coolant flow excites the instrumentation tubes, which start to laterally vibrate. The tubes motion could damage both their own structure but also the neighboring channel boxes and their hosted fuel assemblies. Clearly, the early detection of the extensive vibration of the instrumentation tubes is of key importance to preserve the normal reactor operation and reduce operational costs. The vibrational movement of these guide tubes can be identified by analyzing the in-core neutron detector signals in the frequency domain and by comparing these spectrum against reference plant data, which do not include this specific type of noise source (i.e. neutron detectors far from the effected instrumentation string). It should be mentioned that, the nominal frequency of the instrumentation tubes vibration has been quantified to be in the range of 2-5 Hz, in the case of Swedish BWRs [67].

In addition, the analysis of neutron detectors show some weak spectral peaks at higher frequency range and in particular at the frequency of 25 Hz ([19], [68]). This spectral characteristic corresponds to the rotational speed of commonly utilized primary coolant pumps in PWRs at $1'500$ rpm (i.e. 1 rpm=60 Hz). The rotational speed of the pumps results in pressure pulses in the coolant which enters the core. Consequently, a reactivity impact will be observed at that specific frequency, leading to a spectral peak of the neutron detectors signals. This peak is a plant specific characteristic of neutron noise and clearly depends on the rotational speed of the utilized coolant pump. It is mentioned for completeness that, other analyses showed respective peaks at 53 Hz or 75 Hz [2].

Furthermore, the inlet coolant flow properties have been reported to affect significantly the neutron noise phenomenology, especially at the lower frequency range ([2], [14], [50]). In PWRs, the coolant enters the core from 3 up to 4 coolant loops, depending on the reactor design. Stochastic fluctuations of the coolant flow and temperature are anticipated to be observed due to the coolant strong turbulent behavior. Thermocouples are installed at the cold/hot legs of the loops and downstream/upstream the coolant pumps, and flow-meters can measure the inlet flow rates at the core entrance. Therefore, the stochastic fluctuations of the inlet coolant flow and temperature can be surveilled using the on-line monitoring systems. The fluctuations of the inlet coolant flow properties directly impact, at the core-bottom axial level, the moderation conditions, which is translated to a strong spectrum of the neutron detectors in the lower frequency range (<5 Hz). The impact on the noise levels can be mitigated if the reactor design comprises special structural components (i.e. flow distribution device, secondary core support structure [50]), which homogenize the flow at the core lower plenum and decrease the flow properties perturbation and their strong spatial gradients.

This short literature review indicates a long list of perturbation sources that enrich the neutron flux spectrum with many spectral peaks, especially in the low frequency range (< 5 Hz). All these spectral peaks result in defining the neutron noise signature characteristics of the analyzed reactor. The knowledge of these noise characteristics under normal operation can be helpful for identifying possible deviations from standard performance. The following table, Table 2, summarizes the key perturbation sources that significantly affect the neutron noise phenomenology. These noise sources have been attempted to be modelled with advanced simulation techniques by various researches around the world, as it is presented in the next section.

Table 2: Key noise sources observed in LWRs.

Noise source	Monitored by	Frequency
Fuel assembly vibration *First mode* *Second mode* *Third mode*	In/Ex-core neutron detectors	 0.6-2 Hz 0.8-4 Hz 5-10 Hz
Core barrel motion *Beam mode* *Shell mode* *Tilt mode*	Ex-core neutron detectors	 8 Hz 20-25 Hz 6 Hz
Control rod vibration	In-core neutron detectors	<5 Hz
Guide tubes vibration	In-core detectors	2-5 Hz
Coolant flow and temperature fluctuations	In/Ex-core neutron detectors	<5 Hz
Pump rotation speed	In/Ex-core neutron detectors	25-75 Hz

3.3. Overview of neutron noise modelling techniques

The previous section introduced the reader to a plethora of noise sources, experimentally and analytically investigated in the literature. In parallel to the experimental study of neutron noise phenomena, high interest was always given to the modelling of nuclear stochastic perturbations using simulation tools. Lately, the increase in computer computational capacity and the continuous enhancements of the reactor physics and thermal-hydraulic codes assisted significantly in the development of various simulation tools for the modelling of different types of noise sources. Consequently, the impact of the individual noise sources on the neutron noise behavior can, nowadays, be studied in a more advanced and systematic manner. More importantly, a direct comparison of the simulation results against the real plant data helps on the identification of specific neutron noise characteristics. Therefore, the neutron noise modelling can be used as a supportive tool for improving the nuclear reactor surveillance and monitoring.

On top of that, it is essential to mention that, the European-funded research project, CORTEX, was launched in 2017 with the main goal to develop innovative methods and techniques for the neutron noise study and for improving the nuclear reactor safety [16]. The CORTEX project is coordinated by the Chalmers University and comprised 20 European and oversees partners[15] with long experience in nuclear reactor modeling and

[15] The PSI/LRT and the EPFL/LRS are heavily involved in the CORTEX project by providing neutron noise data based on both simulations and experiments (i.e. CROCUS experimental reactor), respectively, and by further enhancing the modelling of various types of noise sources and developing innovative measuring techniques of neutron noise phenomena, respectively.

diagnostics. In the framework of the interdisciplinary CORTEX project, the development of neutron noise modelling techniques faces a bright renaissance. A brief literature overview on the existing tools and the most recent modelling developments that significantly assist in the study of neutron noise phenomena are further described in the following paragraphs.

Particular attention shall be given to the CORE SIM code that was developed by the Chalmers University in 2011 [15]. CORE SIM is a dedicated neutron noise simulator in the frequency domain based on the two-group diffusion theory with one group of delayed neutrons. It is an open source code solely developed in the MATLAB environment. A reactor can be modelled in CORE SIM by providing as input the respective two-group macroscopic cross-sections and the kinetic parameters, evaluated by a nodal steady-state code (e.g. SIMULATE-3, PARCS, etc.). In addition, it is to note that, the CORE SIM code has been extensively validated and verified using a large set of both analytical scenarios and plant measurements. A stochastic or deterministic noise source can be easily modelled in CORE SIM by directly fluctuating the respective macroscopic cross-sections. The initial version of the code had a coarse discretization scheme mesh and has been already used for the modelling of various types of noise sources, such as vibrating control rods, core flow upwards perturbation, localized absorbers of various strength, fuel assembly vibration, and the core barrel vibrational movement ([15], [62], [69], [70]). In the framework of the CORTEX project, the CORE SIM code has been further improved in order to discretize the 3D space with high spatial resolution by employing advanced numerical techniques without the requirement of enormous computational memory [71]. Consequently, the updated version of CORE SIM can be used for the modelling of sub-millimeter vibrations, and therefore, very localized noise sources can be simulated. Furthermore, Chalmers University has recently developed a 2D neutron noise solver using the discrete ordinates approximate method. Noise sources can be modelled by fluctuating the macroscopic cross-sections [72].

The research center Helmholttz-Zentrum Dresden-Rossendorf (HZDR) has developed, since late ‘90s, the 3D best-estimate reactor dynamics code DYN3D, which solves either the two-group or multi-group neutron diffusion equation, or a simplified expression of the transport equation using nodal expansion methods for simplified geometries. The neutron solver is coupled to a four-equation thermal-hydraulic model with parallel channels without modelling their crossflows [73]. Recently, the DYN3D code has been used by HZDR for modelling various types of noise sources, such as the inlet coolant temperature, mass flow, and moderator density fluctuations [52]. The modelling of these noise sources has demonstrated the capabilities of the DYN3D code to study the neutron noise phenomenology and to explain some of the neutron noise characteristics, observed in the operation of the German KWU pre-Konvoi PWRs.

The Technical University of Dresden (TUD), with a long experience in signal and stability analysis research, has recently developed an analytical solver for the realistic modelling of the dynamic vibration of peripheral fuel assemblies, perturbed by the coolant flow. The vibration of the fuel assemblies is translated to the time-dependent variation of the reflector thickness. To this aim, the 2D lattice code CASMO-5 is used for generating the two group macroscopic cross-sections, which are then transferred to the DYN3D code for modelling the impact of vibrating fuel assemblies on the noise phenomenology ([51], [74]). The researchers have shown that the coherent vibration of the peripheral assemblies can explain, to some extent, the neutron noise phenomenology at the low frequency range (i.e. APSD, coherence, and phase difference) of real plant data. In addition, TUD studied the impact of fuel assembly stiffness characteristics (represented by the frequency of vibration) on the neutron noise amplitude increase, in order to understand better the cycle-to-cycle noise level increasing trend in KWU pre-Konvoi PWRs. In addition, TUD, similarly to HZDR, has modelled also the fluctuation of inlet coolant temperature in order to explain some characteristics of the neutron noise

phenomena. Furthermore, TUD used the probabilistic code Serpent-2 in order to study the impact of a lateral displacement of fuel assemblies on the macroscopic two-group cross-sections [63].

At the French Alternative Energies and Atomic Energy Commission (CEA), notable research with significant contribution in the modelling of neutron noise using both deterministic and probabilistic solvers has been performed. More specifically, CEA has developed an in-house Monte Carlo algorithm for solving the transport neutron noise equation in the frequency domain. The development is based on the so-called modified transport operator, introduced in [75], and has shown improved modelling capabilities compared to other neutron noise probabilistic solvers [76]. In the framework of the CORTEX project, CEA plan is to further improve the existing probabilistic solver by introducing advanced acceleration schemes, and most importantly, intends to implement it in its own developed Monte Carlo code TRIPOLI-4, which is broadly used by research institutes and the nuclear industry [77]. CEA has been also involved in the development of a 3D multi-group diffusion deterministic neutron noise solver implemented in its in-house multi-purpose deterministic code APOLLO3 [78]. So far, CEA has already analyzed the lateral oscillation and the travelling perturbation of a fuel assembly by varying the macroscopic cross-sections, and in the future, the plan is to implement temporal fluctuations of the fission rates at a cell level in order to model the vibrational movement of in-core detectors and control rods.

The Technical University of Valencia (UPV) uses the multi-dimensional diffusion kinetics code PARCS, developed by the U.S. Nuclear Regulatory Commission (NRC), for neutron noise modelling applications. The PARCS code has been utilized for modelling the lateral vibration of a single assembly in different core locations by perturbing the two-group macroscopic absorption cross-sections and by using fine meshes and accurate numerical solvers. In addition, the coolant density is also perturbed in a single channel in order to model the fluctuation of the coolant properties. The PARCS calculations have been compared against respective CORE SIM results, showing a satisfactory agreement [79]. The UPV research activities on this topic are on-going, however, the first results show that the PARCS code is capable of modelling noise sources and analyzing the resulted noise phenomenology. In addition, UPV has developed a dedicated noise solver in the time domain, called FEMFUSION, for the fuel assembly modelling by perturbing the macroscopic cross-sections [80].

At the Technical University of Madrid (UPM), the 3D transient nodal code SIMULATE-3K has been used for investigating the impact of coolant temperature and flow fluctuations on neutron noise phenomena. To this aim, the inlet coolant temperature and flow of each coolant loop is designed to fluctuate and the effect of these noise sources on the in-core and ex-core neutron detectors is studied. Interesting enough, the specificities which can be introduced on the noise behavior by the existence of specific core structural components (i.e. flow distribution device, and secondary core support structure) is in detail analyzed by UPM [50]. The SIMULATE-3K simulation results were compared against real plant data from the Spanish Trillo reactor, which also belongs to the KWU pre-Konvoi PWRs fleet, and some neutron noise characteristics related to the coolant flow stochastic nature have been successfully identified.

Last, the current doctoral thesis introduces the capabilities and assists in further development of the SIMULATE-3K code for the systematic analysis of the impact of fuel assembly vibration and coolant flow properties fluctuation on the neutron noise phenomenology. A detailed description of the PSI neutron noise modelling methodology is described in the following section, i.e. Sec. 3.4. The main characteristics of the neutronic solvers for modelling neutron noise phenomena, described in the current section, are summarized in Table 3.

Table 3: Summary of neutronic solvers for neutron noise modelling.

Codes *[User]*	Type of neutronic solver	Domain	Noise source modelling	Modelling approach
CORE SIM *[Chalmers Uni.]*	Diffusion Deterministic	Frequency	Control rods and fuel assemblies vibration, localized absorber of various strength, travelling perturbation, core barrel oscillation	Macroscopic cross-sections perturbation
DYN3D *[HZDR]*	Diffusion Deterministic	Time	Inlet coolant flow and temperature, and moderator density fluctuations	Perturbation of coolant properties
CASMO-5/DYN3D *[TUD]*	Diffusion Deterministic	Time	Inlet coolant temperature fluctuations, and vibration of peripheral fuel assemblies	Perturbation of coolant properties and macroscopic cross-sections of the reflector
Serpent-2 *[TUD]*	Transport Probabilistic	Static calculations	Fuel assembly lateral deflection	Macroscopic cross-sections modification
MC solver /TRIPOLI-4 *[CEA]*	Transport Probabilistic	Frequency	Fuel pins deflection	Macroscopic cross-sections variation
APOLLO3 *[CEA]*	Diffusion Deterministic	Time	Fuel assembly vibration, and travelling perturbation	Macroscopic cross-sections variation,
PARCS *[UPV]*	Diffusion Deterministic	Time	Absorber of variable strength and oscillation of coolant density	Macroscopic cross-sections variation, and perturbation of coolant properties
FEMFUSION *[UPV]*	Diffusion Deterministic	Time	Fuel assembly vibration	Macroscopic cross-sections variation
SIMULATE-3K *[UPM]*	Diffusion Deterministic	Time	Inlet coolant flow and temperature fluctuations	Perturbation of coolant properties
SIMULATE-3K *[PSI]*	Diffusion Deterministic	Time	Fuel assembly vibration, and coolant properties fluctuation	Macroscopic cross-sections variation, and coolant properties perturbation

3.4. PSI neutron noise modelling methodology

A dedicated neutron noise modelling methodology has been developed at PSI, in the framework of this doctoral thesis. To this aim, the CASMO-5/CMS-LINK5/SIMULATE-3/SIMULATE-3K code sequence has been utilized in this work, due to its strong capabilities on modelling, with high accuracy, the steady-state and the transient core behavior, and also because of the existing know-how acquired through the systematic analysis of the Swiss nuclear reactors using these codes since the late '90s. In addition, a set of MATLAB scripts has been developed in order to overcome the SIMULATE-3K limitation in simulating the fuel assembly vibration in a flexible and user-friendly manner, to reliably automatize the input-deck preparation and for post-processing the simulated results. An overview of the PSI neutron noise modelling methodology is given in Fig. 24.

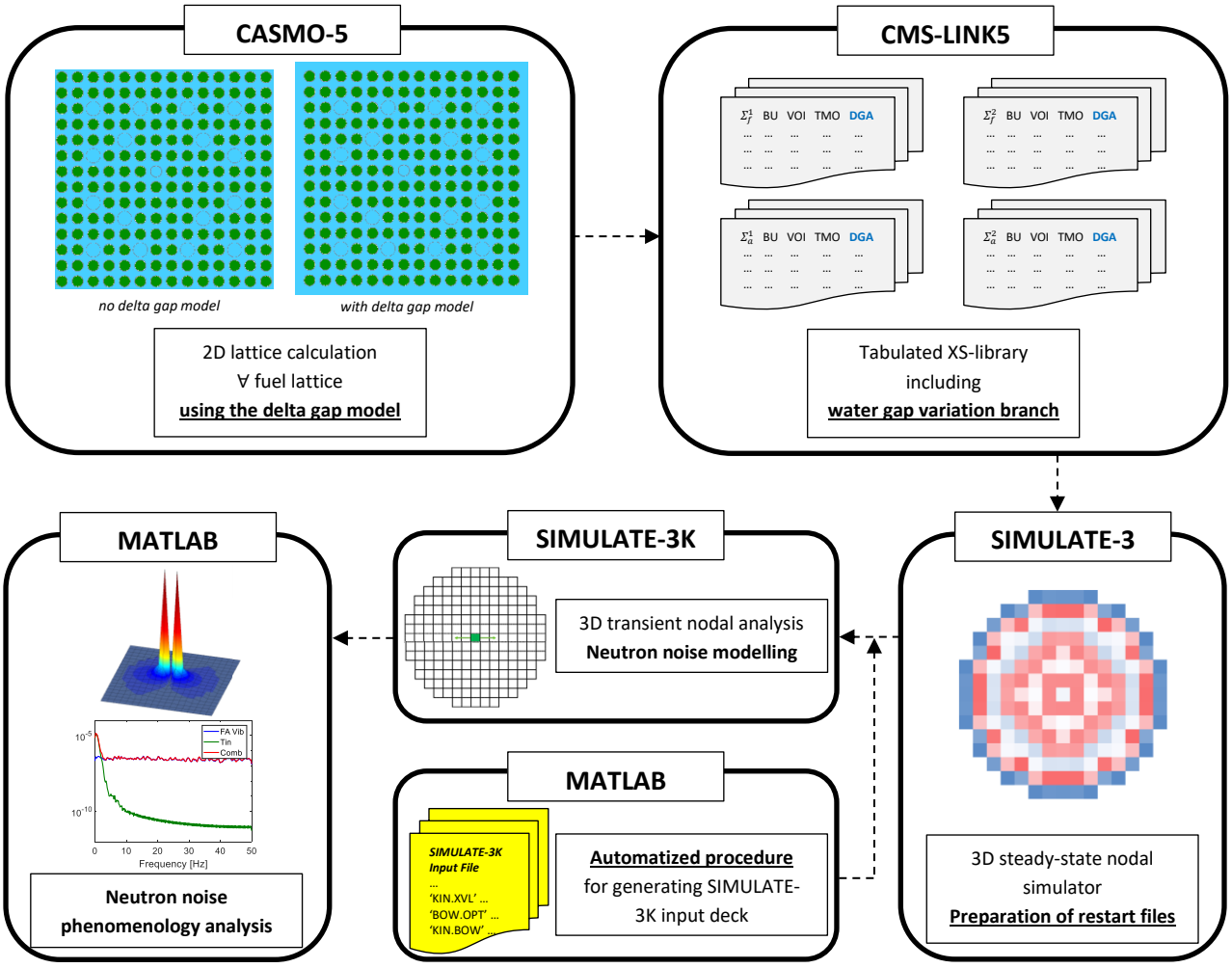

Fig. 24: PSI neutron noise modelling methodology flow chart.

3.4.1. Codes and simulation tools

Neutron noise sources can be modelled using the SSP's codes CASMO-5, SIMULATE-3, and SIMULATE-3K. First, in the current research, the 2D lattice code CASMO-5 is utilized for the preparation of the cross-sections. The generation of the nuclear data library, to be used downstream, is performed via the CMS-LINK5 code. After that, the steady-state and transient 3D full core calculations are carried out using the SIMULATE-3, and SIMULATE-3K codes, respectively. These codes are briefly described in the following sections.

3.4.1.1. CASMO-5

First, the fuel neutronic properties are estimated in terms of two-group parameters (i.e. macroscopic cross-sections, discontinuity factors) for every 2D segment (i.e. lattice) of each fuel assembly using the lattice code CASMO-5 (used version is 2.03.00) ([81], [82]). CASMO-5 is a multi-group 2D lattice and depletion code that solves the transport equation using an approximation technique, called the method of characteristics (MoC)[16]. CASMO-5 has been extensively used by both research institutes and utilities for the modelling of PWR and BWR core designs. In this work, the default number of 19 neutron[17] and 18 gamma energy groups is used for the cross-section library, using the microscopic cross-section data library ENDF/B-VII.1. The two-group homogenized nuclear parameters are evaluated using the geometrical and material composition characteristics of each 2D fuel segment, as they are explicitly defined by the user in the input files, at various state points (e.g. moderator temperature, boron concentration, control rod positions, etc.). A pre-defined selection of branch calculations can be defined by the input card *S3C*. Based on the *S3C* option, the CASMO-5 code generates all the commonly needed two-group homogenized nuclear data for further use by the 3D nodal simulator SIMULATE-3. In addition to the pre-defined matrix of branch cases, CASMO-5 offers the capability to generate supplemental cases for special applications, such as the modelling of bundles bowing or the fuel assembly lateral vibrations. To this aim, the user can activate the so-called *delta gap model* by utilizing the input card *DGA*. The *DGA* card adds a delta water gap branch calculation to the reference case, which permits the modification of the water gap width at any side of a lattice by an additional increment amount δ. The modelling of the water gap width variation at a lattice level is of key importance for the current research, since the generated two group macroscopic cross-sections are crucial for the time-dependent simulation of fuel assembly vibrations, using the transient nodal code SIMULATE-3K, as will be described in details in Sec. 3.4.2.

3.4.1.2. CMS-LINK5

The next step of the PSI methodology is the preparation of the cross-section data library to be called for the 3D nodal SIMULATE-3 and SIMULATE-3K calculations. To this aim, the CMS-LINK5 code (used version is 1.07 [83]) collects all the nuclear data, generated by the lattice and depletion calculations by CASMO-5 for every fuel segment, and then, post-processes them into a binary formatted library for further use by the nodal solvers.

3.4.1.3. SIMULATE-3

After the preparation of the cross-sections library, the next step is the 3D nodal static calculation of the analyzed core using the SIMULATE-3 code (used version is 6.07.17 [84]). The SIMULATE-3 code is a 3D full core solver with coupled neutronic and thermal-hydraulic capabilities for estimating the 3D nodal power at every fuel assembly of a PWR or BWR core. Each fuel bundle is discretized in Z equally sized axial nodes, and could be further divided in $2x2$ sub-nodes for enhancing the spatial precision of the solution. The two-group 3D diffusion equation is solved for each sub-node using the two-group homogenized cross-section, generated by CASMO-5, interpolated at the local operating conditions. The spatial scalar flux is estimated by SIMULATE-3, using a fourth order polynomial with quadratic transverse leakage. The intra assembly exposure is represented by a quadratic polynomial in two directions. In addition, the thermal-hydraulics model of SIMULATE-3 solves

[16] The MoC approximates the neutron transport equation by tracking the generation and removal of neutrons over paths, which are called characteristics. The scalar flux can be evaluated by integrating the neutron fluxes over all the paths.
[17] Up to 586 neutron energy groups can be used in CASMO-5.

the total mixture mass, energy, and momentum equations for each fuel bundle, by estimating the void fraction using a drift flux model. The 3D core is analyzed by SIMULATE-3 code at different operating state points, which describe the reactor states over one operational cycle (i.e. core follow calculations). The 3D core states can be stored in the so-called *restart file*, at specific operating conditions of interest, defined by the analyst, in the SIMULATE-3 input file.

3.4.1.4. SIMULATE-3K

The transient nodal code SIMULATE-3K (used version is 2.06.00 [85]) reads the operating conditions of the core at the analyzed core state via the respective restart file, and then the transient full core calculation can be initiated. The SIMULATE-3K code is a best-estimate 3D transient nodal simulator, with coupled neutronic and thermal-hydraulic capabilities, commonly utilized and validated by various research institutes and nuclear utilities for the evaluation of the dynamic reactor behavior and response [85]. Both the SIMULATE-3 and SIMULATE-3K codes share the same steady-state physics model. The transient solver of SIMULATE-3K is based on the time-dependent two-group diffusion equation using six-group delayed neutron groups; and the thermal-hydraulic model solves the two continuity, two energy, and one mixture momentum equations. The SIMULATE-3K code is used, in this thesis, for modelling various types of stochastic perturbations. The user can impose a fluctuation of the inlet coolant properties by including in the input file the input card *HYD.CLT,* describing the time-dependent evolution of the inlet coolant temperature, inlet coolant flow, and boron concentration of each coolant loop. In addition, the SIMULATE-3K code can be used for modelling the time-dependent variation of the water gap width sizes between neighboring fuel assemblies, by activating the so-called *fuel vibration model*. The latter is based on the two-group homogenized cross-sections generated by CASMO-5 using the *delta gap model*. This approach has the advantage to mimic the fuel assembly dynamic vibration without requiring the modification, at every time step, the computational mesh, which would be a rather computational costly option. The manual preparation of the boundary conditions, describing such stochastic behaviors can be a tedious task, especially if the coolant properties and/or the water gap widths are perturbed at every time step in the SIMULATE-3K calculation.

3.4.1.5. Supportive scripts

A set of supportive MATLAB scripts has been developed in this work, in order to simplify and automatize the SIMULATE-3K input deck preparation. In addition, the developed supportive scripts allow the reliable and flexible modelling of various fuel assembly vibration modes and patterns. This extends the capabilities of the fuel assembly vibration model and allows the systematic investigation of relevant neutron noise phenomena. More details about the modelling of stochastic perturbations and the description of the pre-processing MATLAB scripts are given in the following sections, i.e. Sec. 3.4.2 and Sec. 3.4.3.

The last step of the PSI neutron noise modelling methodology refers to the post-processing analysis of the neutron noise phenomenology. In this context, additional supportive MATLAB scripts have been prepared in this work for the spatial estimation of the neutron noise characteristics in both the time and the frequency domains. The neutron noise amplitude of the fast and thermal scalar fluxes can be estimated at every node by extracting the 3D time-dependent fluxes from the SIMULATE-3K output. Therefore, the spatial localization of the noise source can be identified. Moreover, the spatial characteristics (i.e. APSD, coherence and phase difference functions) of the simulated in/ex-core neutron detectors can be estimated by transforming their responses from the time to the frequency domain. This analysis is very useful for inferring the characteristics of individual simulated noise sources and for evaluating their impact on the noise phenomenology. By doing

so it is possible to compare the simulated neutron noise results against plant data, and attempt to identify the origin of measured neutron noise characteristics.

3.4.2. Fuel assembly vibration modelling

The modelling of the fuel assembly lateral vibrations using the CMSYS platform is of key essence for this work. As explained above, this modelling approach involves, among others, two main aspects; *first*, the homogenized two-group cross-sections generation using the *delta gap model* in the CASMO-5 lattice code, and *second*, the time-dependent simulations of the bundles lateral movement using the *fuel assembly vibration model* in SIMULATE-3K.

3.4.2.1. CASMO-5 delta gap model

CASMO-5 evaluates the few group macroscopic cross-sections ($\Sigma_{x,G}$) according to Eq. 19, by integrating the fine energy cross-sections over the volume of interest followed by a two group condensation scheme approach [86]:

$$\Sigma_{x,G} = \frac{\sum_{g=1}^{G} \Sigma_{x,g} \phi_g V}{\sum_{g=1}^{G} \phi_g V} \qquad \text{Eq. 19}$$

where, the different reaction rates are denoted by x, the fine and few energy group indices are represented by g and G, respectively, and ϕ_g describes the scalar flux in the fine energy group g. In the following paragraphs, emphasis is mainly given to the scattering ($\Sigma_{s,G}$), capture ($\Sigma_{c,G}$), absorption ($\Sigma_{\mathrm{a},G}$), and v-weighted fission ($v\Sigma_{f,G}$) cross-sections in the fast (G=1) and the thermal (G=2) energy groups. v denotes the average number of produced neutrons per fission. The neutron leakage effects in the 2D lattice calculations, when reflective boundary conditions are selected, are taken into account in CASMO-5 by using the *fundamental buckling mode* method for the critical spectrum calculations. In addition, the two-group diffusion coefficients (D_G) are estimated in CASMO-5 as a function of the transport cross-section using the so-called *in-scatter correction method*, as presented in Eq. 20:

$$D_G = \frac{1}{3\Sigma_{tr\ in,G}} \qquad \text{Eq. 20}$$

For the evaluation of the transport cross-section, $\Sigma_{tr\ in,G}$, the expression of Eq. 21 is used in CASMO-5, where $\Sigma_{t,G}$ denotes the total cross-section, $\Sigma^1_{s,g'\to g}$ describes the P_1 scattering macroscopic cross-section from the fine group g' to g, and ϕ^1_g, denotes the P_1 neutron flux moment ([82], [86]).

$$\Sigma_{tr\cdot in,G} = \Sigma_{t,G} - \frac{\sum_{g'=1}^{G} \Sigma^1_{s,g'\to g} \phi^1_{g'}}{\sum_{g'=1}^{G} \phi^1_{g'}} \qquad \text{Eq. 21}$$

Historically, the delta gap model (*DGA*) has been developed and introduced for the first time in CASMO-4 to have the capability of assembly bow modelling in LWR applications[87]. The delta gap model allows the user to simulate the lateral deformation/bow of a selected bundle in 2D by modifying the water gap thickness

between adjacent fuel assemblies in any of its four sides (i.e. south, north, west, and east). For PWR lattices only positive values of water width changes can be defined, while negative values can be imposed for BWR lattices as long as they remain smaller than the half width of the respective outer water gaps [88]. The delta gap model in CASMO-5 is the first key step for the fuel assembly vibration modelling in downstream 3D full core simulation, since it allows the modification of the water gap thicknesses on any side of the analyzed lattice and generates the associated cross-sections, discontinuity factors, and pin powers during a branch lattice calculation. In that frame, the amount δ of the water width increase on any of the lattice side has to be defined, and the lattice symmetry[18] has to be specified in the CASMO-5 input file by the user. The lattice symmetry is of paramount importance for the nuclear data preparation, since for a user-defined water width increase δ on one lattice side, the CASMO-5 delta gap model automatically imposes the same water width increase on the symmetric side.

This modelling particularity of the CASMO-5 delta gap model can be better understood with the illustrative example in Fig. 25. In this example, the nuclear data are evaluated for a given square lattice using the delta gap model. The user specifies the east side water width (δg_E) to be increased by an increment amount δ; equivalent to a lattice lateral displacement (bow) towards the west direction. The input definition of the water width increase depends, though, on the lattice symmetry as specified by the user. The requested lattice calculation (i.e. delta gap model with δg_E=δ) is correctly executed as specified by the user only for a full lattice geometry (Fig. 25a). The same lattice calculation in a half, quarter or octant symmetry (i.e. Fig. 25b-d) automatically assumes larger water width increase than the user request. The delta gap model in half or quarter lattice symmetry calculation imposes an additional water gap increase on the lattice south and west side (i.e. δg_E=δg_S=δ, and δg_E=δg_W=δ; Fig. 25b, c), respectively, whereas in an octant lattice symmetry calculation the water gap increase δ is applied in all four lattice sides (i.e. δg_E=δg_W=δg_N=δg_S=δ; Fig. 25d).

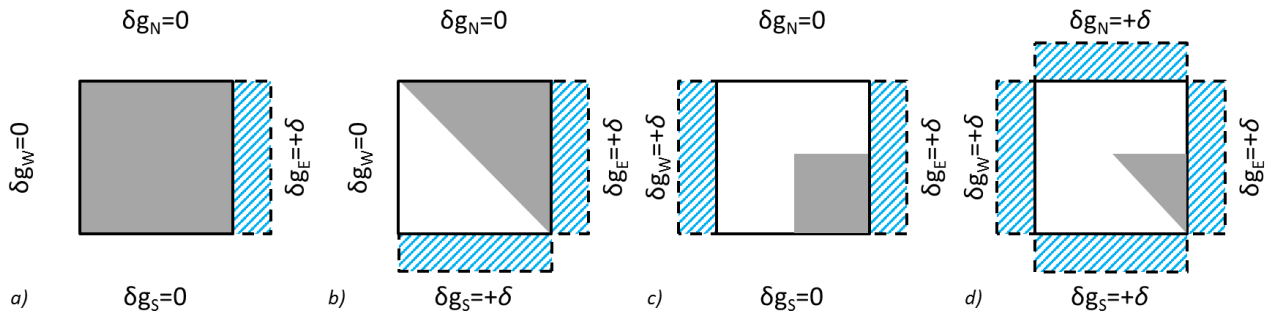

Fig. 25: Impact on water gap width thicknesses on the four lattice surfaces, depending on the assembly symmetry (*a*: full, *b*: half, *c*: quarter, *d*: octant), when the water gap thickness of the east side is requested to increase by δ in the delta gap model of CASMO-5.

The delta gap modelling approach clearly affects the nuclear data generation, since a larger moderator content than the user defined amount is utilized in the half, quarter and octant symmetric lattice calculations, as discussed in more detail in Sec. 4.1. In addition, it is emphasized that, nuclear data generated with the CASMO-5 delta gap model in quarter or octant lattice symmetry (Fig. 25c, d) are the only data compatible (readable) with SIMULATE-3K for the modelling of fuel assembly vibration[19]. It should be noted that, the nuclear data, utilized by SIMULATE-3K for the fuel assembly vibration modelling, represent accurately enough the physical

[18] LWRs lattices have, typically, a square geometry, and therefore, CASMO-5 approximates the transport equation using the MoC not only in a full geometry but also in half, quadrant, or octant symmetry to significantly reduce the computational power and time.

[19] In other words, nuclear data generated with another approach cannot be read, and therefore, utilized by SIMULATE-3K for time-dependent simulations.

mechanism of the laterally displaced lattice, despite the seemingly inaccurate modelling approach of the delta gap model at the CASMO-5 level through considering larger amount of moderator in the lattice. That is achieved through the nuclear data post-processing step in CMS-LINK5, which divides by two the change of the cross-sections (with respect to the unperturbed lattice calculation) generated with the CASMO-5 delta gap model in quarter or octant symmetry, as described in Sec. 4.1.

3.4.2.2. SIMULATE-3K fuel vibration model

The 3D core-wide calculations in SIMULATE-3K for the fuel assembly lateral movement depend on the preparation of the homogenized nuclear data library that includes the delta gap branch cases in CASMO-5 and their necessary post-processing in CMS-LINK5, as described in more detail in Sec. 4.1. The modelling approach in SIMULATE-3K assumes that the lateral movement of a fuel bundle corresponds to an increase or a decrease of the water content within the analyzed lattice and its adjacent neighbors in the direction of the motion. However, this assumption is rather unrealistic since, in reality, only the fuel rods are laterally dislocated from their initial location during the lateral vibration of a fuel bundle without any modification of the total water content of the analyzed lattice. Clearly, the utilized modelling approach of fuel assembly vibration is not reflecting the reality, however, it is an efficient approximation, and the only way available so far, for modelling such phenomena without the need of modifying the computational mesh at every time step, which would result into significant increase of the computational cost for full 3D core dynamic simulations.

The following two sections present in detail the characteristics and the capabilities of the original and improved models for the modelling of fuel assembly vibration in the SIMULATE-3K code. The former, has been developed by SSP, in a first stage, in order to study the global impact of vibrating bundles on the neutron flux behavior. However, during this doctoral thesis, some limitations of the original model have been identified and a series of improvements of the model have been initiated in the framework of a collaboration between PSI and SSP, and resulted in offering the user higher degree of flexibility and allowing more realistic vibrational patterns.

Original model

Starting from version 2.06.00, the transient nodal code SIMULATE-3K offers the capability to simulate the time-dependent lateral vibration of fuel assemblies in the x- or/and y-direction by automatically adjusting the water gap width sizes of both the vibrating fuel assembly and its adjacent ones [57]. To this aim, SSP has developed the so-called *fuel assembly vibration model* in SIMULATE-3K with the goal to study the impact of the lateral oscillation of fuel bundles on the neutron noise behavior of PWR cores. The fuel assembly vibration model has been first introduced in PWR applications in [14]. This model can be activated using the *KIN.BOW* input card and it utilizes the cross-sections, generated using CASMO-5 with the DGA model. A simplified example is used in this section in order to demonstrate the modelling process of the fuel assembly vibration model in SIMULATE-3K.

Three fuel assemblies are designed to have $2x2$ sub-node discretization scheme, for which the central bundle (FA_i) is modelled to laterally vibrate in the x-direction, as shown in Fig. 26. For simplicity, if the central assembly FA_i is assumed to move towards its adjacent assembly FA_{i-1}, at a time step t, then the inter-assembly distance between the assemblies FA_i and FA_{i-1} will decrease by an increment value δ[20]. The correct

[20] It is recalled that, CASMO-5 cannot perform lattice calculation for a configuration with a negative water gap width for PWR fuel assemblies. However, SIMULATE-3K is modelling the decrease of water gap thickness by an increment values δ

modelling would require that the geometrical size of all the involved bundles must be preserved during this dynamic event. To do so, the inter-assembly distance between the assemblies FA_i and FA_{i+1} must increase by the same increment amount δ. However, the original fuel assembly vibration model does not ensure this condition. The inter-assembly distance between the assemblies FA_i and FA_{i+1} will be modified (increase/decrease) by an increment amount δ', different from δ. Therefore, the geometrical size of the vibrating assemblies is not preserved, and consequently the neutron noise will have an erroneous response. This simplified example shows that the instantaneous movement of one bundle to one direction affects the local conditions of eight sub-nodes; i.e. the four sub-nodes of the moving bundle FA_i, the two right sub-nodes of the adjacent bundle FA_{i-1}, and the two left sub-nodes of the adjacent bundle FA_{i+1}.

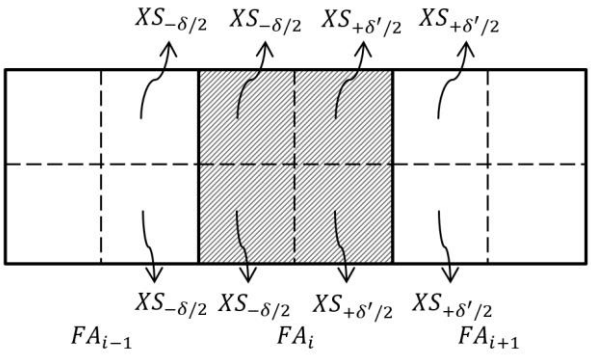

Fig. 26: Non-preservation of the geometrical size of the vibrating assembly in the original fuel assembly vibration model.

The user can activate and control the original fuel vibration model in the officially released SIMULATE-3K version 2.06.00 using the *KIN.BOW* and *BOW.VIB* input cards. All the fuel bundles of the same fuel design type, defined in the input file of the steady-state nodal SIMULATE-3 code, are grouped together and they can be vibrated at a specific amplitude and frequency, specified by the user. An example of the fuel vibration model activation in the SIMULATE-3K input deck is illustrated in Fig. 27. First, the PWR assembly vibration model is activated using the first option in the *KIN.BOW* card (i.e. 'ON'). In addition, a vibrating cluster of size 1 (i.e. just one fuel assembly is selected to vibrate) and the time interval (in seconds), at which the stochastic perturbation is imposed, are defined by the second and third options in the *KIN.BOW* card, respectively.

```
'COM' * FUEL VIBRATION MODEL
'KIN.BOW' 'ON'       1        0.1      / PWR Assembly Vibration MODEL
'BOW.VIB' 'TYPE1'    0.2               / Assembly Vibration Amplitude
'BOW.OPT' 'ON'       'COS'             / Assembly Bow Model Control
```

Fig. 27: Example of the original fuel vibration model activation in the SIMULATE-3K input deck.

Then, the user introduces the *BOW.VIB* input card, which explicitly defines which fuel design type (as defined by the respective identifier) undergoes a lateral vibration and at which amplitude. In this example, all the fuel bundles of a $TYPE1$ fuel design identifier will randomly vibrate with an amplitude of $2\ mm$. It is important to emphasize, that the user is restricted to vibrate all the bundles of the same design identifier regardless their core location, which is one of the limitations of the original model.

between two adjacent fuel bundles (for mimicking the approaching of an assembly to its neighbor) by extrapolating below zero the corresponding cross-section data set based on a water gap width of $+\delta/2$.

Last, the user can optionally impose an axial shape on the vibrating assemblies, using the *BOW.OPT* card, in order to model bowing effects. The user activates the bow model control using the first option in the *BOW.OPT* card, and then a pre-defined cosine shape can be superimposed on the 2D delta gaps by using the 'COS' command in the second option of the *BOW.OPT* card. Alternatively, the user can use the '$1D$' command in order to impose any other kind of axial shape on the x- and/or y-direction. To do so, the use of the *BOW.AXL* input card is necessary, by which the axial delta gap shape at every nodal level is explicitly defined. The activation of the bow model control establishes a constant axial deformation of all the fuel assemblies, which belong to the '$TYPE1$' fuel design. In other words, the selected fuel assemblies will latterly vibrate by having a constant axial shape, imposed by the user, which is not varying over time. Modelling of the latter configuration would be desirable in order to study the impact on the neutron noise behavior of the first and higher vibration modes, which are expected to exist in the core [2].

It is recalled that, SIMULATE-3K is the first commercial code that allows the fuel vibration modeling and the study of the neutron noise phenomenology. The detailed and systematic analysis of the original model capabilities during this doctoral thesis has revealed some limitations, summarized as follows:

- The original fuel vibration model does not ensure the conservation of the gap width at the opposite sides of the vibrating fuel assembly, as shown in Fig. 26. This is a key limitation of the model which produces erroneous neutron noise results.
- The original vibrating modeling approach results in a non-physical lateral movement of the fuel bundles. In other words, the lateral oscillation of a fuel assembly, by an increment amount δ over its nominal position, is translated in the code by a lateral displacement of the entire bundle (i.e. same displacement of all the axial nodes), as presented in the left plot of Fig. 28. However, in reality, the fuel assemblies are fully fixed at the bottom core support plate, which does not allow any lateral displacement of the bottom part of the bundles. Hence, the original modelling approach is anticipated to overestimate the neutron noise levels at the core bottom axial levels. In addition, the axial bow shape deformation can be easily imposed on the fuel bundles using the *BOW.OPT* input card. The assembly bow model is of particular interest for studying the impact of different bow patterns on the neutronic response of the core (e.g. radial flux distribution, leakage, etc.).Therefore, the simultaneous utilization of both the fuel vibration and assembly bow models can be used for studying the impact of axially deformed vibrating bundles on the neutron noise phenomenology. However, the current modelling approach results to a non-physical lateral displacement of the bowed bundle, as illustrated in the right plot of Fig. 28.
- The fuel bundles can be vibrated according to their fuel design identifier (*BOW.VIB* card). Therefore, exactly the same vibrational characteristics (i.e. amplitude and frequency) are automatically imposed to all the bundles having the same fuel design identifier, selected by the user. Consequently, if the analyst would like to model the vibration of only one single bundle, which shares its fuel design identifier with other assemblies, the only way to bypass this issue is via assigning a new fuel design identifier to that single bundle. It is recalled that, in the CMSYS platform, the fuel design identifiers are defined at the steady-state simulation level, i.e. SIMULATE-3, preceding the transient calculations. Two ways can be followed in order to impose a stochastic vibration to any bundle of the core. In the first approach, a single fuel design identifier could be attributed to each fuel assembly during the preparation of the SIMULATE-3 input deck. However, by doing so, the complexity and the risk of an erroneous SIMULATE-3 input file increases significantly. In the second approach, the user could determine in advance which bundles to be vibrated in the SIMULATE-3K calculations, and then for

each of these bundles, a single fuel design identifier is attributed during the preparation of the SIMULATE-3 input deck. Although the latter approach simplifies the preparation of the SIMULATE-3 input file, the risk of repeating the SIMULATE-3 calculations still exists, since the user might want, in the future, to study the behavior of other vibrating bundles, which were not considered in the initial plan, and therefore, no explicit fuel design identifier was defined for them.

- Commonly, the nuclear core is designed in a chess-board pattern. In other words, fuel bundles of different fuel design identifiers might be placed next to each other. Consequently, vibrating a sub-group of the core (i.e. fuel assembly cluster) might be a challenging task. This application is of particular interest for studying phenomena in which the two core-halves are vibrating in an out-of-phase manner.

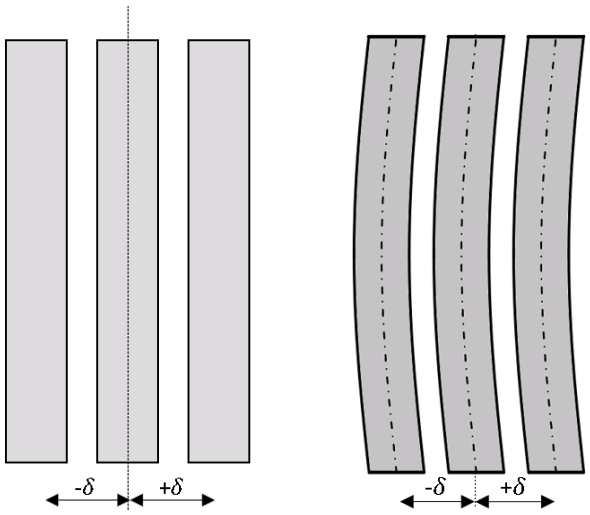

Fig. 28: Non-physical lateral displacement of a single fuel assembly, without (left plot) or with (right plot) axial bow shape, by an increment amount δ over its nominal position, according to the original fuel vibration model in SIMULATE-3K.

Improved model

Despite the abovementioned limitations, the original fuel vibration model has been already applied in the literature for basic and global scoping analyses performed by nuclear utilities [14]. However, the systematic study of neutron noise phenomena at a research level requests the improvement and enhancement of the original model capabilities in order to offer a full flexibility to the user for imposing any type of oscillation pattern on the fuel bundles and to simulate more realistic scenarios in a more rigorous manner. Therefore, a close collaboration between PSI and the codes developers was established and necessary code modifications and refinements were performed. These improvements resulted in an *updated fuel vibration model,* allowing the user to dynamically change the water gap widths of any node of the core at any time step. To do so, a series of additional subroutines has been developed and incorporated in the SIMULATE-3K source code, allowing the processing, in a tabulated form, of the time-dependent 3D delta gap widths, imposed by the user. To this aim, three new input cards have been introduced in the code; these are the *KIN.XVL*, *KIN.YVL*, and *KIN.ZVL* input cards. The two first input cards, describe the dynamic modification of the delta gap sizes in the x- and y-directions, respectively. The user can freely impose any type of oscillation mode (e.g. random, stepwise, sinus patterns, etc.) and vibrational characteristics (i.e. amplitude and frequency) on both water gap width sides of the vibrating bundle by preserving its geometrical size. Fig. 29 shows how the movement of a central assembly towards its west adjacent neighbor can be modelled with the updated fuel vibration model in SIMULATE-3K.

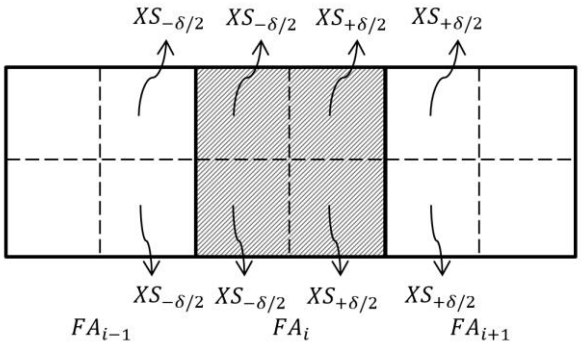

Fig. 29: Modelling of the lateral movement of the central fuel assembly towards the left direction by an increment value $\boldsymbol{\delta}$ at time step $\boldsymbol{t}$.

It is recalled that, SIMULATE-3K has a fixed computational mesh, allowing the efficient solution of the diffusion equation. Therefore, the modelling of the fuel assembly lateral movement can be achieved by only mimicking the vibration with the change of the water gap widths of all the involved sub-nodes, using the previously generated homogenized cross-sections. To this aim, the cross-sections of the two right sub-nodes of FA_{i-1} and the two left sub-nodes of the central assembly are evaluated based on a decrease in the water gap width, by $\delta/2$, at time step t. In the same time, the cross-sections of the two right sub-nodes of FA_i and the two left sub-nodes of the last assembly are evaluated based on an increase in the water gap width, by $\delta/2$, at time step t. Both conditions are necessary to be fulfilled in order to model successfully the movement of FA_i towards FA_{i-1}, by preserving the fuel assembly geometry (i.e. bundles shape and area). The described procedure is applied at every time step by appropriately modifying the delta gap sizes between all the adjacent bundles, involved in this process. The fuel assembly vibration process is activated and controlled by the user, as it is described in the next paragraphs.

The third input card can be used for defining a global axial shape, which will be superimposed on the time-dependent water gap widths in the x- and y-directions. By doing so, it is possible to model different types of vibrational modes (e.g. cantilevered (clamped-free from top), hinged-free shapes, etc. [2]) and study their impact on the local neutron noise behavior. An example of the SIMULATE-3K input file, demonstrating the activation of the updated fuel assembly vibration model is illustrated in Fig. 30. It is to note that, the improved model is included in a beta version of the SIMULATE-3K code, and it has been extensively used during this doctoral thesis. The verification and validation of the updated model is described in detail in *chapter 4*.

```
'COM' * FUEL VIBRATION UPDATED MODEL
'KIN.BOW' 'ON',,,   1       'gaps_control.dat'      / PWR Assembly Vibration MODEL
'BOW.OPT' 'ON'      'CONSTANT'                      / Assembly Bow Model Control
'INC.FIL' 'gaps_x_Direction.inc'                    / Time dependent delta gaps in x-direction (KIN.XVL)
'INC.FIL' 'gaps_y_Direction.inc'                    / Time dependent delta gaps in y-direction (KIN.YVL)
'INC.FIL' 'gaps_z_Direction.inc'                    / Time dependent delta gaps in z-direction (KIN.ZVL)
```

Fig. 30: Example of the updated fuel vibration model activation in the SIMULATE-3K input deck.

Thanks to the new developments, the user can now impose any type of vibrational pattern on the fuel bundles with the help of the improved fuel vibration model. The dynamic modification of the water gap widths is imposed as an input file by the user. Therefore, the precision of the simulated event depends on the correctness of this input deck. It is recalled that, a typical PWR core consists of more than 170 fuel bundles, commonly divided in more than 20 axial nodes when they are analyzed by advanced nodal simulators, as in SIMULATE-3. In addition, transient simulations typically have more than $2'000$ time steps in order to ensure the convergence of the static solution and to capture in detail the dynamic neutronics/thermal-hydraulics

phenomena. Therefore, it is easily understandable that the preparation of an input deck, which explicitly describes the 3D dynamic behavior of the selected vibrating assemblies (even if it is only for a single assembly) can be a challenging and rather complex task. The input deck will be lengthy, even in the simplified case of a single randomly vibrating fuel assembly.

As an example, Fig. 31 shows the content of the *KIN.XVL* input card that describes the random vibration of the central fuel bundle of the KKG core (located at the $H8$ position, as shown in Fig. 7) in the x-direction with a maximum amplitude of $0.011\ cm$. The water gap widths between the central assembly and its two neighbors in the x-direction (i.e. $H7$ and $H9$) are modified at every $10\ ms$. For example, the water gap width between the $H7$ and $H8$ bundles decreases by $0.085\ cm$, and consequently the water gap width between the $H8$ and $H9$ bundles increases by the same increment amount at t=$0.00\ s$, in order to model the instantaneous movement of the central assembly to the left direction. This process is repeated for every time step over $35\ s$, resulting to a total number of $3'501$ input entries for the modelling of a single vibrating assembly only in one direction. The input file length grows significantly as the number of the vibrating assemblies increases and also when a vibration in two dimensions is modelled (i.e. use of both *KIN.XVL* and *KIN.YVL* cards). At the same time, the water gap width sizes on both sides of the vibrating assemblies must comply with the conservation of the bundles surface area. In other words, the surface area of a fuel bundle must not change during the transient simulation. On the whole, it is concluded that the preparation of the input file, describing the time-dependent variation of the 3D delta gaps is a complex task. Therefore, the need of developing an automatized tool is of paramount importance in this work, in order to prepare with high confidence the SIMULATE-3K input deck and to simplify the simulation procedure by avoiding tedious and repetitive activities, and to overcome the difficulty of modelling by hand using the original model.

```
1   'KIN.XVL',   3501,      1,
2   0.000    8  8  9 -0.085  0.085
3   0.010    8  8  9 -0.075  0.075
4   0.020    8  8  9 -0.032  0.032
5   0.030    8  8  9  0.077 -0.077
6   0.040    8  8  9  0.018 -0.018
7   0.050    8  8  9  0.019 -0.019
8   0.060    8  8  9  0.094 -0.094
9   0.070    8  8  9  0.017 -0.017
10  0.080    8  8  9 -0.108  0.108
11  0.090    8  8  9  0.068 -0.068
12  0.100    8  8  9  0.024 -0.024
13  0.110    8  8  9 -0.004  0.004
14  0.120    8  8  9 -0.051  0.051
15  0.130    8  8  9 -0.053  0.053
16  0.140    8  8  9 -0.004  0.004
17  0.150    8  8  9 -0.060  0.060
18  0.160    8  8  9 -0.099  0.099
19  0.170    8  8  9 -0.073  0.073
20  0.180    8  8  9 -0.053  0.053
21  0.190    8  8  9 -0.066  0.066
22  0.200    8  8  9  0.023 -0.023
23  0.210    8  8  9  0.071 -0.071
24  0.220    8  8  9  0.068 -0.068
25  0.230    8  8  9  0.066 -0.066
```

Fig. 31: Example of the *KIN.XVL* input card in SIMULATE-3K for describing the random vibration of a single bundle in the x-direction.

To this aim, an in-house script developed in the MATLAB environment has been prepared during this doctoral work. Fig. 32 presents in a concise scheme the capabilities of the developed automatized script. The preparation of the SIMULATE-3K input deck is based on five main steps. A detailed description of the in-house script functionalities and capabilities is presented in Appendix ii.

- ***step 1***: The user defines the main simulation parameters. These are the simulation duration, its time step, and the maximum amplitude of the bundles lateral displacement.
- ***step 2***: The total number and the location of the vibrating bundles is selected.
- ***step 3***: The direction of the vibration (i.e. in x- and/or in y-directions) is selected.
- ***step 4***: The vibration type (i.e. random oscillation or vibration following a sine-wave function at a specific nominal frequency) is selected.
- ***step 5***: The user selects whether the vibrating bundles are oscillating identically (synchronized) or stochastically (unsynchronized) between each other.

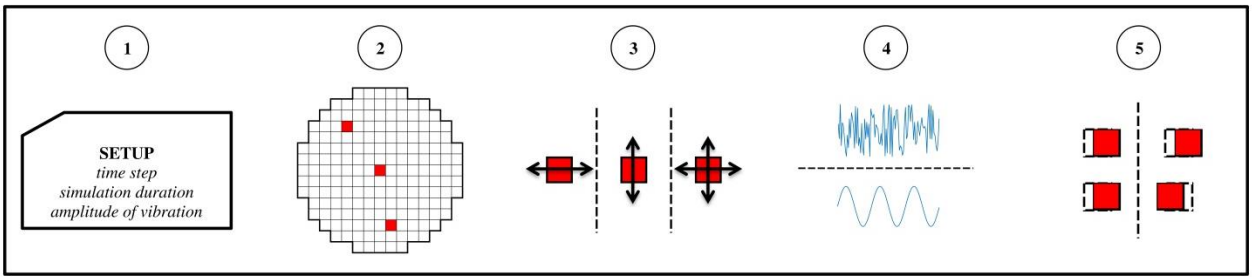

Fig. 32: Developed methodology for evaluating the time-dependent delta gaps of selected vibrating fuel assemblies (*1*: main parameters setup, *2*: selection of number and location of vibrating fuel assemblies, *3*: direction of vibration, *4*: random or sine vibration, *5*: synchronized or unsynchronized vibration mode).

The time-dependent delta gap widths in one and/or two directions for all the selected vibrating assemblies are then automatically printed out in text files, which are incorporated in the SIMULATE-3K input file. The capabilities of the fuel vibration model in SIMULATE-3K and the functionality of the PSI toolbox are systematically analyzed and discussed in the following *chapter 4*, with the help of a series of simplified and more complicated simulated scenarios.

3.4.3. Modelling of thermal-hydraulic parameters fluctuation

This research focuses not only on the neutron noise phenomena due to fuel assembly vibrations, but also on the induced noise due to the stochastic fluctuation of thermal-hydraulic parameters[21], since they were found to have an important impact on the neutron noise behavior. The SIMULATE-3K code has a special module that allows the modeling of the time-dependent fluctuation of the inlet coolant flow, the inlet coolant temperature, and the boron concentration, at every coolant loop of the analyzed reactor. This module is governed by the input cards *HYD.CLG*, *HYD.CLW*, *HYD.CLT* and *HYD.CLB*. The functionality and structure of this module is presented in detail in Appendix iii.

[21] It is recalled that, the significant effect of the turbulent coolant flow on spatial neutron noise behavior has been already described in Sec. 3.2.

Chapter 4: PSI Neutron Noise Methodology: Verification and Qualification

In the current chapter, the capability of the PSI neutron noise modelling methodology to simulate the vibration of fuel assemblies is verified and qualified. First, the performance of the CASMO-5 delta gap model for the generation of nuclear data, at a lattice level, is studied and verified against reference results generated by the Monte-Carlo code Serpent-2. Then, several perturbation scenarios at a nodal level, ranging from a single node vibration up to a large cluster of vibrating assemblies, are simulated and analyzed in order to demonstrate the correctness of the developed modelling approach at a 3D full core level. The analysis focuses on the impact of various vibrational characteristics (i.e. number of vibrating bundles, direction and amplitude of vibration, and bow deformation) on the neutron noise amplitude and phase. It is important to note that, the SIMULATE-3K fuel vibration model cannot be validated against real plant data, since in real power reactors it is practically impossible to isolate individual noise sources and to measure in a very fine detail the impact of vibrating bundles on the neutron flux. Therefore, any assessment of the noise sources modelling shall be performed based on the anticipated underlying physical mechanisms and the use of engineering judgment.

This chapter is based on the researches performed in the following papers:

- D. Chionis, A. Dokhane, L. Belblidia, G. Girardin, H. Ferroukhi, A. Pautz, "*Development and verification of a methodology for neutron noise response to fuel assembly vibrations*", accepted to be published in Annals of Nuclear Energy, (2020) [56].
- D. Chionis, A. Dokhane, M. Pecchia, G. Girardin, H. Ferroukhi, A. Pautz, "*SIMULATE-3K analyses of neutron noise response to fuel assembly vibrations and thermal-hydraulics parameters fluctuations*", Proceedings of the 2017 International Conference on Mathematics & Computational methods applied to nuclear science and engineering (M&C '17), Jeju, Korea, (2017) [57].

4.1. Verification of CASMO-5 delta gap modelling assumptions

In a vibrating fuel assembly, the fuel pins are laterally displaced over their reference positions. The accurate and precise modelling of the fuel pins vibration mechanism using neutronics solvers, would require an adaptive computational mesh following the dynamic movement of the fuel pins. This realistic modelling approach is an expensive computational solution, impossible to be applied in 3D full core geometries. To overcome this computational limitation, SSP decided to model the fuel assembly vibration in SIMULATE-3K based on two-group homogenized cross-sections which are generated by CASMO-5 using the delta gap model, as introduced in *chapter 3*. It is recalled that, the delta gap model increases/decreases the water width thickness by an increment amount δ on the lattices sides, as specified by the user in the CASMO-5 input file, in order to mimic a lattice lateral displacement of δ.

The current section analyzes this modelling simplification and studies its impact on the generated two-group homogenized cross-sections. To do so, it is assumed that the fuel rods of a 2D lattice can be displaced from their initial/reference positions in the x direction. This displacement can be modelled in CASMO-5 using the *LDX* input card, respectively, [88]. The use of the *LDX* card allows the user to statically displace single fuel rods within their own pin cells, without increasing the water content of the analyzed lattice. This approach corresponds to a realistic modelling of the lattice lateral movement and it is used as a reference case for

comparison against the delta gap model. It is important to emphasize that, nuclear data generated using the fuel rods displacement model *LDX* are not compatible with downstream 3D full core simulation of fuel assembly vibration in SIMULATE-3K. It is recalled that, the SIMULATE-3K fuel assembly vibration model is compatible only with cross-sections produced using the CASMO-5 delta gap model in a quadrant or octant lattice symmetry. Therefore, in this section it is attempted to study the impact on nuclear data when the delta gap model and its variations are used instead of the realistic *LDX* approach. To this aim, the homogenized two-group cross-sections are estimated using either the *LDX* or the delta gap models, in CASMO-5, for a simplified 2D lattice with $14x14$ fuel rods layout (Fig. 34), using reflective boundary conditions. The impact of the water gap thickness increase by an increment amount of δ=0.1 cm on the homogenized two-group cross-section is evaluated in both modelling approaches. To this aim, the following five lattice calculations are analyzed and compared, according to Fig. 33:

- ***Case a*** - Unperturbed case: Unperturbed lattice in which all the fuel rods are positioned in their reference locations. Neither the fuel pin displacement *LDX* nor the delta gap model is used in the unperturbed case (Fig. 33a). This calculation allows to estimate the two-group homogenized cross-sections under unperturbed conditions.
- ***Case b***: All fuel rods are displaced to the west direction by an increment amount δ=0.1 cm using the fuel displacement *LDX* model in CASMO-5. Due to the reflective boundary conditions, this scenario corresponds to the movement of the assembly towards its west neighbor (Fig. 33b). This case allows the calculation of the cross-sections change as a result of a realistic modelling of fuel lattice displacement. Nuclear data generated using this approach are not compatible for 3D full core modelling of fuel assembly vibration in SIMULATE-3K. The delta gap model is not used in this case.
- ***Case c***: The east side water gap (δg_E) is increased by δ=0.1 cm using the delta gap model in full assembly symmetry calculation in CASMO-5 (Fig. 33c). The cross-sections are generated over the homogenized region, which includes both the original geometry of the studied lattice and an additional moderator layer of a 0.1 cm width in its east side. The water gap increase is not imposed to any other face of the lattice, since the lattice calculation is performed in full geometry. Nuclear data generated using this approach are not compatible and therefore cannot be read by SIMULATE-3K for the time-dependent simulations of the fuel assembly vibrations.
- ***Case d***: The east side water gap (δg_E) is increased by δ=0.1 cm using the delta gap model in quarter assembly symmetry calculation in CASMO-5. Automatically, the water gap thickness increase δ is imposed also on the symmetric side (i.e. west side) due to the quarter symmetry (Fig. 33d). Cross-sections generated using this variation of delta gap model are compatible with downstream 3D full core calculation of fuel assembly vibration in SIMULATE-3K.
- ***Case e***: The east side water gap (δg_E) is increased by δ=0.1 cm using the delta gap model in octant assembly symmetry calculation in CASMO-5. Automatically, the water gap thickness increase δ is imposed also on all four sides of the assembly (Fig. 33e). This delta gap model variation is the second available option for generating cross-sections used for simulating fuel assembly vibration in SIMULATE-3K.

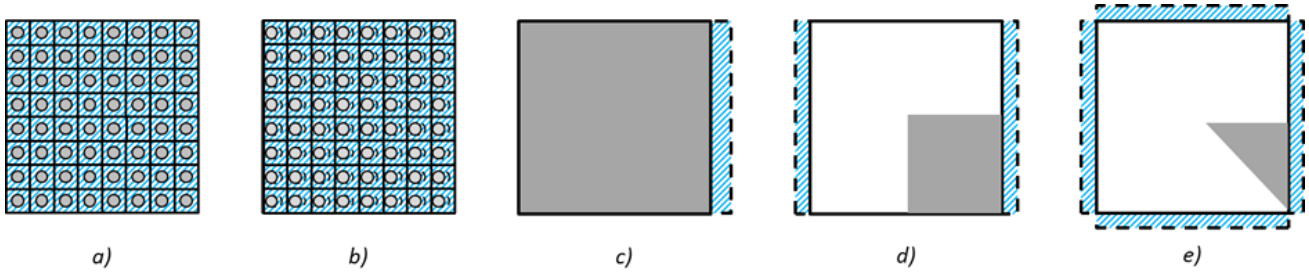

Fig. 33: Five cases for assessing the CASMO-5 capabilities on modelling the water gap thickness modification.

Table 4 summarizes the homogenized macroscopic absorption ($\Sigma_{a,G}$) and nu-fission ($\nu\Sigma_{f,G}$) cross-sections together with the diffusion coefficients (D_G), in the fast and thermal energy groups for each analyzed case. The four perturbed *cases* (i.e. Fig. 33b-e) are compared against the unperturbed configuration (Fig. 33a) in order to assess the impact of the different utilized modelling approaches on the homogenized macroscopic cross-sections. It is observed, that each case gives slightly different results compared to the unperturbed configuration. The cross-sections are modified up to 0.68% with respect to the unperturbed case when the fuel rods are laterally displaced using the *LDX* model (i.e. *case b*; realistic approach), while, the use of the delta gap model (i.e. *cases c*, *d*, and *e*) results into a larger change in the cross-sections up to 1.70% (i.e. "*Rel. to a*" rows in Table 4). The discrepancy between *case b* and *cases d* and *e* is expected, since the nuclear data are generated in the latter cases based on larger moderator content. The thermal diffusion coefficient (D_2) appears to be affected the most in all the analyzed *cases* from the lattice modification. This comparison gives a qualitative indication of the impact the different modelling approaches on the homogenized cross–sections.

In addition, the lattice calculation results, according to the delta gap modelling approach (i.e. *cases c-e*), are compared against the nuclear data generated with the fuel displacement *LDX* model (case b), in order to assess how far each of these modelling approach is from the most realistic model (i.e. "*Rel. to b*" rows in Table 4). As can be seen, a full lattice calculation (*case c*) results in a slight overestimation of the cross-sections up to 0.29%, while an octant symmetric lattice layout (*case e*) indicates an underestimation of the cross-sections up to 1.07% with respect to the fuel displacement *LDX* model (*case b*). In addition, the quarter symmetric lattice calculation (*case d*) shows the smallest discrepancy, from the *LDX* model, compared to the other two symmetry options (*cases c* and *e*) at this stage of the cross-sections preparation. Again, the deviation of *cases d* and *e* as compared to the realistic modelling *case b* is related to the fact that, the CASMO-5 delta gap model in quarter and octant symmetry assume a larger moderator content as the *LDX* model (i.e. Fig. 33b, d, e).

Table 4: Comparison of two-group homogenized cross-sections for five different configurations of a simplified assembly (Fig. 33) as estimated by CASMO-5.

Cases		$\Sigma_{a,1}$	$\Sigma_{a,2}$	$\nu\Sigma_{f,1}$	$\nu\Sigma_{f,2}$	D_1	D_2
a	$[cm^{-1}]$	$1.482E$+00	$3.476E$-01	$1.328E$-02	$2.319E$-01	$1.035E$-02	$3.771E$-01
b	$[cm^{-1}]$	$1.484E$+00	$3.471E$-01	$1.322E$-02	$2.305E$-01	$1.028E$-02	$3.747E$-01
	Rel. to a	0.13 %	-0.14 %	-0.45 %	-0.60 %	-0.68 %	-0.64 %
c	$[cm^{-1}]$	$1.483E$+00	$3.473E$-01	$1.324E$-02	$2.309E$-01	$1.031E$-02	$3.754E$-01
	Rel. to a	0.07 %	-0.09 %	-0.30 %	-0.43 %	-0.39 %	-0.45 %
	Rel. to b	-0.07 %	0.06 %	0.15 %	0.17 %	0.29 %	0.19 %
d	$[cm^{-1}]$	$1.485E$+00	$3.469E$-01	$1.321E$-02	$2.301E$-01	$1.027E$-02	$3.740E$-01
	Rel. to a	0.20 %	-0.20 %	-0.53 %	-0.78 %	-0.77 %	-0.82 %
	Rel. to b	0.07 %	-0.06 %	-0.08 %	-0.17 %	-0.10 %	-0.19 %
e	$[cm^{-1}]$	$1.488E$+00	$3.463E$-01	$1.313E$-02	$2.282E$-01	$1.020E$-02	$3.707E$-01
	Rel. to a	0.40 %	-0.37 %	-1.13 %	-1.60 %	-1.45 %	-1.70 %
	Rel. to b	0.27 %	-0.23 %	-0.68 %	-1.00 %	-0.78 %	-1.07 %

It should be emphasized again that, the user requests the cross-sections to be generated for a laterally displaced lattice by an increment amount δ towards the west direction, in all perturbed *cases* (i.e. Fig. 33b-e). It is recalled that, nuclear data generated based on *cases b* and *c* are not compatible with the SIMULATE-3K fuel vibration model, i.e. cannot be read and therefore utilized by SIMULATE-3K for time-dependent simulations. Only nuclear data generated based on *cases d* and *e* can be used downstream in 3D full core modelling of fuel assembly vibration. It is observed though that, the results obtained from the water gap increase in *cases d* and *e* are doubled and quadrupled, respectively, with respect to the requested gap increase δ. This affects the moderation to fuel ratio at the lattice level, and consequently, CASMO-5 generates cross-sections which deviate from *cases b* and *c*, as presented in Table 4. The CASMO-5 modelling inconsistency in *cases d* and *e* is corrected during the nuclear data library preparation using the CMS-LINK5 code. The latter code collects the nuclear data based on the CASMO-5 delta gap model (in either quarter or octant symmetry; Fig. 33d-e) and divides by two the change of the cross-sections compared to the unperturbed configuration (i.e. Fig. 33a) [87]. Consequently, the nuclear data library used for downstream 3D full core simulation of the fuel assembly vibration contains the properly treated cross-sections, post-processed by CMS-LINK5.

Table 5 shows the original calculated cross-sections at CASMO-5 level (i.e. "*from CASMO-5"* rows, presented also in Table 4), and their corrected values, obtained by CMS-LINK5 for *cases d* and *e* (i.e. *"treated by CMS-LINK5"* rows in Table 5). First, it is observed that, the post-processed nuclear data for *case d* have almost identical results as *case c* (i.e. *"Rel. to c"* rows in Table 5). This is an expected behavior, since the water width increase in *case d* is double as much as in *case c*, at CASMO-5 level, and eventually CMS-LINK5 corrects this effect by dividing by two the change in cross-sections for the former *case*. The exactly same approach is followed also for *case e*, even if its water width increase is quadruple as much in *case c*, at CASMO-5 level. Consequently, the post-processed nuclear data for *case e* continue to have a slight discrepancy up to 0.40 % compared to *case c*.

More importantly, the post-processed nuclear data in both *cases d* and *e* exhibit small discrepancies up to 0.29 % and 0.21 %, respectively, compared to the realistic modelling *case b* (i.e. *"Rel. to b"* rows in Table 5). The resulted differences are even lower than the respective discrepancy of *case c* compared to *case b*; i.e. up to 0.45 %, as shown in Table 4. This is a clear indication of a proper cross-sections treatment in CMS-LINK5 of the cross-sections generated with the CASMO-5 delta gap model in quarter or octant symmetry. It should be mentioned also that, high absolute differences with respect to the reference model for the different delta gap model approaches exist. The study and improvement of these discrepancies are though beyond the scope of this research.

Table 5: CMS-LINK5 treatment of nuclear data generated using the delta gap model in quadrant (case d) or octant (case e) symmetry.

Cases		$\Sigma_{a,1}$	$\Sigma_{a,2}$	$\nu\Sigma_{f,1}$	$\nu\Sigma_{f,2}$	D_1	D_2
d	*from CASMO-5*	$1.485E$+00	$3.469E$-01	$1.321E$-02	$2.301E$-01	$1.027E$-02	$3.740E$-01
	treated by CMS-LINK5	$\mathbf{1.484E}$**+00**	$\mathbf{3.473E}$**-01**	$\mathbf{1.325E}$**-02**	$\mathbf{2.310E}$**-01**	$\mathbf{1.031E}$**-02**	$\mathbf{3.756E}$**-01**
	Rel. to b	-0.03 %	0.04 %	0.19 %	0.22 %	0.29 %	0.23 %
	Rel. to c	0.03 %	-0.01 %	0.04 %	0.04 %	0.00 %	0.04 %
e	*from CASMO-5*	$1.488E$+00	$3.463E$-01	$1.313E$-02	$2.282E$-01	$1.020E$-02	$3.707E$-01
	treated by CMS-LINK5	$\mathbf{1.485E}$**+00**	$\mathbf{3.470E}$**-01**	$\mathbf{1.321E}$**-02**	$\mathbf{2.301E}$**-01**	$\mathbf{1.028E}$**-02**	$\mathbf{3.739E}$**-01**
	Rel. to b	0.07%	-0.04%	-0.11%	-0.20%	-0.05%	-0.21%
	Rel. to c	0.13%	-0.10%	-0.26%	-0.37%	-0.34%	-0.40%

This scoping analysis shows that the CASMO-5 fuel displacement model and the delta gap model in quarter or octant symmetry produce similar cross-section data, even if the latter modelling approach is based on less realistic assumptions; the delta gap model assumes a water gap width increase, instead of an actual fuel pins displacement, to model the entire fuel displacement. Therefore, these modelling simplifications of the CASMO-5 delta gap model are not expected to introduce significant differences in the evaluation of the cross-sections as compared to the realistic *LDX* approach. Consequently, it can be concluded that the delta gap model approach using a quarter and the octant lattice symmetry can be reliably used in downstream 3D full core calculation for modelling the time-dependent vibrations of fuel bundles in SIMULATE-3K.

4.2. Verification of CASMO-5 delta gap model results

The lateral vibration of fuel assemblies in SIMULATE-3K is described by the modification of the water gap width sizes of the selected bundles with their adjacent ones at every time step. This modelling approach corresponds to the time-dependent modification of the cross-sections for all the nodes that are involved in this process. Essential for this work is to understand the variation of the cross-sections with respect to the water gap thickness change. In this context, a simplified 2D lattice for a typical PWR assembly is used with a $14x14$ fuel rods layout, consisting of 180 fuel pins and 16 guide tubes with a 2.2% initial enrichment, as shown in Fig. 34. CASMO-5 is used for evaluating the cross-sections at nine different water gap thicknesses, ranging from $0\ cm$ up to $0.15\ cm$ using the delta gap model in quarter symmetry, as introduced in the previous section. In addition, the same lattice is modelled with the Serpent-2[22] code. It is noted that, all lattice calculations have been simulated at beginning of life and at room temperature conditions ($300\ K$). The Serpent-2 results are used as a reference solution in this analysis and are compared against those of CASMO-5 (before any post-treatment at CMS-LINK5 level), in order to verify the latter capability on modelling appropriately the increase of water gap width sizes. This comparison focuses on the key homogenized macroscopic two-group cross-sections (i.e. $\Sigma_{a,G}$, $\Sigma_{c,G}$, and $\nu\Sigma_{f,G}$), along with the macroscopic scattering cross-section, the diffusion coefficients in two-groups and the multiplication factor k_{inf}.

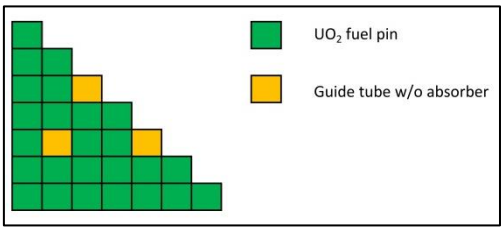

Fig. 34: Simplified fuel lattice layout in octant symmetry.

A consistent comparison between the two codes is ensured by following the undermentioned procedure. *First*, the homogenized two-group macroscopic cross-sections are generated without the activation of the fuel pin thermal expansion option, and additionally, the fundamental mode for the critical buckling correction is not taken into account in CASMO-5 lattice calculations, in order to ensure that the simulation options of the deterministic solver are in agreement with the default solution in Serpent-2. *Second*, the diffusion coefficients and the transport cross-section are evaluated in Serpent-2 using the recently developed cumulative migration

[22] Serpent-2 is a 3D Monte-Carlo particle transport code, developed at VTT Technical Research Center of Finland, which has been used since 2009 in large range of reactor physics applications [141]. Serpent-2 evaluates the kinetic parameters and cross-sections based on the neutron flux distribution, estimated by tracking neutron paths within an analyzed geometry. Serpent-2 is a continuous energy solver, which provides a more accurate solution of the neutron flux distribution, in contrast to deterministic lattice codes such as HELIOS-2, CASMO-5, etc.

method, found to give consistent results with the in-scatter method used in CASMO-5 [89]. *Last*, the ENDF/B-VII.1 nuclear data library is utilized by both solvers. It is to note that, 10^3 cycles of 10^5 neutrons with 50 inactive cycles are used in all Serpent-2 calculations, in order to reduce the simulation results uncertainty.

The cross-section results of the comparison between the two codes with respect to the variation of values of water gap width size are summarized in Fig. 35 and Fig. 36. In general, it is observed that, the two codes have a satisfactory agreement with a relative difference up to 1.5%, for all the analyzed parameters. The diffusion coefficient in the thermal group (D_2) is the only parameter exhibiting a high discrepancy that can reach about 9.5%. This discrepancy between the two codes is a known issue to the codes developers[23], and until the preparation of this thesis no satisfactory explanation has been given. Moreover, the relative difference in the eigenvalue lies in the acceptance range of 175-$215\ pcm$, which indicates that CASMO-5 and Serpent-2 are giving similar results and relevant trends as the water gap width increases.

The explanation of the macroscopic cross-sections tendencies as the water gap thickness increases can be explained as follows. First, it is to note that, a higher moderator to fuel ratio is achieved as the water content increases in the lattice configuration. Consequently, the overall absorption, capture and fission reaction rates (which are mainly driven by the fuel properties rather than the moderator in the lattice) will get smaller values within the homogenized lattice, as depicted in Fig. 35 and Fig. 36, in which the absorption, capture and nu-fission cross-sections in both fast and thermal energy groups found to decrease as the water content in the analyzed lattice increases. Moreover, the fast diffusion coefficient shows an increasing trend, which is explained by the fact that the high energetic neutrons (fast group) tend to diffuse in longer/larger areas as the water gap thickness increases. In addition, the neutrons have more space to interact with the hydrogen atoms (i.e. leading to higher values of the scattering cross-section) as the water gap width increases, and therefore, the thermalized neutrons will have higher probability to be trapped in the water. This behavior leads to smaller diffusion lengths in the thermal region, and consequently, the thermal coefficient shows a decreasing trend, as shown in Fig. 35 and Fig. 36. Last, it is observed that the increase of the moderator to fuel ratio (i.e. increase of the water gap thickness) leads to an increase of the lattice reactivity. A further increase of the water gap thickness (not shown in Fig. 36) will result to an over-moderated system, and therefore, the eigenvalue is expected to decrease when the optimal moderation configuration is exceeded.

This verification study confirms that, CASMO-5 and Serpent-2 predict quantitatively and qualitatively very similar results for the homogenized two-group cross-sections when the water gap width size is varied. Consequently, it can be concluded that, the neutronic data library generated by CASMO-5, using the DGA model, can be confidently utilized for downstream 3D full core dynamic simulation, using SIMULATE-3K, for the fuel assembly lateral vibrations. This scoping analysis illustrates clearly the reliability of the generated nuclear data library that will be used for the full-core transient calculations.

[23] According to a private conversation between the author and the codes developers.

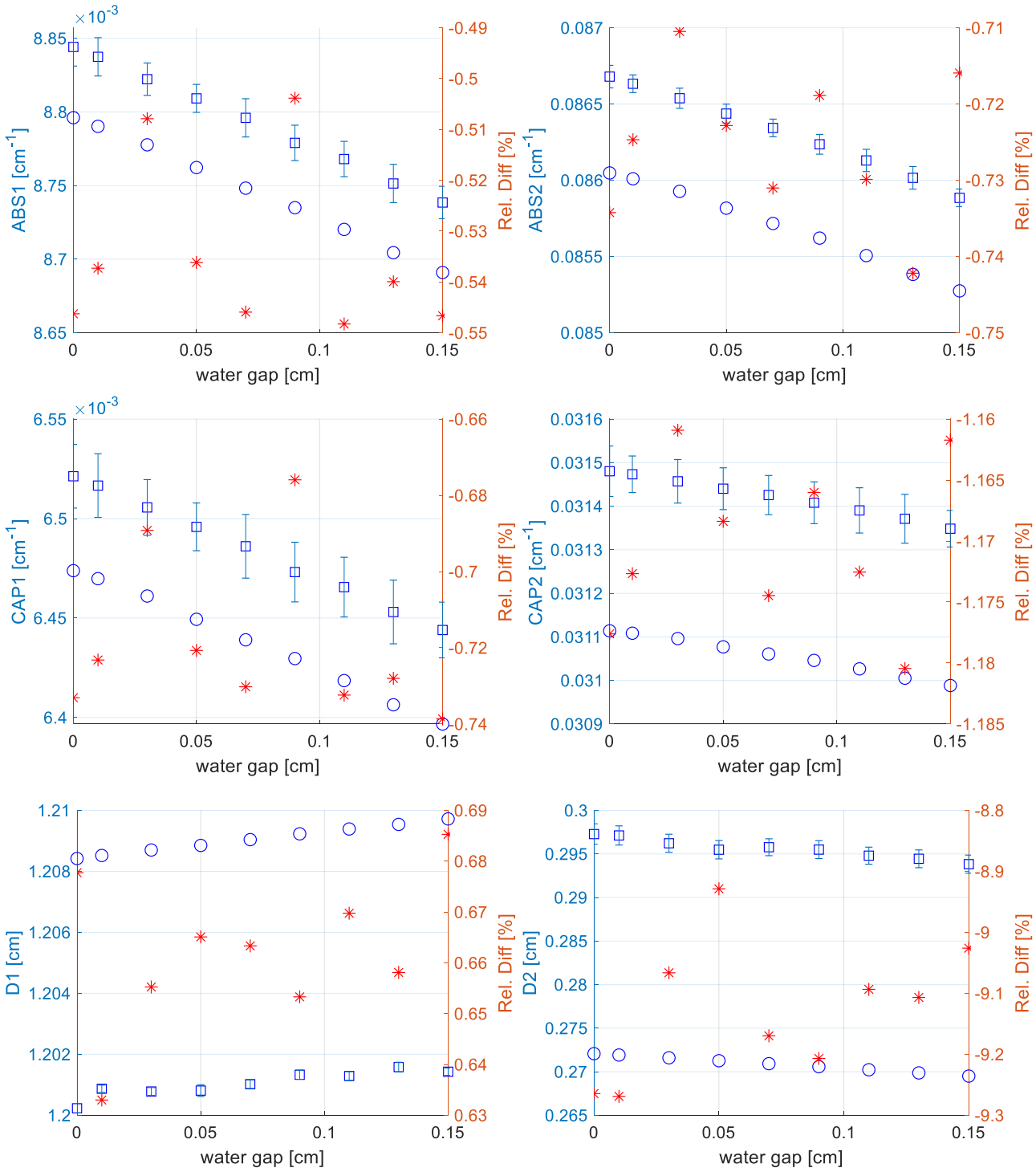

Fig. 35: Comparison of lattice calculation results between CASMO-5 (circle signs) and Serpent-2 (square signs with 1-sigma error bars) for different lattice water gap thicknesses (their relative difference is denoted with the red asterisks); part 1.

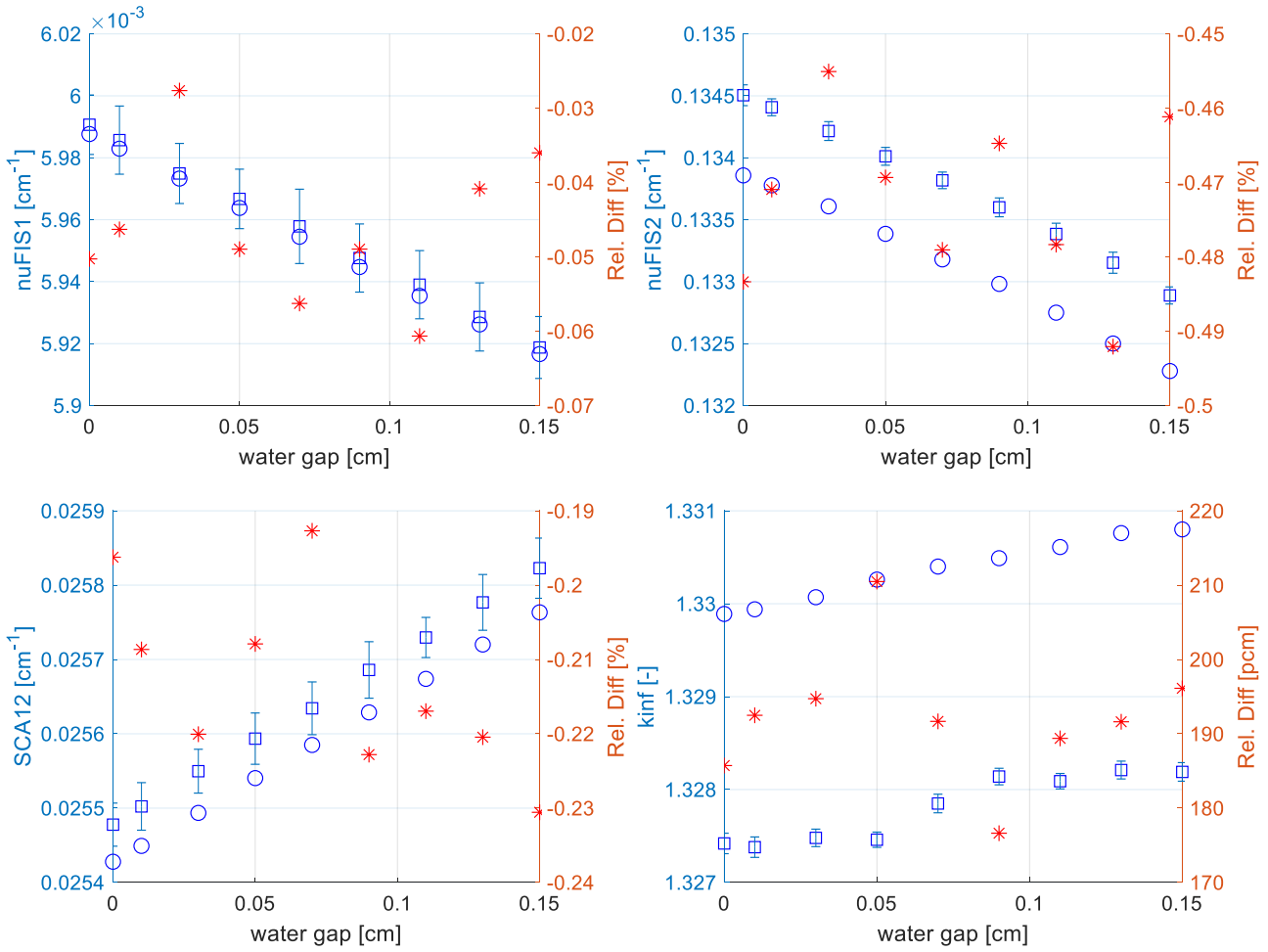

Fig. 36: Comparison of lattice calculation results between CASMO-5 (circle signs) and Serpent-2 (square signs with 1-sigma error bars) for different lattice water gap thicknesses (their relative difference is denoted with the red asterisks); part 2.

4.3. Qualification of fuel vibration model at a nodal level

In this section, a systematic assessment of the modeling capabilities of the SIMULATE-3K code, to simulate the fuel assembly vibration, is presented. To this aim, a series of simplified scenarios are used ranging from the vibration of a single node at the center core up to the lateral displacement of almost the entire core. This assessment, on the one hand, helps to gain more confidence about the SIMULATE-3K capabilities on noise modeling, and on the other hand, demonstrates the effect of various vibrational patterns on the neutron noise behavior and its spatial propagation.

In all the following simulations, the model of KKG core is used. Each of the 177 fuel assemblies is divided in 40 axial nodes, resulting in a total number of 7'080 nodes. Each node has a square lattice with a dimension of 21.56 cm and a height of 8.95 cm, and it is further divided in $2x2$ sub-nodes. The active core is surrounded by a single column of radial reflector and a bottom and an upper row of axial reflectors, as shown in Fig. 37. All transient simulations have a duration of 35 s with a time step of 0.01 s (i.e. 3'501 steps in total), in order to minimize the statistical error of the results in the time and frequency domain. It should be noted that, the steady-state solution of the transient solver is ensured to be fully converged at the initialization step of the simulations, and therefore, potential numerical noise can be eliminated. Nuclear data based on the CASMO-5 delta gap model in quarter symmetry are utilized in all following simulations.

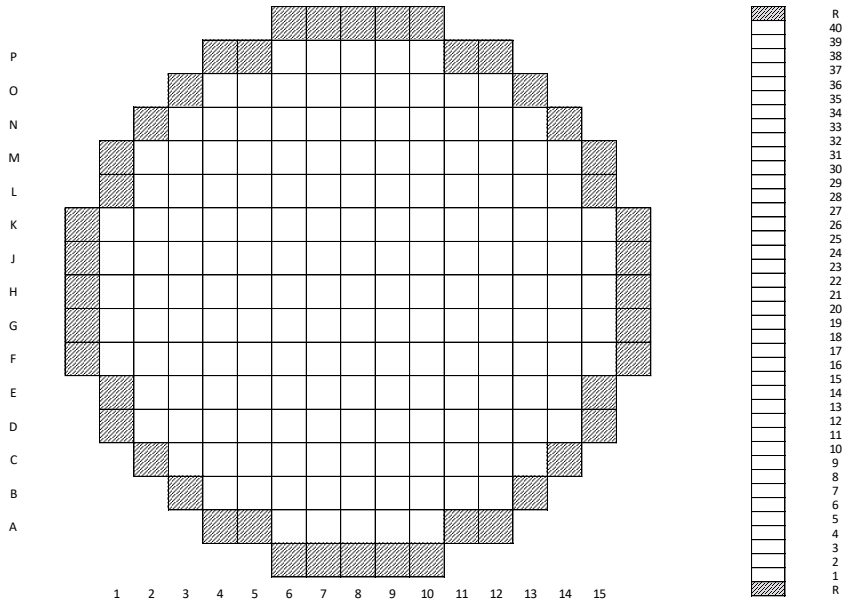

Fig. 37: Radial (left) and axial (right) illustration of the KKG core modelled with the CMSYS codes. The reflector zone is represented with grey shaded color.

In all the following examples, the neutron noise is expressed in terms of CV of the nodal neutron flux, described in Eq. 22:

$$CV_G = 100 \cdot \frac{\sigma_{\phi_G^{i,j,z}}}{\bar{\phi}_G^{i,j,z}} \qquad \text{Eq. 22}$$

where, $\bar{\phi}_G^{i,j,z}$ and $\sigma_{\phi_G^{i,j,z}}$ are the mean value and the standard deviation, respectively, of the homogenized neutron flux in the energy group G at a node located at the core position i, j, z. The homogenized neutron flux in the fast and thermal groups are evaluated by the SIMULATE-3K transient solver at each node and for every time step. The user can extract from the simulation output the time dependent fast and thermal fluxes and then estimate the neutron noise levels, at every node of the core using Eq. 22.

4.3.1. Vibration of a single node

The functionality of the fuel assembly vibration model in SIMULATE-3K is assessed here by analyzing the most simple scenario, in which the central node of the core, located at the 20^{th} node (starting from the core-bottom) of the central fuel assembly at location $H8$, is simulated to vibrate randomly, in the x-direction, with a maximum displacement of $0.11\ cm$[24] , as shown in Fig. 38.

[24] A displacement of $0.11\ cm$ corresponds to the half gap between two adjacent fuel bundles in a typical pre-Konvoi/Konvoi PWR.

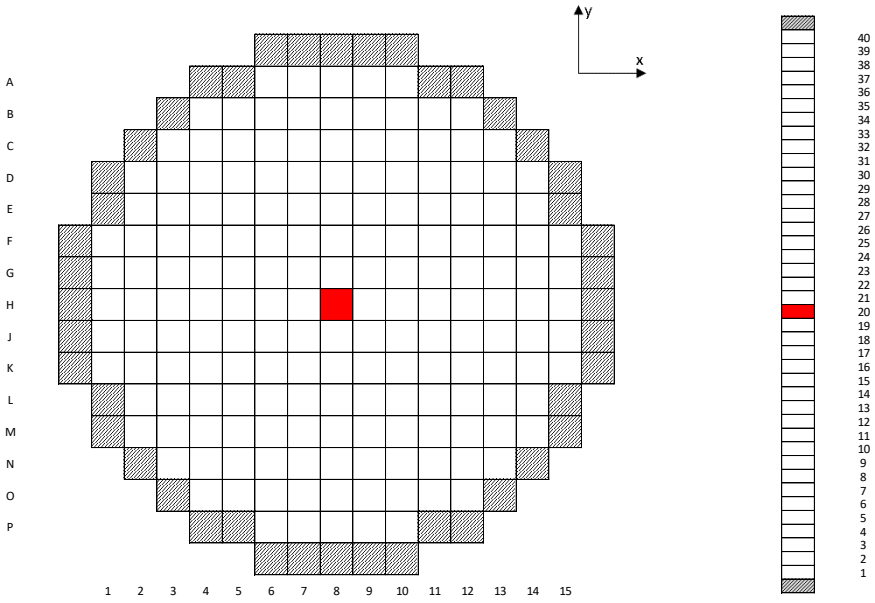

Fig. 38: The radial (left) and axial (right) location of the central node in the KKG core is depicted with red color.

The preparation of the SIMULATE-3K input file, describing the lateral random vibration of the central node (i.e. n_{H8}^{20}), is performed following the procedure, described in Sec. 3.4, using the improved fuel assembly vibration model. For the modeling of this scenario, it is needed to impose a change on the water gap widths between the central node and its adjacent ones (i.e. n_{H7}^{20} and n_{H9}^{20}) at every time step. For instance, it is assumed that at time step t, the water gap width between the nodes n_{H8}^{20} and n_{H9}^{20} increases by an increment amount δ=0.04 cm. Consequently, the water gap width between the nodes n_{H8}^{20} and n_{H7}^{20} must decrease by the same increment amount δ, in order to simulate the movement of the central node towards the core-west side, by preserving the nodal size. It is recalled that, the lateral movement of the central node in the x-direction is translated by the SIMULATE-3K code as a modification of the homogenized two-group cross-sections of the central node and its two adjacent nodes. Thus, on the one hand, the homogenized cross-sections of the nodes n_{H8}^{20} and n_{H9}^{20} will be modified based on a water gap width change of +$\delta/2$=0.02 cm, and on the other hand, the homogenized cross-sections of the nodes n_{H8}^{20} and n_{H7}^{20} will be modified based on a water gap width change of -$\delta/2$=-0.02 cm, following the modeling procedure as introduced in Fig. 26. It is worth noting that, cumulatively the changes of the cross-sections of the central node, i.e. the vibrating node, will cancel out at every time step. Consequently, it is anticipated that the vibration of the central node will have a key impact on the neutron fluxes at the adjacent nodes n_{H7}^{20} and n_{H9}^{20}.

The neutron noise resulting from the lateral vibration of the central node is presented in Fig. 39. Plots a and b show the neutron noise amplitude according to the fast and thermal fluxes, respectively. These plots show the neutron noise spatial behavior in a 2D radial representation at the core-bottom axial level in combination with a 2D axial depiction at the direction of vibration. This representation will be used in all the studied scenarios of this section. As can be observed, the neutron noise amplitude in both energy groups exhibit the maximum values at the nodes n_{H7}^{20} and n_{H9}^{20}. At the same time, the noise level at the central node is practically zero. This behavior is expected due to the modeling approach that is followed in SIMULATE-3K. In addition, the neutron noise spatial behavior has a fully symmetric shape, which proves that the transient solver utilizes correctly the input file generated by the user. Moreover, it is observed also that, the neutron noise in the fast group has a more dispersed nature, but with lower amplitude, compared to the noise in the thermal group. This behavior can be explained by the fact that the mean free path is bigger in the fast compared to the thermal group.

Therefore, an imposed perturbation of the cross-sections in one node will have a broader spatial impact on the neutron fast flux than on the neutron thermal flux. In a nutshell, this simplified scenario indicates that the SIMULATE-3K code can properly model the lateral vibration of a single node.

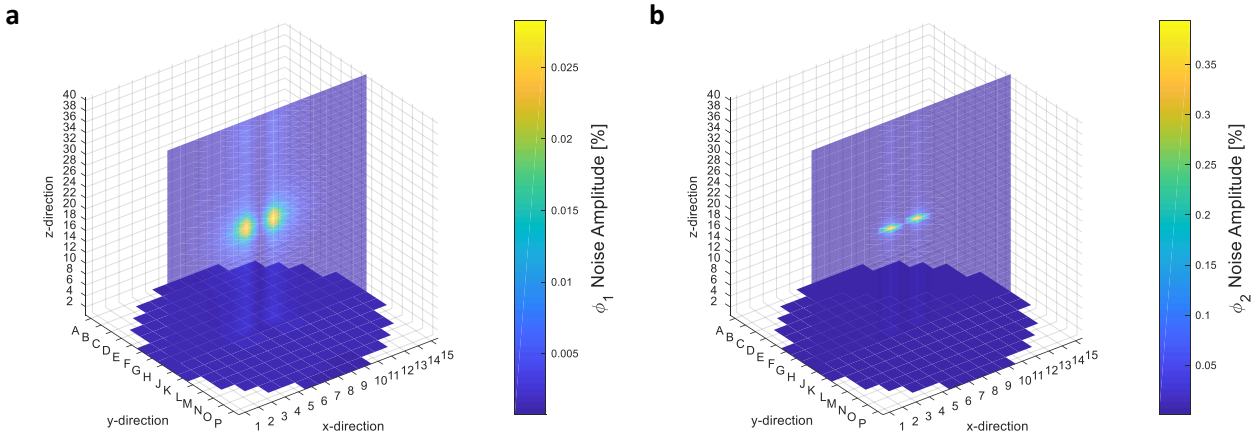

Fig. 39: Amplitude of the fast (a) and thermal (b) neutron noise induced by a randomly vibrating central node in the x-direction.

The estimation of the neutron noise phase pattern is one additional important aspect for the qualitative determination of the correct neutron noise modelling. The vibration of the central node should result in an out-of-phase behavior between the two core-halves. In order to examine this pattern, the phase[25] of the neutron noise in each energy group is calculated for each node in the direction of the movement; i.e. the 15 nodes in the row H at an axial level 20. The phase pattern in both energy groups is illustrated in Fig. 40. The resulted pattern is the expected one. It is clearly observed that the $H7$ and $H9$ nodes, which are the adjacent nodes to the vibrating node $H8$, exhibit a phase difference of $180°$. In addition, the two core-halves show an out-of-phase behavior too, due to the lateral vibration of the central node. This example shows that, the SIMULATE-3K code is capable of capturing the key aspects of the neutron noise behavior even if it is not a dedicated neutron noise solver with a very refined computational mesh.

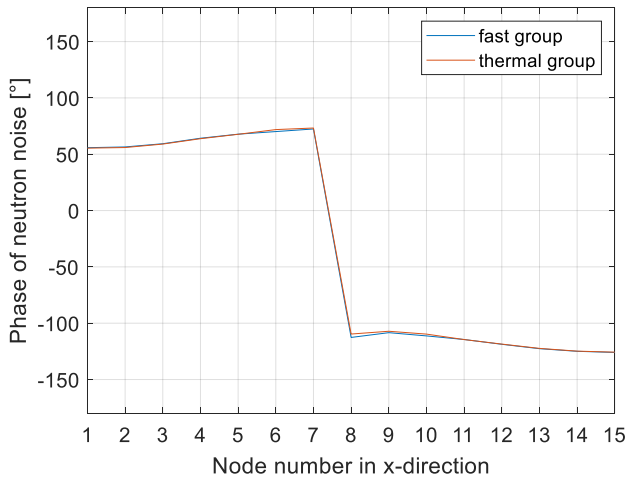

Fig. 40: Phase of neutron noise in the direction of movement induced by the central node vibration.

[25] To calculate the phase in MATLAB, first the nodal flux time series is transformed in the frequency domain using the *fft* MATLAB function, and then, the *angle* MATLAB function is used to extract the phase content of the transformed signal.

4.3.2. Single fuel assembly vibration

In the next scenario, the central fuel assembly located at the $H8$ position is selected to vibrate randomly (Fig. 41). First, a lateral vibration, only in the x-direction, is studied, and then followed by a vibration in two directions. The random vibration in two directions is based on Eq. 60, describing an equally distributed movement in the x-y space. For both cases, a maximum displacement of $0.11\ cm$ is modeled.

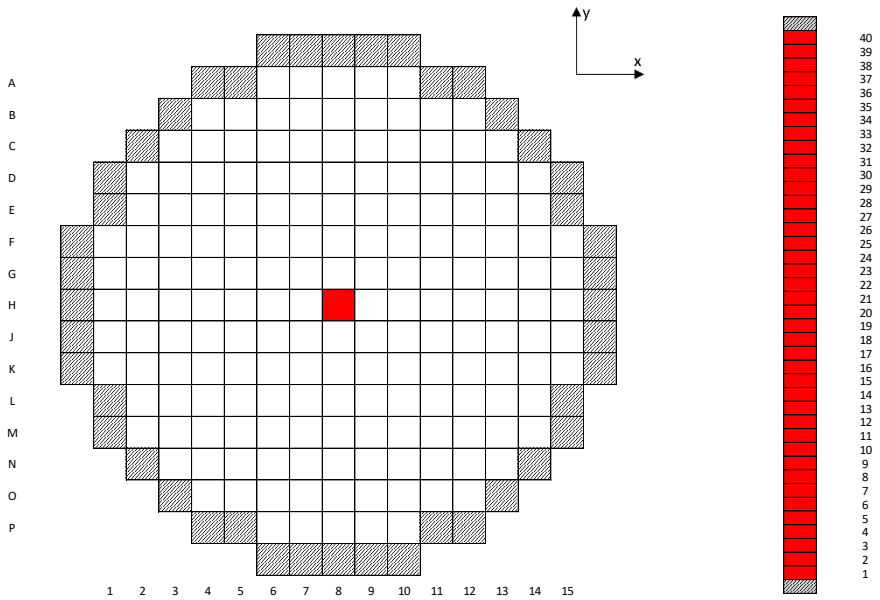

Fig. 41: Lateral vibration of the entire central fuel assembly in x- and y-directions. The vibrated nodes are depicted with red color.

The SIMULATE-3K input deck is prepared using the PSI automatized MATLAB script in order to describe the time-dependent modification of the water gap widths for all the axial nodes between the bundles $H8$ and $H7$, and the bundles $H8$ and $H9$. The following figures, i.e. Fig. 42 and Fig. 43, present the fast and thermal components of the neutron noise in case of the central bundle vibration in one or two directions, respectively.

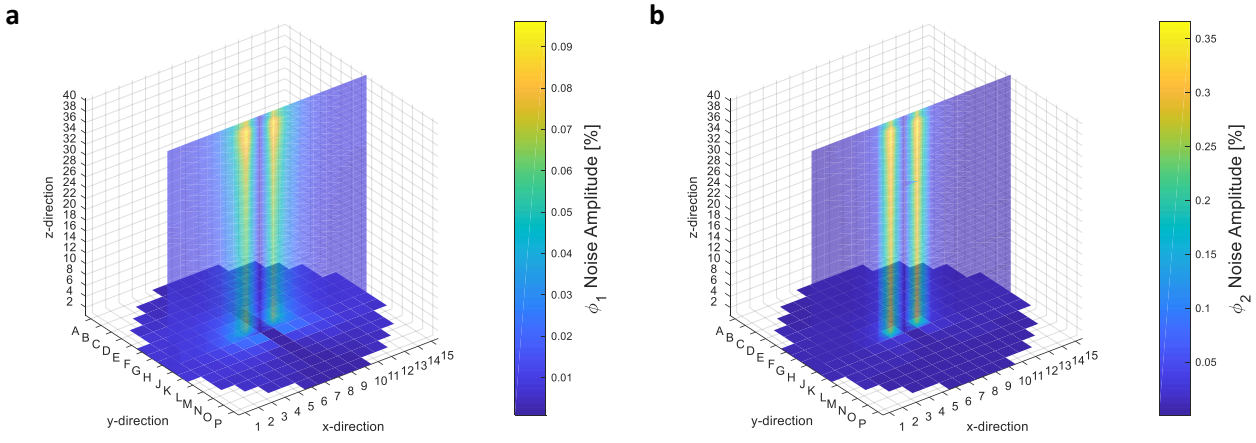

Fig. 42: Amplitude of the fast (a) and thermal (b) neutron noise induced by the lateral vibration of the central fuel assembly $H8$ in the x-direction.

First it is observed that, the localized noise source results to the highest noise levels at the adjacent bundles, as expected. Moreover, the radial representation of neutron noise shows a clear symmetric shape in both

cases, as expected. Concerning the direction of vibration, it is observed that lateral vibration in only one direction reflects the highest noise levels in the two adjacent assemblies next to the vibrating source (Fig. 42), whereas the vibration in two directions affects equally the neutron noise amplitude of all four neighboring bundles (Fig. 43). Interesting enough, it is observed that there is an axial distribution of the neutron noise levels, with systematic higher noise at the top levels, even if all the axial nodes are displaced by the same increment amount δ. This behavior can be explained by the fact that the coolant density decrease, at the core-top axial level, leads to larger (negative) reactivity MTC, and consequently resulting in higher noise levels. Again, the fast noise has a more dispersed behavior, but at lower amplitudes, as compared to the thermal noise.

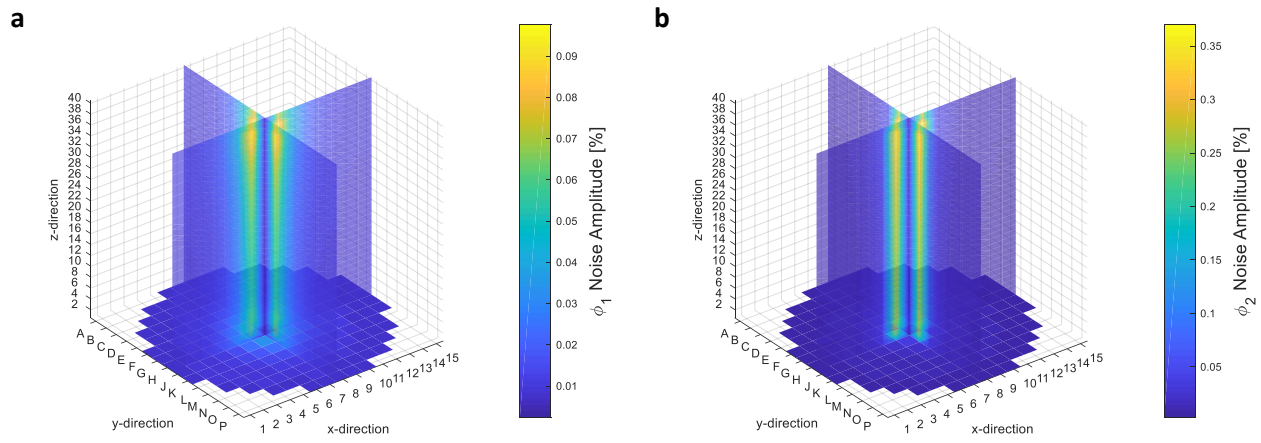

Fig. 43: Amplitude of the fast (a) and thermal (b) neutron noise induced by the lateral vibration of the central fuel assembly $H8$ in the x- and in the y-directions.

The correct pattern of the neutron noise phase for both scenarios is presented in Fig. 44. First, plot a shows the spatial phase behavior for all nodes located in row H and at an axial elevation 20 for the case of the central assembly vibration in the x direction. As expected, the two core halves exhibit a clear out-of-phase behavior. The same observations can be made also for plots b and c, describing the spatial phase pattern at the axial level 20 in the row H and the column 8, respectively, for the vibration of the central assembly in two directions.

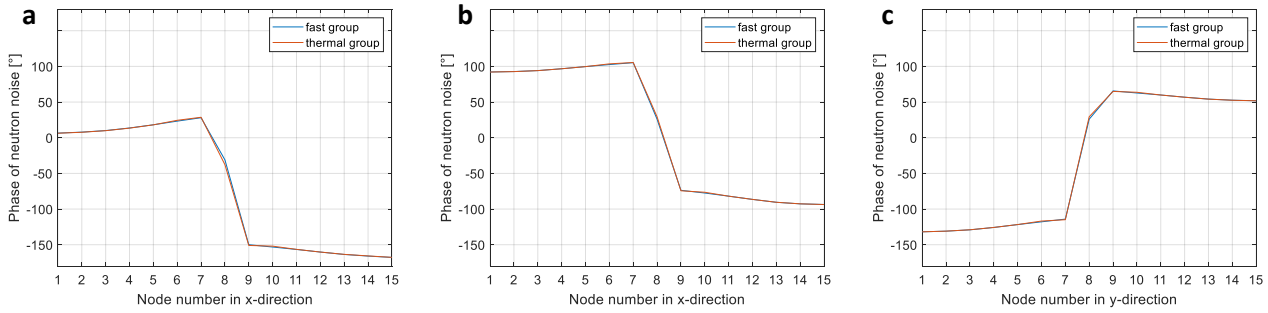

Fig. 44: Phase of neutron noise in the direction of movement induced by the central fuel assembly vibration in (a) x-direction and in (b, c) x-y-directions.

It should be emphasized that, this simplified scenario studies a rather unrealistic lateral movement of a fuel assembly, in which all the axial nodes are displaced by the same increment amount δ at a time step t. It is recalled that, this movement is physically impossible to take place in a nuclear reactor, since the fuel bundles

are fully fixed at the core bottom support plate. Nevertheless, this hypothetical scenario serves as an excellent and simple case for assessing the functionality of the SIMULATE-3K fuel vibration model by modeling the oscillation of a single fuel assembly. However, more realistic scenarios will be presented in the next sections.

4.3.3. Vibration of fuel assembly clusters with different sizes

The neutron noise behavior as a function of the number of vibrating fuel bundles is studied in this section. A series of calculations is performed, in which a cluster of fuel bundles, of various sizes, at the center of the core is simulated to randomly vibrate either in one or two directions. The central cluster size ranges in these simulations from $1x1$ (i.e. vibration of only the central fuel assembly located at the core position $H8$) up to $11x11$ (i.e. vibration of the 121 fuel assemblies located at the center of the core in an $11x11$ square formation). The fuel assemblies are simulated to randomly vibrate with a maximum displacement of $0.11\ cm$ and in a synchronized manner, i.e. all the vibrating bundles within the cluster follow an identical dynamical displacement during the transient simulation. The random vibration in two directions follows Eq. 60 in order to simulate an equally distributed movement in the x-y space.

Fig. 45a and b present the maximum neutron noise levels in the fast and thermal groups, respectively, as function of the vibrating cluster size. The blue and red signs correspond to the lateral oscillation in one or two directions, respectively. It is observed that, in both plots the highest neutron noise amplitude is almost linearly increasing with the size of the vibrating cluster (i.e. the total number of vibrating bundles). In addition, the fast neutron noise levels seem to be independent from the direction of vibration for all the cluster sizes, except for the case of a $9x9$ cluster, as shown in Fig. 45a. The reason behind this difference is still not clear. Related to the thermal neutron noise, it can be seen that the direction of vibration can have an impact up to 35% on the neutron noise amplitude depending on the vibrating cluster size (Fig. 45b).

Moreover, the fast and thermal components of neutron noise can be observed in the next figures for various vibrational cluster sizes. First, Fig. 46 and Fig. 47 present the neutron noise levels for a $3x3$ cluster, vibrating in the x-direction and in x-y direction, respectively. Then, Fig. 48 and Fig. 49 show the neutron noise amplitude for a vibrating central cluster of size $11x11$ in one and two directions, respectively. Similarly to the previous analyzed cases, it is observed that the neutron noise behavior follows some specific characteristic trends. First, the center of the vibrating cluster exhibits negligible noise, since the selected bundles are moving in a synchronized way, and therefore, the relative movement of central assemblies with respect to the entire cluster is zero. In addition, it is observed that the neighboring areas to the vibrating cluster show the maximum neutron noise amplitudes. Interesting enough, this scoping analysis indicates that the vibration of assembly clusters with high size can contribute to the understanding of high heterogeneities on the neutron noise spatial behavior[26]. In other words, Fig. 48 and Fig. 49 indicate the high noise amplitudes in the periphery and lower values at the core center due to the synchronized vibration of an $11x11$ cluster. Last, the neutron noise has a symmetric spectral phenomenology in both energy groups, as it would be expected.

[26] Such heterogeneities have been discussed in *chapter 2*, in which the neutron noise analysis based on KKG data revealed significant higher neutron noise levels at the east-core side as compared to the rest of the core.

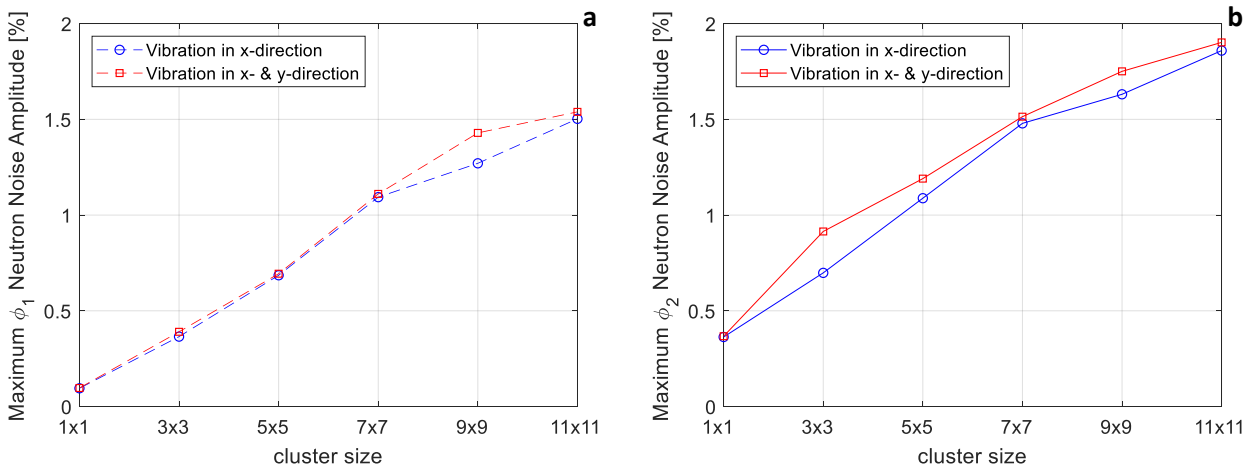

Fig. 45: Maximum fast (a) and thermal (b) neutron noise level for different sizes of vibrating clusters. The fuel assemblies within the cluster are vibrating randomly in the x-direction (blue circles) or in x- and y-directions (red squares).

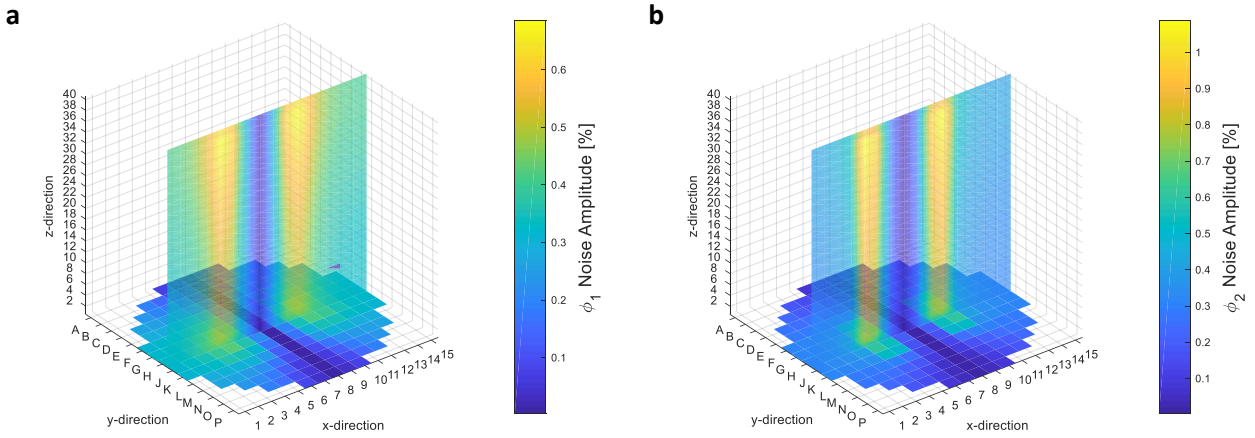

Fig. 46: Amplitude of the fast (a) and thermal (b) neutron noise induced by the lateral vibration of a $3x3$ cluster of fuel assemblies in the x-direction.

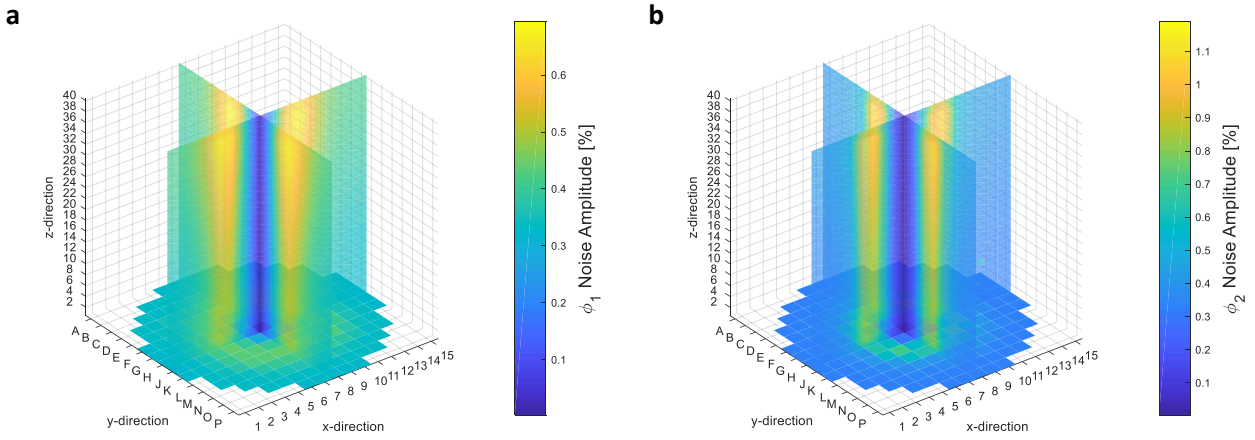

Fig. 47: Amplitude of the fast (a) and thermal (b) neutron noise induced by the lateral vibration of a $3x3$ cluster of fuel assemblies in the x- and y-directions.

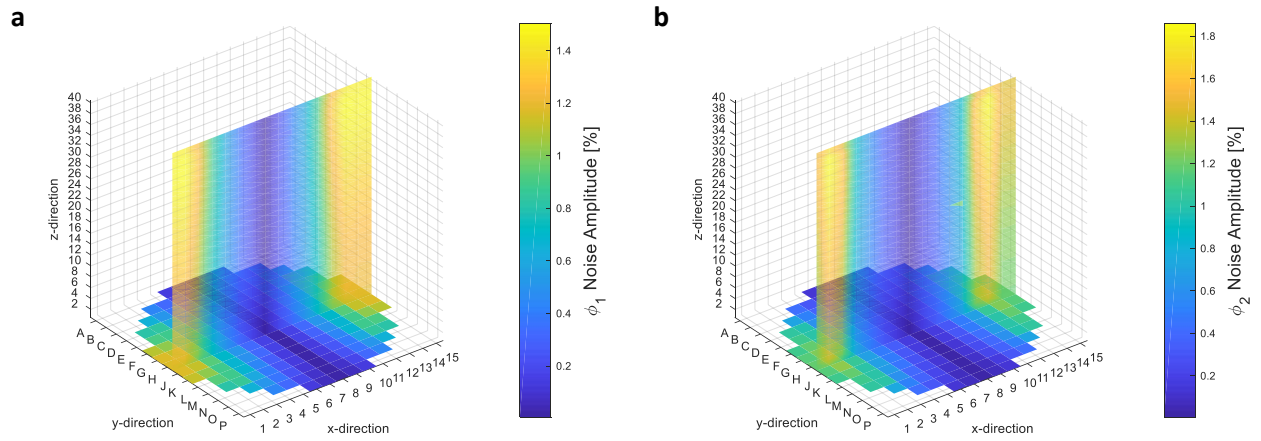

Fig. 48: Amplitude of the fast (a) and thermal (b) neutron noise induced by the lateral vibration of a $\mathbf{11x11}$ cluster of fuel assemblies in the x-direction.

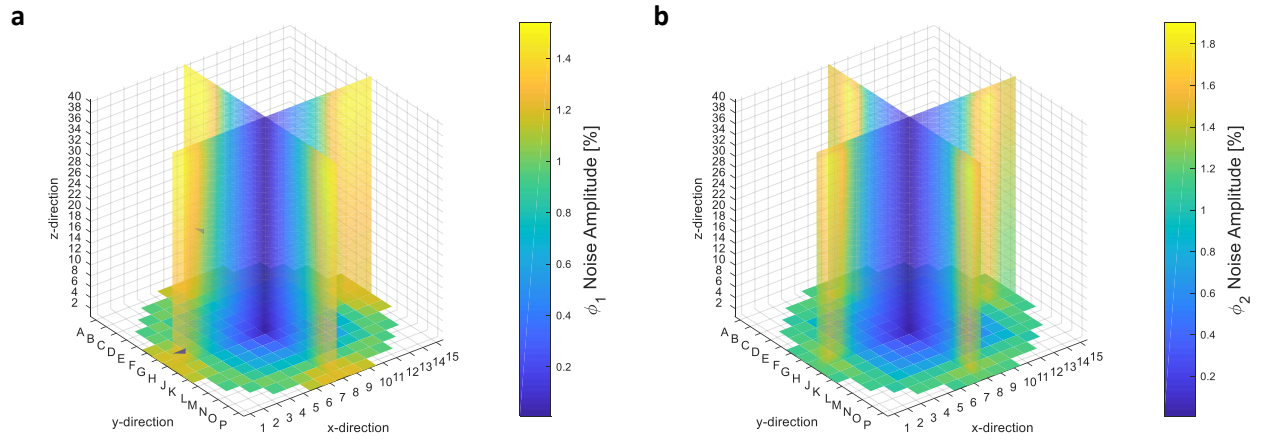

Fig. 49: Amplitude of the fast (a) and thermal (b) neutron noise induced by the lateral vibration of a $\mathbf{11x11}$ cluster of fuel assemblies in the x- and y-directions.

The out-of-phase pattern of the neutron noise phase in both groups is properly captured in all examined cases, as presented in Fig. 50 and Fig. 51, representing the $3x3$ and the $11x11$ vibrating clusters, respectively. The proper pattern of neutron noise phase has been consistently observed in all the simulated scenarios ranging from the vibration of a single node up to large vibrating clusters

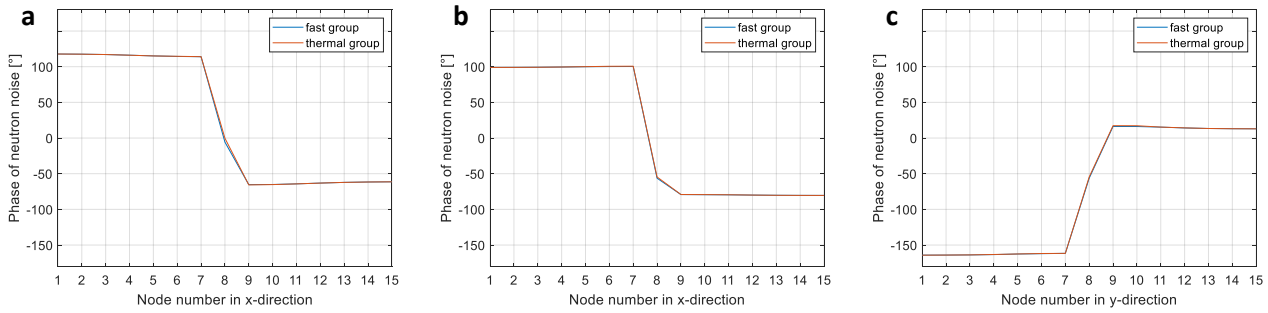

Fig. 50: Phase of neutron noise in the direction of movement induced by the central $\mathbf{3x3}$ cluster vibration in (a) x-direction and in (b, c) x-y-directions.

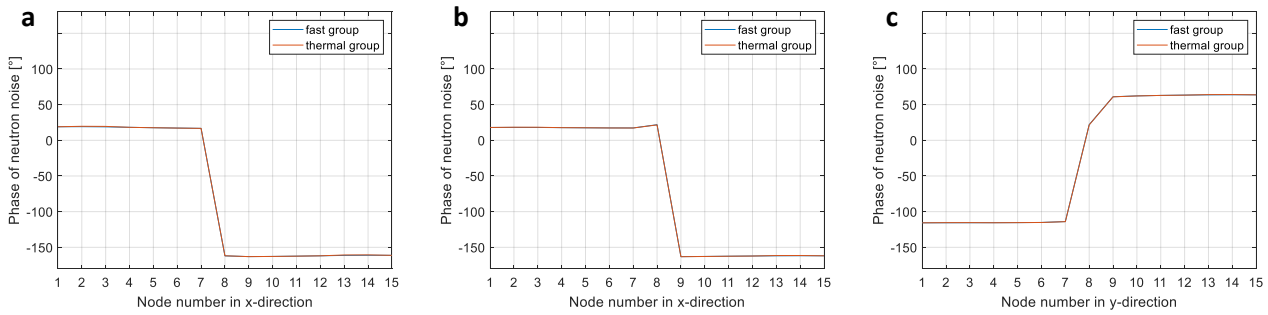

Fig. 51: Phase of neutron noise in the direction of movement induced by the central $\mathbf{11}x\mathbf{11}$ cluster vibration in (a) x-direction and in (b, c) x-y-directions.

4.3.4. Impact of the displacement amplitude on the neutron noise level

The structural integrity of a fuel assembly mainly depends on the design and performance of the tie plates and the spacers located at different axial elevations. These structural components are responsible, among others, for ensuring the mechanical compatibility of the fuel design with the reactor operating conditions. More specifically, each spacer is typically made of zircaloy material and has good neutronic and mechanical properties. Conventional spacers designs are based on a grid structure equipped with flow vanes that create high turbulent flow, and therefore, the heat can be efficiently transferred from the rod cladding to the coolant. In addition, one of the key roles of the spacers is to minimize the lateral displacement or tilting of the fuel rods, in order to reduce to the minimum the friction at the spacer, and consequently, to preserve the fuel integrity. However, it has been observed that the restriction mechanism of the fuel rods by the spacer grid is deteriorated due to the irradiation damage, leading to increased friction and cladding failure due to fretting [90]. In addition to that, the nuclear industry pushed towards higher enriched fuel in order to achieve better fuel utilization and to remain competitive in the demanding energy market during the last decade. The higher enrichment levels result in higher thermo-mechanical and irradiation loads on the fuel bundles that can in turn lead to fuel degradation.

Having all these in mind, the fuel vendors undergo continuous development and improvement of their fuel design, aiming for the better fuel reliability and performance. Among other fuel enhancements, some vendors replaced the flow vanes with the so-called dimples structures within the fuel cell. The dimples, on the one hand, allow the efficient coolant mixing and decrease local hot spots, and on the other hand, have lower stiffness property in order to reduce the frictional forces to the fuel cladding during irradiation relaxation. By doing so, the fuel damage can be prevented. However, the lower stiffness of the spacer dimples gives more freedom for the fuel rods to be laterally displaced or deformed. Interesting enough, experimental data have shown a significant force relaxation from the dimples to the fuel rod after approximately one operational cycle, which leads to the collective movement of the fuel rods, and eventually, to a more intensive oscillatory movement with higher displacement amplitude of the entire fuel assembly as the burnup increases [91].

A small scoping analysis is performed in order to assess the impact of increasing the fuel vibration amplitude on the neutron noise level. To this aim, a series of simulations are performed in which the central fuel assembly of the KKG core (i.e. core location $H8$; Fig. 7) oscillates randomly in the x-direction using different maximum displacement amplitudes; i.e. ¼, ½ and full maximum displacement of $0.11\ cm$ which corresponds to the half distance between adjacent bundles in typical KWU pre-Konvoi PWRs. Fig. 52 shows that the maximum neutron noise level increases almost linearly with the vibration amplitude. This is an indication that, the increasing noise level trend over the cycles and within the cycles, as observed in KWU pre-Konvoi PWRs during the last

decade, might be significantly influenced by the possible increase of the fuel assembly maximum displacement due to the force relaxation over burnup. This behavior is further studied in Sec. 5.4, in which real KKG core loading patters are used and the effects of increasing the bundles displacement amplitude over burnup is studied.

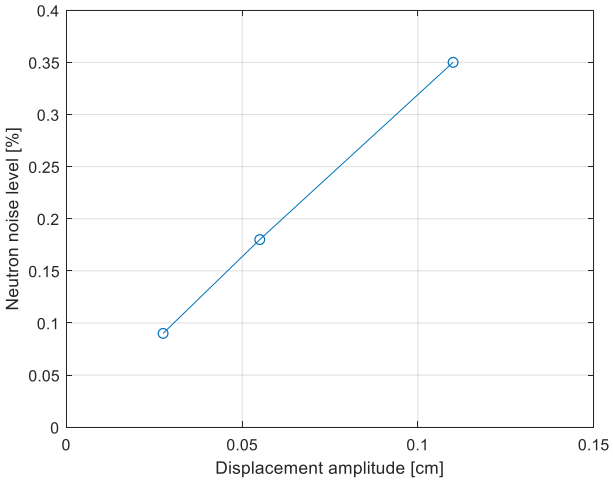

Fig. 52: Dependency of neutron noise on fuel assembly displacement amplitude.

4.3.5. Impact of bowing shape on neutron noise

A key challenge in reactor operation is related to the collective fuel assembly bow, which might challenge the safety margins and introduce significant problems during fuel handling and control rod insertion [92]. The bow development commonly appears in LWRs and corresponds to the permanent axial deformation of the fuel assembly centerline. The main cause of fuel bow is the significant flux gradients across the four sides of the bundles, causing irradiation induced differential growth. In other words, the dimensions of the zirconium alloy materials (e.g. rod cladding, spacers, fuel channels, etc.), such as the length, the thickness, the width, etc., undergo a change due to the high irradiation gradients even if there are no applied stresses [93]. In addition, the strong hydraulic forces originating from the turbulent coolant flow will also contribute with additional stresses on the fuel bundle, and consequently can affect the bow formation.

The fuel vendors tend to monitor the evolution of the bow deformation of the fuel assemblies during the yearly outage by means of visual inspections and dedicated measuring campaigns. The inspection experience, on the one hand, assists the operators to optimize the core loading pattern by taking into account the spatial dependency of the bow deformation, and on the other hand, it helps the fuel vendors to further develop and enhance their fuel design in order to become more bow-resistant, without impacting its performance. The operational experience has shown that the fuel assemblies tend to develop a C- or S-axial deformation, which has a growing amplitude as the burnup increases [92]. In addition to that, the fuel bundles do not develop the same bow shape with the same amplitudes across the entire core. On the contrary, the neutronic and thermal-hydraulic heterogeneities contribute to the different bow deformation characteristics of the fuel bundles, based on their core location.

From a neutronics perspective, the bow development is of paramount concern since hot spots (i.e. high power peaking factors) are anticipated to appear at the axial locations with the minimum water gap widths (i.e. the location with the highest axial deformation). The bow deformation has a significant impact on the thermal

margins, and therefore, the best-estimate nodal simulators tend to take into account the bow phenomenon in order to ensure adequate margin from the safety thermal limits. In addition to that, the bow formation can contribute significantly to the spatial heterogeneity of the neutron noise behavior. This can be explained by the fact that, a vibrating fuel assembly, already axially deformed, will directly affect the time-dependent water gap widths with its adjacent bundles. A short scoping analysis is performed here in order to better understand the impact of the bow deformation on the neutron noise behavior. To this aim, the central bundle of the KKG core (i.e. at core position $H8$; Fig. 7) is selected to laterally randomly vibrate in three different scenarios; *first*, without imposing any bow deformation (i.e. similar to what was described in Sec. 4.3.2); *second*, by imposing a C-shape; and *third*, by imposing an S-shape on the axial deformation. In all the three cases the same amplitude of vibration is assumed.

Fig. 53 summarizes the neutron noise results for the three cases at the location of the highest noise amplitude; i.e. next to the vibrating bundle. The unbowed case shows an increasing evolution of neutron noise level as the axial height increases. As discussed before, this increasing profile can be related to the decrease of coolant density and the corresponding reactivity effects at the core-top level. Interesting enough, both plots show an impact of the axial spacers on the noise axial profiles of the unbowed case. Typically, the neutron flux exhibits local dips at the spacers elevations due to the associated parasitic absorption. Consequently, the neutron noise is amplified at the spacers locations, since for a given perturbation source the average flux has lower values at those axial locations. Concerning the bowed scenarios (i.e. red and yellow lines in Fig. 53), it is observed that the neutron noise axial profiles follow the axial deformation shape. In other words, higher noise levels can be found at the axial locations with the highest bow deformation. This can be explained by the fact that the most deformed axial locations introduce a stronger impact on the variation of the water gap width with the adjacent bundle. In addition to that, the noise levels seem to follow an increasing trend; for example, higher noise is observed at node 30 compared to that at node 12 in the case of the S-shape, even if both nodes are displaced by the same amplitude. Similarly, the upper axial deformation in the S-shape case exhibits higher neutron noise than the bottom axial deformation. In a nutshell, it is clearly observed that the axial deformation of the fuel assemblies can considerably impact the neutron noise axial phenomenology.

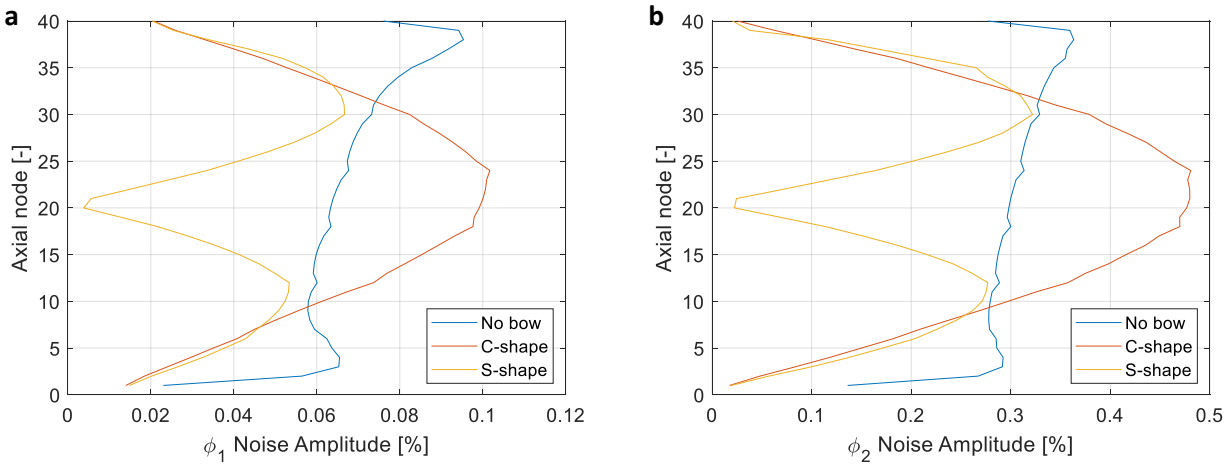

Fig. 53: Fast (a) and thermal (b) neutron noise axial evolution due to the vibration of the central fuel bundle. An unbowed case (blue), a C- (red) and S (yellow)-axial deformations are examined.

4.3.6. Modelling of different vibration modes

The simulation scenarios described in the previous sections focus on the modelling of the lateral displacement of fuel assemblies, in which all the axial nodes are displaced simultaneously with the same amplitude. This is a rather simplified approach of the fuel motion vibrations, since in reality the fuel assemblies are well positioned on the core support plate without being free to dynamically dislocate at the core-bottom level. However, it is commonly believed that the top part of the fuel assemblies is relatively free to move laterally due to the strong hydraulic forces originating from the coolant flow, propagating from the bottom to the top of the core. In addition, as stated in Sec. 3.2, analytical models and experimental studies concur that the cantilevered vibrational mode (a clamped-free assembly, Fig. 54a) has a nominal frequency in the range of 0.6 to $2\ Hz$, depending on the reactor type [2].

As mentioned in the Sec. 3.4, additional improvements and enhancements of the fuel vibration model in SIMULATE-3K have been performed, allowing the user to model a time-dependent variation of the axial shape of the vibrating assemblies and to simulate more realistic vibrational modes of the fuel. To this aim, any pre-defined axial shape (e.g. cantilevered mode, C-shape or first mode, S-shape or second mode, and higher modes etc.) can be superposed by the user on the water gap widths axial distribution between a vibrating fuel assembly and its neighbors. In this section, the central fuel assembly of the analyzed PWR core is modelled to vibrate in the x-direction with a nominal frequency of $1.8\ Hz$, following a dynamic modification of the axial shape, as showed in Fig. 54a (i.e. clamped-free shape). The maximum water gap width variation at the top of the active core is $0.11\ cm$, and the water gap width is linearly decreased to a value of zero at the core-bottom axial level. Additionally, two similar simulations are performed for which the axial shape is dynamically modified based on the first (Fig. 54b) and the second (Fig. 54c) vibration modes. The axial shape for each case is imposed by the user employing the input card *KIN.ZVL* using respective axial displacement factors, as presented in Fig. 55. The latter are superposed on the water gap width variation amplitude in the x-direction, which results in the modelling of the different fuel assembly vibrational modes.

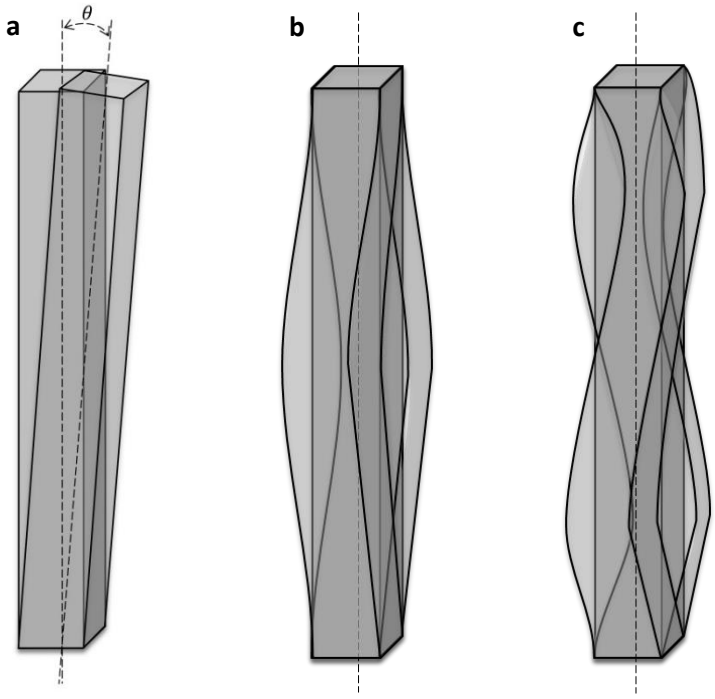

Fig. 54: Illustration of the clamped-free shape (a), the first (b) and second (c) modes of a vibrating fuel assembly [2].

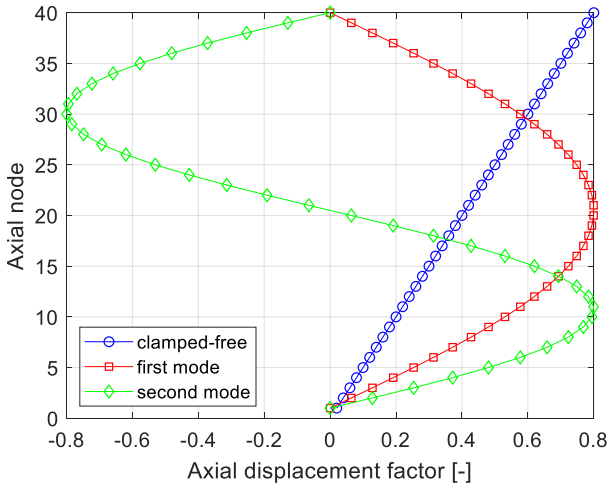

Fig. 55: Axial displacement factor (*KIN.ZVL* input card) for modeling the clamped free (blue circles), first (red squares) and second (green diamonds) vibrational modes of a fuel assembly.

The neutron noise amplitude in the fast and thermal energy groups is presented in Fig. 56 to Fig. 58 for the three analyzed cases. The impact of the time-dependent variation of the axial shape is clearly observed on the neutron noise phenomenology in all three cases. Larger modification of the water gap widths corresponds to higher noise levels at the core-top, whereas smaller variation of the water gap widths results in much smaller noise amplitudes at the core-bottom level for the clamped-free mode (Fig. 56). In addition, the first and second vibration modes result to higher noise levels at the axial locations with the larger displacement; at the center of the core for the first mode (Fig. 57), and at the core-top and bottom for the second mode (Fig. 58). This behavior clearly differs compared to Fig. 42 in which the entire fuel assembly simultaneously vibrates laterally and, consequently, results in significant noise along the entire axial level. This simplified simulation analysis demonstrates that the code implementations for simulating dynamic variation of the assemblies axial shape has been properly performed and the analyzed simulating configuration is producing the expected neutron noise behavior. More extensive assessment of the analyzed phenomena are already under investigation at PSI [94].

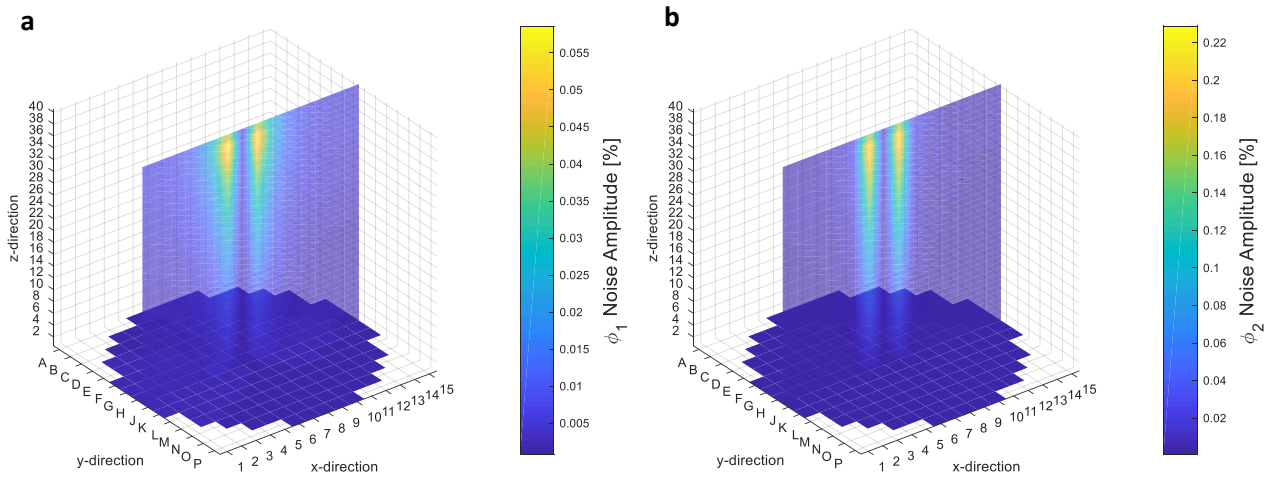

Fig. 56: Amplitude of the fast (left plots) and thermal (right plots) neutron noise induced by the lateral vibration of a clamped-free fuel assembly in the x-direction.

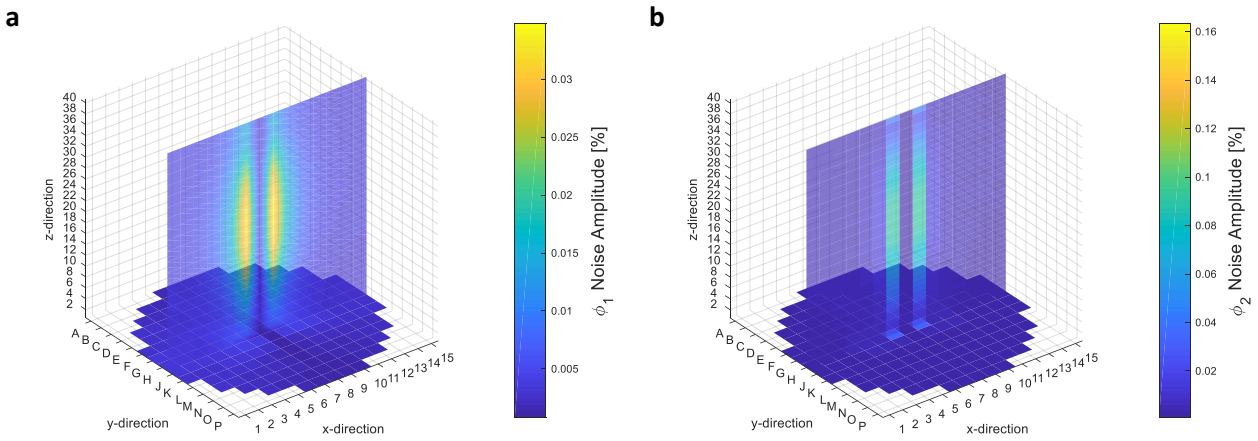

Fig. 57: Amplitude of the fast (left plots) and thermal (right plots) neutron noise induced by the first mode vibration of fuel assembly in the x-direction.

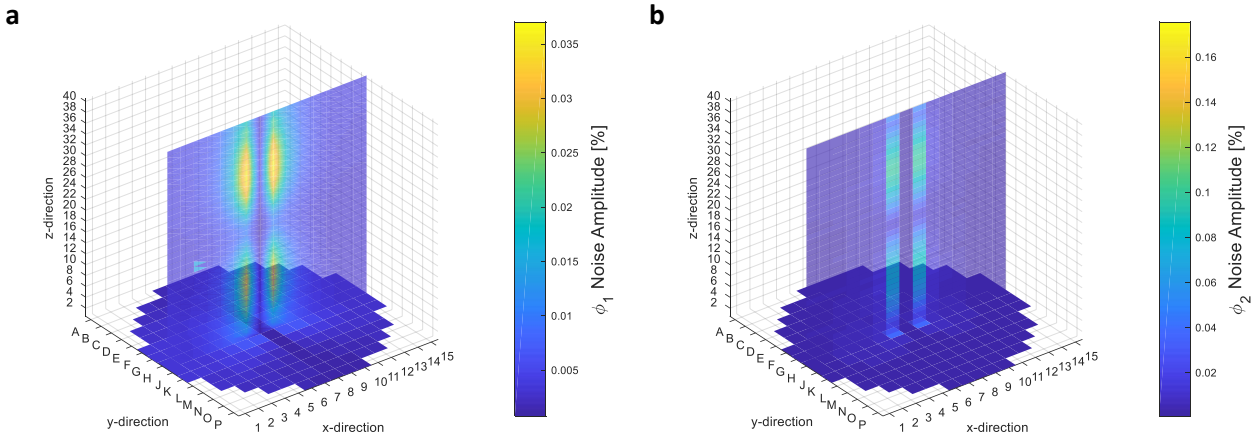

Fig. 58: Amplitude of the fast (left plots) and thermal (right plots) neutron noise induced by the second mode vibration of fuel assembly in the x-direction.

Chapter 5: PSI Neutron Noise Methodology: Simulation Results

The current chapter presents the results of a systematic neutron noise modelling simulations using the SIMULATE-3K code. The neutron noise phenomenology is studied in both the time and the frequency domains based on single-source perturbations (i.e. fuel assembly vibrations, inlet coolant temperature and flow fluctuations) and on combined noise sources scenarios. By doing so, a further understanding of the neutron noise phenomena can be acquired. In addition, a comparison of the simulated noise phenomenology against the measured noise characteristics based on neutron detector signals, presented in chapter 2, could assist in explaining the root-cause of the neutron noise behavior in KKG. Last, the neutron noise level increase trend, as observed in KKG, is reproduced using real core loading patterns.

This chapter is based on the researches performed in the following papers:

- D. Chionis, A. Dokhane, L. Belblidia, G. Girardin, H. Ferroukhi, A. Pautz, "*Development and verification of a methodology for neutron noise response to fuel assembly vibrations*", accepted to be published in Annals of Nuclear Energy [56].
- D. Chionis, A. Dokhane, M. Pecchia, G. Girardin, H. Ferroukhi, A. Pautz, "*SIMULATE-3K analyses of neutron noise response to fuel assembly vibrations and thermal-hydraulics parameters fluctuations*", Proceedings of the 2017 International Conference on Mathematics & Computational methods applied to nuclear science and engineering (M&C '17), Jeju, Korea, (2017) [57].
- D. Chionis, A. Dokhane, H. Ferroukhi, A. Pautz, "*PWR neutron noise phenomenology: Part I – Simulation of stochastic phenomena with SIMULATE-3K*", Proceedings of the 2018 International Conference on the Reactor Physics (Physor '18), Cancun, Mexico (2018) [95].
- D. Chionis, A. Dokhane, H. Ferroukhi, A. Pautz, "*PWR neutron noise phenomenology: Part II – Qualitative comparison against plant data*", Proceedings of the 2018 International Conference on the Reactor Physics (Physor '18), Cancun, Mexico (2018) [17].
- L. A. Torres, D. Chionis, C. Montalvo, A. Dokhane, A. García-Berrocal, "*Neutron noise analysis of simulated mechanical and thermal-hydraulic perturbations in a PWR core*", Annals of Nuclear Energy, vol. 126, pp. 242-252 (2019) [96].

5.1. Phenomenology based on single-source perturbation

First, the neutron noise phenomenology is studied based on the modelling of individual perturbation sources. To this aim, six *scenarios* are analyzed using the SIMULATE-3K code. These *scenarios* describe either the stochastic fluctuation of thermal-hydraulic parameters, or the vibration of fuel assemblies following different oscillation patterns. The description of the analyzed *scenarios* is as follows:

i. Modelling of the inlet coolant temperature fluctuations based on a stochastic (i.e. white noise) distribution. An amplitude of $1°C$ over the mean coolant temperature is used. This is a typical amplitude of the fluctuation of the coolant temperature over its mean value for the KKG cold legs under normal operating conditions, according to plant data. The inlet coolant temperature is modelled to fluctuate with the same amplitude over the same mean value in all three coolant loops of KKG,

however, at every time step the coolant temperature is stochastically different between the three loops (i.e. unsynchronized fluctuation).

ii. Modelling of the inlet coolant flow fluctuations based on a stochastic (i.e. white noise) distribution. An amplitude of 1% over of the rated flow level is assumed. Again, this corresponds to a typical amplitude of the coolant rated flow under normal operating conditions in KKG, according to plant data. The exact same stochastic fluctuation is modelled across the three coolant loops (i.e. synchronized fluctuation).

iii. Modelling of a lateral vibration, in the x-direction, of a central cluster of $5x5$ bundles. The vibration follows a stochastic (i.e. white noise) distribution. All the 25 assemblies are moving identically to each other (i.e. synchronized vibration) without assuming any bow shape nor a dynamic axial deformation.

iv. Modelling of a lateral vibration, in the x-direction, of a central cluster of $5x5$ bundles. The vibration follows a stochastic (i.e. white noise) distribution. The 25 assemblies are moving stochastically to each other (i.e. unsynchronized vibration) without assuming any bow shape nor a dynamic axial deformation.

v. Modelling of a lateral vibration, in the x-direction, of a central cluster of $5x5$ bundles. The vibration follows a sinusoid function at a frequency of $1.8\ Hz$. All the 25 assemblies are moving identically to each other (i.e. synchronized vibration) without assuming any bow shape nor a dynamic axial deformation.

vi. Modelling of a lateral vibration, in the x-direction, of a central cluster of $5x5$ bundles. The vibration follows a sinusoid function at a frequency of $1.8\ Hz$. The 25 assemblies are moving stochastically to each other (i.e. unsynchronized vibration) without assuming any bow shape nor a dynamic axial deformation.

The selected *scenarios* represent common types of noise sources observed in a LWR. The simulated neutron noise is extracted from the SIMULATE-3K calculations and the neutron noise behavior is post-processed in both the time and the frequency domains. First, the neutron noise spatial behavior for all *scenarios* is presented in Sec. 5.1.1. Then, the in-core detectors responses are analyzed in the frequency domain in Sec. 5.1.2. To this aim, the detectors spectral behavior is extracted and the pairwise coherence and phase difference functions are evaluated for each simulated *scenario*.

5.1.1. Neutron noise levels

First, the neutron noise spatial dependency is evaluated. It is recalled that, one of the main focuses of the current chapter is the comparison between the measured and simulated neutron noise phenomenology. Therefore, the simulated neutron noise is estimated based on the neutron detectors responses rather than the time-dependent fluctuation of the neutron flux. By doing so, a comparison against the measured neutron detector signals from KKG can be performed and the measured neutron noise characteristics can be identified with the help of the simulation results.

As described in *chapter 2*, the in-core neutron flux is monitored in KKG using SPNDs, which operate in the ionization region. Therefore, the produced current signal is directly proportional to the incident flux of the neutrons. The CASMO-5/SIMULATE-3/SIMULATE-3K codes sequence utilize a flux reconstruction approach in order to calculate the in-core detector responses [85]. More specifically, the reaction rates at the detector location are reconstructed using the intranodal fluxes at the respective locations as estimated by the nodal solver, based on Eq. 23.

$$det_{i,j} = \varphi_{1,i,j} \cdot FFF_{1,i,j} \cdot \sigma_{1,i,j} + \varphi_{2,i,j} \cdot FFF_{2,i,j} \cdot \sigma_{2,i,j} \quad \text{Eq. 23}$$

where, the reaction rate at a detector position i, j is estimated as function of the reconstructed intranodal fluxes, the flux form functions, and the microscopic cross-sections in the two energy groups. It should be noted that, the flux form functions are estimated at the detector location during the lattice solution in order to account for the assembly heterogeneities due to the specificities of the lattice [84].

In-core neutron detectors are modelled at every azimuthal core location in order to estimate in higher detail the neutron noise distribution. Every instrumentation tube hosts six neutron detectors at equal axial distances, ranging from core-bottom (i.e. level 1) up to the core-top (i.e. level 6). In total $1'062$ neutron detector signals are extracted after the successful termination of the transient calculation using the SIMULATE-3K code. All simulations last $35\ s$ and have a time step of $0.01\ s$, which ensure, based on a scoping analysis, the statistical convergence of both the time and frequency domain results. The neutron noise level is estimated at each detector position by estimating the signal coefficient of variation (i.e. the standard deviation over the average value).

The radial and axial distribution of neutron noise according to each one of the six analyzed *scenarios* is presented in Fig. 59 and Fig. 60, respectively. First, the radial distribution (i.e. neutron noise map) is illustrated based on the neutron detectors, located at the core-bottom axial level (i.e. level 1)[27]. Fig. 59i shows the neutron noise map due to the stochastic fluctuation of the inlet coolant temperature. It is observed that, higher neutron noise levels are located at the azimuthally north, southeast, and southwest regions of the core. The highest neutron noise regions correspond to the areas closest to the coolant loop cold legs. On the contrary, lower neutron noise levels are observed at the central, south, northeast, and northwest core areas. These regions are affected by the coolant inlet temperature fluctuations from more than one coolant loop. For instance, the northeast core-region is driven by fluctuations in the coolant loops 1 and 3. This example shows that the fluctuation in each individual coolant loop has a significant impact on the radial distribution of neutron noise. Consequently, core regions exhibiting significantly higher noise levels might be influenced by more intensive inlet coolant temperature fluctuations of the respective coolant loop.

Moreover, the neutron noise map due to the stochastic fluctuation of the inlet coolant flow (i.e. *scenario ii*) is presented in Fig. 59ii. As expected, the radial distribution of neutron noise has a flat profile due to the fact that only synchronized flow fluctuation between the three coolant loops can be simulated with the current version of the SIMULATE-3K code. Therefore, all the fuel bundles are equally influenced by the stochastic fluctuations of the inlet coolant flow, leading to similar neutron noise levels across an entire radial level.

In addition, the plots Fig. 59iii and v show the neutron noise maps resulting from *scenarios iii* and *v*, respectively, which simulate the lateral synchronized vibration, in the x-direction, of the $5x5$ central cluster under random and sinusoidal vibrational patterns, respectively. In both *scenarios*, the core regions, located adjacent to the noise source, exhibit the highest neutron noise levels, as expected, since they are the most affected from the variation of the water gap widths. Furthermore, the two neutron noise maps are symmetric over the y-axis, due to the lateral movement of the central cluster, only in the x-direction. Furthermore, it is observed that, the synchronized vibration of the selected fuel bundles in the x-direction results into zero noise levels at the core-center, since no relative change of the water gap widths exist for the central assemblies of

[27] The reference elevation is selected at the core-bottom, because at that axial level the thermal-hydraulic fluctuations are introduced.

the vibrating cluster (i.e. Fig. 59iii, v). Last, the sine-wise vibration (i.e. Fig. 59v, vi) results in higher maximum neutron noise levels compared to the random vibration cases (i.e. Fig. 59iii, iv). This can be understood by the fact that, neutron noise cancelling effects can be attributed to the fuel assembly random vibration.

However, the radial distribution of the neutron noise behaves differently when the selected fuel bundles vibrate in an asynchronous pattern between each other (i.e. *scenarios iv* and *vi*; Fig. 59iv, vi). In these two *scenarios*, the 25 bundles of the central cluster are vibrating independently to each other, and therefore, the core-central region has the highest neutron noise amplitude due to the cumulative effect of the individual stochastic fuel assembly lateral movement. In addition, it is observed also that, the neutron noise levels are lower compared to the synchronized vibration cases (i.e. *scenarios iii* and *v*; Fig. 59iii, v). This is due to the cancelling effect on the local neutron noise level, which is introduced by the stochastic movement of each vibrating bundle with respect to its vibrating adjacent ones. In addition, the bundles vibration based on a sinusoid movement exhibits higher neutron noise levels compared to the pure stochastic movement, as presented in Fig. 59v, vi, and Fig. 59iii, iv, respectively.

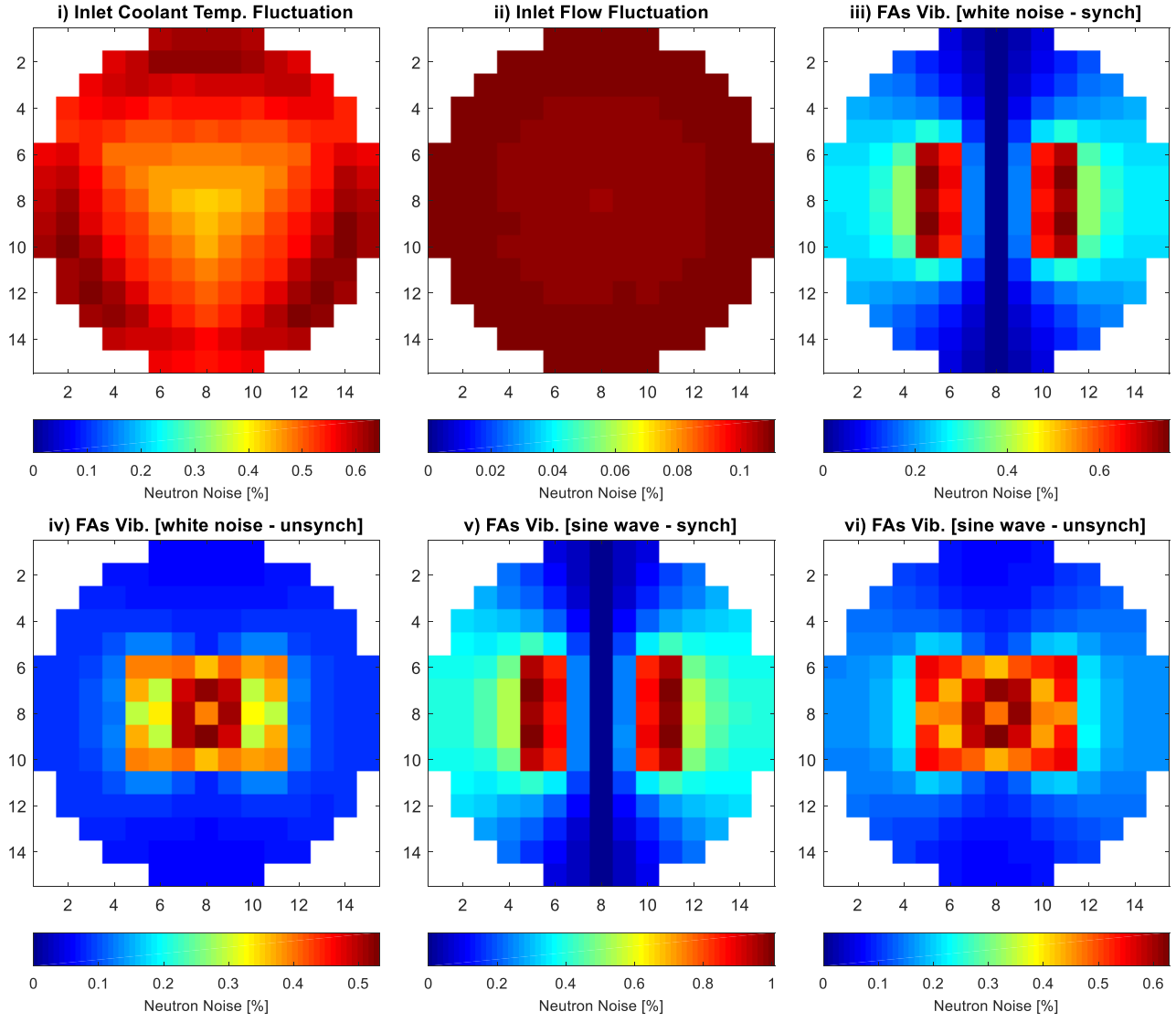

Fig. 59: Neutron noise levels at the core-bottom axial level for the simulated *scenarios i-vi*.

The axial distribution of neutron noise focuses on the azimuthal locations of the existing instrumentation tubes at KKG (i.e. N08, J06, J14, G02, G10, and C08.). The results of the neutron noise levels at different axial elevations are summarized in Fig. 60. Generally, an almost linear increase of the noise level is observed as the axial elevation increases, although the fuel assemblies are modelled to laterally vibrate by assuming the same axial displacement for all axial nodes, as shown in Fig. 28, left plot. This behavior is evident in all the examined *scenarios* (i.e. both thermal-hydraulic parameters fluctuation, and fuel bundles vibrations. It is recalled that, this trend can be related to the decrease of the coolant density along higher axial nodes, which results in higher noise amplitudes.

Moreover, it can be observed that, higher noise levels exhibit next to the source of perturbation. In addition, the synchronized vibration of fuel bundles corresponds to higher neutron noise level compared to the asynchronous movement. Last, the cluster vibration at a specific nominal frequency results in higher noise amplitudes compared to a stochastic movement. These observations are in agreement with the findings above.

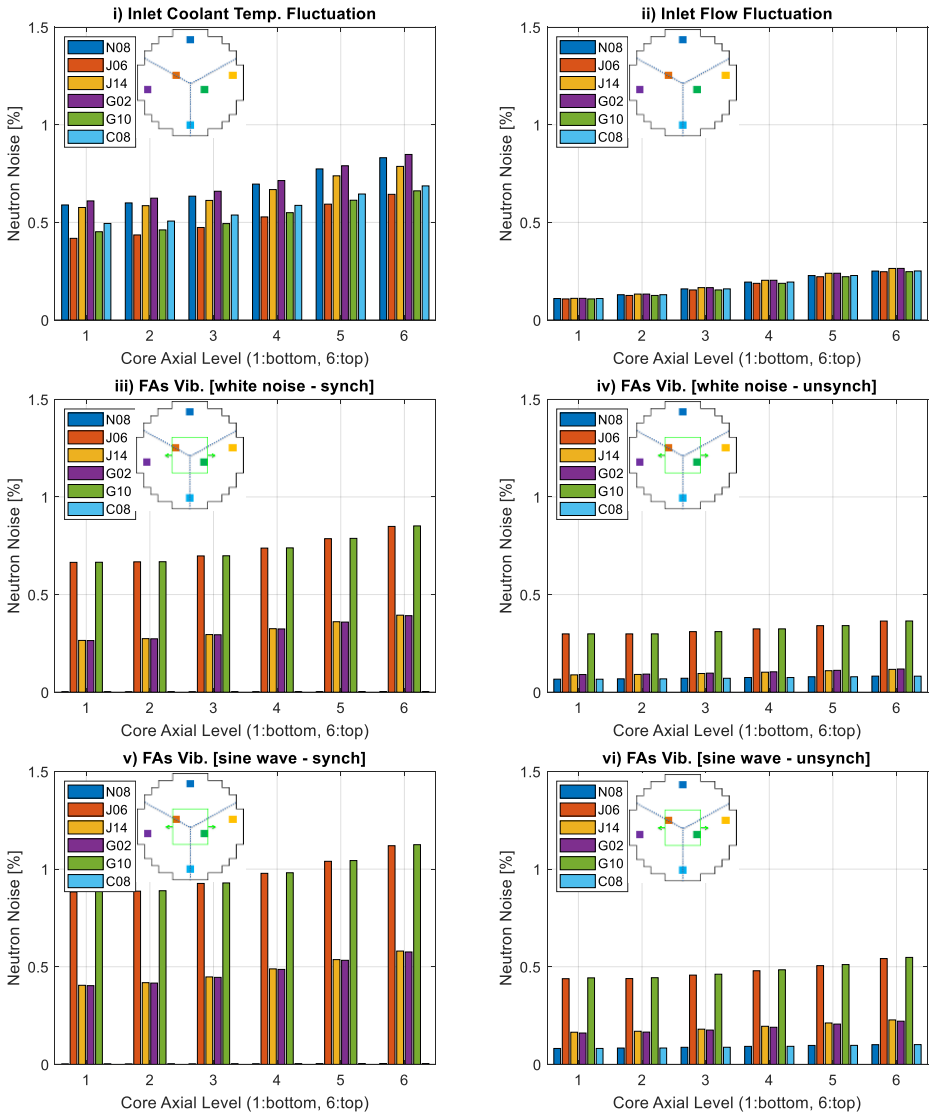

Fig. 60: Neutron noise axial distribution at six azimuthal locations across the core for the simulated *scenarios i-vi*.

5.1.2. Neutron noise spectral analysis

The current section describes in detail the neutron noise phenomenology in the frequency domain based on the simulated in-core neutron detectors of the KKG core. This part focuses on the estimation of the frequency spectrum (i.e. APSD) and the pairwise coherence and phase difference functions of the simulated detector signals. The main goal of this analysis is the identification of the spectral characteristics of neutron noise due to the occurrence of different types of individual perturbations. Ultimately, this section could assist in identifying similar characteristics between simulated and measured neutron noise and might help in understanding the observed trends. Throughout the following sections, the in-core detector located at the core position J14 at the bottom axial level is used as a reference. The J14 instrumentation tube is selected since it corresponds to the core location with the highest neutron noise levels measured in KKG, as described in *chapter 2*.

5.1.2.1. Inlet coolant temperature fluctuations

First, the neutron noise behavior in the frequency domain due to the stochastic fluctuation of the inlet coolant temperature (i.e. *scenario i*) is described in Fig. 61. The left and right plots present the radial and axial neutron noise phenomenology, respectively, in terms of APSD (top plots), coherence (middle plots), and phase difference functions (bottom plots).

The resulted neutron noise spectrum is colored although the fluctuations of the inlet coolant temperature are stochastic (white noise), as illustrated in Fig. 61, top plots. The spectrum has a stronger content in the lower frequency range (i.e. $<3Hz$). This can be explained by the fact that the reactivity is more affected by slower than more rapid temperature fluctuations (i.e. at lower than higher frequencies). Moreover, the in-core detectors, which are solely driven by the inlet coolant temperature fluctuation of a single coolant loop (i.e. N08, J14, and G02), exhibit a stronger neutron noise spectrum compared to those influenced by multiple coolant loops (i.e. J06, G10, and C08).

In addition, those in-core detectors that are driven by the stochastic fluctuation of the same coolant loop will experience strong radial pairwise coherence (i.e. Fig. 61, left-middle plot), as expected. In other words, detectors J14 and G10 (i.e. green line) are highly coherent because they are both positioned at the core region that is solely driven by the inlet coolant temperature stochastic fluctuation of coolant loop 1. On the contrary, as expected, low values of pairwise coherence can be observed between the in-core neutron detectors J14 and N08 (i.e. blue line), both located at the core regions, which are affected solely by the coolant loops 1 and 3, respectively.

Concerning the radial phase difference phase behavior phenomenology (i.e. Fig. 61, left-bottom plot), it is observed that the radially adjacent detectors J14 and G10 (i.e. green line) are fully synchronized (i.e. $0°$ phase difference) since they are both driven by the same stochastic noise source. The phase difference becomes significantly noisy between those detectors, which are affected by perturbations originating from different loops (e.g. J14 and N08; blue line). It is to be noted that, a rapid increase in the phase difference can be identified for those frequencies at which the pairwise coherence function gets very low values, as presented by the purple line, which corresponds to the coherence between the in-core detectors J14 and G02 at around 2 and $3\ Hz$. Clearly, such high phase difference values at frequencies with low pairwise coherence levels do not have significant physical relevance.

Last, the right plots of Fig. 61, show the axial pairwise coherence and phase difference phenomenology, with respect to the azimuthally east detector at core-bottom axial level (i.e. J14 at level 1). A rapid decrease in the axial coherence can be seen at a frequency around $1\ Hz$, which becomes more pronounced for axially furthest detectors (i.e. Fig. 61, right-middle plot). The so-called "*sink frequency*" is also observed in the simulated results similarly to the plant data (i.e. Sec. 2.3.2.2). It is recalled that, this very rapid axial coherence decrease is correlated to the transport time of the coolant temperature fluctuations through the core ([33], [51]). Moreover, a linear phase behavior increase can be observed in the entire frequency range for those detectors positioned in the same instrumentation tube (Fig. 61, right-bottom plot).

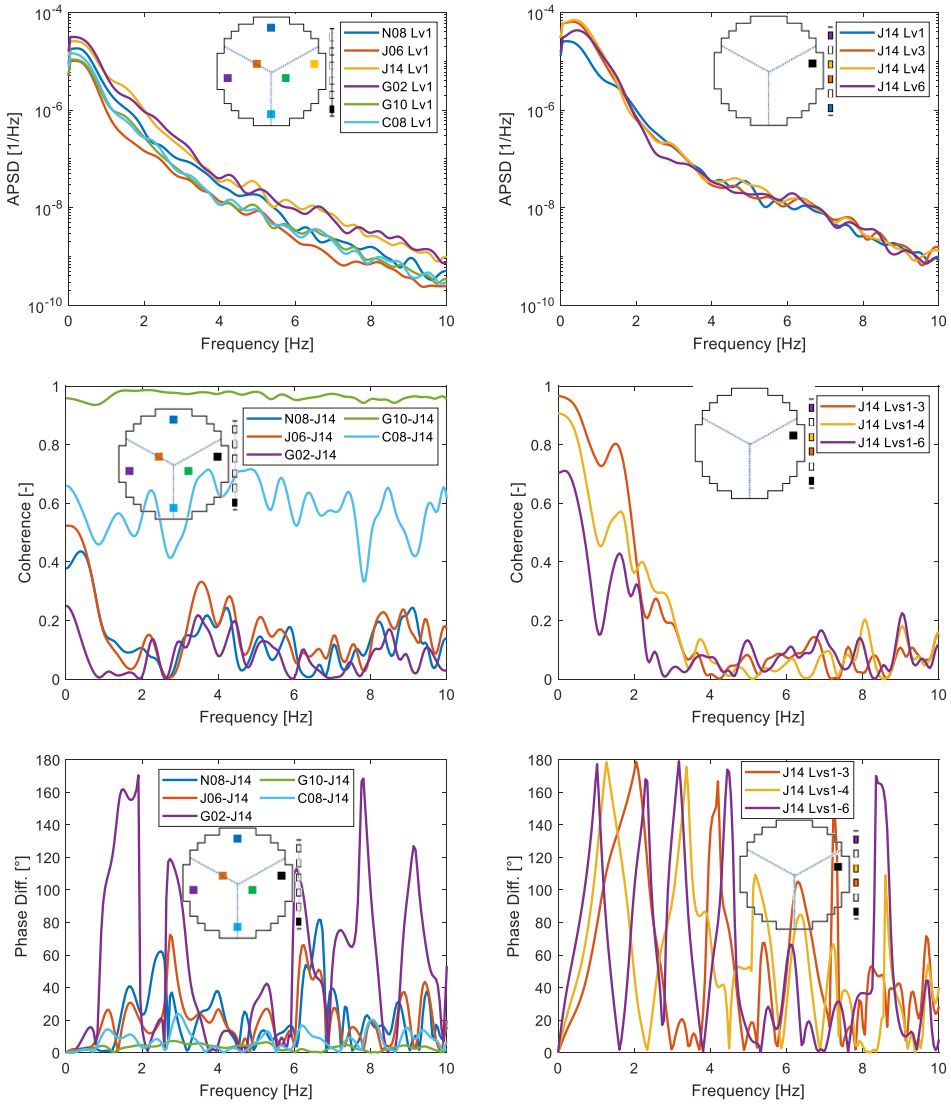

Fig. 61: *Scenario i* – In-core neutron detectors radial (left plots) and axial (right plots) noise phenomenology based on the APSD (top plots), coherence (middle plots), and phase difference functions (bottom plots). The in-core detector J14 at axial level **1** (black square) is used as reference for the coherence and phase difference function plots.

5.1.2.2. Inlet coolant flow fluctuations

Next, Fig. 62 summarizes the radial and axial neutron noise phenomenology due to the stochastic fluctuation of the inlet coolant flow (i.e. *scenario ii*). It is recalled that, the inlet coolant flow fluctuates following a white noise function in an identical manner for all three loops; i.e. synchronized fluctuations (the only option available in SIMULATE-3K). Consequently, it is expected that the inlet coolant flow fluctuation impacts both

radial pairwise coherence and in-phase difference response between all the azimuthal in-core neutron detectors, located at the same axial level. This behavior is illustrated in the left plots of Fig. 62, where it is clearly observed the complete coherence and the full in-phase behavior between all the illustrated signals, as expected.

Concerning the axial phenomenology, presented in the right-middle and right-bottom plots of Fig. 62, it can be observed that those neutron detectors, located at the same instrumentation tube, are almost perfectly coherent and synchronized. This response is due to the fact that the inlet flow perturbations are propagating axially with very high speed, i.e. almost instantaneous, along the core height due to the coolant compressibility properties. This is a particular characteristic of this noise source, which is clearly different from that of the inlet coolant temperature fluctuation, found to propagate along the core height due to transport phenomena, as shown in the previous section.

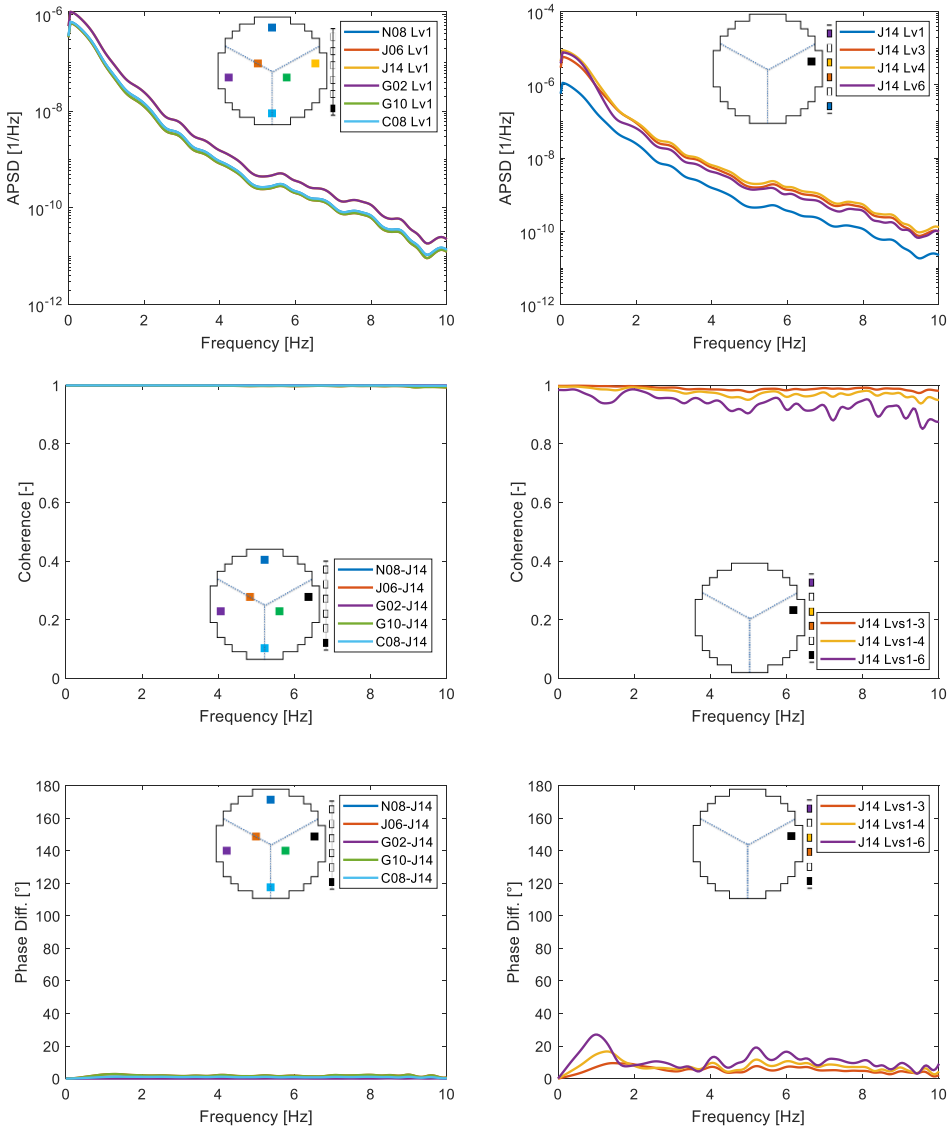

Fig. 62: *Scenario ii* – In-core neutron detectors radial (left plots) and axial (right plots) noise phenomenology based on the APSD (top plots), coherence (middle plots), and phase difference functions (bottom plots). The in-core detector J14 at axial level **1** (black square) is used as reference for the coherence and phase difference function plots.

5.1.2.3. Fuel assembly random lateral vibration (white noise)

This section analyzes the influence of the fuel assembly vibrations, based on a random displacement (i.e. stochastic vibration), on the neutron noise phenomenology. A central cluster of $5x5$ fuel bundles is modelled to vibrate only in the x-direction, without modelling any deformation of the axial shape. The bundles within the cluster are vibrating either in a synchronized or unsynchronized way between each other (i.e. *scenarios iii* and *iv*, respectively), and their impact on neutron noise phenomenology is presented in the following paragraphs.

Synchronized vibration

The stochastic vibration of the fuel bundles produces a white neutron noise spectrum, as it can be observed in Fig. 63, top plots. This behavior is clearly different from that produced by the fluctuation of the thermal-hydraulic parameters (i.e. *scenarios i* and *ii*), found to show a colored noise spectrum response. This is a clear demonstration that different noise sources impact differently the neutron noise phenomenology, and therefore, their systematic analysis can assist in better understanding of the underlying neutron noise phenomena. More importantly, in a real nuclear reactor, the analysis of the detector response could help in deducing the type of the associated neutron noise source (perturbation).

The radial phenomenology study of neutron noise shows that those in-core neutron detectors, positioned in the direction of vibration (i.e. J06, J14, G02, and G10 corresponding to the ref, yellow, purple, and green lines, respectively), exhibit the strongest noise spectrums, with more than four order of magnitudes larger than those obtained from detectors located in opposite direction of the vibration (i.e. N08 and C08). This is because the detectors positioned in the direction of the vibration are influenced the most by the lateral movement of the fuel assemblies (Fig. 63, left-top plot). Since, the fuel assemblies within the vibrating cluster are displaced in a synchronized manner, the in-core detectors located in the direction of perturbation exhibit full coherence (i.e. Fig. 63, left-middle plot). Moreover, the in-core neutron detectors positioned at the same core-half, with respect to the vibrating cluster, exhibit an in-phase behavior, while an out-of-phase behavior is observed between those detectors belonging to different core-halves (i.e. Fig. 63, left-bottom plot).

Related to the axial neutron noise phenomenology, the in-core neutron detectors, located at the same instrumentation tube, are perfectly synchronized (i.e. Fig. 63, right-bottom plot) and equally strongly coherent between each other (i.e. Fig. 63, right-middle plot), as expected. It should be noted that, this neutron noise characteristics are encountered in all the next examined *scenarios* (i.e. Fig. 64, Fig. 65, and Fig. 66, right-middle and right-bottom plots).

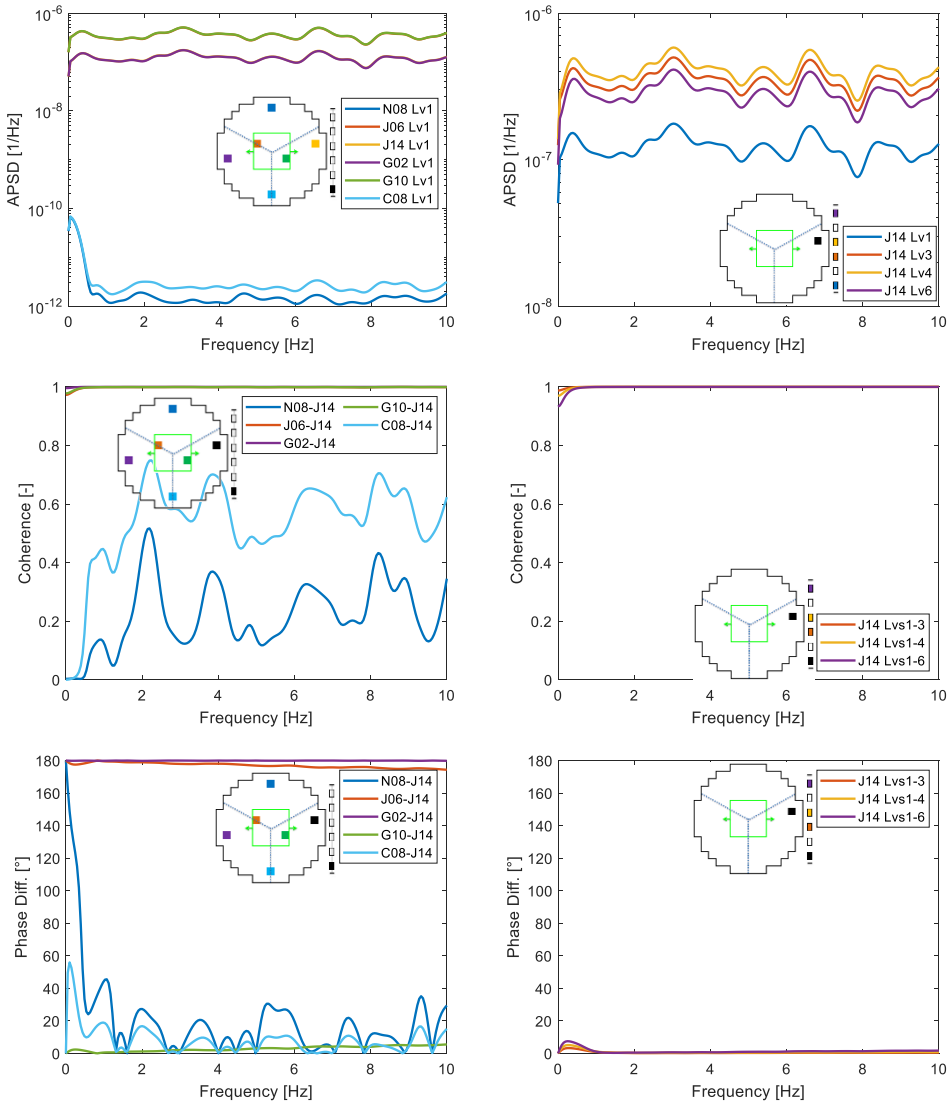

Fig. 63: *Scenario iii* – In-core neutron detectors radial (top plots) and axial (bottom plots) noise phenomenology based on the APSD (left plots), coherence (middle plots), and phase difference functions (right plots). The in-core detector J14 at axial level **1** (black square) is used as reference for the coherence and phase difference function plots.

Unsynchronized vibration

The *scenario iv* studies the $5x5$ cluster vibration in which the involved bundles are modelled to vibrate in an unsynchronized manner between each other. Since the noise source is of a different type, it is observed in Fig. 64 that, the neutron noise phenomenology has also different characteristics. First, the in-core neutron detectors spectrums differentiate between each other, depending on the relative distance of the analyzed detector from the vibrating cluster (i.e. Fig. 64, left-top plots). Moreover, the radial pairwise coherence between the analyzed detectors in the direction of vibration (i.e. J14 with J06, G02, and G10) is considerable lower and noisier (i.e. Fig. 64, left-middle) compared to the synchronized vibration case (i.e. Fig. 63). This can be explained by the fact that each one of the four detectors J14, J06, G02 and G10 are mainly influenced by the independently vibrating bundles which are located in their neighborhood in the unsynchronized *scenario*, in contrast to the synchronized vibrating cluster where all four detectors are driven by a single noise source (i.e. the vibrating central cluster). Moreover, the analysis of the reference detector J14 and the detectors N08 and C08 which are not in the direction of vibration shows the same moderate radial coherence, as seen in the synchronized *scenario* (i.e. Fig. 64 and Fig. 63, left-middle plots). The radial phase difference response exhibits

also a noisier behavior due to the unsynchronized fuel assembly lateral movement (i.e. Fig. 64, left-top plot). It is to be noted that, a rapid linear increase of the phase difference can be seen at frequencies corresponding to almost zero value for the coherence function, similarly to the finding of *scenario i* (i.e. Fig. 61).

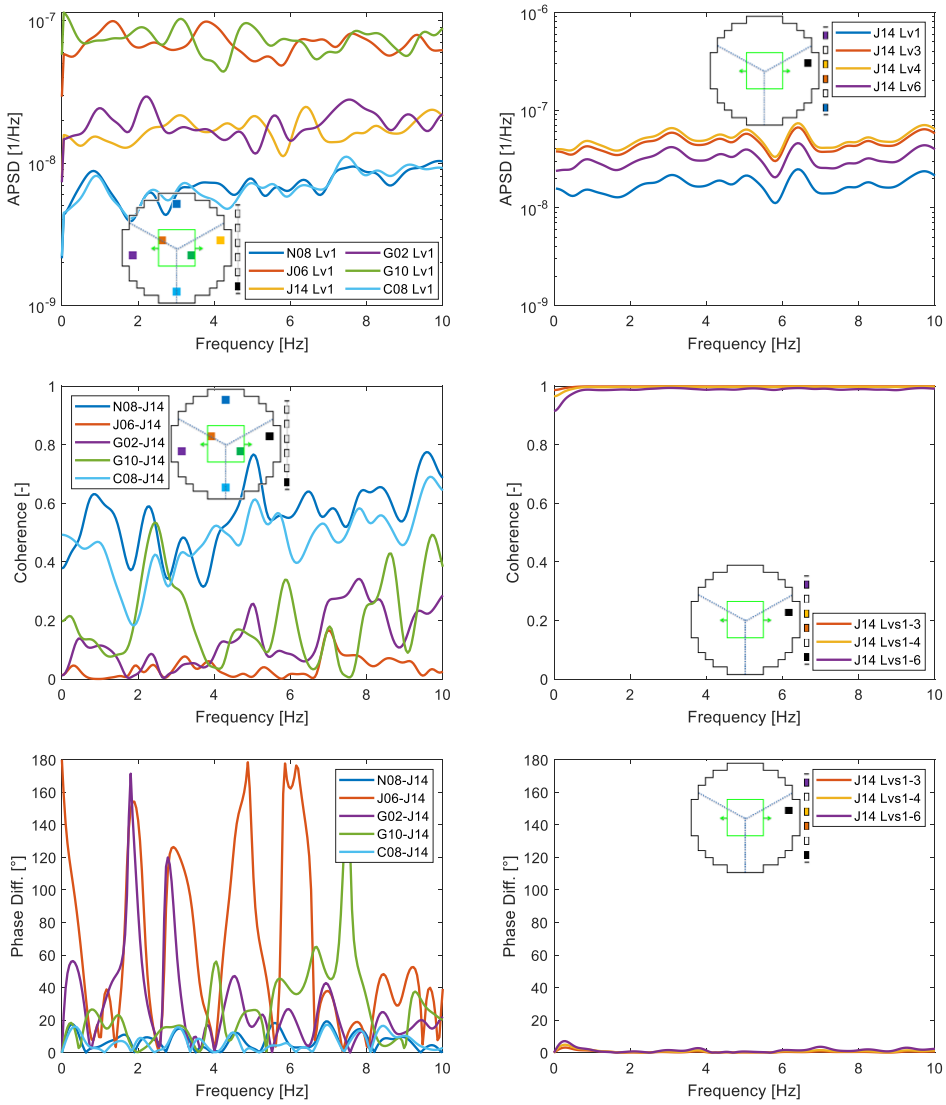

Fig. 64: *Scenario iv* – In-core neutron detectors radial (left plots) and axial (right plots) noise phenomenology based on the APSD (top plots), coherence (middle plots), and phase difference functions (bottom plots). The in-core detector J14 at axial level 1 (black square) is used as reference for the coherence and phase difference function plots.

5.1.2.4. Fuel assembly sinusoidal lateral vibration

It has been extensively discussed in Sec. 3.2 that, the fuel bundles tend to laterally vibrate at a specific eigenfrequencies (e.g. at about $1.8\ Hz$, corresponding to the first vibration mode [2]), originating from the strong hydraulic forces of the coolant flow. Therefore in this thesis, the impact of this type of vibration on the neutron noise phenomenology is studied. In the following sections, the central cluster of $5x5$ fuel bundles is modeled to vibrate with a nominal frequency of $1.8\ Hz$, in the x-direction. The bundles within the cluster are vibrating either in a synchronized or unsynchronized way between each other (i.e. *scenarios v* and *vi*, respectively).

Synchronized vibration

The left plots in Fig. 65 show that the synchronized vibration of the bundles results into a neutron noise spectrum, exhibiting a strong spectral peak at $1.8\ Hz$ followed by smaller spectral peaks at the higher harmonics. It can be seen also that, as expected, all the in-core neutron detectors are perfectly coherent to each other at the eigenfrequency of $1.8\ Hz$ (i.e. Fig. 65, top-middle plot). In addition, the neutron detectors, located at the same core-half, with respect to the vibrating cluster, show an in-phase behavior, which differentiates from the out-of-phase behavior observed between the signals located at different core- halves (i.e. Fig. 65, top-right plot).

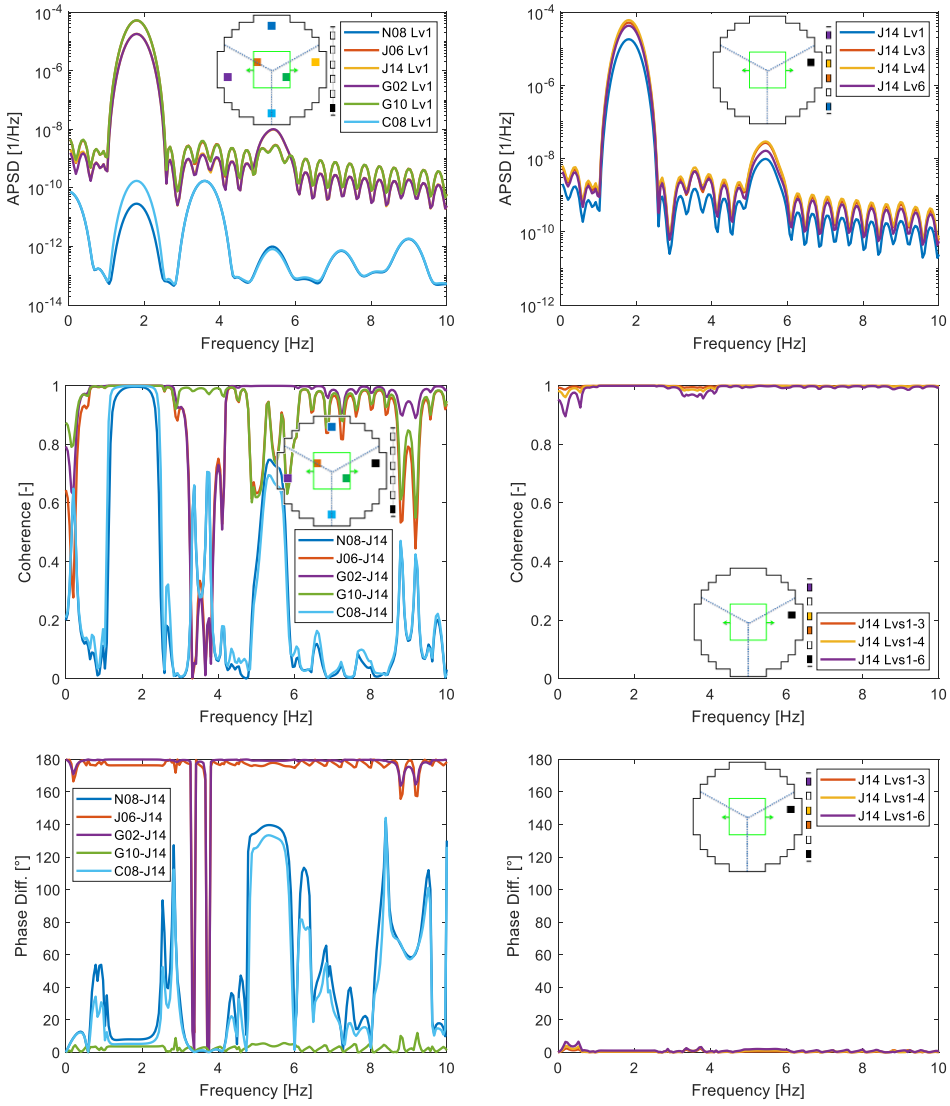

Fig. 65: *Scenario v* – In-core neutron detectors radial (left plots) and axial (right plots) noise phenomenology based on the APSD (top plots), coherence (middle plots), and phase difference functions (bottom plots). The in-core detector J14 at axial level **1** (black square) is used as reference for the coherence and phase difference function plots.

Unsynchronized vibration

The last analyzed *scenario* focuses on the modelling of the central cluster vibration at the eigenfrequency of $1.8\ Hz$, in which the bundles are vibrating in an unsynchronized manner between each other (i.e. *scenario vi*). The radial and axial noise phenomenology due to this vibrational pattern is presented in Fig. 66. The resulting

neutron noise spectrum exhibits a strong spectral peak at the eigenfrequency of vibration (i.e. Fig. 66, top plots), similarly to the synchronized vibration (i.e. Fig. 65), except for the detectors N08 and C08, which are not positioned in the direction of the vibrating cluster. Interesting enough, it is observed that the unsynchronized vibration results in significantly damped spectral peaks at the eigenfrequencies harmonics as compared to the synchronized case. In addition, the in-core neutron detectors, positioned in the direction of the vibration (i.e. x-direction), are highly coherent between each other at $1.8\ Hz$ (i.e. Fig. 66, left-middle plot). Furthermore, the same detectors exhibit either an in-phase behavior, if they located at the same core-half, with respect to the vibrating cluster; or an out-of-phase behavior, if they are positioned in different core-halves (i.e. Fig. 66, left-bottom plot).

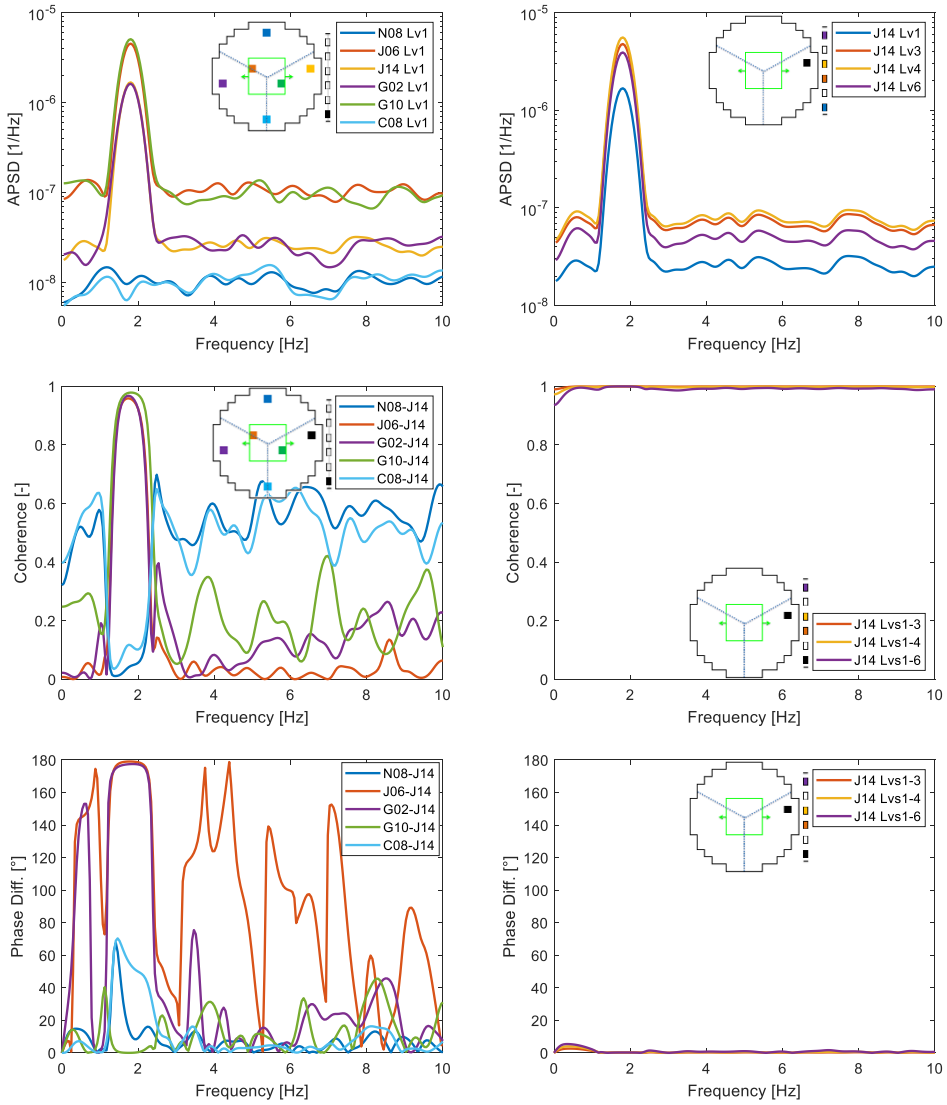

Fig. 66: *Scenario vi* – In-core neutron detectors radial (left plots) and axial (right plots) noise phenomenology based on the APSD (top plots), coherence (middle plots), and phase difference functions (bottom plots). The in-core detector J14 at axial level **1** (black square) is used as reference for the coherence and phase difference function plots.

5.2. Importance of inlet coolant temperature fluctuations

The previous section, i.e. Sec. 5.1, presented the neutron noise characteristics based the introduction of a single type of perturbation, comprising the inlet coolant temperature and flow fluctuations and the fuel assembly vibration. The current section studies the importance of the inlet coolant temperature fluctuations on the neutron noise phenomenology when multiple noise sources are combined together. Three additional *scenarios* are modelled in this section[28]:

vii. Modelling of the combined effect of inlet coolant temperature and flow fluctuations. Similarly to Sec. 5.1, both fluctuations follow a stochastic distribution. The amplitude of $1°C$ over the mean coolant temperature and of 1% over of the rated flow level is assumed. The three coolant loops behave in an unsynchronized manner with respect to the former perturbation, and in a synchronized manner with respect to the latter perturbation type.

viii. Modelling of the combined effect of inlet coolant temperature fluctuation and the lateral vibration in the x-direction of a central cluster of $5x5$ bundles. The former perturbation type has the same characteristics as the respective one in *scenario vii*. The cluster vibration follows a stochastic (i.e. white noise) distribution with all the 25 assemblies moving identically to each other (i.e. synchronized vibration) without assuming any bow shape nor a dynamic axial deformation.

ix. Modelling of the combined effect of inlet coolant flow fluctuation and the lateral vibration in the x-direction of a central cluster of $5x5$ bundles. The former perturbation type has the same characteristics as the respective one in *scenario vii*. The cluster vibration has the same characteristics as the respective one in *scenario viii*.

5.2.1. Neutron noise levels

First, the axial distribution of the neutron noise based on the six in-core neutron detectors for the *scenarios vii-ix*, is presented in Fig. 67. As a general remark, it is observed that the combination of two noise sources does not always result to a noise level equal to the linear summation of individual noise sources amplitude. This observation might be attributed to the presence of non-linear effects. On the one hand, the combination of the inlet coolant temperature and flow perturbations (i.e. *scenario vii,* Fig. 67a) seems to have the same noise distribution of the former noise source (i.e. *scenario i,* Fig. 60i) and to be independent from the latter source (i.e. *scenario ii,* Fig. 60ii). On the other hand, the combination of the vibrating cluster in the x-direction with either thermal-hydraulic perturbation, shows that the N08 and C08 detectors are driven by the latter noise source (i.e. Fig. 67b,c as compared to Fig. 60iii). It is recalled, that the N08 and C08 detectors exhibit zero noise amplitudes in *scenario iii* as they are not located at the direction of the cluster vibration (Fig. 60iii). This behavior shows that, as a general trend, the result of combination of the noise sources is driven by the noise source having the strongest effect on the noise level.

[28] The s*cenarios* numbering continues from Sec. 5.1.

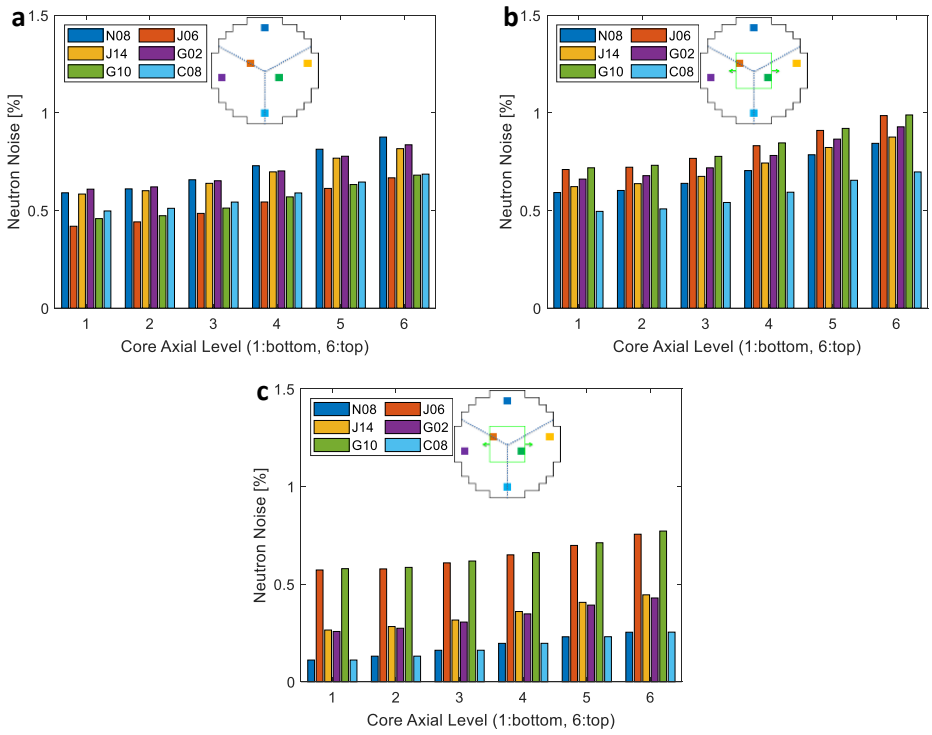

Fig. 67: Neutron noise axial distribution at six azimuthal locations across the core for the simulated *scenarios vii* (a), *viii* (b), and *ix* (c).

5.2.2. Neutron noise spectral analysis

The neutron noise spectral characteristics of the three analyzed *scenarios* are presented in Fig. 68 to Fig. 70 following the same representation as in Sec. 5.1. First, it can be clearly observed that the effect of the inlet coolant temperature fluctuation on the noise phenomenology prevails over the inlet coolant flow fluctuation. This is a common feature in all spectral measures (i.e. APSD, coherence and phase) in both the radial and axial phenomenology, as depicted in the combined *scenario vii*, and the *scenarios i* and *ii* of the individual noise source modelling (i.e. Fig. 68, and Fig. 61 and Fig. 62, respectively).

In addition to that, the key role of inlet coolant temperature fluctuation is also depicted in the combined *scenario viii*. The spectral noise phenomenology seems to be mainly driven by the inlet coolant temperature fluctuation in the very low frequency range (up to $2\ Hz$), whereas the fuel assembly vibration starts to have an important role above $2\ Hz$. This observation is consistent among all spectral measures as depicted in Fig. 69, in contrast to Fig. 61 and Fig. 63.

Last, the inlet coolant flow fluctuation seems to impact the spectral noise phenomenology of the combined *scenario ix* only up to the frequency of $1\ Hz$, as presented in Fig. 70. The resulted spectral noise phenomenology seems to be solely affected by the fuel assembly vibration. Interesting enough, a peculiar behavior is observed in the radial coherence between the reference detector J14 and the detectors J06, G02, and G10, which are located in the direction of the cluster vibration (i.e. Fig. 70, left-middle plot). The coherence exhibits considerably low values up to $2\ Hz$ in the combined *scenario ix*, even if the modelling of the individual noise source (i.e. *scenarios ii* and *iii*) results into a clear full coherence between the respective detectors over the entire frequency range (i.e. Fig. 62 and Fig. 63, left-middle plots). In order to understand this behavior, further sensitivity analysis is needed which is beyond the current research

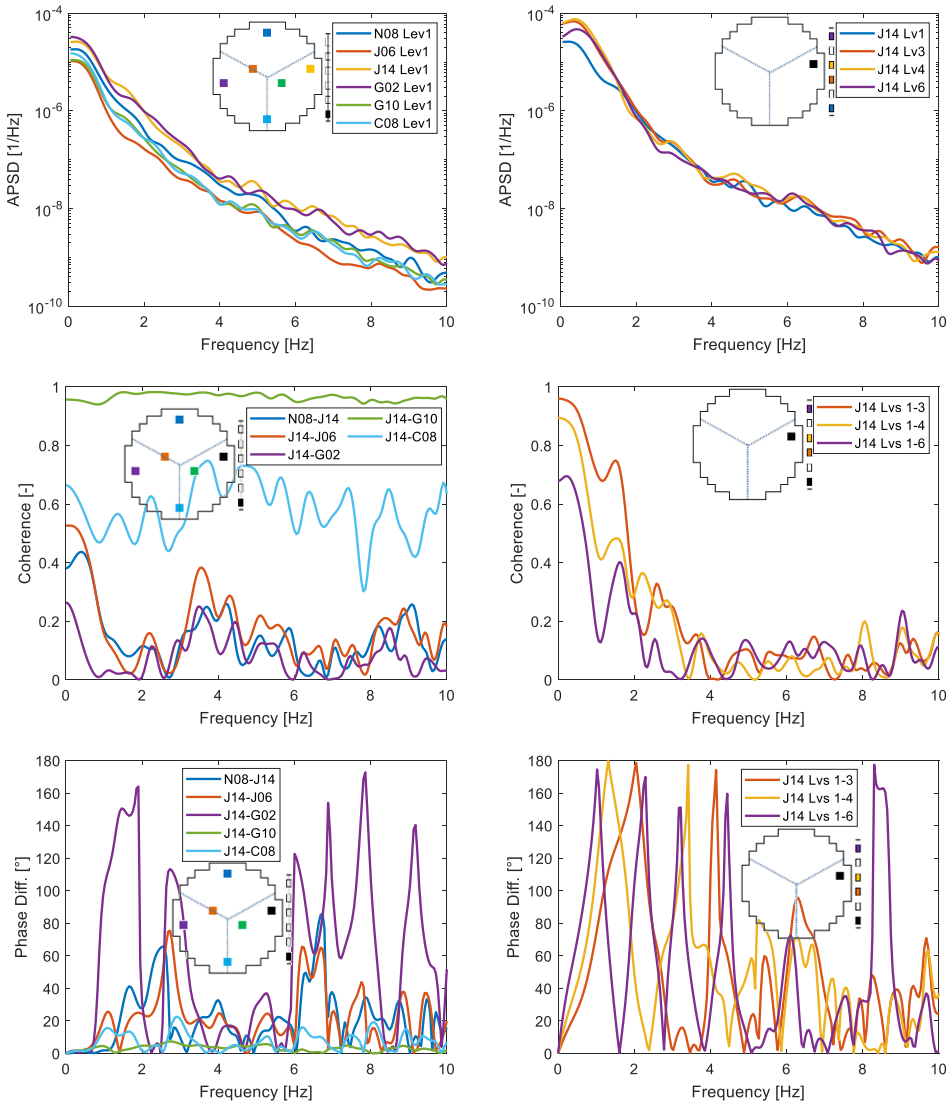

Fig. 68: *Scenario vii* – In-core neutron detectors radial (left plots) and axial (right plots) noise phenomenology based on the APSD (top plots), coherence (middle plots), and phase behavior functions (bottom plots). The in-core detector J14 at axial level **1** (black square) is used as reference for the coherence and phase behavior function plots.

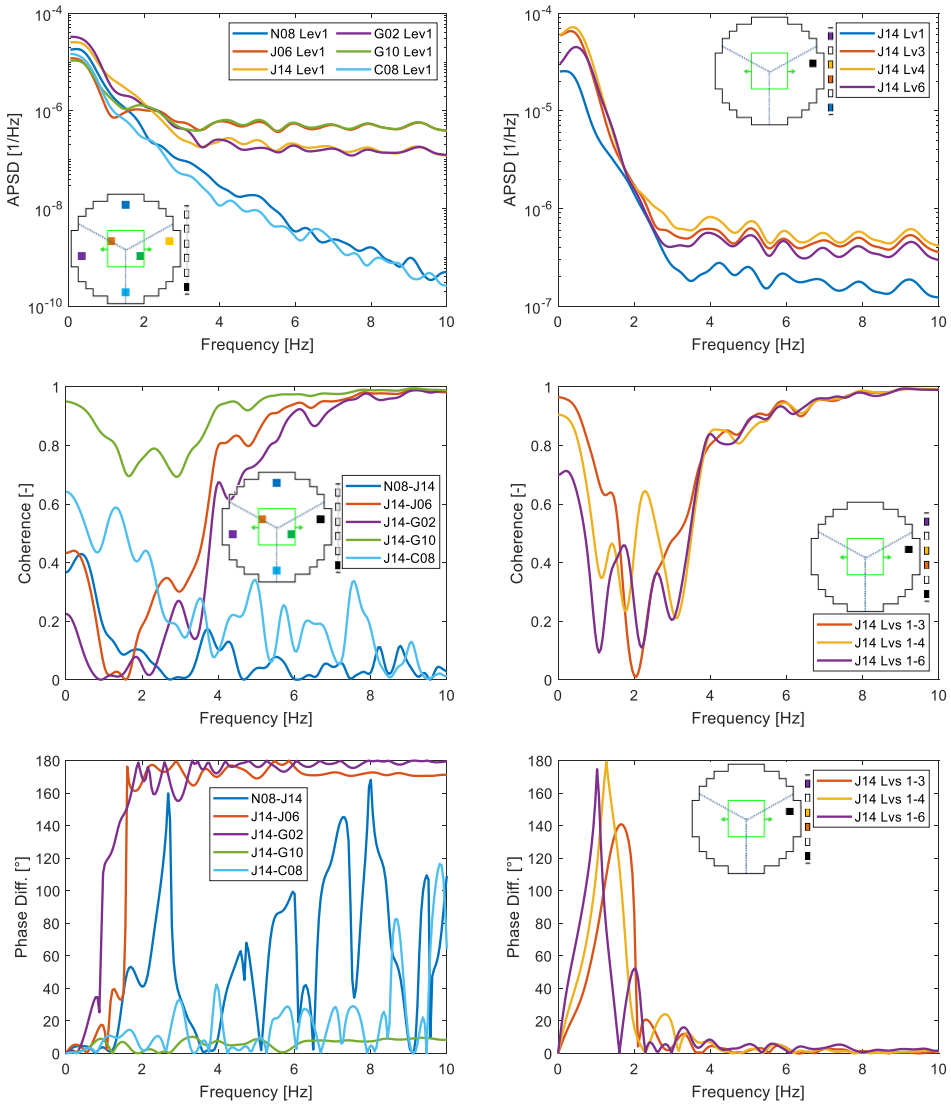

Fig. 69: *Scenario viii* – In-core neutron detectors radial (left plots) and axial (right plots) noise phenomenology based on the APSD (top plots), coherence (middle plots), and phase behavior functions (bottom plots). The in-core detector J14 at axial level **1** (black square) is used as reference for the coherence and phase behavior function plots.

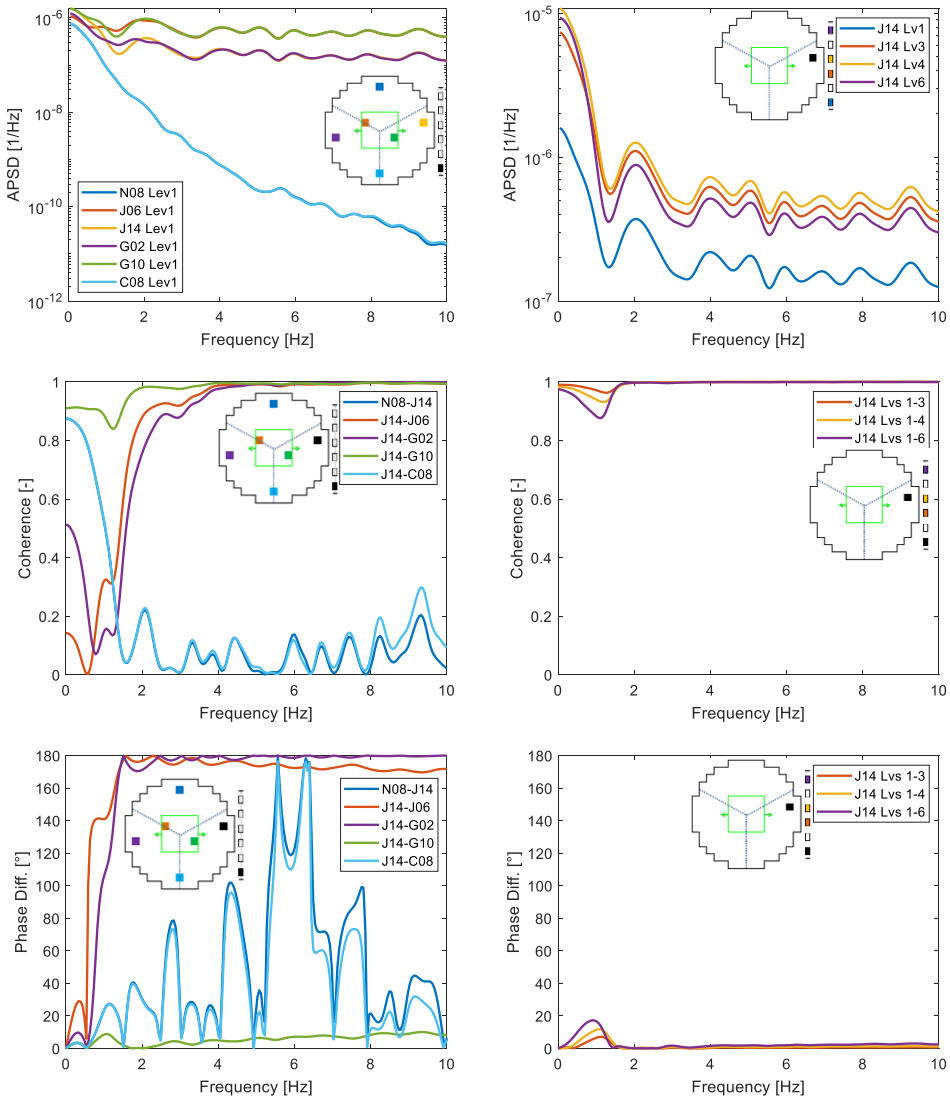

Fig. 70: *Scenario ix* – In-core neutron detectors radial (left plots) and axial (right plots) noise phenomenology based on the APSD (top plots), coherence (middle plots), and phase behavior functions (bottom plots). The in-core detector J14 at axial level **1** (black square) is used as reference for the coherence and phase behavior function plots.

In a nutshell, this scoping analysis indicates the leading role of the inlet coolant temperature fluctuation as compared to the inlet coolant flow fluctuation. In addition, the noise amplitude of a combined *scenario* does not clearly correspond to a linear summation of the noise amplitudes of the individual noise sources, i.e. non-linear effects and/or cancelling effects seem to have an important role. Last, it has been observed that the inlet coolant temperature fluctuation has a primary role in the low frequency range, whereas the fuel assembly vibration has a key impact above $2\ Hz$ in the combined *scenarios*. It should be noted that, a first sensitivity analysis on examining how the neutron noise behavior is affected by different perturbation amplitudes of the inlet coolant temperature and flow is already assessed in [97].

5.3. Phenomenology based on combination of all perturbation types

The systematic analysis of the neutron noise phenomenology continues in the current section by modelling the combination of all types of noise sources (i.e. both fuel bundles vibrations and thermal-hydraulic fluctuations). It should be noted that under real operating conditions various sources of perturbation co-exist,

and therefore, the resulted neutron noise has a rather complex phenomenology. To this aim, five additional combined *scenarios* are modelled[29].

x. Modelling of the combined effect of inlet coolant temperature and flow fluctuations and the lateral vibration in the x-direction of a central cluster of $5x5$ bundles (i.e. combination of *scenarios i*, *ii*, and *iv*). The inlet coolant temperature and flow are selected to stochastically fluctuate with amplitudes of $1°C$ and 1%, respectively. The inlet coolant flow perturbation fluctuates in a perfect synchronization between the three coolant loops, while the inlet coolant temperature is stochastically fluctuating in an unsynchronized manner between the three coolant loops. In addition, the fuel assemblies of the central cluster are vibrating in an unsynchronized way to each other and their lateral displacement follows a white noise signal (i.e. random vibration).

xi. This *scenario* has the same characteristics as *scenario x*. The only difference is that the lateral displacement of the vibrating fuel assemblies follow a sine wave with a frequency of $1.8\ Hz$ (i.e. eigenfrequency of the fuel assembly first mode [2]); i.e. combination of *scenarios i*, *ii* and *vi*.

xii. This *scenario* has the same characteristics as *scenario x*. The only difference is that the fuel assemblies within the central cluster vibrate in a synchronized way to each other; i.e. combination of *scenarios i*, *ii* and *iii*.

xiii. This *scenario* has the same characteristics as *scenario xi*. The only difference is that the fuel assemblies within the central cluster vibrate in a synchronized way to each other; i.e. combination of *scenarios i*, *ii* and *v*.

xiv. This *scenario* has the same characteristics as *scenario* xii. The only difference is that the central cluster is vibrating in two directions. The random lateral displacement follows Eq. 59.

Similarly as for previous simulations, all current *scenarios* are performed with the 3D transient nodal code SIMULATE-3K and have a time step of $0.01\ s$ for the modelling of dynamic perturbations of $35\ s$.

The examined simulated *scenarios* of this section attempt to model combined noise sources that exist under normal operating conditions in LWRs. The ultimate goal of this section is to compare and try to explain the observed neutron noise characteristics, based on the KKG plant data presented in *chapter 2*, with the simulated results. Therefore, first, the key findings of the KKG neutron noise phenomenology are briefly listed below, once more, to assist the reader in carrying out the comparison against the simulated results.

- Higher neutron noise levels are consistently observed at the east-core region.
- The core-top elevation shows higher noise amplitude at BOC.
- All neutron detectors show similar spectral behavior; strong spectrum at the low frequency region, and two spectral peaks at around $1.5\text{-}2\ Hz$ and $8\ Hz$. The former peak is related to the fuel assembly vibration and the latter peak corresponds to the core barrel pendular movement, according to the literature.
- Azimuthally neighboring in-core neutron detectors are strongly coherent and exhibit an in-phase relationship.
- A relative out-of-phase relationship has been observed between the core-halves.
- In-core detectors belonging to the same instrumentation string are highly coherent and exhibit a linear increase of the phase over the entire low frequency range except at frequencies around $1\ Hz$ and $6\ Hz$ (coherence dips).

[29] The *scenarios* numbering continues from Sec. 5.1 and Sec. 5.2.

5.3.1. Neutron noise levels

First, emphasis is given to the neutron noise spatial levels due to the modelling of the combined noise sources. Fig. 71 shows the neutron noise levels at six azimuthal locations and at six axial levels for all simulated *scenarios*. The neutron noise levels are estimated based on the in-core neutron detector signals, positioned in KKG reactor core. The in-core detectors azimuthal locations are illustrated in Fig. 71 together with the location of the vibrating central cluster of $5x5$ fuel assemblies (i.e. green square) in order to assist in the interpretation of the results. In addition, the three core-regions (i.e. blue dotted lines) that are individually affected by the three coolant loops are also presented in Fig. 71.

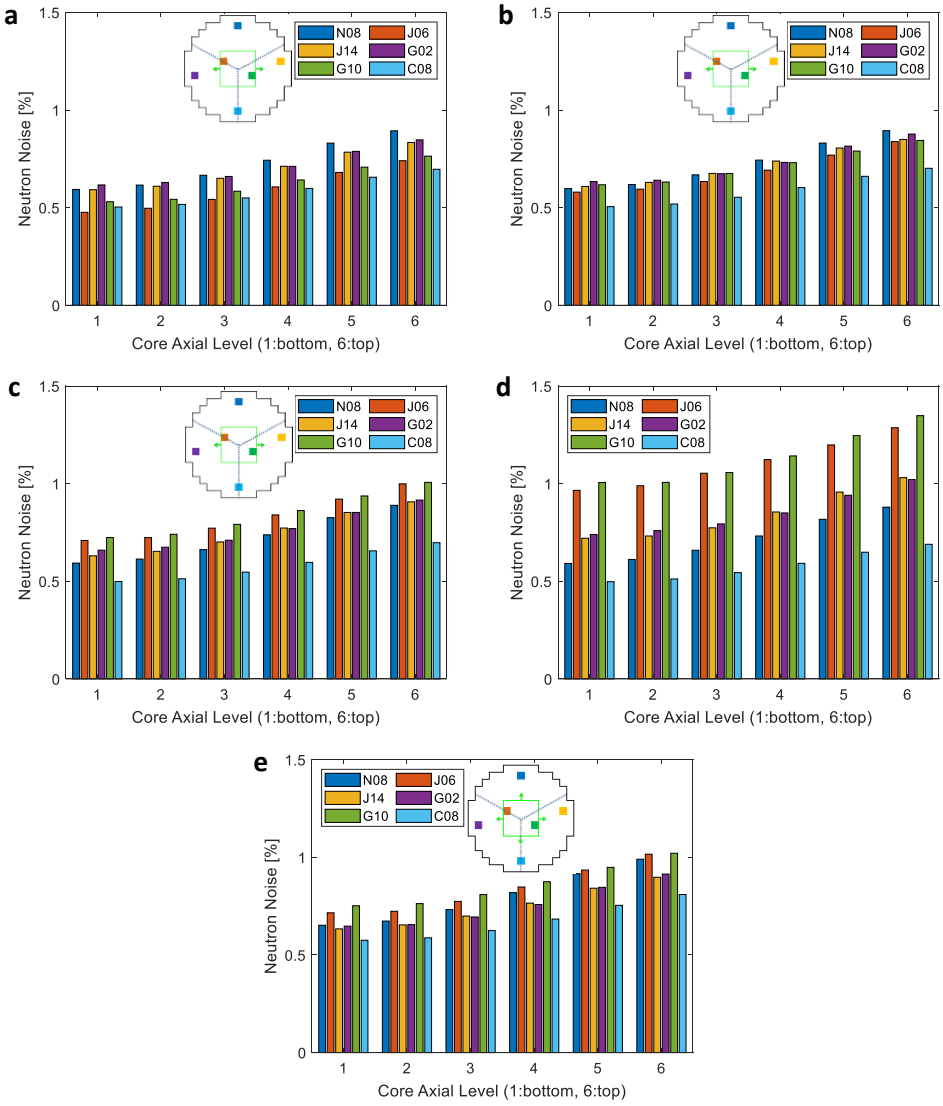

Fig. 71: Neutron noise axial distribution at six azimuthal locations across the core for the simulated *scenarios x-xiv*.

For the proper assessment of the neutron noise spatial levels under the five examined combined *scenarios* it is important to recall the separate effect of each of the stochastic fluctuations on the noise amplitude, analyzed in the previous sections. First, it has been shown that, the N08, J14, and G02 in-core detectors exhibit the highest neutron noise levels, under the influence of inlet coolant temperature fluctuations, since they are located at core regions, closest to the coolant loop cold legs (i.e. noise source). Furthermore, it has been also observed that, the J06 and G10 in-core neutron detectors exhibit considerably higher neutron noise levels

compared to the other detectors, when only the vibration of the central cluster of $5x5$ fuel assemblies in the x-direction is taken into account. This behavior is explained by the fact that the J06 and G10 detectors are right next to the noise source, and affected the most from the water gap thickness variation.

Concerning the simulated *scenario x* (i.e. Fig. 71a), it can be seen that the neutron noise behavior has very similar characteristics as in the case of the inlet coolant temperature stochastic fluctuation (i.e. Fig. 60i); i.e. higher neutron noise levels at the in-core detectors N08, J14, and G02. In addition, the same plot shows that the in-core detectors J06 and G10 have slightly higher neutron noise levels compared to C08, which is solely driven from the inlet coolant temperature fluctuation. This is due to the fact that the detectors J06 and G10 are strongly affected also from the vibration of the central cluster, representing the second noise source. It is to note that, the J06 detector has smaller neutron noise level than the detector G10 (as compared to the solely central cluster vibration, at which detectors J06 and G10 had equally noise levels; Fig. 60iii-vi). It is recalled that, this behavior can be explained since in the analyzed *scenario* the J06 detector is affected by the inlet coolant temperature fluctuation from both coolant loops 2 and 3, whereas the G10 detector is solely affected by the fluctuation in coolant loop 1, as already described in Sec. 5.1.2.1. More importantly, it is observed that the combination of multiple noise sources does not result in a summation of the noise amplitudes of the individual components, probably due to the presence of non-linear effects. This observation is similar to the previous section findings.

Concerning the simulated *scenario xi* (Fig. 71b), it can be seen that. the detectors N08, J14, and G02 exhibit similar noise trends like in *scenario x* (Fig. 71a), as they are mainly driven by the inlet coolant temperature fluctuation. In addition, the detectors J06, J14, G02, and G10, located in the direction of the cluster vibration have slightly higher noise levels compared to *scenario x*, due to the sine-wise cluster displacement. This observation is in agreement with Fig. 60iii and Fig. 60v, which indicates that a sine-wise assembly vibration results in higher noise amplitudes compared to a random vibration. The main difference between *scenarios x* and *xi* has to do with the C08 results, which shows the lowest neutron noise amplitude, as it is located far away from the vibrating central cluster and at the same time it is driven by the inlet coolant temperature fluctuations from both coolant loops 1 and 3.

Scenarios xii and *xiii* (i.e. Fig. 71c, d) show clearly higher noise amplitudes compared to *scenarios x* and *xi*, respectively, as they model a synchronized lateral displacement of the vibrating fuel bundles within the central cluster in contrast to the unsynchronized movement in the latter cases. This is in agreement with the previous finding in the single noise source analysis (Fig. 60iii-vi), showing that cancelling effects on the total noise level exist when fuel bundles are vibrating in an unsynchronized manner.

Last, the *scenario xiv* reveals that the cluster vibration in one and two directions results to similar neutron noise levels, which is in agreement with the findings of Sec. 4.3.3. However, it is observed in Fig. 71e that, the detectors N08 and C08 have considerably higher noise levels compared to the previous four cases, as this last *scenario* models the cluster vibration in two directions. Consequently, these two detectors are subject to the cluster vibration in the y direction. Last, the detectors J14, G10, J06, and G02 exhibit the same neutron noise amplitudes as in *scenario xii*, since the cluster vibration in the y-direction has a minor impact on them.

5.3.2. Neutron noise spectral analysis

The neutron noise phenomenology in the frequency domain for the examined *scenario x* is shown in Fig. 72. The top and bottom plots present the radial and axial neutron noise behavior, respectively, in terms of APSD (top plots), coherence (middle plots) and phase difference functions (bottom plots). The overall neutron noise

spectral shape (i.e. Fig. 72, top plots) has globally the same behavior as in the plant data (i.e. Fig. 12), i.e. strong spectrum in the low frequencies, due to the thermal-hydraulic fluctuations. It should be noted that, any related neutron noise characteristic at $8\ Hz$ cannot be observed, since the model for simulating the pendular movement of the core-barrel, observed at such frequency, has not been developed yet.

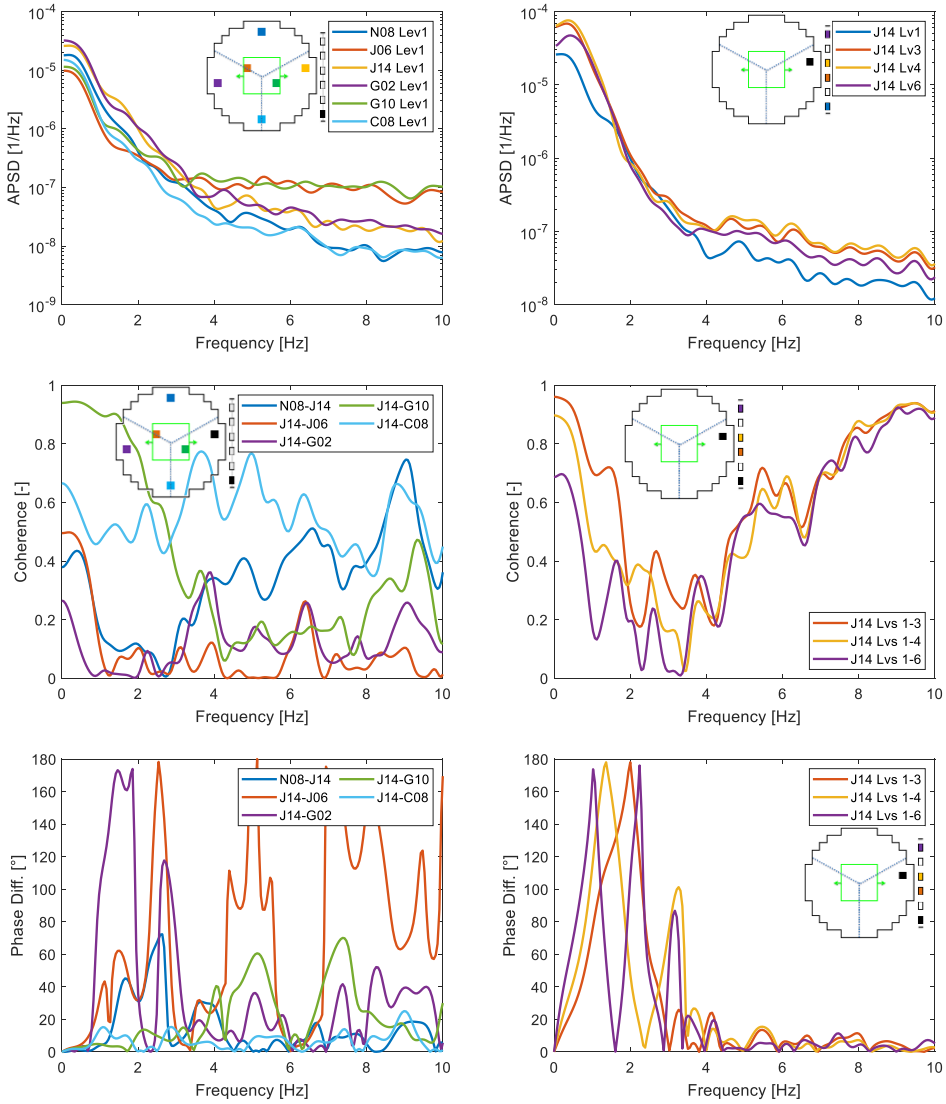

Fig. 72: *Scenario x* – In-core neutron detectors radial (left plots) and axial (right plots) noise phenomenology based on the APSD (top plots), coherence (middle plots), and phase difference functions (bottom plots). The in-core detector J14 at axial level **1** (black square) is used as reference for the coherence and phase difference function plots.

Concerning the radial phenomenology (i.e. Fig. 72, left plots), higher pairwise coherence and in-phase behavior is observed between in-core neutron detectors, driven by the inlet coolant temperature fluctuations from the same coolant loop. For instance, the in-core detectors J14 and G10 are affected only by fluctuations in coolant loop 1, and therefore, they are strongly coherent with an in-phase behavior between each other (i.e. green lines in Fig. 72, left-middle/bottom plots). The comparison of the frequency domain results between the analyzed *scenario x* and those obtained due to individual perturbation cases in Sec. 5.1.2, shows that, the radial neutron noise phenomenology seems to be strongly affected by the stochastic fluctuations of the thermal-hydraulic parameters up to $2\ Hz$. Above $2\ Hz$ the lateral vibration of the fuel assemblies becomes the main contributor to the radial neutron noise phenomenology.

The axial neutron noise phenomenology shows a rapid decrease on the pairwise coherence at a frequency around $1\ Hz$ (i.e. "*sink frequency*"). This coherence decrease becomes more clear as the axial distance between the analyzed detectors increases too (i.e. Fig. 72, right-middle plot). At the frequency of $1Hz$, a linear phase difference increase is observed (i.e. Fig. 72, right-bottom plot). It is recalled that, the frequency of $1\ Hz$ corresponds to the time interval that is needed for the coolant in order to travel from the core-bottom to the core-top, as already observed from the simulation results in the previous section and as also reported in ([51], [98]). The simulated axial neutron noise phenomenology up to $2\ Hz$ behaves very similar to what was measured in real KKG data (i.e. Fig. 15 and Fig. 16). Above $2\ Hz$ the simulated axial pairwise coherence becomes stronger between all in-core detectors mainly due to the vibrating central cluster, as it has been seen in the previous sections for the individual *scenarios* that include fuel assembly vibration.

The noise phenomenology for *scenario xi* in which the fuel bundles vibrate following a sinusoid pattern with a nominal frequency of $1.8\ Hz$ combined with the stochastic fluctuation of the thermal-hydraulic parameters is presented in Fig. 73.

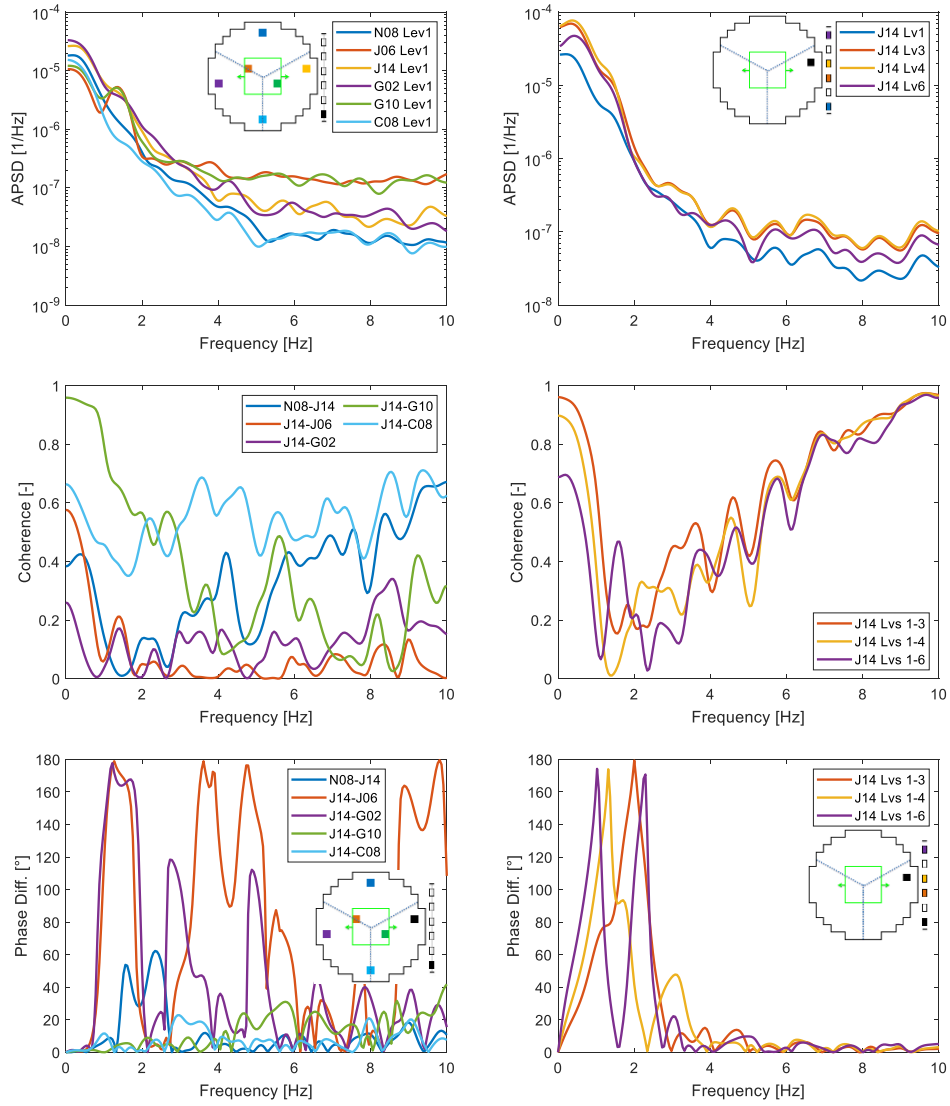

Fig. 73: *Scenario xi* – In-core neutron detectors radial (left plots) and axial (right plots) noise phenomenology based on the APSD (top plots), coherence (middle plots), and phase difference functions (bottom plots). The in-core detector J14 at axial level **1** (black square) is used as reference for the coherence and phase difference function plots.

The vibrating central cluster results into a spectral peak, mainly for detectors G02 and J06, at the respective specific frequency of $1.8\ Hz$ (i.e. Fig. 73, top plots), as expected. Similarly to the KKG plant data analysis (i.e. Fig. 12), it is observed that the spectral peak at $1.8\ Hz$ is more pronounced at the core-top than at the core-bottom (i.e. Fig. 73, right-top plot). Moreover, it can be seen that the global radial neutron noise phenomenology is similar between the two analyzed *scenarios* (i.e. Fig. 72 and Fig. 73, left plots). The key difference in the noise phenomenology in *scenario xi* is that the in-core neutron detectors located in the direction of the vibrating central cluster (i.e. x-direction) exhibit a noticeable pairwise coherence peak at $1.8\ Hz$ (i.e. green, red and purple lines in Fig. 73, left-middle plot). It is recalled that, the measured plant data exhibit strong radial pairwise coherence between in-core detectors at a frequency around $1.8\ Hz$ (i.e. Fig. 13 and Fig. 14). This is a potential indication that the fuel bundles lateral vibration at a specific nominal frequency can influence the neutron noise phenomenology. This behavior is more pronounced in the next cases *xii* and *xiii* in which the cluster vibrates in a synchronized manner. Last, similarly to *scenario x*, the axial neutron noise phenomenology exhibits both a rapid decrease of the axial pairwise coherence, and a linear increase of the phase difference at around $1\ Hz$ (i.e. Fig. 73, right-middle/bottom plots) due to transport phenomena similarly to Fig. 72.

Next, Fig. 74 and Fig. 75 present the neutron noise phenomenology for *scenarios xii* and *xiii*, respectively, describing the synchronized vibration of the 25 fuel assemblies within the central cluster. In general terms, these two *scenarios* result in similar qualitative noise characteristics in the frequency domain as the respective *scenarios x* and *xi*, in which an unsynchronized vibration is imposed. Despite that, some differentiations can be observed. The top plots in both Fig. 74 and Fig. 75 reveal stronger APSDs for frequencies greater than $2\ Hz$, as compared to the respective plots in Fig. 72 and Fig. 73, due to the synchronized vibration of the fuel assemblies. In addition, the in-core detectors seem to be strongly coherent in both radial and axial directions above $2\ Hz$ (i.e. Fig. 74 and Fig. 75 , middle plots). Furthermore, the detector pair J14-G10 shows a clear in-phase behavior and the pairs J14-G02 and J14-J06 exhibit a pronounced out-of-phase for frequencies greater than $2\ Hz$ (i.e. Fig. 74 and Fig. 75 , left-bottom plots). The detectors located in the same instrumentation string J14 show an axial in-phase behavior above $2\ Hz$. It should be also noted that, the synchronized sine-wise vibration (i.e. *scenario xiii*, Fig. 75) results to pronounced spectral characteristics at $1.8\ Hz$, the frequency of cluster vibration. All these observations are in agreement with the noise characteristics, described in the previous Sec. 5.1 and Sec. 5.2. Overall, this comparison demonstrates that, the inlet coolant temperature fluctuation continues to drive the noise phenomenology up to $2\ Hz$. For higher frequencies, the impact of the vibrating fuel assemblies become more evident in the *scenarios xii* and *xiii* (i.e. synchronized vibration) as compared to *scenarios x* and *xi* (i.e. unsynchronized vibration).

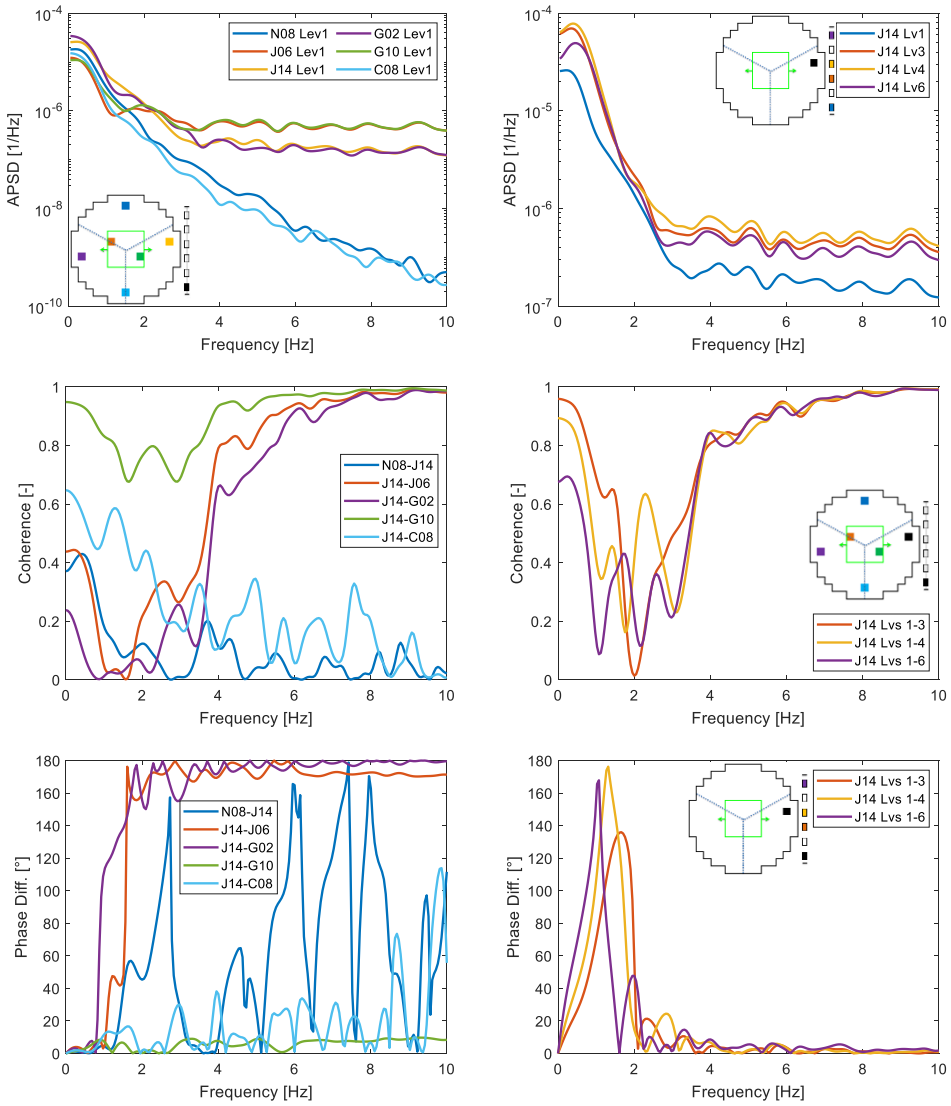

Fig. 74: *Scenario xii* – In-core neutron detectors radial (left plots) and axial (right plots) noise phenomenology based on the APSD (top plots), coherence (middle plots), and phase behavior functions (bottom plots). The in-core detector J14 at axial level **1** (black square) is used as reference for the coherence and phase behavior function plots.

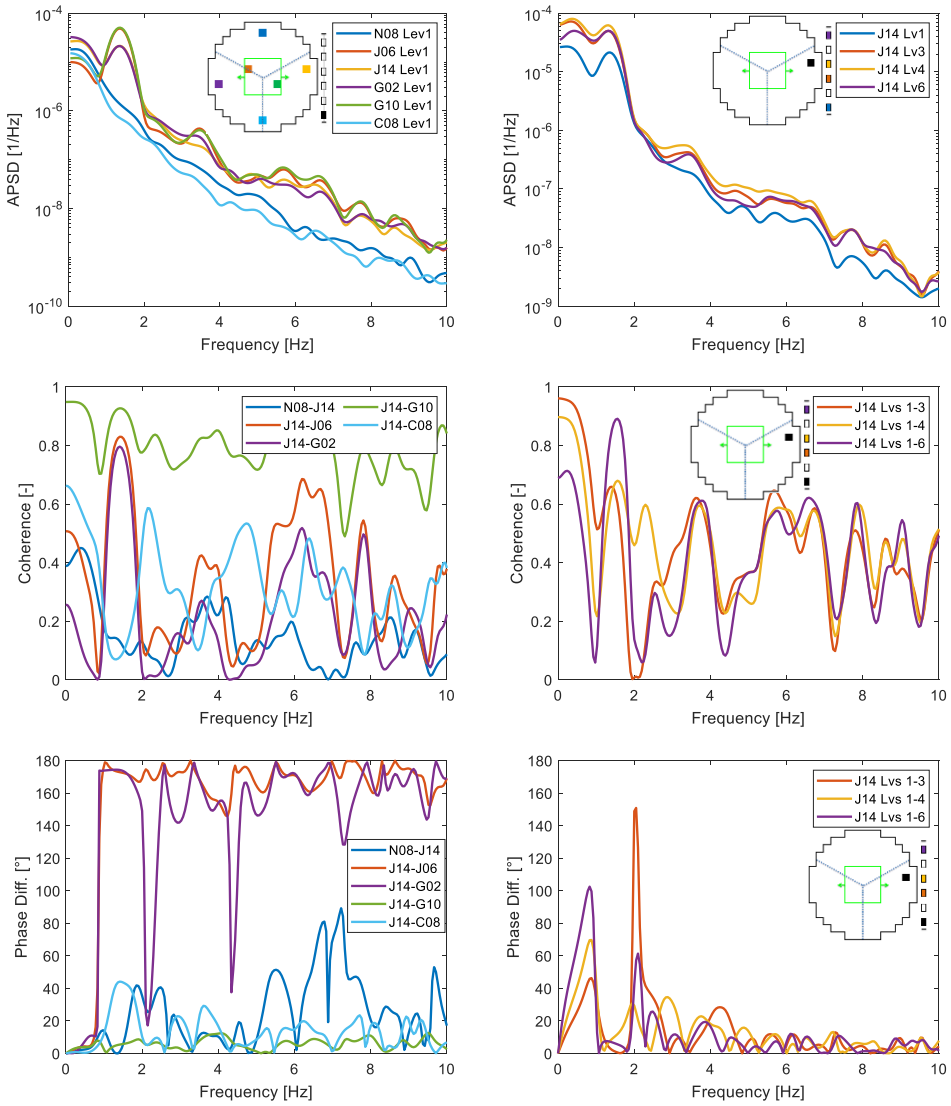

Fig. 75: *Scenario xiii* – In-core neutron detectors radial (left plots) and axial (right plots) noise phenomenology based on the APSD (top plots), coherence (middle plots), and phase behavior functions (bottom plots). The in-core detector J14 at axial level **1** (black square) is used as reference for the coherence and phase behavior function plots.

The last analyzed *scenario xiv* describes the random vibration of the central cluster in a synchronized manner in both directions. This case results in almost identical noise phenomenology (Fig. 76) as in the respective *scenario* with vibration in just one direction (i.e. *scenario xii*, Fig. 74), as it would be expected. The only main difference is with respect to detectors N08 and C08 which exhibit considerably stronger spectrum, as they are directly influenced by the lateral vibration of the central cluster in the y-direction (Fig. 76, left-top lot).

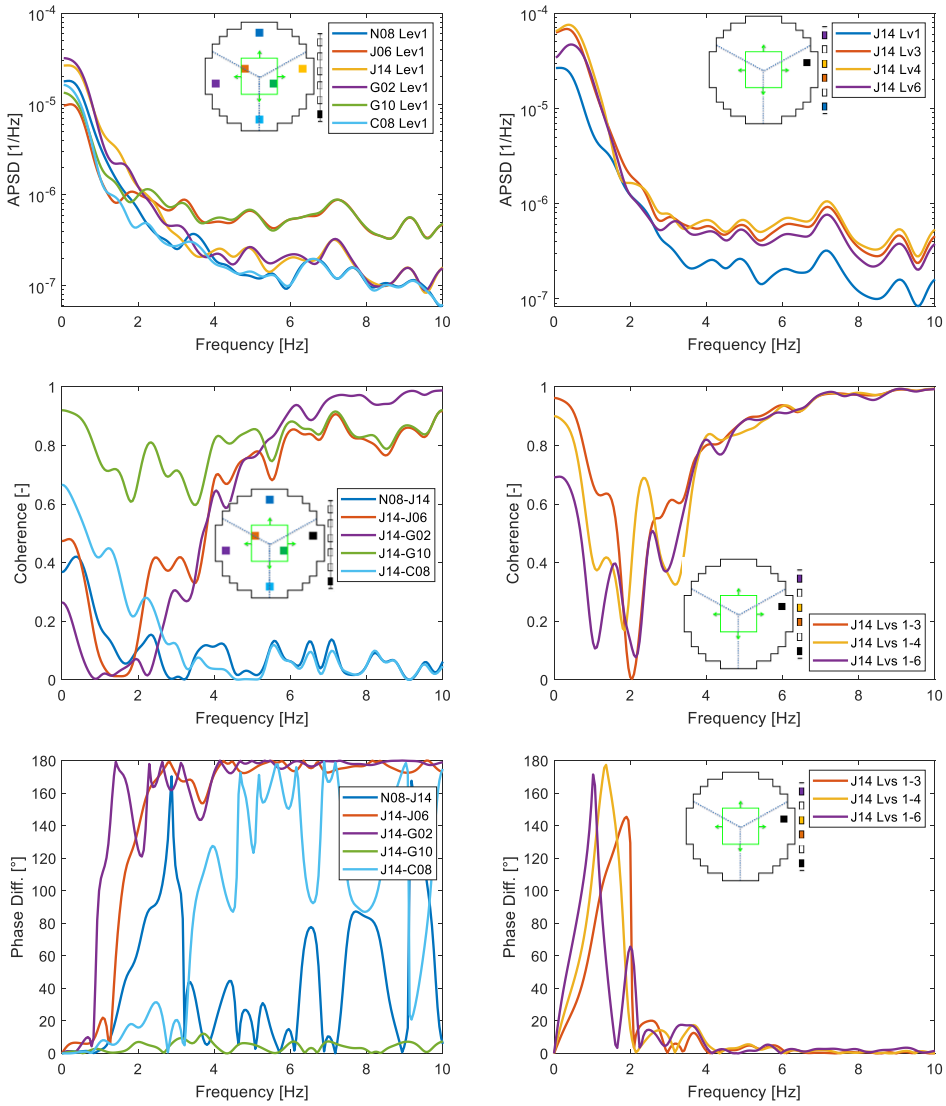

Fig. 76: *Scenario xiv* – In-core neutron detectors radial (left plots) and axial (right plots) noise phenomenology based on the APSD (top plots), coherence (middle plots), and phase behavior functions (bottom plots). The in-core detector J14 at axial level **1** (black square) is used as reference for the coherence and phase behavior function plots.

5.4. Neutron noise evolution

The neutron noise level increase trend, observed in several KWU pre-Konvoi PWRs, has been identified to coincide with the time of introduction of a new fuel assembly design into their cores. Historically, several KWU pre-Konvoi PWRs experienced fuel failures due to the fact that the fuel rods were well fixed within the fuel bundle structure. In order to overcome this costly operational issue, a new fuel design has been developed and introduced in most of the KWU pre-Konvoi PWRs. The spacers dimples of the newer fuel assembly type are designed to have lower stiffness properties allowing the fuel rods to laterally vibrate more easily, and therefore, the thermo-mechanical properties of the fuel could be enhanced. The spacers lower stiffness implies that the fuel pins, and subsequently the entire fuel assembly, are able to move more freely around their center of mass. Naturally, the introduction of this new fuel bundle type, being more sensitive to lateral vibrations, is assumed to be one of the main causes behind the neutron noise level increase trend.

Similarly to other KWU pre-Konvoi PWRs, the new fuel bundle design has been also introduced into the KKG core just before the neutron noise levels started to get higher amplitudes. Since cycle 28, the number of these

new assembly type has been steadily increased until reaching an equilibrium configuration in cycle 36, as presented in Fig. 77. As the number of this bundle type increased in KKG core, the neutron noise behavior showed a level increase trend, as presented in Fig. 9. Therefore, in the current section, a preliminary analysis is performed in order to identify how the KKG core loading pattern over the cycles could be related to the measured neutron noise evolution. In other words, this section focuses on modelling the fuel assembly vibrations, using the SIMULATE-3K code, for realistic loading patterns of the KKG core.

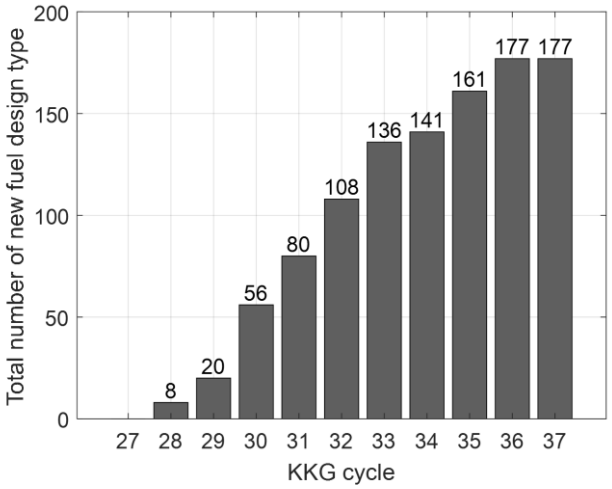

Fig. 77: Total number of newer fuel bundle type loaded in the KKG core.

Since PSI/LRT is involved in the yearly safety calculations of the core licensing of all the Swiss reactors, all KKG core loading patterns for all cycle are available and accessible and therefore the corresponding models were developed using the CASMO-5/SIMULATE-3 code sequence. The exact locations of the newer fuel design type have been extracted from the SIMULATE-3 core models and depicted in Fig. 78, showing the bundles locations in the KKG core from cycle 28 up to cycle 37. The different colors correspond to the cycle number, at which each fuel bundle was freshly loaded in the core (i.e. cycle 28, green; cycle 29, blue; cycle 30, orange; cycle 31, pink; cycle 32, brown; cycle 33, grey; cycle 34, yellow; cycle 35, red; cycle 36, purple; cycle 37, aqua). In addition, the dashed squares show the location of the six in-core neutron detector instrumentation tubes (i.e. N08, J06, J14, G02, G10, and C08).

In the literature, it has been already shown that the spacers dimples of the newer fuel design type undergo a progressive relaxation as their exposure increases ([91], [99]). More specifically, fuel bundles, which have spent up to two cycles in the core are expected to face a full relaxation of the spacers dimples force on their fuel rods. Consequently, the amplitude of vibration of these bundles is expected to progressively increase within the first two cycles before reaching a maximum value for the remaining cycles.

In this section, a first quantitative attempt for understanding the impact of the increase of the number of vibrating fuel bundles using real core loadings is performed, despite the uncertainties and assumptions that might be related to the irradiation damage mechanism on the spacers dimples. This analysis is meant to provide an insight about the possible mechanisms that drive the neutron noise level increase trend in KWU pre-Konvoi PWRs. To this aim, the PSI neutron noise modelling methodology is utilized and the KKG core is studied by focusing on cycles 28 up to 37. Depletion steps at the BOC, MOC, and EOC for each cycle are analyzed, and the amplitude of vibration of each bundle is imposed according to their cumulative burnup exposure, as presented in Table 6. It is recalled that, the water gap distance between two adjacent bundles in

a typical KWU pre-Konvoi PWR is $0.22\ cm$, and therefore, the maximum allowable amplitude of vibration in this analysis is assumed to be $0.11\ cm$ in order to avoid any bundles contact.

Propriety information.
More information can be found in [19] under request (https://www.psi.ch/stars/).

Fig. 78: Location of the newer fuel bundle type in the KKG core in cycles **28** to **37**.

Table 6: Bundles amplitude of vibration based on their burnup level.

Bundle burnup		Maximum amplitude of vibration
1^{st} time loaded (fresh)	BOC	$1/5 \cdot 0.11\ cm$
	MOC	$2/5 \cdot 0.11\ cm$
	EOC	$3/5 \cdot 0.11\ cm$
2^{nd} time loaded	BOC	$3/5 \cdot 0.11 cm$
	MOC	$4/5 \cdot 0.11\ cm$
	EOC	$0.11\ cm$
$3^{rd} - 6^{th}$ time loaded	BOC/MOC/EOC	$0.11\ cm$

Concerning the vibration pattern that the selected bundles are modelled to undergo, it is decided to select the unsynchronized lateral oscillation in both directions, based on Eq. 60 (Appendix ii), by following a sinus profile at a nominal frequency of $1.8\ Hz$. This choice is made based on the previous observations (Sec. 5.1 and Sec. 5.3), indicating that a sinusoidal fuel vibration results in a comparable neutron noise characteristics as the measured noise phenomenology (i.e. strong spectral peak at the frequency of $1.8\ Hz$, etc.).

The results of the neutron noise evolution are summarized in Fig. 79 to Fig. 90. First, the maximum neutron noise level at each simulated burnup step over the ten cycles are presented in Fig. 79 for the fast and thermal energy groups. The combination of the increasing number of vibrating assemblies (i.e. from 8 to 177 over a period of ten cycles) and the increase of vibrating amplitude over burnup results in a neutron noise level increasing trend. Similarly to the plant data, the simulated noise level increasing trend is much more pronounced at the EOC compared to the BOC operating conditions. A more careful sight on the operating conditions indicates that the neutron noise amplitude at the BOC has the tendency to be directly influenced by the boron concentration, as shown in Fig. 80. Higher boron concentration level at the BOC of cycle N_i compared to the BOC of the previous cycle N_{i-1}, results in lower neutron noise amplitude at BOC of cycle N_i compared to the noise at EOC of cycle N_{i-1}, and vice-versa. In addition, the neutron noise level seems almost identical between cycles 36 and 37. This is mainly due to the fact that the maximum number of vibrating fuel assemblies has been reached and the maximum possible induced noise from this mechanism has been established.

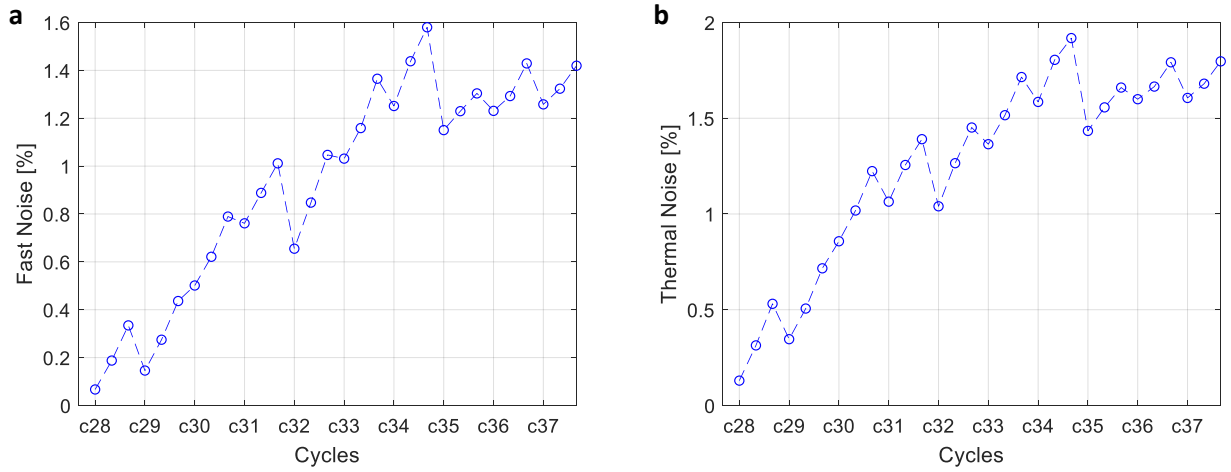

Fig. 79: Maximum fast (a) and thermal (b) neutron noise evolution based on the KKG core loading patterns in cycles **28-37**.

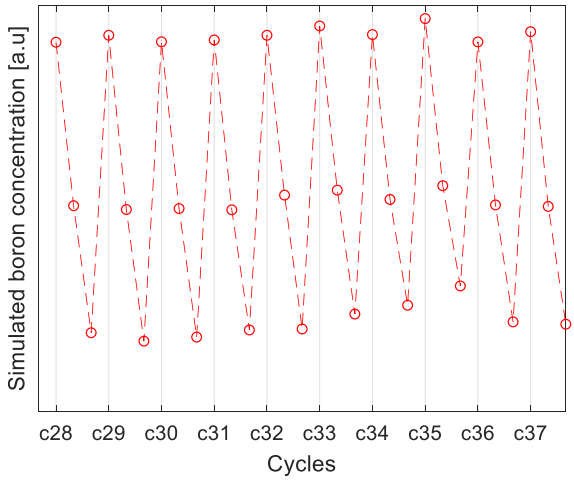

Fig. 80: Simulated boron concentration evolution based on the KKG core loading patterns in cycles **28**-**37**.

In addition, the neutron noise maps in the fast and thermal energy groups at the middle axial elevation and at the BOC of each cycle are illustrated in Fig. 81 to Fig. 90. The resulted noise maps confirm the previously obtained findings with regard to the simulated noise phenomenology: *1)* the highest noise amplitudes are observed next to the vibrating bundles and, *2)* the spatial noise phenomenology has a symmetric shape which corresponds to the quadrant-symmetric loading pattern of KKG. Moreover, the resulted neutron noise maps are in agreement with the loading pattern, as presented in Fig. 78. In other words, the noise levels increase next to the vibrating bundles. It is also observed that, more bundles of interest are loaded close to the core-periphery as the cycle number increases. Consequently, the neutron noise shape becomes stronger at the core-periphery compared to the core-center.

Even if this preliminary analysis is based on rough assumptions concerning the vibrating pattern (i.e. type and amplitude), there is a clear indication that the neutron noise level increasing trend can be related to the KKG core loading pattern and the utilization of the newer fuel bundle design, which is more susceptible to lateral vibration. The plausibility of this mechanism is further supported by the fact that the operating conditions in KKG (e.g. rated power and flow levels, inlet coolant temperature, control rod pattern, etc.) have not experienced any worth-noting modification, which would justify the neutron noise trend. Clearly, a continuation of this analysis by performing a series of sensitivity analyses using different vibration parameters and superposing the effects of other noise sources (e.g. inlet coolant parameters fluctuations, core barrel modes, etc.) will further enhance the understanding of the neutron noise evolution. The continuation of this research is already planned to be performed after the completion of this doctoral thesis.

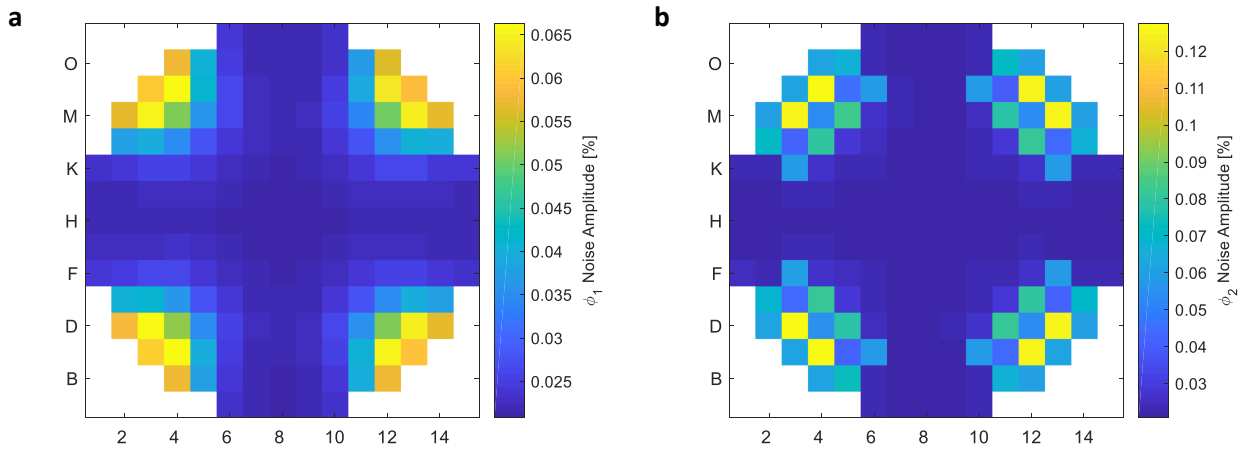

Fig. 81: Simulated fast (a) and thermal (b) neutron noise based on the KKG core loading for cycle **28**.

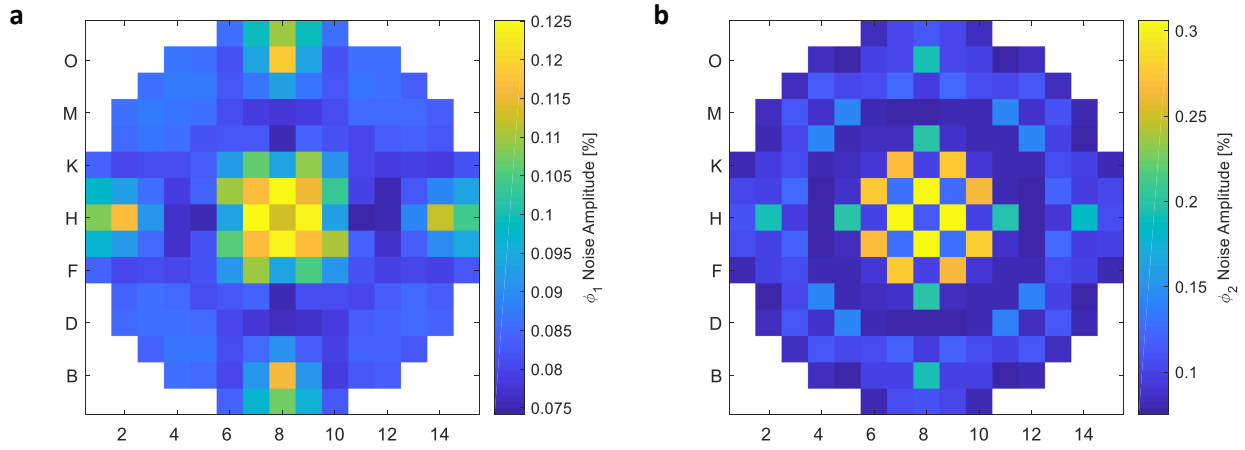

Fig. 82: Simulated fast (a) and thermal (b) neutron noise based on the KKG core loading for cycle **29**.

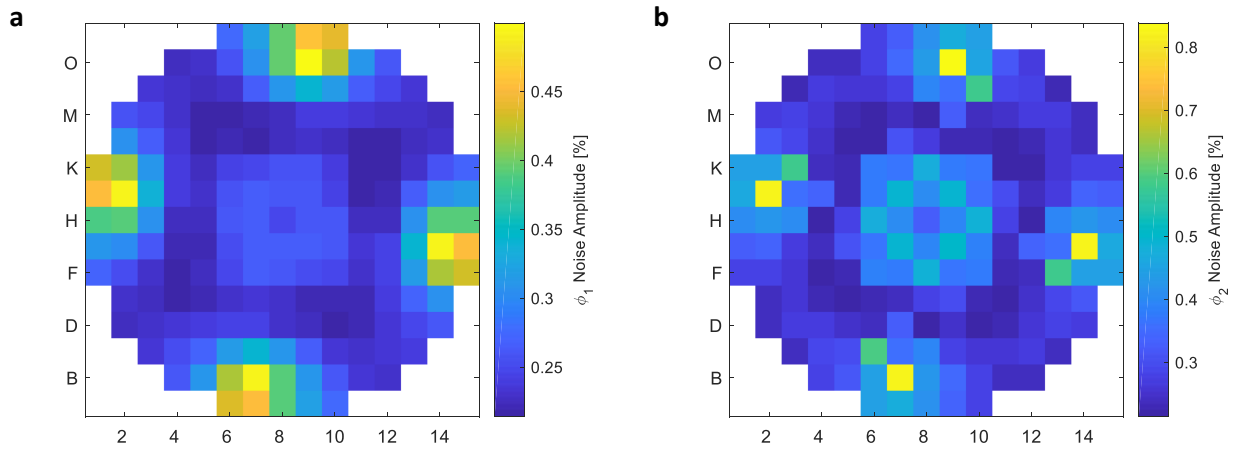

Fig. 83: Simulated fast (a) and thermal (b) neutron noise based on the KKG core loading for cycle **30**.

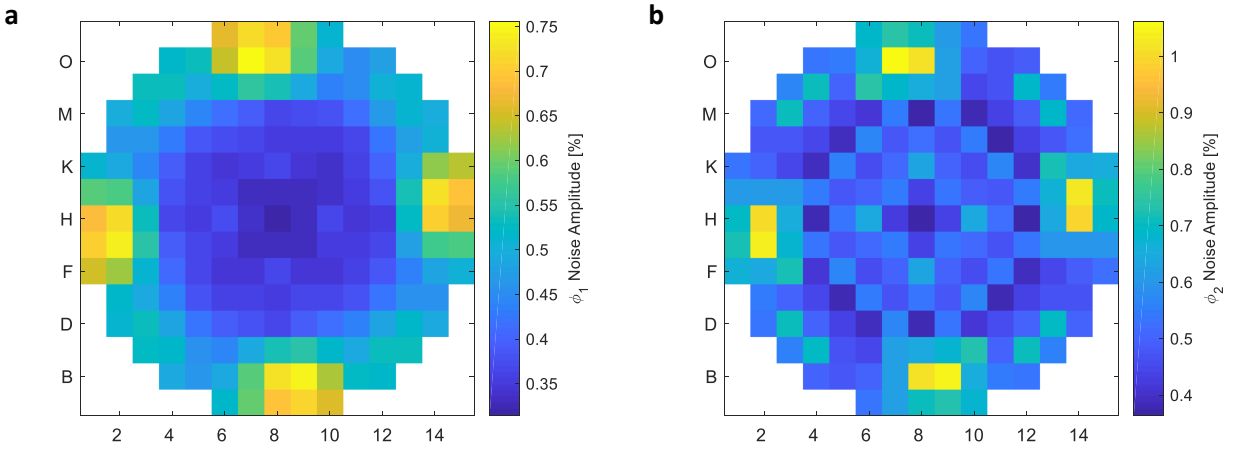

Fig. 84: Simulated fast (a) and thermal (b) neutron noise based on the KKG core loading for cycle **31**.

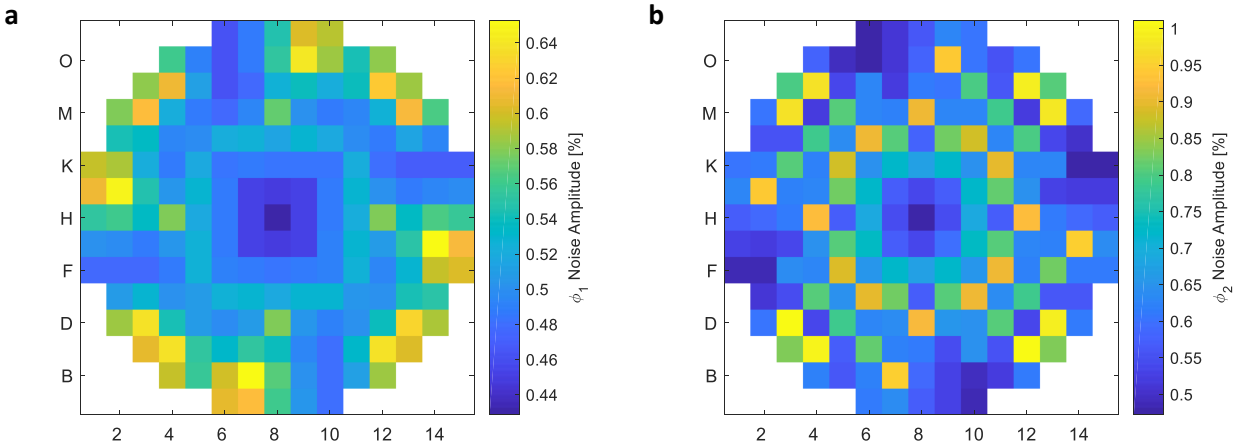

Fig. 85: Simulated fast (a) and thermal (b) neutron noise based on the KKG core loading for cycle **32**.

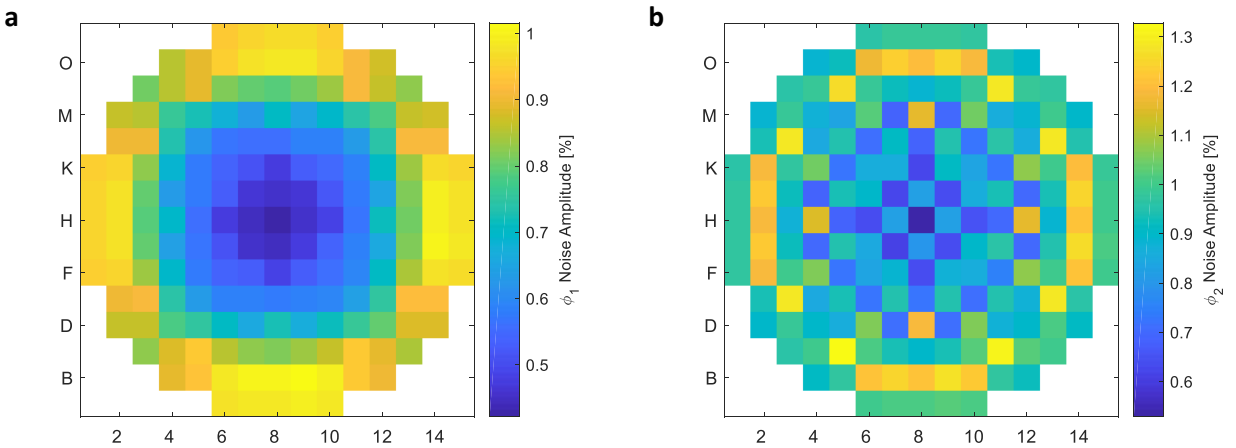

Fig. 86: Simulated fast (a) and thermal (b) neutron noise based on the KKG core loading for cycle **33**.

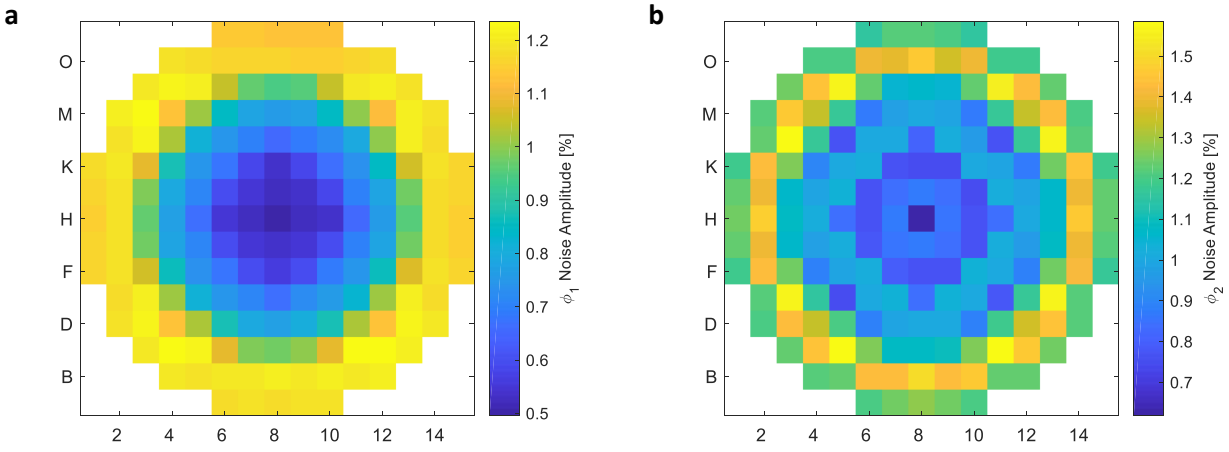

Fig. 87: Simulated fast (a) and thermal (b) neutron noise based on the KKG core loading for cycle 34.

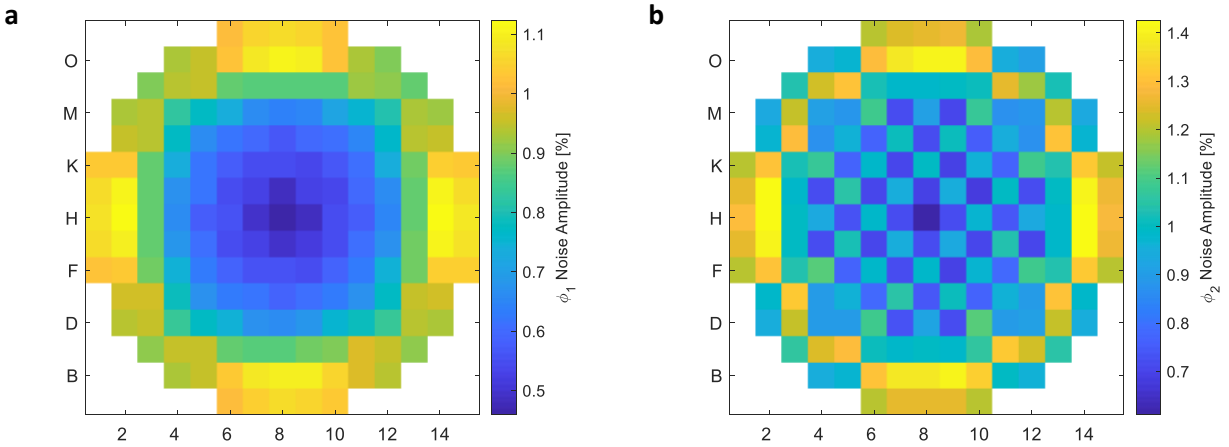

Fig. 88: Simulated fast (a) and thermal (b) neutron noise based on the KKG core loading for cycle 35.

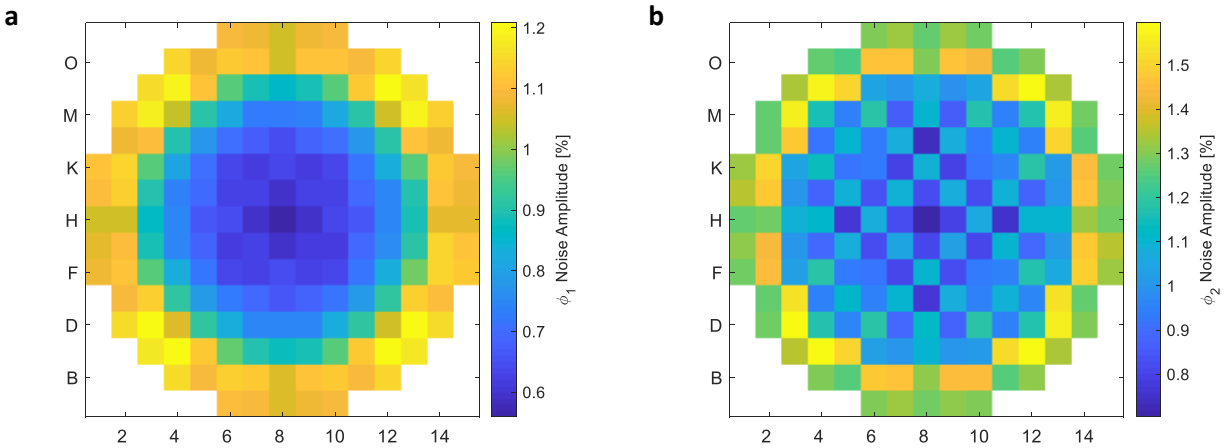

Fig. 89: Simulated fast (a) and thermal (b) neutron noise based on the KKG core loading for cycle 36.

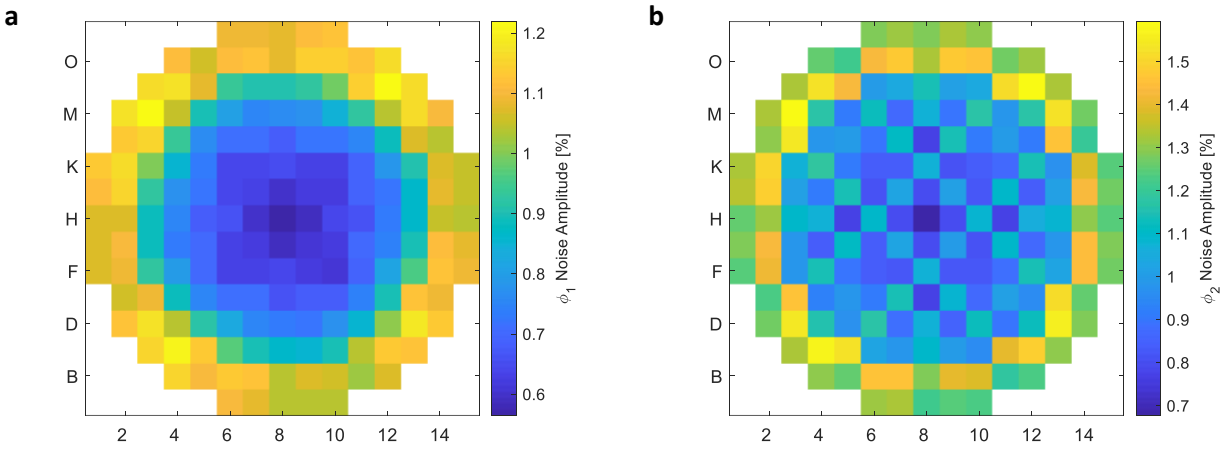

Fig. 90: Simulated fast (a) and thermal (b) neutron noise based on the KKG core loading for cycle **37**.

5.5. Conclusions and future steps

The current chapter presents a theoretical background of the neutron noise phenomenon and highlights its significant impact on reactor operation. A description of previous experience on identifying the key mechanisms that considerably affect the neutron noise phenomenology is given, followed by a literature review of the main developments on neutron noise modelling using advanced reactor physics solvers in both the time and frequency domains.

Then, the reader has been introduced to the PSI neutron noise modelling methodology that was developed in the framework of this doctoral thesis. This methodology is practically based on three main steps; *i)* the generation of nuclear data with CASMO-5 which can be used for the 3D full core simulation of fuel assembly vibration, *ii)* the modelling of noise sources using the transient nodal code SIMULATE-3K, and *iii)* the preparation of an automatized process for simulating the vibration of fuel assemblies using SIMULATE-3K.

Concerning the first step, a cross-section library is to be generated which allows the user to modify the water gap widths between adjacent fuel bundles. To this aim, the *delta gap model* in the CASMO-5 lattice code is utilized. A detailed description of the model capabilities and the cross-sections generation process is presented. In addition, a verification of the model correctness is demonstrated by comparing cross-sections data at various water gap widths against reference results generated by the probabilistic solver Serpent-2.

The *second* main step of the developed methodology emphasizes on the modelling of various types of noise sources using the 3D transient nodal code SIMULATE-3K. Even if previous works have already tackled similar modelling approaches ([14], [50]), in this thesis a systematic strategy is followed in order to model the impact of individual and combined noise sources on the neutron noise phenomenology. The modelling of thermal-hydraulics properties fluctuation (i.e. inlet coolant flow and temperature, and boron concentration) is simply defined by imposing a time-dependent perturbation on the relevant input parameter. Major emphasis is given to the elaborated description of the fuel bundles lateral vibration modelling based on the *fuel assembly vibration model*. SIMULATE-3K utilizes the cross-sections library, generated by using the delta gap model in CASMO-5, in order to mimic the lateral movement of the fuel bundles in a time-dependent manner. To this aim, the user has to impose a 3D map, which explicitly describes the water gap widths evolution between all the adjacent bundles that are involved in this dynamic process. The complexity of the input deck preparation is directly related to the number of vibrating bundles and their vibrating characteristics.

The *last* main step of the developed methodology focuses on the automatisation of the preparation of the SIMULATE-3K input deck for simulating the fuel assembly lateral vibration. To this aim, a user-friendly platform has been developed in the MATLAB environment, which allows the user to simplify the generation process of the 3D water gap widths map. The advantage of this platform is its flexibility on preparing the boundary conditions that describe any possible fuel bundles movement. By doing so, a systematic modelling of various types of vibrational patterns can be performed. The simulation of several verification studies (i.e. modelling a single node vibration up to vibrating the entire core) indicates that the developed methodology and the utilized solvers can properly model the examined mechanisms and have the capability to reproduce neutron noise phenomena.

A series of modelling scenarios have been performed with the aim to identify the resulting neutron noise characteristics that could assist in explaining the measured neutron noise phenomenology based on KKG data, presented in *chapter 2*. The main conclusions of these analyses can be summarized as follows:

- The highest neutron noise amplitudes are observed to the adjacent bundles of the vibrating fuel assemblies/cluster in the case of a synchronized vibration. This is explained by the fact that the adjacent bundles are affected the most by the water gap widths modification. In the case of unsynchronized vibration of fuel assemblies within a cluster, the maximum noise level shifts to the cluster center. This can explain the existence of core regions with higher noise levels.
- The studied simulated scenarios indicate higher neutron noise amplitudes at the core-top axial elevation.
- The modelling of fuel assembly vibrational modes (i.e. clamped free, first and second modes) results in higher noise amplitude at the axial elevation with the highest fuel displacement.
- The modelling of unsynchronized vibration within a cluster results in lower neutron noise amplitudes compared to synchronized vibration.
- The fuel assembly vibration results in a full coherence between neutron detectors, belonging to the same instrumentation tube and located at different axial elevations.
- Higher neutron noise amplitudes are observed at the core regions that are affected the most by the random fluctuation of the inlet coolant temperature (i.e. closer to the coolant loops).
- The random fluctuations of the inlet coolant flow and temperature shift the strong spectrum behavior of neutron noise in the low frequency range.
- A rapid coherence decrease (i.e. coherence dip at the sink frequency) is estimated between simulated neutron detectors positioned at the same instrumentation tube due to transport phenomena, in the case of inlet coolant temperature fluctuation.
- Inlet flow perturbations are observed to propagate instantaneously across the core.
- Inlet coolant temperature fluctuations have a dominant role compared to inlet coolant flow perturbations.
- In case of combined noise sources, it is observed that the inlet coolant temperature and flow perturbations are responsible for the neutron noise spectral phenomenology in the low frequency range (up to $2\ Hz$), whereas the fuel assembly vibration has a leading role above $2\ Hz$.

In a nutshell, the simulation studies indicate that noise sources based on the fuel assembly vibration and the random fluctuation of the inlet coolant temperature considerably affect the neutron noise phenomenology. It should be noted that, the developed PSI neutron noise modelling methodology has been used as a basis for generating simulation data-sets for the CORTEX project partners. These data set have been utilized by various

consortium partners in order to develop further improvements of their neutron noise solvers and dedicated machine learning techniques.

The ultimate goal of this chapter is to indicate the significance impact of individual noise sources on the neutron noise behavior by comparing measured against simulated data. Therefore, it has been demonstrated in this chapter that the following measured noise characteristics can be related to specific noise sources, as follows:

- The strong spectrum in the low frequency range (i.e. <2 Hz) of the measured neutron noise can be explained by the stochastic fluctuation of the inlet coolant temperature.
- The spectral peak at the frequency of 1.8-2 Hz can be related to the lateral vibration of fuel bundles at the respective frequency which corresponds to the clamped free oscillation model.
- The axial coherence rapid decrease at the frequency of 1 Hz and the strong radial and axial coherence, observed in the measured neutron noise data, could be reproduced by modelling the inlet coolant temperature fluctuation.
- The neutron noise level increase trend, observed in plant data, can be explained by the loading of the newer fuel design, which is more susceptible to lateral vibrations.

However, some neutron noise characteristics where not able to be identified based on the analyzed simulation cases. These are the axial coherence dip at 6 Hz, the axial noise distribution, the low radial coherence values at frequencies above 4 Hz, for which the cause in unknown, and the noise phenomenology related to the core barrel oscillation at 8 Hz. The noise phenomenology at 8 Hz is expected to be properly captured in a future work in which the core barrel pendular movement will be properly modelled. The continuation of this analysis through the participation of PSI/LRT in the CORTEX project intents to further examine the neutron noise characteristics, which could not be identified using the simulation results.

It is recalled that, this doctoral thesis is the first attempt to establish a consolidated and systematic neutron noise modelling methodology. Modelling limitations and areas of improvement have been identified during this work and a series of future work activities is proposed, as follows:

- A collaboration between PSI and SSP can be established in order to implement, in the SIMULATE-3K code, the MATLAB based script module, developed in the framework of this thesis, for the preparation of the water gap widths maps. By doing so, the preparation process of the SIMULATE-3K input deck for simulating fuel assembly vibration will be considerably simplified. In addition, this tool can be provided to the user community for performing similar analysis for other power plants.
- The latest development in the SIMULATE-3K for modelling the fuel bundles higher modes vibration (i.e. imposed by the user through the *KIN.ZVL* input card), has the limitation that only a single axial shape can be used for all the selected bundles. In other words, it is not possible to impose axial shapes with different characteristics at different regions of the core. That would be of particular interest in the case of modelling the real bow-shape patterns, which are varying based on the local conditions. A further improvement in the SIMULATE-3K source code would be of high interest in order to allow the described process.
- A more detailed modelling of the different vibration modes by using real core loading patterns would further assist in understanding the neutron noise phenomenon.
- The developed neutron noise modelling methodology can be used for modelling the core barrel oscillation modes (i.e. beam mode and shell mode). This can be achieved by modifying appropriately

the water gap widths between the peripheral fuel bundles and the radial reflector zone. The modelling of the core barrel modes will produce simulated neutron noise data, which would be more similar to the measured neutron noise phenomenology.

- A combination of all the possible noise sources (i.e. bundles vibrational modes, core barrel oscillation, inlet coolant parameters fluctuation) has to be systematically studied in a further analysis in order to enhance the understanding of the neutron noise phenomenology.
- Peculiar simulated results (e.g. as the low radial coherence at low frequencies in the combined scenario of inlet coolant flow fluctuation and fuel assembly vibration; Sec. 5.2.2, etc.) could be further analyzed via sensitivity studies.
- Source code modifications of SIMULATE-3K can allow the modelling of a time dependent fluctuation of the inlet coolant flow at each fuel assembly. By doing so, local fluctuations of the core flow can be modelled at the assembly inlet.
- Ultimately, further verification and validation studies can be performed in order to compare the simulated results of the SIMULATE-3K code against the already validated CORE SIM code, which is a dedicated neutron noise solver in the frequency domain. In addition, the point-kinetic component of the simulated neutron noise response in SIMULATE-3K can be compared against a recently developed analytical formulation, and therefore, the PSI neutron noise modelling methodology can be further validated [62].
- The current version of the SIMULATE-3K fuel vibration model can be applied only on PWR cores. However, a modelling extension for BWR applications would be beneficial for both the research community and the industry. For instance, it is known that laterally vibrating fuel channels affect the in-core detectors signals in BWRs (i.e. LPRMs) and can deteriorate the response of the transverse in-probes (i.e. TIPs), used for the calibration of the in-core monitoring system and the verification of the nodal simulators.

Chapter 6: Advanced Signal Analysis Techniques for Causality Analysis

The systematic monitoring of the neutronic and thermal-hydraulic processes is of key importance for the surveillance of the safe operation of a nuclear reactor. The utilization of standard signal analysis techniques in both the time and frequency domains reveals the reactor signals characteristics under normal and transient conditions. However, the traditional techniques cannot provide a reliable and detailed information about the signals interconnectivity patterns and the identification of the cause-and-effect relationships that could assist in the localization of perturbation sources that might affect the safe reactor operation. To this aim, this chapter introduces the so-called causality analysis techniques in order to investigate the dynamical causal interconnections between the nuclear reactor processes. The ultimate goal of this chapter is to demonstrate the capabilities and the limitations of the causality analysis on estimating the reactor signals links and to identify the connectivity patters between the reactor processes during normal dynamical scenarios as well as during the occurrence of anomalies. Therefore, causality analysis can be used as a complementary tool for enhancing the understanding of the reactor operation and to assist for a safer core operation.

This chapter is based on the analyses performed in the following papers:

- D. Chionis, A. Dokhane, H. Ferroukhi, A. Pautz, "*On causality analysis of nuclear reactor noise using partial directed coherence*", Proceedings of the 2016 International Conference on the Reactor Physics (Physor '16), Sun Valley, ID, USA (2016) [100].
- D. Chionis, A. Dokhane, H. Ferroukhi, A. Pautz, "*Application of causality analysis on nuclear reactor systems*", CHAOS, vol. 29, issue 4 (2019) [101].
- D. Chionis, A. Dokhane, H. Ferroukhi, A. Pautz, "*Spatial localization of perturbation propagation in LWRs using causality and connectivity analysis*", Proceedings of the 2019 International Conference on Mathematics & Computational Methods Applied to Nuclear Science and Engineering (M&C '19), Portland, OR, USA, (2019) [102].

6.1. Introduction on causality concept

Historically, the term *cause* is encountered for the first time in the 5^{th} century BC in the *Hippocratic Corpus* (i.e. a collection of ancient Greek medical documents) in order to explain the status of a medical condition based on the observations and examinations made by the physicians. One century later, the ancient Greek philosopher *Aristoteles* continued the study of the *causality* concept in his books *Physics*, *Metaphysics*, and *Posterior Analytics*. His motivation was to enhance the understanding of how nature works by trying to answer *why* a specific action or process is occurring. To this aim, Aristoteles introduced the analytical concept of the so-called *four causes* (i.e. material, formal, efficient, and final causes)[30] which are able to identify and explain the cause of an action. The Aristotelianism principle of causation is the backbone of all fields, since science and research always try to explain the root-cause of an observed behavior or action. Consequently, the study

[30] As an example, the *cause of the existence of a bridge* is the following, according to Aristoteles' concept of *four causes*: A bridge is solid because it is made of bricks (*material cause*), it has a stable structure and it is resistant to earthquakes because it is constructed to have a specific robust design (*formal cause*), it has this form because the engineer build it in such a way (*efficient cause*), and it is functional because it helps people and vehicles to move from one side to the other (*final cause*).

of a phenomenon focuses on the cause-and-effect relationships between the involved processes and on understanding how the information is propagating within a system. In addition to the Aristotelian philosophy, the importance of the root-cause concept has been also raised by the ancient Greek philosopher *Plutarch* at the end of the 1^{st} century AD. The "*chicken and the egg*" philosophical dilemma is discussed in Plutarch's collection *Moralia* with the intention to focus on processes for which it is not straightforward which has the role of a *first cause* and which the role of an *effect*. This causality paradox highlights in an intuitively simplified way the complexity of the interconnectivity patterns that might exist between the analyzed processes. The philosophical explorations on understanding the origin of nature and the meaning of life using the causality concept were further developed and matured during the Roman times (e.g. *Cicero*, etc.) and the Renaissance (e.g. *R. Descartes*, *B. Spinoza*, etc.).

Philosophy and science were always closely related to each other, and therefore, the use of the philosophical concept of causality in order to analytically study the causal interactions between processes was just a natural consequence. Even though, a unique and catholic accepted definition of causality does not exist [103], in common sense, the term causality is interpreted as the interrelation between two processes (the cause and the effect). The first attempt to estimate the level of interconnection between processes has been performed via the well-known *correlation* and *coherence analyses* in the time and frequency domains, respectively. Both measures estimate the level of synchronization between two signals based on their linear dependencies. The correlation function is commonly expressed using the Pearson correlation coefficient, as shown in Eq. 24.

$$r_{xy} = \frac{1}{N}\sum_{i=1}^{N}\frac{(x(i)-\mu_x)\cdot(y(i)-\mu_y)}{\sigma_x \cdot \sigma_y} \qquad \textbf{Eq. 24}$$

where, μ and σ are the mean value and the standard deviation of two signals x and y, and N is the sample size. The correlation function provides a quick estimation of the level of instantaneous dependency between two signals, without though allowing any assessment on the direction of interconnection (i.e. does signal x cause the behavior of signal y, or vice versa). In other words, the correlation function is an *undirected measure*. However, using the cross-correlation function, as introduced in Eq. 3, it is possible to calculate the time shift between a pair of signals, and therefore, a first estimation of the causal behavior of the two processes can be performed.

The correlation results are easy to be interpreted since they are defined in the time domain and they estimate how strong two signals are correlated. It is important to note that, many systems are rich in oscillatory content, and therefore, their study in the frequency domain reveals additional information about their structure. The coherence function, defined in Eq. 5, is the counterpart of the correlation function in the frequency domain, and it is commonly used for estimating the spectral power in a given frequency component, common for both analyzed signals [104]. As stressed in chapter 2, the coherence function is a powerful signal processing tool because it can estimate, without the need of high computation power, if there is a strong dependency between two signals by quantifying the strength of the link between their oscillatory components [46]. The coherence function, similarly to the correlation function, is expressed as a bivariate reciprocal estimator (i.e. $Coh_{xy}(f)$=$Coh_{yx}(f)$) that cannot distinguish between direct and indirect causal interactions (i.e. whether two signals x and y are connected between each other directly or a third signal z interferes between them). In order to overcome this limitation, the *partial coherence function* was introduced in order to evaluate the level of coherence between two signals after the removal of the influence of all other signals in the system [105].

The first step for the estimation of the partial coherence function is the calculation of the CPSD matrix (Eq. 25), containing the pairwise CPSDs of all the m-signals of the analyzed system.

$$P(f) = \begin{bmatrix} P_{11}(f) & \cdots & P_{1m}(f) \\ \vdots & \ddots & \vdots \\ P_{m1}(f) & \cdots & P_{mm}(f) \end{bmatrix} \quad \text{Eq. 25}$$

Then, the minor $M_{ij}(f)$ of $P(f)$ is calculated for each pairwise combination. The matrix $M_{ij}(f)$ is defined as the determinant of matrix $P(f)$ when the i^{th} row and the j^{th} column are removed. Last, the pairwise partial coherence function is defined as:

$$PCoh_{ij}(f) = \frac{\left|M_{ij}(f)\right|^2}{M_{ii}(f)M_{jj}(f)} \quad \text{Eq. 26}$$

The partial coherence has the advantage of differentiating the direct from indirect interactions in the frequency domain, and therefore, the understanding of the structural interconnectivity within a system can be enhanced. However, the limitation of the undirected character of this measure remains, since no information about the direction of interaction between signals can be extracted (i.e. $PCoh_{ij}(f)$=$PCoh_{ji}(f)$).

The use of standard signal processing techniques (e.g. correlation and coherence function, etc.) provides important information about the signals relationships (and how statistical significant is the signals correlation), but it is clearly observable that they cannot be utilized for a reliable estimation of the causal interactions and the identification of a root-cause. It is recalled that, the phrase "*correlation does not imply causation*" is commonly used in the field of signal analysis for highlighting the inability of the standard techniques to indicate cause-and-effect relationships between signals. The limitation of standard signal analysis techniques on estimating the signals causal interactions has been overcome by the development of advanced statistical techniques. The most important attempt for a mathematical formulation of the *causality concept* has been proposed by the Nobel Prize winner Sir Clive Granger. Granger fundamentally changed the way that econometric and stock market data are treated, by identifying causal relationships between time series. He argued that, a time series "Y_t *is causing* X_t *if we better able to predict* X_t *using all available information that if the information apart from* Y_t *had been used*" [11]. The so-called *granger-causality* formulation intended to enhance the understanding of the directional causation that was not able to be studied using traditional signal analysis techniques (i.e. cross-correlation and cross-spectral methods). Granger-causality gained quickly popularity since it has a simple mathematical formulation that can be easily implemented in computer codes, and most importantly, it can robustly distinguish the dominant role of one process within multi-variate analyzed systems. Consequently, granger-causality started to be applied in many areas of science, such as in physiology, brain connectivity, biology, and engineering for extracting key causal interactions between the analyzed systems. The significant improvement of signal acquisition techniques (i.e. simultaneous measuring of multiple processes at high sampling frequency) and the high interest on understanding the functionality of the human brain revealed quickly some limitations of granger-causality on identifying the causal interactions when the analyzed system becomes large and the processes have a highly complicated interconnectivity pattern. In order to overcome these issues, many *causality measures* based, to some extent, on the granger-causality concept have been developed, aiming for the study of multi-variate systems by inferring reliably the underlying causal interactions. This doctoral thesis is emphasizing on the use of the *partial directed coherence (PDC)*, *renormalized partial directed coherence (rPDC)*, and *directed transfer function (DTF)* estimators, which are some of the most eminent causality measures with frequent and successful applicability on various

scientific areas. In the following sections, the modelling of a system using linear multi-variate autoregressive techniques, being the backbone of the causality analysis, is briefly described, followed by a detailed introduction and discussion of the above-mentioned causality measures. Finally, the connectivity methodology being developed at PSI in the framework of this work is presented, and then the effectiveness of causality analysis is demonstrated through several simulated and measured nuclear reactor data sets.

The goal of the current chapter is to demonstrate the capability of the causality analysis techniques to reliably infer the cause-and-effect connections between nuclear reactor processes and to identify the root-cause of simulated disturbances or measured anomalies. Most importantly, this chapter presents a complementary method for analyzing the nuclear reactor signals and for extracting key connectivity patterns, which could assist the nuclear research and the nuclear reactor operators to enhance their understanding of the underlying mechanisms in a nuclear reactor.

6.2. Multi-variate autoregressive modelling

As stated previously, standard signal analysis techniques commonly focus on estimating the statistical quantities of individual signals (i.e. mean value, standard deviation, signal to noise ratio, etc.), and on the level of synchronization between signals pairs via the correlation and coherence functions. These single- and bi-variate methods can provide important information about the signals characteristics. However, real systems are typically quite complicated and they involve processes, which are highly coupled between each other. In such cases, the single- and bi-variate analysis techniques cannot be used for inferring causal influences between the signals. These limitations can be overcome using multi-variate models.

In multi-variate analysis, a set of simultaneously recorded signals is analyzed in order to identify, in a holistic approach, the system characteristics and behavior. The analysis of a multi-variate system contains more information about both the analyzed system structure and the signals interdependencies, compared to what the analysis of individual signals can provide. Multi-variate linear regressive methods have been extensively applied in many research areas (e.g. biomedical research, econometrics, process engineering, geophysics, etc.) in order to analyze multi-variate systems. The broadly used parametric approach of multi-variate linear autoregressive (MVAR) modelling is an effective method for characterizing with high spatial and frequency resolution the causal relations between different signals [106]. For a set of m simultaneously observed stationary signals, $\boldsymbol{y}(t) = [y_1(t), y_2(t), \dots, y_m(t)]^T$, a MVAR model is defined as:

$$\boldsymbol{y}(t) = \sum_{k=1}^{p} \boldsymbol{\alpha}(k) \cdot \boldsymbol{y}(t-k) + \boldsymbol{\varepsilon}(t) \qquad \text{Eq. 27}$$

where $\boldsymbol{\varepsilon}(t) = [\varepsilon_1(t), \varepsilon_2(t), \dots, \varepsilon_m(t)]^T$ is the vector containing the uncorrelated multi-variate white noise (Gaussian) at time t with a zero mean value and covariance $var\{\varepsilon\}$, and $\boldsymbol{\alpha}(k)$ is the two dimension $[m\ x\ m]$ MVAR model parameters matrix at time lag k=1, …, p:

$$\alpha(k) = \begin{pmatrix} \alpha_{11}(k) & \cdots & \alpha_{1m}(k) \\ \vdots & \ddots & \vdots \\ \alpha_{m1}(k) & \cdots & \alpha_{mm}(k) \end{pmatrix} \qquad \text{Eq. 28}$$

The $\boldsymbol{\alpha}(k)$ model coefficients indicate the variable dependencies between the analyzed signals at time lag k. Therefore, Eq. 27 expresses the present value of a signal $y_i(t)$ as a function of the p past time steps of all the simultaneously observed processes, and the MVAR model coefficients $\alpha_{ij}(k)$ describe the linear prediction of

the y_j signal at time lag k on predicting the current value of y_i. In other words, the model coefficients $\alpha_{ij}(k)$ can be thought as a measure of the level of dependency of the signal y_i from a second signal y_j at the time step k.

The goal of the MVAR modelling is to derive the model coefficients $\boldsymbol{\alpha}(k)$ for the minimum model order by minimizing the prediction error. Therefore, the MVAR modelling can be split in two steps; *first*, the estimation of the minimum model order p, and *second*, the estimation of the model coefficients $\boldsymbol{\alpha}(k)$ for time steps k=1, … , p. The accurate fitting of the MVAR model on the multi-variate system $y(t)$ determines the precise estimation of the causal interactions between the observed signals. The MVAR modelling methodology that is used throughout this work is described in more details in the following paragraphs.

6.2.1. MVAR model order estimation

The first step of the MVAR modelling is the estimation of the model order p, which is of highest importance, as it determines how many time steps are needed to be taken into account for the accurate fitting of the MVAR model and for minimizing the prediction error as compared to the original time series dataset. Various algorithms, the so-called *information criteria*, have been presented in the literature for the estimation of the model order of the MVAR model. The information criteria that are used are, generally, composed of two terms; the first term characterizes the model prediction error, and the second term characterizes the number of freely estimated model parameters [107]. The model order estimation objective is to optimally balance both terms of the selected information criteria in order to avoid overfitting the data set. However, when the model order is very small there is a risk that the MVAR model cannot describe adequately enough the signal components [106].

The approach for selecting the optimum model order is as follows. Initially, a maximum number of time lags K is defined by the user. Then, the time series dataset is fitted to a MVAR model using a given MVAR fitting algorithm (as presented in the next section) for time lags k=1. A series of information criteria are employed to estimate how precise was the fitting. Therefore, each information criterion results to a value for the time lag k=1. The same process is repeated for time lag k=2, … , K. Consequently, each information criterion shows the level of accurate fitting for a given MVAR algorithm as a function of time lags k=2, … , K. The time lag k, which gives the minimum value among all the utilized information criteria results to the model order p.

The most commonly used information criteria for the model order selection are the following. More detailed description of the utilized criteria could be found in [4].

Bayesian Information Criterion (BIC)

$$SBC(k) = \ln\left|\tilde{\Sigma}(k)\right| + \frac{\ln(\hat{T})}{\hat{T}} km^2 \qquad \text{Eq. 29}$$

Akaike Information Criterion (AIC)

$$AIC(k) = \ln\left|\tilde{\Sigma}(k)\right| + \frac{2}{\hat{T}} km^2 \qquad \text{Eq. 30}$$

Final Prediction Error Criterion (FPE)

$$\ln(FPE(k)) = \ln\left|\tilde{\Sigma}(k)\right| + m \cdot \ln\left(\frac{\hat{T} + mr + 1}{\hat{T} - mr - 1}\right) \quad \text{Eq. 31}$$

Hannan-Quinn Criterion (HQ)

$$HQ(k) = \ln\left|\tilde{\Sigma}(k)\right| + \frac{2\ln\left(\ln\left(\hat{T}\right)\right)}{\hat{T}} km^2 \quad \text{Eq. 32}$$

All the information criteria have the same expression as a first term, which is the logarithm of the residual covariance matrix of the estimated noise ($\ln\left|\tilde{\Sigma}(k)\right|$). In other words, the first term can be seen as a reward for minimizing the residual variance of the MVAR fitted model compared to the time series dataset [104]. The main differentiation between the above-listed information criteria is related to the second term, indicating how each algorithm penalizes the overfitting of the MVAR model (as the model order increases the model free parameters increase too) [107]. The information criterion selection mainly depends on the size of the data set $\hat{T}$=mN_m (i.e. N_m are the data points per signal, and m is the total number of signals). For small data sets, the AIC and FPE criteria have been shown to exhibit a better performance, whereas the BIC and HQ criteria are more consistent estimators with broader applicability [108]. In the current work, all the above-listed criteria are utilized, and finally the selected information criterion is the one that results in the minimum model order (p_{sel}).

6.2.2. MVAR algorithm fitting

The next step of the MVAR modelling focuses on the concluding estimation of the $\boldsymbol{\alpha}(k)$ model coefficients, based on the model order p, which give valuable information about the information interconnections between the analyzed signals, as they describe the dependencies between the time series. Therefore, their accurate estimation has an important role in MVAR analysis. Several algorithms have been developed over the years for the direct estimation of the MVAR model coefficients from the time series dataset. These algorithms are time efficient and robust and they are based on the principle of minimizing the prediction error. The most commonly used algorithms are presented in the following paragraphs. The interested reader can find more information and detailed derivation of the utilized algorithms in [4].

Vieira-Morf method

A. Vieira and M. Morf proposed a multichannel version of the geometric algorithm for evaluating the autoregressive parameters $\boldsymbol{\alpha}(k)$ by estimating the partial correlation $PC(k)$ in the time domain [4]:

$$\widehat{PC}(k) = \left(\hat{P}_f(k-1)^{1/2}\right)^{-1}\left(\hat{P}_{fb}(k-1)\right)\left(\hat{P}_b(k-1)^{1/2}\right)^{-H} \quad \text{Eq. 33}$$

where, $k \in [1, p_{sel}]$ is the number of time lags, and p_{sel} is the selected model order, evaluated during the model order selection step. The superscript *H* indicates the conjugate transpose of the matrix. This partial correlation estimate expression is based on the estimate of the covariance of the driving noise process (residual variance, $\hat{P}_f$), on the estimate of the covariance of the driving noise process for the backward AR process ($\hat{P}_b$), and on their cross correlation ($\hat{P}_{fb}$). These three estimates are defined as:

$$\hat{P}_f(k-1) = \frac{1}{N_m} \sum_{n=k+1}^{N_m} e_f[n]\, {e_f}^H[n] \quad \text{Eq. 34}$$

$$\hat{P}_b(k-1) = \frac{1}{N_m} \sum_{n=k+1}^{N_m} e_b[n-1]\, {e_b}^H[n-1] \quad \text{Eq. 35}$$

$$\hat{P}_{fb}(k-1) = \frac{1}{N_m} \sum_{n=k+1}^{N_m} e_f[n]\, {e_b}^H[n-1] \quad \text{Eq. 36}$$

where, e_f and e_b are the forward and backward linear prediction errors for a data sample range $n \in [k{+}1, N_m]$, which are updated at each time lag $k \in [1, p_{sel}]$ using appropriate recursion formulas in order to minimize the prediction error. The (forward) MVAR coefficient matrix $\boldsymbol{\alpha_{ij}}(k)$ is then calculated based on the Viera-Morf method as:

$$\boldsymbol{\alpha}_{ij}(k) = -\left(\hat{P}_f(k-1)^{\frac{1}{2}}\right) \widehat{PC}(k)\left(\hat{P}_b(k-1)^{1/2}\right)^{-1} \quad \text{Eq. 37}$$

Nuttall-Strand algorithm

A. Nuttall and O. Strand [4] proposed an alternative algorithm for the MVAR model coefficients $\boldsymbol{\alpha}(k)$ estimation, very similar to the Vieira-Morf method. The Nuttall-Strand algorithm is based on the estimation of the residual cross correlation $CC(k)$ instead of the partial correlation $PC(k)$. For the estimation of the residual cross correlation, the Nuttall-Strand algorithm uses the following expression:

$$\hat{P}_f(k-1)\left(P_f(k-1)\right)^{-1} \widehat{CC}(k) + \widehat{CC}(k)\left(P_b(k-1)\right)^{-1} \hat{P}_f(k-1) = -2\hat{P}_{fb}(k-1) \quad \text{Eq. 38}$$

The above equation is a bilinear matrix equation in the formulation of a Sylvester equation of the form $AX{+}XB{=}C$. The Sylvester equation can be numerically solved in MATLAB using the continuous Lyapunov equation solution function (i.e. *X=lyap(A, B, C)*). The resulted estimate of the residual cross correlation $CC(k)$ is a matrix with $[m\ x\ m]$ dimensions. Finally, the (forward) MVAR coefficient matrix $\boldsymbol{\alpha}(k)$ is then calculated based on the Nuttall-Strand algorithm as:

$$\boldsymbol{\alpha}_{ij}(k) = -\widehat{CC}(k)\left(P_b(k-1)\right)^{-1} \quad \text{Eq. 39}$$

Least Squares estimation

One of the most frequently used methods is the algorithm of least squares estimation. This method estimates the MVAR model coefficients by minimizing the squared discrepancies between the recorded data and their expected values. The (forward) MVAR coefficients are calculated using the following expression:

$$\boldsymbol{A}_p \boldsymbol{R}_p = \begin{pmatrix} P_f & 0 & \dots & 0 \end{pmatrix} \quad \text{Eq. 40}$$

where, the multi-channel coefficients are expressed via Eq. 45, and the matrix $\boldsymbol{R}_p$ is calculated based on Eq. 42 and has entries as given in Eq. 43.

$$\boldsymbol{A}_p = \begin{pmatrix} I & \boldsymbol{\alpha}_{ij}(1) & \dots & \boldsymbol{\alpha}_{ij}(p) \end{pmatrix} \quad \text{Eq. 41}$$

$$\boldsymbol{R}_p = \begin{pmatrix} \boldsymbol{R}_y(0,0) & \boldsymbol{R}_y(0,p) \\ \boldsymbol{R}_y(p,0) & \cdots \boldsymbol{R}_y(p,p) \end{pmatrix} \quad \text{Eq. 42}$$

$$\boldsymbol{R}_y = \sum_{t=p+1}^{N_m} \boldsymbol{y}(t-i)\boldsymbol{y}^H(t-j) \quad \text{Eq. 43}$$

ARfit

ARfit, introduced in 2001, is a collection of MATLAB modules for modelling multi-variate time series and estimating the autoregressive model parameters [109]. The ARfit module estimates the MVAR model coefficients by using the stepwise least squares algorithm, introduced in [110].

An extensive and systematic comparison of the above-mentioned algorithms has been performed in [111] with the goal to evaluate the best algorithm resulting in MVAR model coefficients with smaller prediction error and with the most robust and accurate estimates. This comparison has shown that the Nuttall-Strand algorithm yields to better results compared to all the other methods even when the data sample is relative short, and therefore, it is used, throughout this doctoral thesis, as the default MVAR algorithm for estimating the $\boldsymbol{\alpha}(k)$ MVAR model coefficients. It should be emphasized that, one important concern in MVAR modelling is whether sufficient data points are available to accurately fit the model [107]. In order to have a MVAR model with good statistical relevance, the total number of data points mN_m shall be larger (ideally by one order of magnitude) than the number of model parameters, as suggested in the literature [112]. The total number of model parameters (free parameters) is defined as m^2p.

6.3. Causality measures

In the previous section, all the necessary steps, required for fitting a set of multiple simultaneously recorded signals into a linear MVAR model, have been introduced. The purpose of the MVAR modelling is to estimate the model coefficients $\boldsymbol{\alpha}(k)$ that describe the linear dependencies between the analyzed processes in the time domain. The model coefficients, $\boldsymbol{\alpha}(k)$, give a preliminary indication about the signals interconnectivity. Several statistical techniques, based to some extent on the Granger-causality concept, have been developed and reported in the literature in order to estimate the causal interconnections between the analyzed processes using the model coefficients $\boldsymbol{\alpha}(k)$. A comprehensive overview and comparison between the various causality measures that have been developed in the time or in the frequency domains can be found in ([106], [112]–[114]). In this work, emphasis is given to those causality measures that are mathematically formulated in the frequency domain, rather than performing similar analyses in the time domain (i.e. transfer entropy, etc.). This is mainly due to the fact that, the nuclear reactor system, being the focal point of this work, is rich in oscillatory contain, and therefore, the causal interconnectivity pattern at specific frequencies are of highest importance.

It should be emphasized that, the analysis of a multi-variate system in terms of causality measures can be challenging, since spurious and erroneous conclusions can be made if the quality of the analyzed data set is poor. In other words, the causality analysis results must be carefully assessed and critically judged according to the physical mechanisms, governing the analyzed system. More specifically, on the one hand, misleading

conclusions about the true cause-and-effect interactions can be made if key parameters or even the true root-cause of a perturbation are missing from the analyzed system. In this context, the causality analysis will still manage to capture the information flow paths within signals, which are highly coupled, and it will point out the first available parameter, directly affected by the missing root-cause signal. On the other hand, the detection of root-cause might be deteriorated when high number of simultaneously analyzed signals are analyzed, leading to erroneous results about the connectivity pattern [115]. Moreover, another factor that might affect the reliability of the causality results is the noise content, in the signals, which was found to lead to wrong connectivity patterns and identification of spurious coupling behavior [116]. This limitation can be overcame by differentiating the noisy content from the real signal, or by estimating the MVAR parameters using advanced state space modelling approaches [116]. Spurious interconnections can be estimated also if the measured signals have a short duration and with a low sampling frequency, leading to low measurement resolution ([117], [118]). In addition, it should be emphasized also that, the causality measures, used in the current work, are based on a linear modelling of the analyzed system. In other words, non-linear directional influences within a multi-variate system might be difficult to be inferred unless a kernelized version of the PDC measure is used [119]. It can be concluded therefore that, the causality analysis shall not be treated as a *black box*, but on the contrary, an intermediate step is necessary in which a systematic and detailed post-processing of the measured processes must be performed in order to identify the key signals of the analyzed system, leading to a minimization of the erroneous interpretation of the causality results.

The following sections describe, in more detail, the PDC, rPDC, and DTF causality measures that have been defined and frequently applied in neuroscience for studying the human brain connectivity patterns. All these measures, in contrast to the coherence and correlation functions, can be applied in multi-variate systems by identifying the direction of interaction (i.e. non-reciprocal measures). This work likens the structure of a nuclear reactor with that of a human brain, and tries to infer the causal interactions between reactor processes in a similar way as neuroscientists estimate how the information flows through the human neurons using the causality measures.

6.3.1. PDC: partial directed coherence

The PDC statistical measure has been introduced in [120] to provide a spectral formulation of the Granger-causality concept in the multi-variate domain. The novelty of PDC is its capability to differentiate direct from indirect directional interactions. In other words, the PDC measure can identify whether or not an intermediate process z interferes between a driving signal x and a sink signal y (Fig. 91). This *direct directionality* nature of PDC is clearly important when the root-cause of a perturbation is investigated.

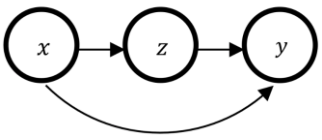

Fig. 91: Simple three-variate system. The activation signal x interacts with signal y in a direct or indirect (through the intermediate signal z) way.

The derivation of the PDC measure starts with the Fourier transformation of the previously estimated MVAR model coefficients $\boldsymbol{\alpha}(k)$:

$$\boldsymbol{A}_{ij}(f) = I - \sum_{r=1}^{p} \boldsymbol{\alpha}_{ij}(r) e^{-2\pi f r\sqrt{-1}} \quad \text{Eq. 44}$$

where, I is the $[m\ x\ m]$ identity matrix. Then, the PDC measure is simply defined as the frequency dependent causal interaction of a source signal y_j to a sink signal y_i, over all the causal interactions of y_j within the system (including itself). The mathematical formulation of the normalization, used for the derivation of the PDC measure, is expressed by Eq. 45:

$$PDC_{ij}(f) = \frac{\left|\boldsymbol{A}_{ij}(f)\right|}{\sqrt{\sum_{q=1}^{m}\left|\boldsymbol{A}_{qj}(f)\right|^2}} \quad \text{Eq. 45}$$

In other words, the PDC measure expresses the influence of a signal y_j on a signal y_i with respect to the influences of signal y_j on all the signals of the analyzed system. The calculation of the PDC measure is rather simple and it does not require significant computational resources since it is directly depending on the model coefficients $\boldsymbol{A}(f)$. The PDC results take values between 0 (i.e. full absence of causal interaction from one signal to the other) and 1 (i.e. clear indication of direct causal relationship from one signal to the other) due its normalization scheme definitions (Eq. 45). The interpretation of causal interactions in terms of the PDC results is straightforward; a direct causal interaction from a signal y_j to a signal y_i at a frequency f exists, if and only if $PDC_{ij}(f)>0$. It is important to emphasize that, in contrast to the correlation and coherence functions, all the causality expressions based on the granger-causality concept have a non-reciprocal nature. Consequently, the direction of the interaction can be estimated using the PDC results (i.e. $PDC_{ij}(f)\neq PDC_{ji}(f)$).

6.3.2. rPDC: renormalized partial directed coherence

PDC is one of the most frequently utilized causal estimator with an extended applicability in many scientific areas. The PDC measure serves commonly as a first candidate for analyzing the causal interactions within multi-variate systems due to its simple formulation and its rigorous interpretation of the existence of a causal interaction at a specific frequency (i.e. $PDC_{ij}(f)>0$). Despite these advantages, several drawbacks have been identified in the literature, related to the PDC formulation, and consequently, makes it harder to conduct clear conclusions about the causal interactions of the analyzed system ([105], [118], [121]). First, the PDC measure estimates the strength of direct influences with respect to a given signal, and therefore, no clear conclusions can be made about the coupling strength at different frequencies (i.e. $PDC_{ij}(f)$ compared to $PDC_{ij}(f')$) or between different pairs of signals (i.e. $PDC_{ij}(f)$ compared to $PDC_{kq}(f)$). In addition, the PDC formulation depends on the scale/units of the measured signals. In other words, the PDC results might be misleading if the analyzed signals are of different nature (i.e. system that includes neutron detector signals and process responses, etc.) and have not been normalized and standardized to a common scale. Last, the PDC calculations are independent of the signals APSDs, and therefore, it is possible to observe high PDC values at a frequency with low spectral value. As a result, difficulties can be introduced on interpreting the causal interactions.

In order to overcome these limitations and to avoid interpretability issues, a modified version of the PDC measure has been proposed, namely the rPDC [121]. The rPDC measure is based on a different normalization scheme compared to the PDC measure, in order to evaluate not only the direct causal interactions but more importantly to estimate the strength of the directed connections within the analyzed multi-variate system.

The derivation of the rPDC measure requires the estimation of the two-dimensional vector $\boldsymbol{Z}_{ij}(f)$, consisting of the real and imaginary part of the transformed MVAR model coefficients $\boldsymbol{A}_{ij}(f)$.

$$\boldsymbol{Z}_{ij}(f) = \begin{pmatrix} Re\ \boldsymbol{A}_{ij}(f \\ Im\ \boldsymbol{A}_{ij}(f \end{pmatrix} \quad \text{Eq. 46}$$

Then, the rPDC measure is calculated according to Eq. 47, as described in more details in [121]:

$$rPDC_{ij}(f) = \boldsymbol{Z}_{ij}(f)' \cdot \boldsymbol{V}_{ij}^{-1}(f) \cdot \boldsymbol{Z}_{ij}(f) \quad \text{Eq. 47}$$

where the matrix $\boldsymbol{V}_{ij}(f)$ is estimated according to the covariance matrix $\boldsymbol{\Sigma}_{\hat{Z}}$ (Eq. 48) of the estimator $\widehat{\boldsymbol{Z}}_{ij}(f)$, as introduced in [122]:

$$\boldsymbol{\Sigma}_{\hat{Z}} = \frac{\boldsymbol{V}_{ij}(f)}{N_m} = \sum_{r,l=1}^{p} \boldsymbol{R}_{jj}^{-1}(r,l)\,\Sigma_{ii} \times \frac{1}{N_m}\begin{bmatrix} \cos(rf)\cos(lf) & \cos(rf)\sin(lf) \\ \sin(rf)\cos(lf) & \sin(rf)\sin(lf) \end{bmatrix} \quad \text{Eq. 48}$$

where, N_m is the number of data points, $\boldsymbol{R}$ is the covariance matrix of the MVAR model, and $\boldsymbol{\Sigma}$ is the covariance matrix of the noise process $\boldsymbol{\varepsilon}(t)$ [121]. The rPDC measure has a non-reciprocal expression, and therefore, a signal y_j can directly influence a second signal y_i without necessarily implying a causal interaction from y_i to y_j (i.e. $rPDC_{ij}(f) \neq rPDC_{ji}(f)$). Most important, the rPDC measure can be used for comparing the direct directed interactions between all possible pairwise combinations of signals at different frequencies. Consequently, the rPDC formulation can be used for estimating the root-cause of a perturbation.

The rPDC measure has gained significant popularity during the last years, due to its advantages and has been extensively used in several applications in the neuroscience field. More specifically, the rPDC has been utilized for analyzing the complex structure of the human brain and has successfully provided insights on the brain networks by identifying direct coupling between various brain areas ([123], [124]). Interesting enough, the rPDC measure has been used for localizing those brain areas which are related to specific pathophysiological syndromes and disorders ([125], [126]). In addition to the neural studies, rPDC has been applied to ecological systems for inferring the climatology interactions and for explaining various climatic phenomena [127]. In the current doctoral work, the rPDC measure is one of the main causality estimators, used for analyzing the causal interactions between nuclear reactor processes, in a similar manner as the brain connectivity and the climatological phenomena are analyzed in neuroscience and in ecology, respectively.

6.3.3. DTF: directed transfer function

The last causality estimator to be studied in the current work is the DTF measure. DTF has been introduced in [128] and focuses on estimating how each signal is influencing the other processes without making any differentiation between direct or indirect interactions. In other words, the DTF measure can be efficiently utilized for identifying the so-called *reachability* nature of each signal within the analyzed system [129]. Even if DTF is not identifying the direct interactions, as the PDC and rPDC measures do, it is still a powerful connectivity estimator since it can provide valuable information about the direction of information flow within the signals.

The derivation of the DTF measure is based on the inverse formulation of the MVAR model coefficients in the frequency domain, i.e. $\boldsymbol{H}_{ij}(f) = \boldsymbol{A}_{ij}(f)^{-1}$, where $\boldsymbol{H}(f)$ defines the transfer function of the MVAR model and can

be used to calculate the information flow between the analyzed signals. The DTF estimator has a similar normalization scheme as the PDC measure, and it is defined as follows (Eq. 49)[31]. It is important though to mention that, the DTF expresses the ratio between the inflow from signal y_j to signal y_i to the total inflows towards the latter, whereas the PDC measure describes the outflow from y_j to signal y_i to the total outflows from the former [130].

$$DTF_{ij}(f) = \frac{\left|\boldsymbol{H}_{ij}(f)\right|}{\sqrt{\sum_{q=1}^{m}\left|\boldsymbol{H}_{iq}(f)\right|^2}} \qquad \text{Eq. 49}$$

DTF is also a non-reciprocal measure normalized in $[0, 1]$ interval, and it indicates a directional connection from signal y_j to signal y_i at frequency f if and only if $DTF_{ij}(f)\neq 0$ (rejection of null hypothesis). In addition, the DTF measure depends only on the $\boldsymbol{H}(f)$ and not on the noise covariance matrix of the MVAR model, and therefore, any possible correlation between the noise processes will not affect the DTF results [105]. Last, it is important to mention that, the calculation of the DTF measure becomes significantly more demanding compared to the PDC and rPDC measures due to the fact that the inverse transfer function $\boldsymbol{H}(f)$ has to be calculated. The computational time of DTF increases with larger and more complex systems, which require a higher number of model order in the MVAR modelling.

6.3.4. Significance levels

An important topic, which is briefly tackled in this chapter, is the significance assessment of the causality measures results. Theoretical distributions have been proposed in the literature for assessing the statistical significance of the PDC, rPDC, and DTF results in order to identify if an estimated causal relationship truly exists. In the current work, the significance limits are determined as follows. The critical value of the PDC estimator, which determines whether or not a direct interconnection is statistically significant at the ϑ-significance level of $5\ \%$ (i.e. rejection of null hypothesis), is estimated according to a χ^2 distribution with 1 degree of freedom [122]. The rPDC measure asymptotically follows a χ^2 distribution with 2 degrees of freedom, and the critical value for a ϑ-significance level of $5\ \%$ for rejecting the null hypothesis is estimated by $\chi^2_{2,1-\vartheta}/N_m$, where $\chi^2_{2,1-\vartheta}$ indicates the 1-ϑ quantile of the χ^2 distribution [121]. The statistical properties of the DTF measure follow a χ^2 distribution with 1 degree of freedom using a ϑ-significance level of $5\ \%$ (i.e. rejecting the null-hypothesis) [131]. All these significant assessments are asymptotically following a χ^2 distribution and the corresponding critical levels can be estimated without any requirement of substantial computational time. This approach gives a quick understanding of the significance levels of the utilized causality measures and it is used throughout this doctoral thesis. It is important to add that, a more reliable and robust estimation of the significance levels can be performed using surrogate data methods. Surrogate data are based on a random permutation of the phase of the Fourier transform of each signal which expects to remove any time dependency between the analyzed processes, and therefore, the default correlation between the signals can be estimated [132].

[31] It is important to note that, the DTF and PDC measures coincide to the same connectivity patterns when bi-variate models are analyzed since the direct and indirect interactions in bi-variate systems are conceptually the same notions. The similarity of DTF and PDC in bi-variate models exist because both measures depend on the model coefficients of the MVAR model.

6.3.5. Connectivity measures properties summary

The advantages, limitations, and properties of the various causality measures (i.e. coherence function, PDC, rPDC, and DTF estimators), utilized in the framework of this doctoral thesis are summarized in Table 7. In a nutshell, the coherence function is a frequently used measure that can be applied on signals pairs for estimating their level of correlation in the frequency domain. However, the coherence function has an un-directed formulation (i.e. reciprocal expression), and therefore, no conclusion can be made about the cause-and-effect interactions between the signals. The causal influences of a multi-variate system could be estimated using the PDC, rPDC, and DTF measures for estimating the directional nature of the causal influences (i.e. non-reciprocal expressions). In addition, the PDC and rPDC measures can differentiate between direct and indirect interactions, whereas the DTF measure can capture the reachability nature of the analyzed signals. Therefore, the causality measures can be used for studying the information flow paths within an analyzed system and for indicating the root-cause of possible perturbations or anomalies.

Table 7: Summary of connectivity measures properties in the frequency domain.

Causality Measures	Bi-variate	Multi-variate	Un-directed	Directed	Indirect	Direct
Coherence	x		x			
PDC		x		x		x
rPDC		x		x		x
DTF		x		x	x	

In addition, a simplified illustrative example is presented in order to demonstrate how the causality analysis results can be interpreted. To this aim, a three-variate model is used, in which the activation signal y_1 directly influences the signal y_2 and that in turn affects the third signal y_3 (Fig. 92). This illustrative example focuses on the differences between the different causal measures, and therefore, the equations governing the analyzed model are ignored here for simplicity.

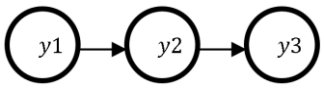

Fig. 92: Simplified three-variate model.

The connectivity analysis results in terms of the coherence function and the PDC, rPDC, and DTF causality measures are presented in the following Fig. 93. The coherence function, PDC, rPDC, and DTF results for the simplified model are presents in plots a, b, c and d, respectively. For each plot the off-diagonal sub-plots show the frequency dependency of the examined connectivity measure between two signals. For instance, the sub-plot, located at the second raw and first column (i,j=2,1) of Fig. 93a shows the coherence between signal y_1 and y_2. The diagonal sub-plots of each plot (red curves) present the APSD of each signal. As an example, the (i,j)=(1,1) sub-plot of Fig. 93a shows the ASPD of signal y_1. The spectral analysis (i.e. diagonal sub-plots) assists in the estimation of the nominal frequency of perturbation of the analyzed model. In this example, the system is clearly oscillating with a nominal frequency of $1\ Hz$. Therefore, the causality analysis results focus on that specific spectral component. The coherence function, which is a reciprocal measure, gives symmetric results (Fig. 93a). In other words, no information can be extracted about the direction of interactions. The non-reciprocal character of the causality measures is demonstrated by the non-symmetric results of PDC, rPDC, and DTF. The correct connectivity structure of the three-variate model is estimated by both the PDC and rPDC measures, as they correctly identify all the direct interconnections by calculating non-zero values only for

PDC_{21}, PDC_{32}, and $rPDC_{21}$, $rPDC_{32}$, respectively. Moreover, the reachability character of the DTF measure is depicted from the non-zero values of DTF_{21}, DTF_{31}, and DTF_{23}. In this illustrative example, the DTF measure predicts a causal influence from signal y_1 to y_3 due to the intermediate role of the y_2 signal. This is due to the fact that, the DTF measure cannot differentiate direct from indirect interconnections. It is important to note that, the PDC/rPDC and DTF measures can be used complementary to each other for estimating the direct interconnections and for identifying the central role of the most important signals (i.e. root-cause). This will be demonstrated in detail in Sec. 6.6 with the help of several simulated and measured data sets.

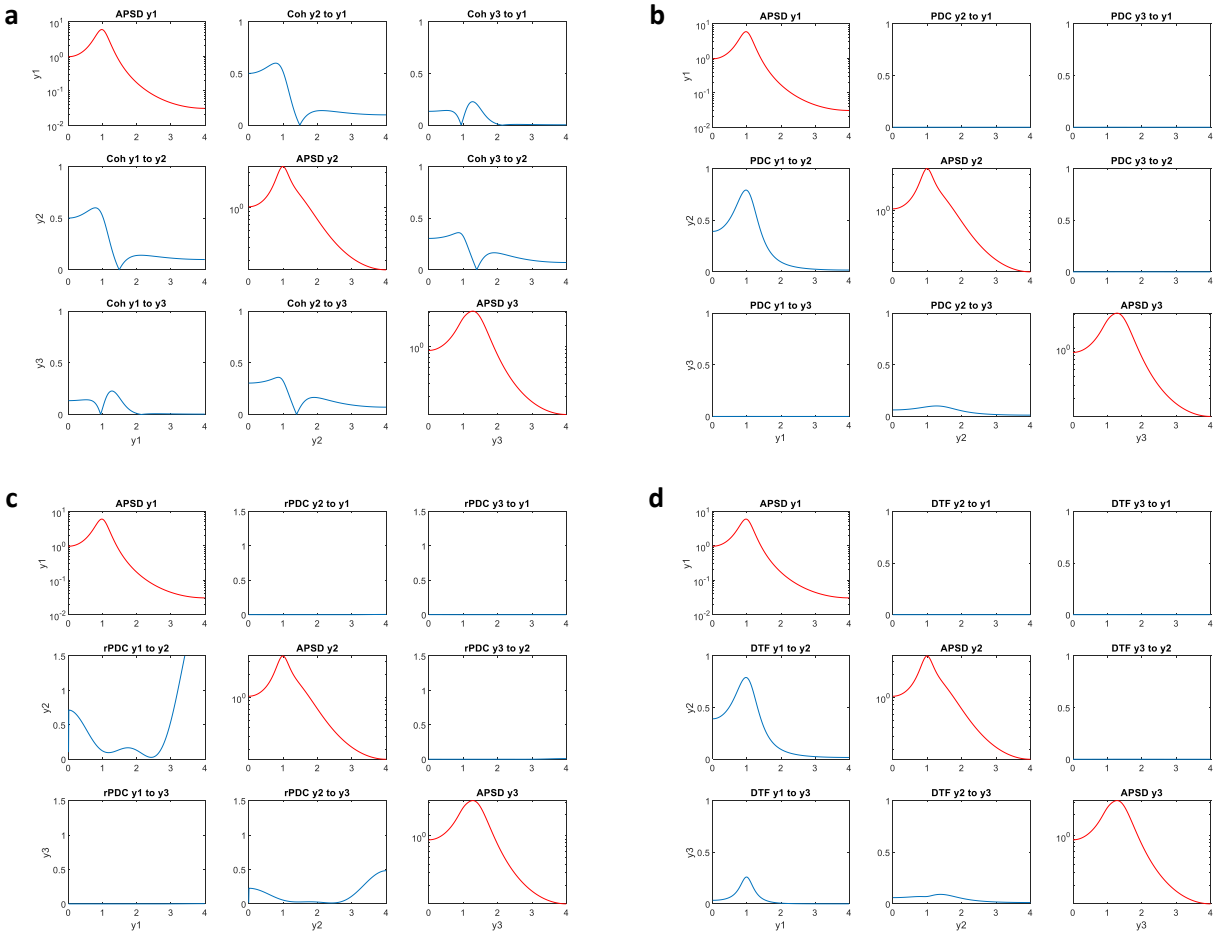

Fig. 93: Demonstration of causality analysis plots for a simplified three-variate model: coherence (a); PDC (b); rPDC (c); and DTF (d). The x-axis corresponds to the frequency domain in Hz.

6.4. Connectivity graphs and network measures

The results of a connectivity analysis can be summarized and presented in causality plots, as illustrated in Fig. 93. These plots describe the level of interconnection between two signals at a time (i.e. bi-variate plots) in the frequency domain, based on the utilized causality measure. Clearly, these plots become more difficult to be interpreted as the number of the analyzed signals increases and as the number of interconnections increases too. In order to improve the interpretability of the causality analysis results and to extract easier the structural information of the analyzed system, the so-called *connectivity graphs* (or *path diagrams*) have been introduced in the literature. The causality analysis results therefore can be summarized and represented in terms of the connectivity graphs, following the principles of the *graph theory* [133]. According to the graph theory, each signal (e.g. neutron detector response, process signal, etc.) is considered as a *node*, called also

vertex, and each interconnectivity between two nodes is called an *edge*. Therefore, any studied system can be expressed as a graph G consisted of N nodes and E edges (i.e. abbreviated as G=(N, E)). The number of nodes is fixed and equal to the total number of analyzed signals for a given system. The number and characteristics of the edges depend on the causality analysis results. It should be noted that, a connectivity graph focuses on one single frequency component and cannot provide a broad description of the causal influences over the entire frequency spectrum. Therefore, it is important to first identify what are the key frequency components of interest, before estimating the causal interconnections and generating the connectivity graphs.

A connectivity graph can be characterized according to its directionality nature (i.e. directed-digraph or undirected), and also according to its weighs (i.e. weighted or unweighted-binary). The connectivity graphs can be used for the visualization of the causality analysis results, and more important, for the estimation of the so-called *network measures* and *topological characteristics,* which offer a further understanding of the signals importance within the analyzed model. A large variety of network measures have been proposed in the literature ([117], [134]). In the current work, the utilized network measures are the *node degree* and the *node strength,* which focus on the identification of the source (i.e. activation signal) that might be responsible for a perturbation on a given simulated or measured system. The node degree is a fundamental estimator, which simply counts the number of interconnections that one node has within the analyzed model. The node degree can be subdivided in in-degree (d^{in}) and out-degree (d^{out}), in the case of directed graphs (i.e. PDC, rPDC, and DTF graphs), indicating the number of incoming and outgoing connections with respect to a given signal, respectively. For a multi-variate system with m signals, the in- and out-degrees of a signal y_i can be expressed by the following formulas (Eq. 50):

$$d_i^{in} = \sum_{j=1}^{m} E_{ij} \qquad d_i^{out} = \sum_{j=1}^{m} E_{ji} \qquad \text{Eq. 50}$$

In addition, the node strength is used in weighted graphs (i.e. PDC, rPDC, and DTF graphs) for calculating the total strength that a signal has within the analyzed system. Similarly to the node degree, the node strength can be subdivided in in-strength (s^{in}) and out-strength (s^{out}), according to the direction of interaction [134]. For each weighted connectivity measure con (i.e. con=PDC, $rPDC$, DTF), the frequency dependent in- and out-degrees of a signal y_i can be estimated according to the following expressions (Eq. 51):

$$s_i^{in} = \sum_{j=1}^{m} con_{ij}(f) \qquad s_i^{out} = \sum_{j=1}^{m} con_{ji}(f) \qquad \text{Eq. 51}$$

The simplified three-variate model, introduced in Fig. 92, is also used here to demonstrate the connectivity graph results according to the coherence function and the PDC, rPDC, and DTF measures results. Fig. 94 is composed of four plots for the four utilized measures. Each graph is made up of three nodes and a number of edges, which depend on the results of the causality analysis at the nominal frequency of 1 Hz. The coherence function produces an undirected weighted graph by estimating interconnectivity edges between all three nodes, and fails to indicate any root-cause (Fig. 94a). The connectivity graphs of the three causality estimators (Fig. 94b-d) assist in the quick and easy interpretation of the causal influences between the analyzed signals. In addition, valuable information about the information flow paths can be easily extracted by those connectivity graphs (e.g. indication of signal y_1 as a root-cause of this model).

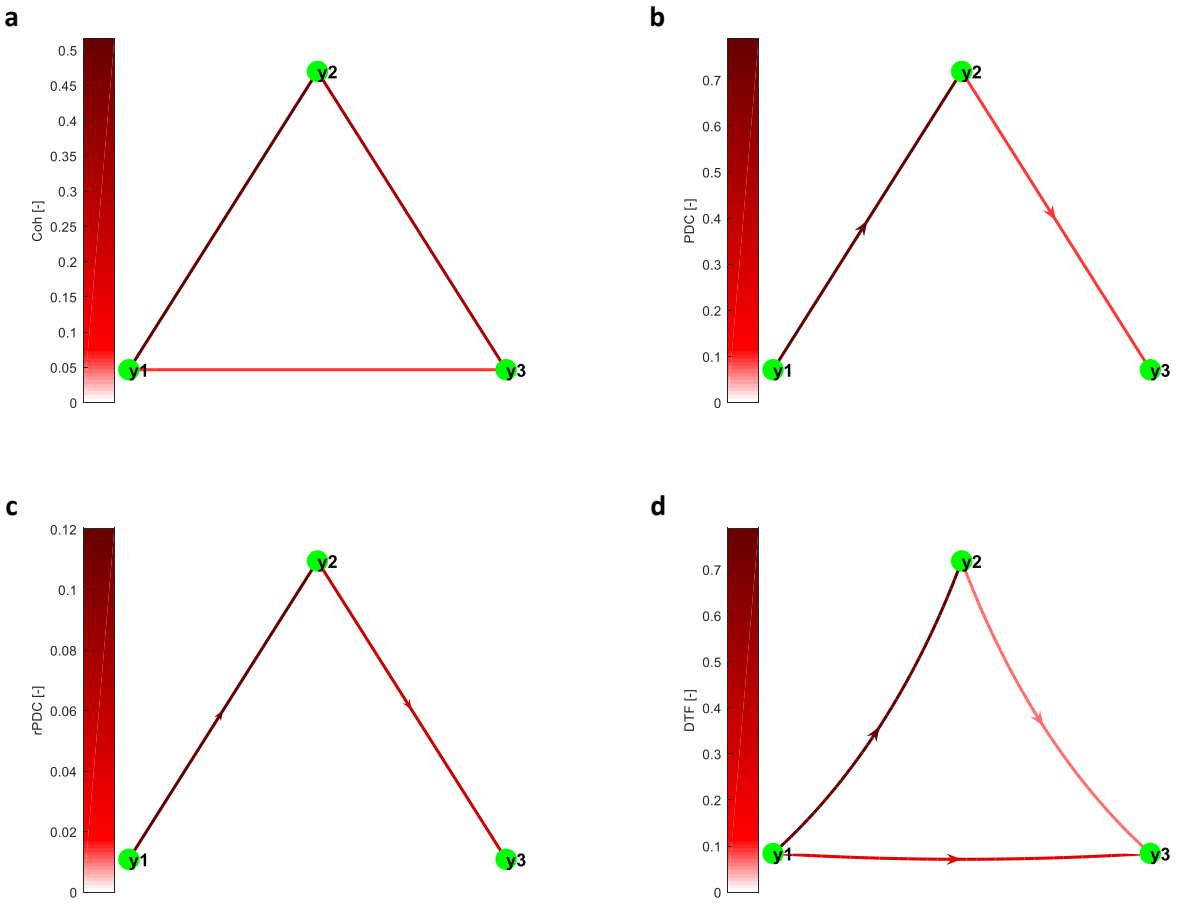

Fig. 94: Demonstration of connectivity graphs for a simplified three-variate model: coherence (a); PDC (b); rPDC (c); and DTF (d).

Finally, the network measures results of the simplified three-variate model at the nominal frequency of $1\ Hz$, according to the Eq. 50 and Eq. 51, are presented in Table 8. The network measures summarize in a table all the information that are included in the connectivity graphs concerning the structural behavior of the analyzed system. In simplified models, like the current one, the connectivity graphs and the accompanied network measures might look trivial. However, in complicated and highly coupled systems, like those that will be demonstrated in Sec. 6.6, the connectivity graphs and network measures provide additional valuable information related to the information flow pattern and the signals interconnectivity relationships.

Table 8: Network measures results for a simplified three-variate model.

		Coh			PDC			rPDC			DTF		
Measure	**Node**	y_1	y_2	y_3	$\boldsymbol{y_1}$	y_2	y_3	$\boldsymbol{y_1}$	y_2	y_3	$\boldsymbol{y_1}$	y_2	y_3
Node degree	**out**	2	2	2	1	1	0	1	1	0	**2**	1	0
	in				0	1	1	0	1	1	0	1	2
Node strength	**out**	0.58	0.84	0.38	**0.79**	0.10	0.00	**0.12**	0.05	0.00	**1.05**	0.07	0.00
	in				0.00	0.78	0.10	0.00	0.12	0.05	0.00	0.79	0.33

6.5. PSI connectivity analysis methodology

The principles of the causality analysis, presented in the previous sections of this chapter, have been implemented as an additional block in the PSI-TSAR methodology (Fig. 6), in the framework of this doctoral thesis. To the author's knowledge, this work is the first-ever attempt to systematically analyze nuclear reactor signals by means of causality analysis estimators in order to identify the signals interconnections whether during normal operating conditions or under the occurrence of a malfunction or anomaly. The PSI connectivity analysis methodology is fully developed in the MATLAB environment and has been appropriately adjusted in order to analyze efficiently and in a user-friendly manner either simulated or measured nuclear reactor data series. The flow chart of the PSI connectivity analysis methodology is summarized in Fig. 95.

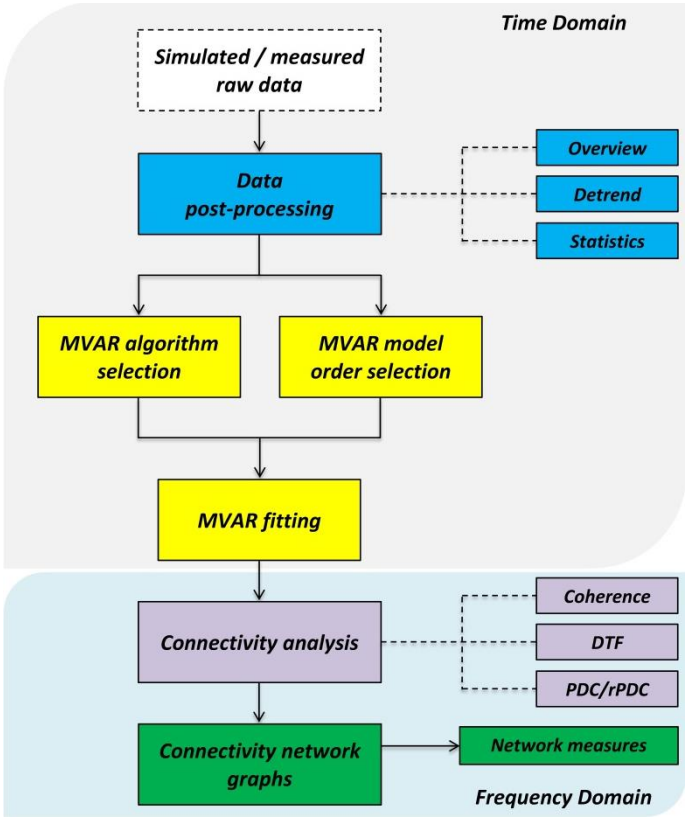

Fig. 95: PSI connectivity analysis methodology flow chart.

This methodology consists of a set of MATLAB scripts, comprising basic signal analysis functionalities and advanced causality analysis techniques. The PSI connectivity toolbox is divided in two parts; the *time-domain* and the *frequency-domain* analysis parts. First, any data set (composed of simulated or measured raw data) is imported in the toolbox in an EXCEL/MATLAB matrix or in ASCII format. The input data corresponds to a set of simultaneously recorded time signals of various parameters (e.g. in/ex-core neutron detector responses, coolant temperature and flow responses, valves opening positions, etc.). These signals are analyzed in a preliminary stage (i.e. *data post-processing*) in order to extract the first indications about their quality. To this aim, the raw data are screened in the time-domain and any erroneous, faulty or corrupted recorded signals are identified and removed from further stage analyses, since they will disturb the analysis functionality. In addition, key statistical quantities are estimated for each time signal (e.g. mean value, standard deviation, noise to signal ratio, etc.), and therefore, a preliminary identification of the data set structure is achieved.

Next, a MVAR model is fitted to the multi-variate set of input signals. This is a key step of the connectivity analysis methodology, since all the causality measures are estimated based on the model coefficients, evaluated at this stage. The fitting process requires the evaluation of the optimal model order and the estimation of an appropriate fitting algorithm, ensuring the best possible fitting approach and consequently to avoid any over- or under-fitting. The BIC, AIC, FPE, and HQ (Sec. 6.2.1) algorithms have been implemented in the PSI connectivity toolbox, and the criterion that is associated with the minimum model order is further used in the connectivity analysis. In addition, the Vieira-Morf, Nuttel-Strand, Least-Square Estimation and ARfit algorithms (Sec. 6.2.2) for the MVAR fitting of the analyzed data-set are all available in the PSI toolbox, however, the Nuttel-Strand algorithm is used as the default one throughout this work due to its better performance, according to the literature [111].

Then the estimated MVAR model coefficients are transformed in the frequency domain, and the causality analysis is applied by using the coherence function and the PDC, rPDC, and DTF estimators[32]. Finally, the connectivity analysis results are summarized using causality plots and connectivity graphs. The capabilities of the PSI connectivity analysis methodology are demonstrated in the following section with the help of a series of simulated and measured data sets.

6.6. Application on simulated and measured data

In this section, the PSI connectivity analysis methodology is validated against simplified analytical models, in Sec. 6.6.1. Then, its capabilities and limitations on predicting the perturbation source in nuclear reactor simulated system is demonstrated, in Sec. 6.6.2. After that, the methodology is applied on real nuclear reactor plant data, in Sec. 6.6.3.

6.6.1. Analytical verification

The importance of the causality analysis on identifying the information flow patterns within a multi-variate system is demonstrated through a series of simplified analytical models. In these models, predefined direct interconnections are designed. An activation signal (root-cause) is modelled to follow a damped-oscillation movement of a mass m, which is derived using the second-order differential expression of Newton's second law of motion (Eq. 52):

$$m\frac{d^2x}{dt^2} + c\frac{dx}{dt} + kx = 0 \qquad \text{Eq. 52}$$

where, x describes the mass-spring oscillatory motion, k is the spring stiffness constant, and c is the viscous damping coefficient. The time dependent motion of the mass m, oscillating at a specific damped frequency f_0, can be estimated by solving the following recursion equation [135]:

$$x(t_n) + \mathrm{a}_1 x(t_{n-1}) + \mathrm{a}_2 x(t_{n-2}) = 0 \qquad \text{Eq. 53}$$

[32] The causality measures algorithms have been based on the publically available connectivity toolboxes *AsympPDC-v.3* (http://www.lcs.poli.usp.br/~baccala/pdc/dtf.html) and *SIFT* (https://sccn.ucsd.edu/wiki/SIFT), accessed on 26.06.2020.

In other words, Eq. 53 describes the displacement of a mass m as a function of the two preceding displacement values $x(t_{n-1})$ and $x(t_{n-2})$. The system coefficients a_1 and a_2 are estimated according to the following equations [135]:

$$\mathrm{a}_1 = -2e^{-\frac{dt}{\tau}}\cos(\omega_0 dt) \quad \text{Eq. 54}$$

$$\mathrm{a}_2 = e^{-2\frac{dt}{\tau}} \quad \text{Eq. 55}$$

where, τ=2m/c is the relaxation time of the mass m, and ω_0=$\sqrt{k/m}$=$2\pi f_0$ is the un-damped angular frequency. Consequently, an activation signal $x(t)$ at a frequency f_0 can be generated according to Eq. 53, by simply providing the system coefficients a_1 and a_2.

In the following, a series of simple analytical models (also called *toy models*) are generated based on the damped oscillator system. The advantage of these toy models is that the direct interconnections are predefined by the user, and therefore, the capabilities of the causality measures to correctly estimate the connectivity pattern can be assessed.

***Toy model I**: bivariate case*

The first simplified model is composed of two signals (Fig. 96). The activation signal y_1 is designed to oscillate at $1\ Hz$, by setting the system coefficients a_1=-1.2 and a_2=0.7, and is directly influencing the second signal y_2. Therefore, the model coefficient a_{21} has a non-zero value (a_{21}=-0.3 for time lag k=1) according to the system of Eq. 56. This is the most fundamental example that can be used for introducing the characteristics of the different causality measures.

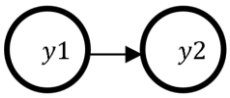

Fig. 96: Bivariate analytical model.

$$\begin{aligned} y_1(t) &= 1.2y_1(t-1) - 0.7y_1(t-2) + \varepsilon_1(t) \\ y_2(t) &= 0.5y_2(t-1) - 0.3y_2(t-2) - 0.3y_1(t-1) + \varepsilon_2(t) \end{aligned} \quad \text{Eq. 56}$$

Both signals are sampled over a period of $1'250$ seconds with a sampling frequency of f_s=$8\ Hz$. It is recalled that, the sampling frequency shall be greater than the spectral components of the system (i.e. $f_s/2$>$1\ Hz$), in order to avoid any aliasing phenomena that might deteriorate the signals quality. The signals behavior in the time and the frequency domains is presented in the two plots of Fig. 97. The oscillatory behavior of both signals is clearly visible in the time domain plot (Fig. 97a), however, their spectral characteristics can be reliably extracted only by transforming them in the frequency domain (Fig. 97b). The time and spectral nature of the two signals provide some first insights of their characteristics. In order to identify the connectivity pattern and the causal influence within the system, the application of causality analysis is needed. To that aim, the bi-variate system is fitted to a MVAR model, for which the minimum model order is estimated by the AIC algorithm with a value of p=2 (i.e. the model is abbreviated as MVAR(2); this notation will be used throughout this manuscript).

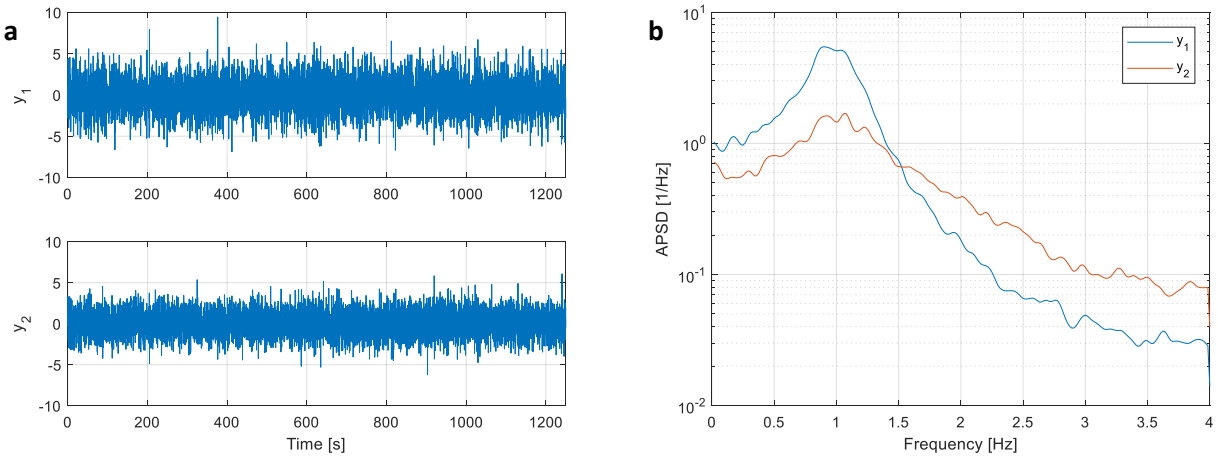

Fig. 97: Simulated signals of the bivariate model in the time (a) and the frequency (b) domains.

The frequency dependency of the coherence function and the three utilized causality measures is presented in the four plots of Fig. 98. It is recalled that, the causality analysis focuses on the key spectral components of the analyzed signals, identified from the APSD analysis (Fig. 97b). Therefore, in the following, the discussion emphasizes on the nominal frequency of $1\,Hz$. First, the coherence results show a strong synchronization between the two signals at $1\,Hz$ (Fig. 97a). Clearly, no conclusion can be made about the causal influences between y_1 and y_2, since the coherence function gives symmetric results, i.e. $Coh_{12}(f) = Coh_{21}(f)$. More interesting, all the causality measures are able to identify the correct connectivity pattern of the analyzed model. In other words, all three causality measures have non-zero values for the causal influence from y_1 to y_2 at the frequency of $1\,Hz$ (i.e. $PDC_{21}(1) = 0.80$, $rPDC_{21}(1) = 0.12$, and $DTF_{21}(1) = 0.80$). It is important to mention that, the PDC and the DTF measures (Fig. 98b, d) give exactly the same results for bi-variate systems, as discussed in the literature [136]. This is due to the fact that, the expressions of both measures (i.e. Eq. 45 and Eq. 49) become identical for bi-variate models. The differentiation of the connectivity patterns according to the PDC and DTF results becomes clear when multi-variate systems are analyzed. Furthermore, the advantage of the rPDC measure to correctly estimate the strength of the direct interactions, compared to the PDC results, becomes also evident in multi-variate systems, as it is demonstrated in the next toy models.

In addition, the connectivity analysis results are demonstrated in the form of connectivity graphs at the frequency of $1\,Hz$ in Fig. 99. The representation of the connectivity results via the connectivity graphs assists in the easier interpretation of the connectivity structure of the analyzed system. The comparison of the designed system (Fig. 96) with the connectivity graphs (Fig. 99) illustrates the capability of the causality measures to properly capture the structure of the analyzed system. The capability of the causality analysis to indicate the signals causal influences is further discussed in the following toy models. In the following, only the connectivity graphs will be presented for simplifying the interpretability of the causality analysis results.

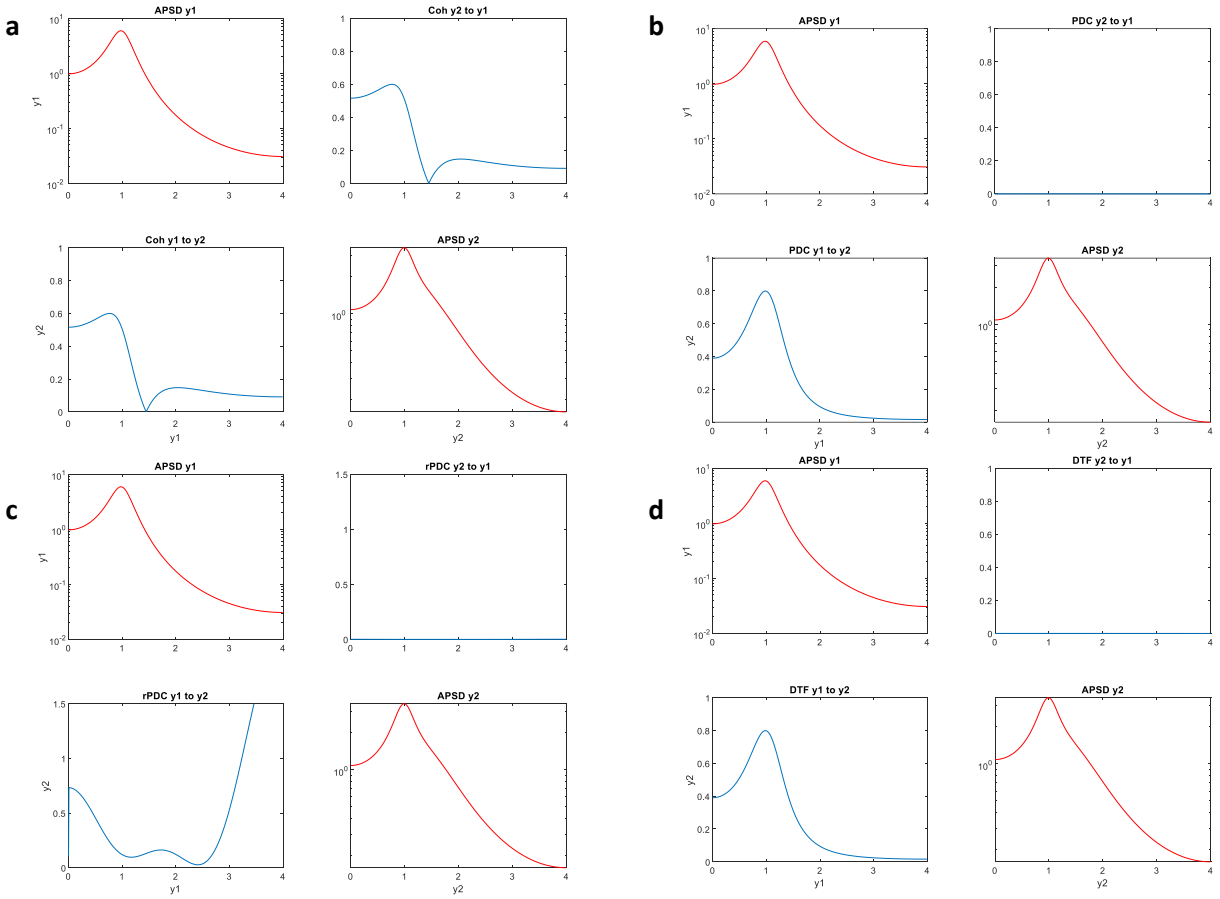

Fig. 98: Frequency dependent connectivity analysis results for a simplified bivariate model in terms of coherence (a), PDC(b), rPDC (c), and DTF (d). The x-axis corresponds to the frequency domain in Hz.

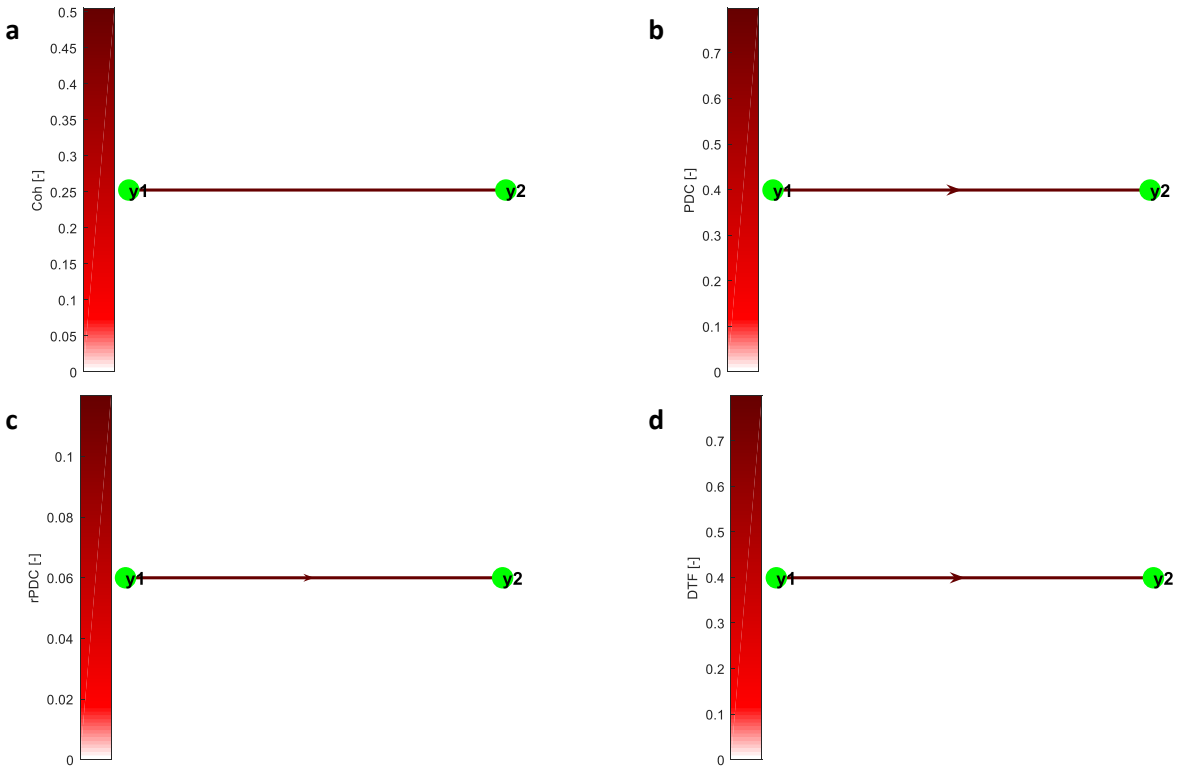

Fig. 99: Connectivity graph at $1\ Hz$ for the simplified bi-variate model in terms of coherence (a), PDC (b), rPDC (c), and DTF (d).

***Toy model II**: fourvariate model*

The previous toy model is enriched here with two additional signals: y_3 and y_4. The activation signal y_1 is directly influencing both the signals y_2 and y_3, which in turn are driving the behavior of the signal y_4 (Fig. 100). The entire system is excited at the nominal frequency of $1\ Hz$, by modelling the activation signal y_1 to have system (Eq. 53) coefficients a_1=-1.2 and a_2=0.7.

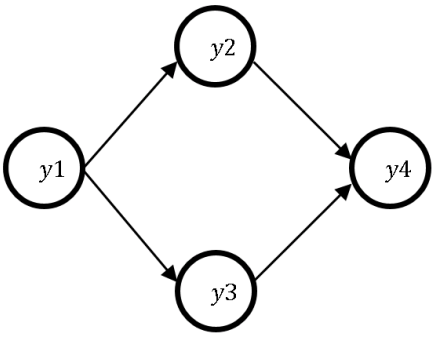

Fig. 100: Simplified fourvariate model in a diamond formation.

The analytical expressions of the four signals are presented in Eq. 57. The exact direct directional interactions between all the processes are characterized by the non-zero model coefficients α_{21}, α_{31}, α_{42}, α_{43} for time lag k=1.

$$
\begin{aligned}
y_1(t) &= 1.2y_1(t-1) - 0.7y_1(t-2) + \varepsilon_1(t) \\
y_2(t) &= 0.5y_2(t-1) - 0.3y_2(t-2) - 0.3y_1(t-1) + \varepsilon_2(t) \\
y_3(t) &= 0.7y_3(t-1) - 0.5y_3(t-2) - 0.2y_1(t-1) + \varepsilon_3(t) \\
y_4(t) &= 0.5y_4(t-1) + 0.5y_2(t-1) + 0.4y_3(t-1) + \varepsilon_4(t)
\end{aligned}
\qquad \text{Eq. 57}
$$

The signals are sampled with a sampling frequency of $8\ Hz$ over a period of $1'250$ seconds, and they are presented in the time domain and frequency domain in Fig. 101.

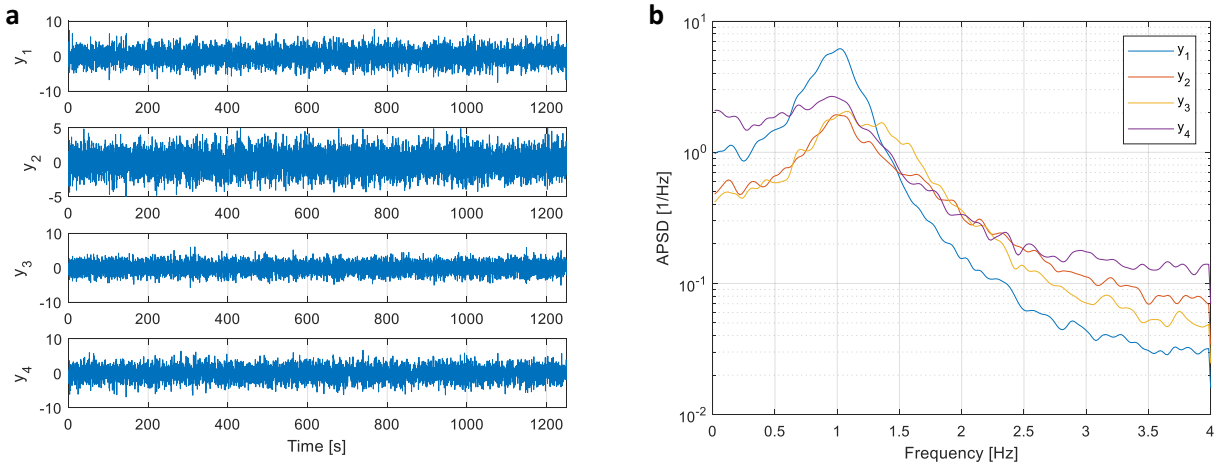

Fig. 101: Simulated signals of the analytical model (Eq. 57) in the time (a) and frequency (b) domains.

The causal influences between the signals are estimated by fitting a MVAR(2) model to the simulated data. The model order (p=2) has been estimated by the AIC algorithm, as it is the criterion that results to the minimum model order among all the available algorithms. The causality analysis results are presented in Fig. 102, using the connectivity graphs representation at the nominal frequency of $1\ Hz$. First, the coherence function (Fig. 102a) indicates strong undirected interactions between all possible signals combinations. That clearly confirms the highly coupled mechanism that drives the behavior of the analyzed system. However, the inference of causal interactions cannot be performed according to the coherence function. The PDC, rPDC, and DTF causal estimators are used to analyze this toy model, and their results are presented in Fig. 102b-d. First, it is observed that the PDC and rPDC connectivity graphs (Fig. 102b, c) are correctly predicting the designed connectivity structure of Fig. 100 by appropriately inferring all the direct directional interactions between all signals (i.e. $y_1 \to y_2$, $y_1 \to y_3$, $y_2 \to y_4$, and $y_3 \to y_4$). In addition, the DTF graph (Fig. 102d) presents the total directional outflow of each signal. The multi-variate model shows that the DTF analysis contributes with additional information about the analyzed system, in contrast to the bi-variate model (i.e. toy model I) in which the PDC and DTF results were identical. This is because the DTF estimator does not differentiate between direct and indirect interactions, and therefore, the central role of a root-cause can be identified. In this example, the DTF graph (Fig. 102d) infers a causal interaction from signal y_1 to y_4, which has not been designed to exist in the original model (Fig. 100). This interaction is correctly predicted by DTF, since the information flows from the activation signal y_1 to y_4 through the intermediate signals y_2 and y_3. Hence, the reachability property of the driving signal y_1 is reflected by the DTF measure [129].

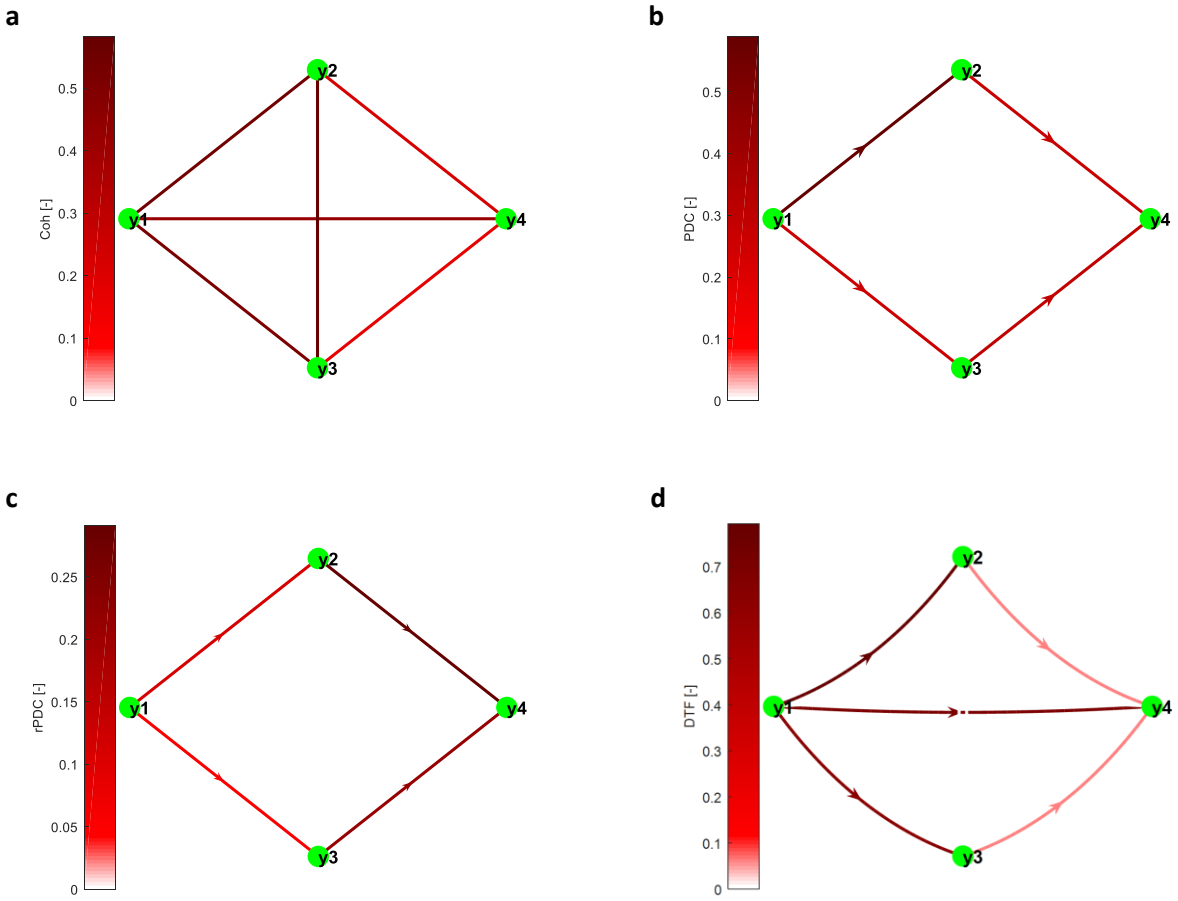

Fig. 102: Connectivity network graphs for the fourvariate system (Eq. 57) at the nominal frequency of $1\ Hz$: coherence function (a), PDC (b), rPDC (c), and DTF (d).

The above toy models showed that both the PDC and the rPDC causality measures are able to correctly infer the direct directional interconnections between the analyzed signals. In other words, both the PDC and rPDC measures have estimated properly the connectivity structure of the system. However, it is recalled that, the big advantage of the rPDC expression compared to PDC, is the capability of the former to preserve the relative interaction strengths between all signal pairs. This characteristic is demonstrated in Fig. 103, in which the connectivity strength values (i.e. $PDC_{ij}(f)$, $rPDC_{ij}(f)$, $DTF_{ij}(f)$, and $Coh_{ij}(f)$), for all the existing interconnections between the four analyzed signals at the nominal frequency of $f=1\,Hz$, are plotted as function of the respective MVAR model coefficients $\alpha_{ij}(t)$. For example, the activation signal y_1 influences the signal y_2 via the model coefficient $|\alpha_{21}(t\text{-}1)|=0.3$, and the signal y_3 is affecting y_4 via a larger model coefficient, $|\alpha_{43}(t\text{-}1)|=0.4$ (Eq. 57). The connectivity graphs (Fig. 102) show that the predicted connection strength between the signals y_1 and y_2 are $PDC_{21}(1\,Hz)=0.6$, $rPDC_{21}(1\,Hz)=0.1$, $DTF_{21}(1\,Hz)=0.8$, and $Coh_{21}(1\,Hz)=Coh_{12}(1\,Hz)=0.55$, whereas the results between the signals y_3 and y_4 are $PDC_{43}(1\,Hz)=0.3$, $rPDC_{43}(1\,Hz)=0.21$, $DTF_{43}(1\,Hz)=0.06$, and $Coh_{43}(1\,Hz)=Coh_{34}(1\,Hz)=0.4$. This example shows that, higher model coefficient values $\boldsymbol{\alpha_{ij}}$ (i.e. $|\alpha_{43}(t\text{-}1)|>|\alpha_{21}(t\text{-}1)|$) lead in a consistent manner to higher $rPDC_{ij}$ values (i.e. $|rPDC_{43}(1)|>|rPDC_{21}(1)|$) at the designed frequency of vibration. However, it is not the case for the other three measures (i.e. PDC, DTF, and Coh), since it could be clearly observed that higher model coefficients do not consistently lead to higher connectivity values for these three parameters. Hence, Fig. 103 clearly demonstrates the capability of rPDC measure to estimate correctly the connectivity strengths, and therefore, the understanding of the signals pairwise connections importance could be enhanced.

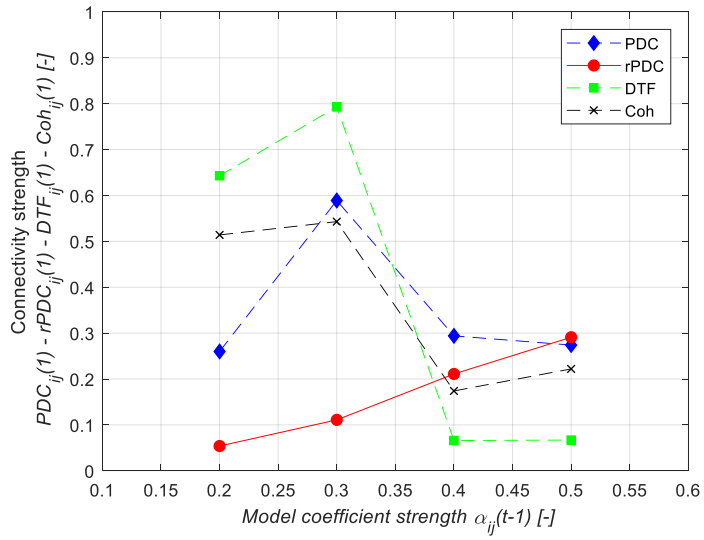

Fig. 103: Connectivity strength values as function of coefficient values of the MVAR model (Eq. 57) at the nominal frequency of 1 Hz.

In addition to the connectivity graphs, the causality analysis results are also assessed using the connectivity network measures (i.e. node degree and strength). The key role of the activation signal y_1 compared to the other three signals, is highlighted in Table 9, characterized by its higher node out-degree values for the PDC, rPDC and DTF causality measures. Moreover, the reachability property of signal y_1 is evident by the higher out-strength value given by the DTF measure. In other words, the information generated by the signal y_1 is transferred to the entire system, and consequently, this signal can be correctly identified as the root-cause of the perturbation. It is recalled that, the coherence results do not differentiate between nodal in- and out-degree/strength values, as shown in Table 9, since it is an undirected connectivity measure.

Table 9: Node degree and strength based on the PDC, rPDC, DTF, and coherence measures for the MVAR model (Eq. 57) at 1 Hz.

		PDC				rPDC				DTF				Coh			
Measure	**Node**	$\boldsymbol{y_1}$	y_2	y_3	y_4	$\boldsymbol{y_1}$	y_2	y_3	y_4	$\boldsymbol{y_1}$	y_2	y_3	y_4	y_1	y_2	y_3	y_4
Node degree	**out**	**2**	1	1	0	**2**	1	1	0	**3**	1	1	0	3	3	3	3
	in	**0**	1	1	2	**0**	1	1	2	**0**	1	1	3				
Node strength	**out**	**0.85**	0.27	0.29	0.00	**0.17**	0.29	0.21	0.00	**2.14**	0.07	0.07	0.00	1.48	1.35	1.27	0.82
	in	**0.00**	0.59	0.26	0.57	**0.00**	0.11	0.05	0.50	**0.00**	0.79	0.64	0.83				

These two simple analytical models demonstrate the advantages and drawbacks of the utilized causality measures. The connectivity graphs and network results showed that the rPDC and DTF are the best measures, to be used in a complementary manner, to study the connectivity structure of a system and to infer the possible root-cause of a perturbation. Therefore, in the following analytical models and nuclear reactor applications, emphasis will be limited to rPDC and DTF measures.

***Toy model III**: trivariate model*

The current example is based on the signals that are generated using the Eq. 57. However, now the activation signal y_1 is intentionally removed from the analyzed data set (Fig. 104). This example focuses on the interpretation of the causal interactions when the root-cause is missing from the recorded data set. This can be a common issue in "real life" in many fields, since the process that is responsible for a perturbation of the system might be impossible to be recorded or its measurement might be distorted or corrupted.

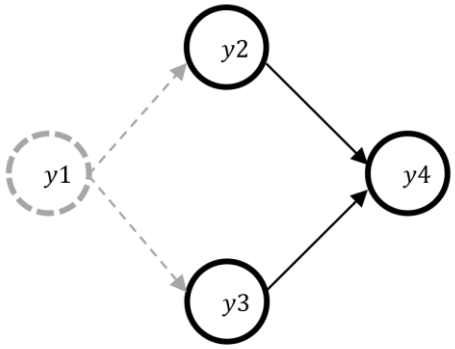

Fig. 104: Simplified model (according to Eq. 57) in which the activation signal y_1 is not included in the analyzed data set.

The time and frequency responses of the signals y_2, y_3, and y_4 are illustrated in Fig. 101. Fig. 105 presents the connectivity graphs based on the rPDC and the DTF results between the three signals, at the nominal frequency of 1 Hz. The rPDC plot (Fig. 105a) properly identifies, once more, the direct directional interactions from y_2 and y_3 to y_4, as designed (Fig. 101), even if the activation signal y_1 is not included in the analysis. In addition, the rPDC strengths have approximately the same values like in the original analysis results of toy model II (i.e. in toy model III: $rPDC_{42}(1)$=0.31, and $rPDC_{43}(1)$=0.22; in toy model II: $rPDC_{42}(1)$=0.29, and $rPDC_{43}(1)$=0.21). However, an interconnection with low feedback between signals y_2 and y_3 is observed due to their mutual dependency from the, absent, activation source, y_1. The DTF plot (Fig. 105b) can also infer the information flow paths from y_2 and y_3 to y_4 which have, though, considerable higher connectivity values compared to the complete model (i.e. in toy model III: $DTF_{42}(1)$=0.30, and $DTF_{43}(1)$=0.29; in toy model II: $DTF_{42}(1)$=0.07, and $DTF_{43}(1)$=0.07). Interesting enough, the DTF measure predicts erroneous interactions from signal y_4 to y_2 and y_3, but hopefully with very low levels that could be neglected if an appropriate significant level is chosen. More

importantly, a relatively strong interconnection with feedback between y_2 and y_3 is also identified by the DTF results.

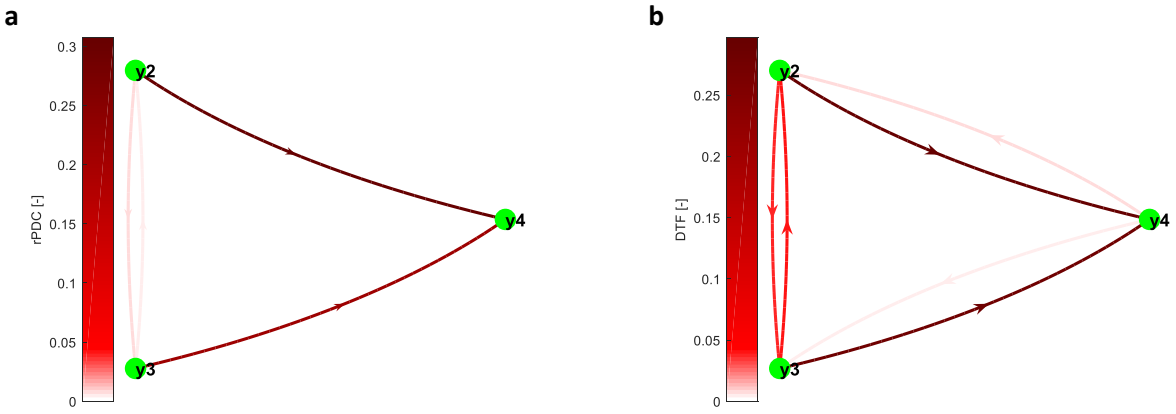

Fig. 105: Connectivity network graphs for the toy model III at 1 Hz: rPDC (a) and DTF (b) measures.

This feedback mechanism between y_2 and y_3, predicted by both rPDC and DTF results, is erroneous and can lead to wrong interpretation of the connectivity structure but can be considered as an indication of the absence of the activation signal. In addition, this example has shown that, the missing activation signal from the analyzed system is mainly affecting the DTF results. It is clear though that, the causality analysis is able to estimate the correct information flow paths among the available recorded signals even if the root-cause is not included in the analysis. More important, this example showed that the causality analysis will indicate the central function of those signals, which are directly influenced by a root-cause when this latter is missing from the studied system. This behavior will be demonstrated in more detail in the next example.

***Toy model IV**: five-variate model*

This last analytical example is also based on Eq. 57, however, this time an additional signal (y_5) is introduced between the activation signal y_1 and the remaining three processes, as presented in Fig. 106. The analytical expression of the time-dependent evolution of all signals is presented in Eq. 58. The activation signal y_1 is modelled to oscillate at a frequency of 1 Hz and is directly influencing the signal y_5 via the model coefficient $\alpha_{51}(t\text{-}1)$=-0.5. In this example, both signals y_2 and y_3 are directly influenced by y_5, in contrast to Eq. 57 (toy model II) where they were influenced directly by the activation signal y_1. The signals responses in the time and frequency domains are presented in Fig. 107.

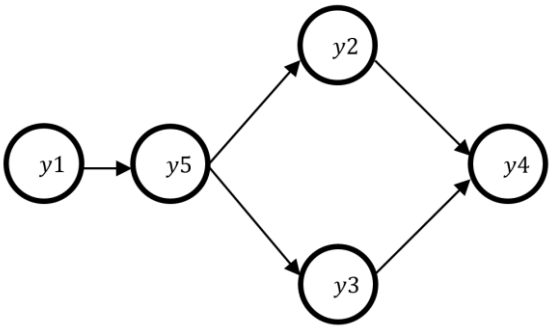

Fig. 106: Simplified five-variate model (according to Eq. 58).

$$
\begin{aligned}
y_1(t) &= 1.2y_1(t-1) - 0.7y_1(t-2) + \varepsilon_1(t) \\
\boldsymbol{y_5(t)} &= \boldsymbol{0.5y_5(t-1) - 0.4y_5(t-2) - 0.5y_1(t-1) + \varepsilon_1(t)} \\
y_2(t) &= 0.5y_2(t-1) - 0.3y_2(t-2) - 0.3y_5(t-1) + \varepsilon_2(t) \\
y_3(t) &= 0.7y_3(t-1) - 0.5y_3(t-2) - 0.2y_5(t-1) + \varepsilon_3(t) \\
y_4(t) &= 0.5y_4(t-1) + 0.5y_2(t-1) + 0.4y_3(t-1) + \varepsilon_4(t)
\end{aligned}
\qquad \text{Eq. 58}
$$

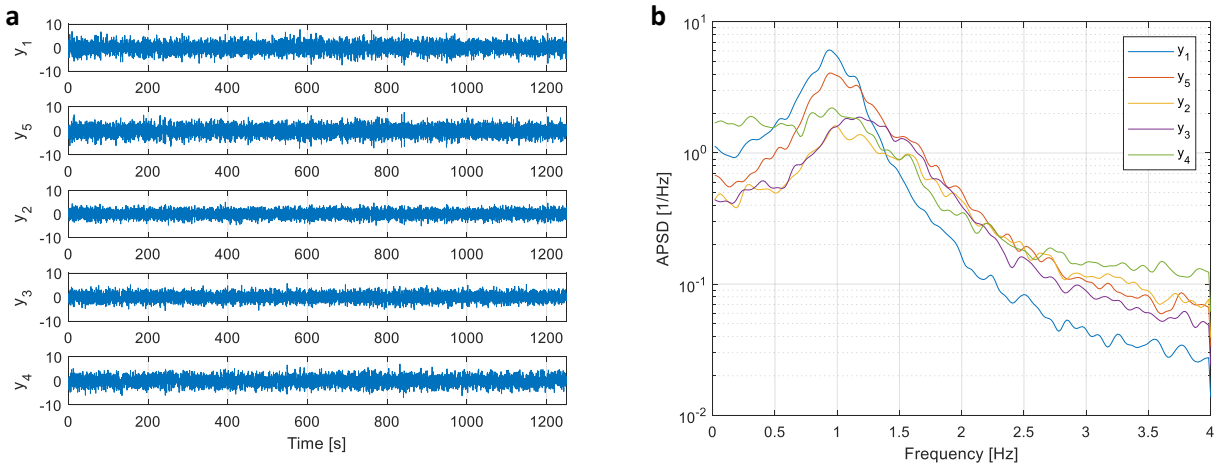

Fig. 107: Simulated signals of the analytical model (Eq. 58) in the time-(a) and frequency-domain (b).

A MVAR model of order p=2, using the AIC algorithm for the minimum model order estimation, is fitted to the five-variate model. The results of the causality analysis in terms of the rPDC and DTF measures are presented in Fig. 108. First, the rPDC graph (Fig. 108a) properly identifies all the direct interconnections and can reproduce the designed connectivity structure of Fig. 106. In addition, the rPDC measure estimates correctly the strength of interconnections by predicting higher connectivity strengths for the interconnections with higher model coefficient values (Fig. 110). The DTF measure (Fig. 108a) results to a rather complicated graph by identifying many connections between the analyzed signals. Once more, the DTF graph assists in indicating the central role of the activation signal within the multi-variate system by inferring all the directional edges from y_1 to all the other signals.

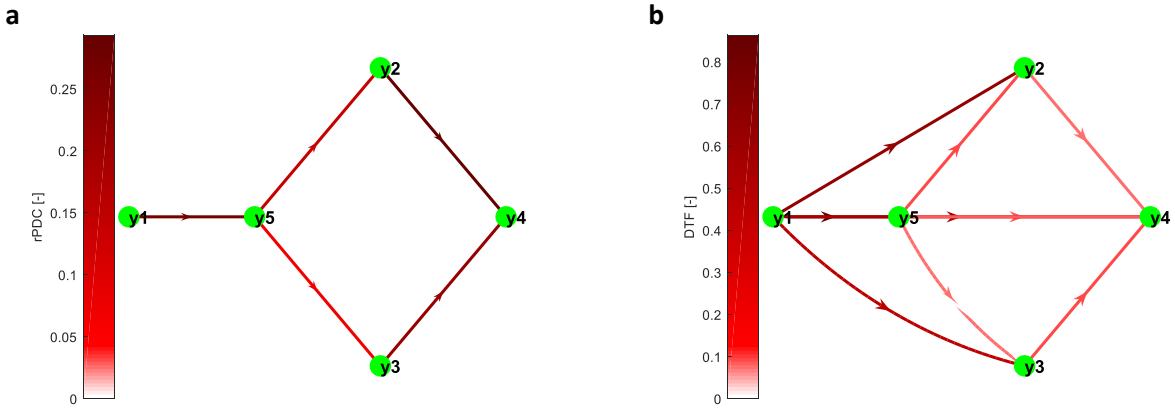

Fig. 108: Connectivity network graphs for the toy model IV at 1 Hz: rPDC (a) and DTF (b) measures.

Now, a new data set is generated here that includes all the signals of Eq. 58 except the activation signal y_1. A MVAR model of order $p=2$ is fitted in this four-variate system and the causality analysis is applied for identifying the causal interactions under the condition of the missing root-cause. The connectivity graphs in terms of rPDC and DTF measures are presented in Fig. 109. The rPDC measure (Fig. 109a) correctly identifies both all the direct directional interactions between the four signals and their strengths (Fig. 110), and additionally infers the signal y_5 as the root-cause of the analyzed perturbation. In addition, the DTF measure (Fig. 109b) predicts that the information flow paths are originating from y_5 towards all the other three signals. Therefore, the key role of y_5 within the system is clearly highlighted from the rPDC and DTF results. From the first sight, this can be said that is a wrong interpretation of the true connectivity structure of the system (Fig. 106). The signal y_5 appears to be the root-cause of the four-variate model since it is the only signal that is directly driven by the activation signal $y_1$in the original underlying system (Fig. 106). This example justifies that, both the rPDC and DTF measures indicate the first available signal, which is directly influenced by the missing root-cause, as the driving force of the analyzed model.

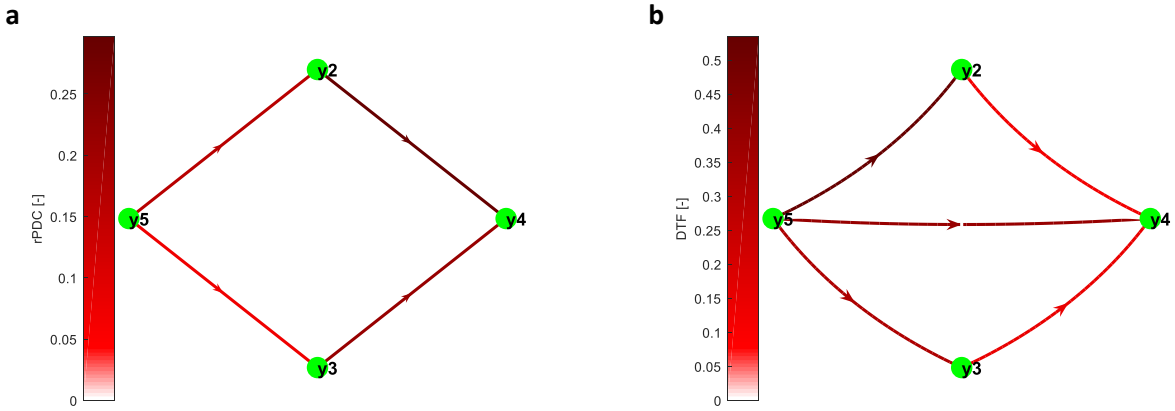

Fig. 109: Connectivity network graphs for the toy model IV at 1 Hz when the activation signal y_1 is removed from the data set: rPDC (a) and DTF (b) measures.

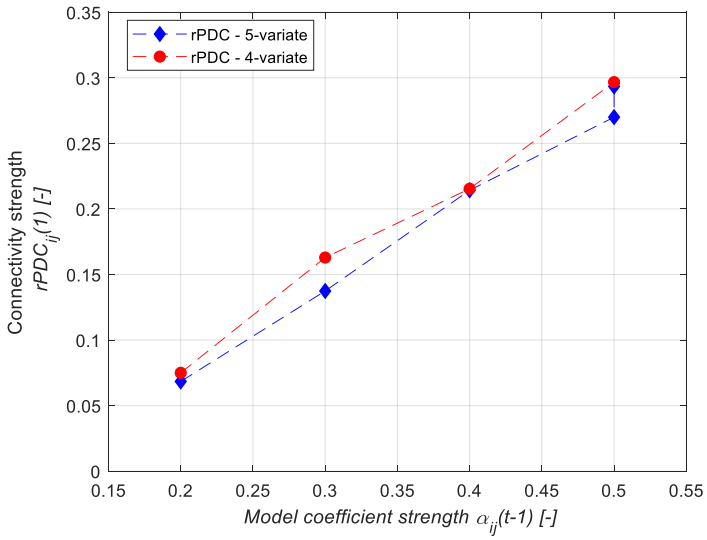

Fig. 110: rPDC strengths as function of the model coefficient values, at 1 Hz for the original toy model IV (blue diamonds) and the respective system without the activation signal y_1 (red circles).

The challenge of this connectivity analysis methodology is to interpret as accurate as possible the existing connectivity structure of the analyzed system using only those signals which have been measured. However, processes that have not been recorded or signals of low quality (e.g. poor resolution, rich in noise, etc.) are factors that diminish the effectiveness of the causality analysis results. It is recalled that, the causal estimators shall not be treated as black boxes, which intend to identify causal interactions of any given data set. The engineering judgment of the analyzed system is of high importance and must be always taken into account in order to assess the real physical meaning of the resulting cause-and-effect interactions. In the next sections, further elaborated applications of causality analysis are performed on simulated and real nuclear reactor data.

6.6.2. Simulated nuclear reactor system

***Case I**: Propagation of noise source throughout the core*

The advantages and limitations of the causality analysis have been investigated in the previous section with the help of simplified analytical models. The analytical verification of the connectivity analysis methodology, implemented in the PSI-TSAR, was an important step in this work since it provides confidence that the utilized causality measures can be used reliably for identifying the causal interactions of an analyzed system. The next step focuses on the application of connectivity analysis methodology on nuclear reactor systems. It is well known that, a nuclear core is a highly coupled system characterized by processes of various types (i.e. neutronics, thermal-hydraulic, mechanical structures, etc.), interacting with each other with strong feedbacks. Consequently, the application of causality analysis in such a complicated system is expected to be a challenging task. In order to tackle this issue, a simulated nuclear reactor system is first studied in the current section. For this, a pre-defined perturbation is imposed as a boundary condition on the simulated system, and a transient calculation is then executed through which the disturbance propagates throughout the different components/processes of the system. In such a system, the characteristics of the imposed perturbation are fully known in advance, and therefore, the causality analysis results can be verified and compared against the anticipated structural connectivity pattern.

In the current application, a previously developed simulated model of the Swedish Oskarshamn-2 BWR is used [137]. The best-estimate transient nodal code SIMULATE-3K is utilized for modelling the time-dependent fluctuation of the feedwater flow (Q_{FW}). The Q_{FW} is modelled to fluctuate following a damped noisy oscillations (introduced in Sec. 6.6.1), with a frequency of $1\ Hz$. The transient simulation is sampled with $8\ Hz$ sampling frequency and lasts for $94\ sec$ during which the imposed perturbation propagates throughout the system. The first step of the post-processing analysis emphasizes on the identification of the key processes affected by this dynamic event. The statistical analysis and the screening of the simulated signals in both the time and the frequency domains reveal that the inlet core coolant flow (Q_C), the exit liquid flow (Q_{LE}) and the core pressure drop (PD_C) exhibit strong oscillatory behavior and appear to be influenced the most from the imposed perturbation. The location of these processes with respect to the BWR system are illustrated in the following simplified scheme.

The oscillatory nature of the key processes of interest (i.e. Q_{FW}, Q_C, Q_{LE}, and PD_C) is clearly observable in both the time and the frequency domains, as presented in Fig. 112. In particular, all four signals exhibit strong spectral peak at the frequency of $1\ Hz$, which corresponds to the imposed frequency of excitation.

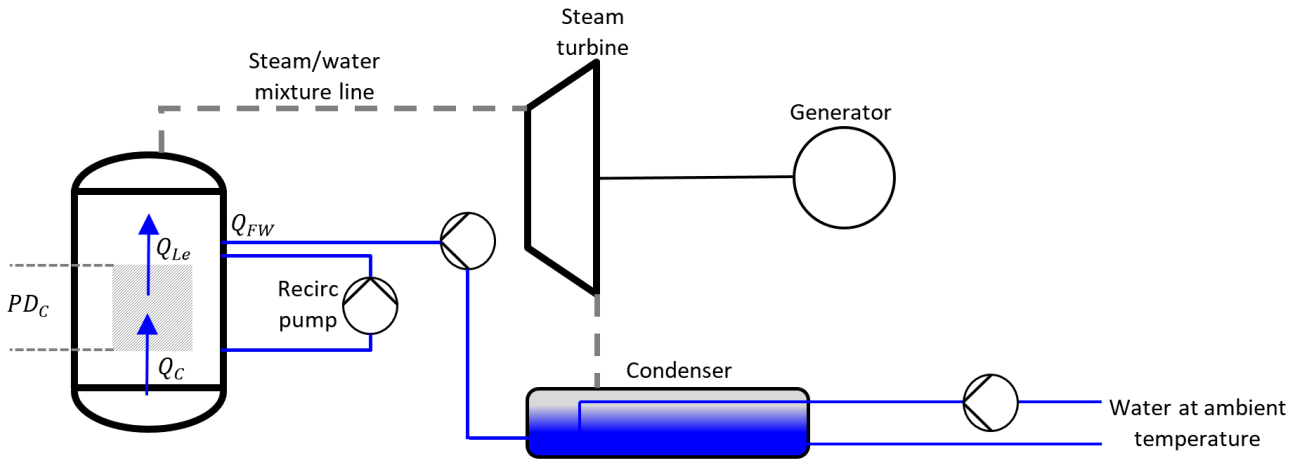

Fig. 111: Simplified scheme of the simulated BWR system.

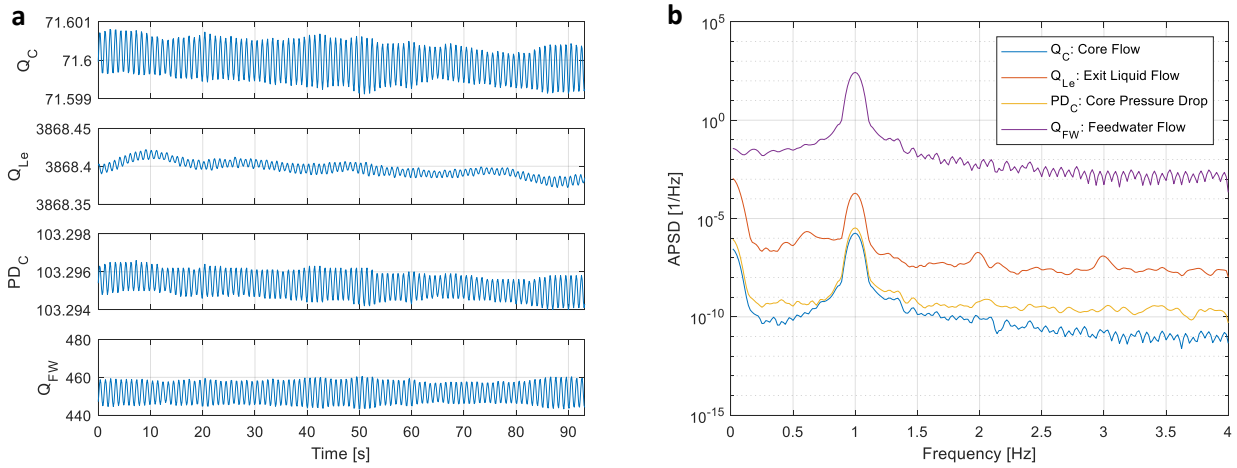

Fig. 112: Time (a) and frequency (b) responses of the key reactor processes during the simulated perturbation of the feedwater flow (Q_{FW}) perturbation at 1 Hz.

The connectivity analysis methodology is then applied on the four-variate model in order to study the interconnections between the signals, identified to be affected most by the system disturbance. A MVAR model of an order p=2, estimated using the AIC algorithm, is fitted to the simulated system. The causality analysis focuses on the rPDC and DTF causal measures for estimating the signals directional dependencies. The rPDC graph (Fig. 113a) reveals that the Q_{FW} is directly driving the behavior of all the other three signals, as expected. In addition, it can be observed that Q_C, Q_{LE}, and PD_C exhibit directional interconnections with feedback effects due to the inherently strongly coupled nature of the nuclear reactor system. Moreover, the DTF graph (Fig. 113b) indicates how strongly the imposed perturbation is propagating from Q_{FW} to the other three signals. This enhances the understanding of the underlying connectivity structure and highlights the central role of Q_{FW}. Interesting enough, the DTF connections between Q_C, Q_{LE} and PD_C signals have weak strengths, even if the respective rPDC results exhibit relative stronger values. This can be explained by the nature of the DTF measure that does not distinguish direct from indirect interconnections. Since the Q_{FW} is designed to be the perturbation source, then the total DTF results from Q_{FW} to all the other three signals are amplified, which makes their values much higher than the DTF results between the remaining three signals.

Therefore, the interconnections between those signals that are commonly influenced by the same root-cause appear to be weaker in the DTF graph.

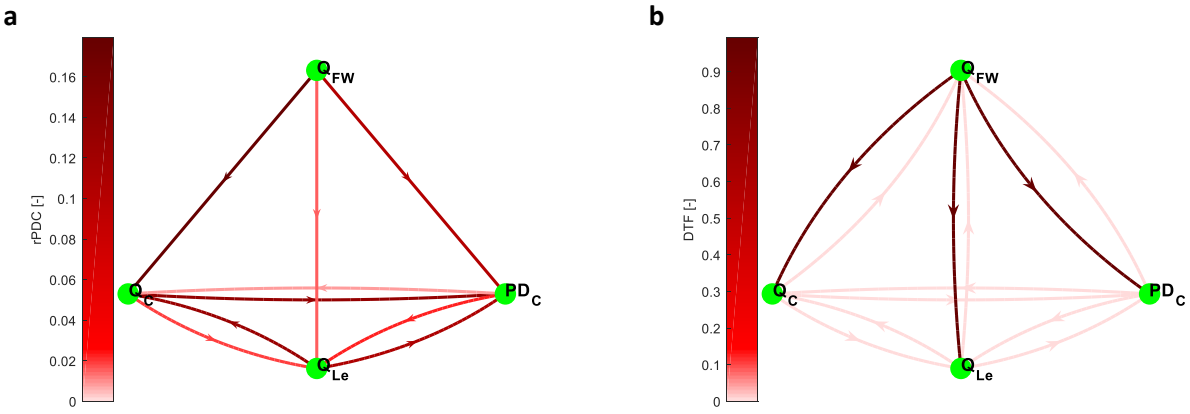

Fig. 113: Connectivity network graphs at $1\ Hz$ resulting from a simulated perturbation of the feed-water flow (Q_{FW}) within a BWR: rPDC (a) and DTF (b) measures.

Table 10 presents the connectivity network measures (i.e. nodes degree and strength) of the analyzed four-variate system. The important role of the activation signal Q_{FW} is clearly identified by the higher out-degree values based on both the rPDC and DTF measures. In addition to that, the Q_{FW} shows the highest out-strength value among all the involved processes. Therefore, it can be concluded that, the connectivity analysis methodology is able to identify the root-cause of the simulated perturbation.

Table 10: Node degree and strength based on the rPDC and DTF measures for the simulated BWR system at $1\ Hz$.

		rPDC				DTF			
Measure	**Node**	Q_C	Q_{LE}	PD_C	$\boldsymbol{Q_{FW}}$	Q_C	Q_{LE}	PD_C	$\boldsymbol{Q_{FW}}$
Node degree	**out**	2	2	2	**3**	3	3	3	**3**
	in	3	3	3	**0**	3	3	3	**3**
Node strength	**out**	0.15	0.24	0.03	**0.30**	0.05	0.03	0.05	**2.98**
	in	0.32	0.06	0.35	**0.00**	0.99	0.99	0.99	**0.01**

In this simulated scenario, the perturbation source was apriori known. Therefore, the capability of the rPDC and DTF measures could be verified and confirmed, by estimating the propagation of the disturbance throughout the BWR system. This example, confirmed once more that, the rPDC and DTF measures should be used complementary to each other in order to understand in depth the connectivity pattern and the information flow paths of complex systems such as a nuclear reactor.

***Case II**: Perturbation location identification based on in-core detectors simulated signals*

As a second illustrative example, it is attempted to identify the location of a stochastic perturbation solely based on the in-core neutron detector responses, commonly used for monitoring the reactor power. In this example, the PWR core developed for the OECD/NEA transient benchmark [138] is modelled utilizing the CMSYS codes, and the transient nodal code SIMULATE-3K is used again for the simulation of a series of stochastic perturbation scenarios. The core is a typical Westinghouse four-loop PWR with 193 fuel assemblies

of a UO2 and MOX mixed configuration. In these scenarios, the neutron flux response is monitored using twelve neutron detectors in total, i.e. four radial locations and three axial elevations, as shown in Fig. 114.

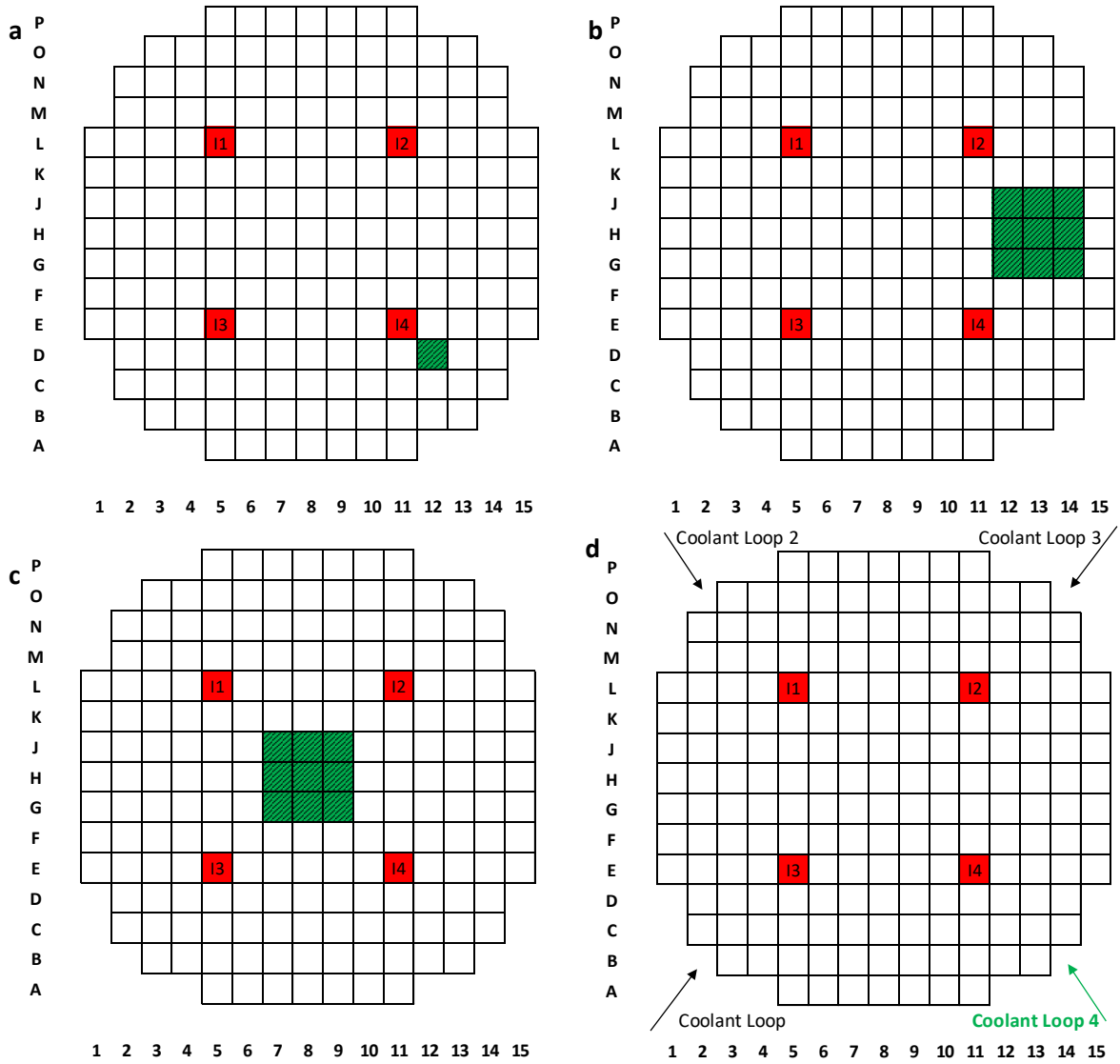

Fig. 114: PWR core layout: In-core neutron detectors (red boxes) are modelled at positions L5, L11, E5 and E11. The vibrating assemblies in scenarios a - c, are shown as green boxes in the respective plots. The azimuthal orientation of the four coolant loops is shown in plot d.

SIMULATE-3K is used in order to model localized noise sources originating either from the lateral vibration of fuel assemblies or from the stochastic fluctuation of the inlet coolant temperature, which are both common noise sources in LWRs, contributing significantly to the neutron noise phenomenology. The former noise source is modelled by perturbing the water gap widths between adjacent fuel assemblies, following the modeling approach, described in detail in Sec. 3.4.2.2. The perturbation follows a sine wave of $1\ Hz$ frequency and with $1\ mm$ amplitude. As shown in Fig. 114, three simulations have been performed:

- Lateral vibration in the x-direction of the D12 fuel assembly, next to the I4 instrumentation tube (Fig. 114a).
- Lateral vibration in the x-direction of a $3x3$ cluster of fuel assemblies, located between the I2 and I4 instrumentation tubes (Fig. 114b).
- Lateral vibration in the x-direction of a centrally located $3x3$ cluster of fuel assemblies (Fig. 114c).

For the simulation of the later noise source, four coolant loops are modelled and a stochastic fluctuation of the inlet coolant temperature at loop 4 by ±1℃ over the nominal value is imposed, as presented in Fig. 114d. The other three loops are assumed to be noise-free. Consequently, it is expected that the south-east part of the core will be significantly affected by the noise source. The modelling of both perturbation types is described in detail in *chapter 4*. In all scenarios, the goal is to localize as accurate as possible the perturbation source using only the neutron flux response at the twelve in-core locations.

It is noted that, in all these simulated examples it is trivial to localize any perturbation source in the core by just analyzing the neutron noise levels at all 3D nodes. This is illustrated in the following Fig. 115 which depicts the radial neutron noise map, in terms of coefficient of variation values as extracted from the SIMULATE-3K output for each scenario at the core-bottom axial level. However, in reality it is not possible to extract such a detailed description of the neutron flux behavior using the online monitoring systems. On the contrary, nuclear reactors are equipped with a limited number of detectors for monitoring the reactor thermal power and surveilling the reactor status. Therefore, in this example the developed connectivity analysis methodology is applied by utilizing solely the twelve in-core detectors simulated responses. The rPDC and DTF connectivity networks are used to illustrate the connectivity patterns in each of the four scenarios, in Fig. 116 to Fig. 121.

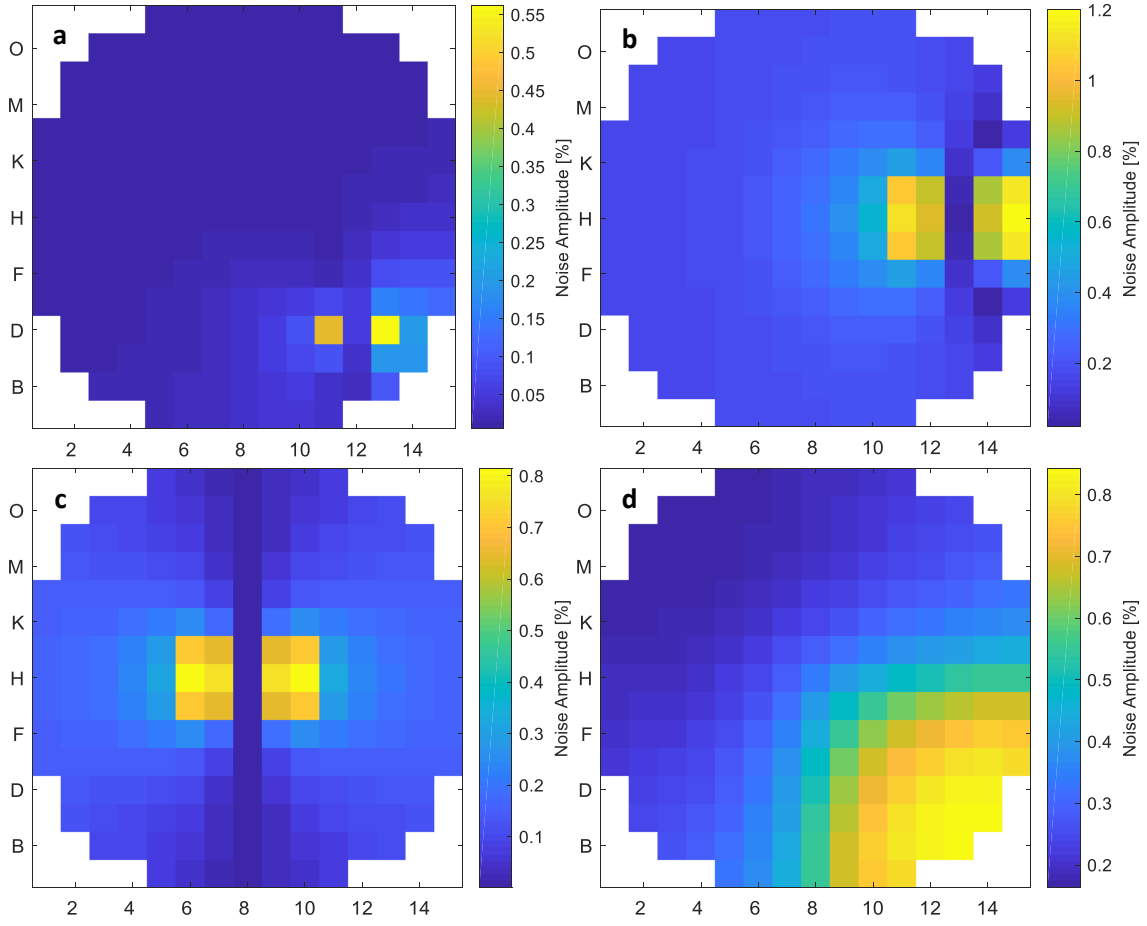

Fig. 115: Radial neutron noise map at core-bottom axial level for each of the four simulated scenarios.

Fig. 116 and Fig. 117 show the rPDC and DTF connectivity network graphs at the core-bottom and core-top axial levels, respectively for the first scenario, in which the fuel assembly at the core location D12 (Fig. 114a) is modelled to vibrate at a frequency of $1\ Hz$. The leading role of the detectors at the I4 instrumentation tube is highlighted in all four graphs. This, on the one hand, indicates the significant direct interconnections from

the radial location I4 towards the rest of the core through the rPDC results. On the other hand, the DTF graphs indicate the reachability property characteristic of signal I4, which corresponds to the information propagation from I4 to the other three instrumentation tubes. This is the expected response, since the I4 detectors are in the vicinity of the vibrating assembly, and consequently, they are affected the most from the perturbation source. Surprisingly, the rPDC results at the core-top axial level indicate a rather strong feedback mechanism between the I1 and I4 detectors, even if the vibrating assembly is next to the latter detector and far from the former (i.e. Fig. 117). Unfortunately, this behavior could not be explained, and therefore, further investigations and verifications are needed to be performed in a future work.

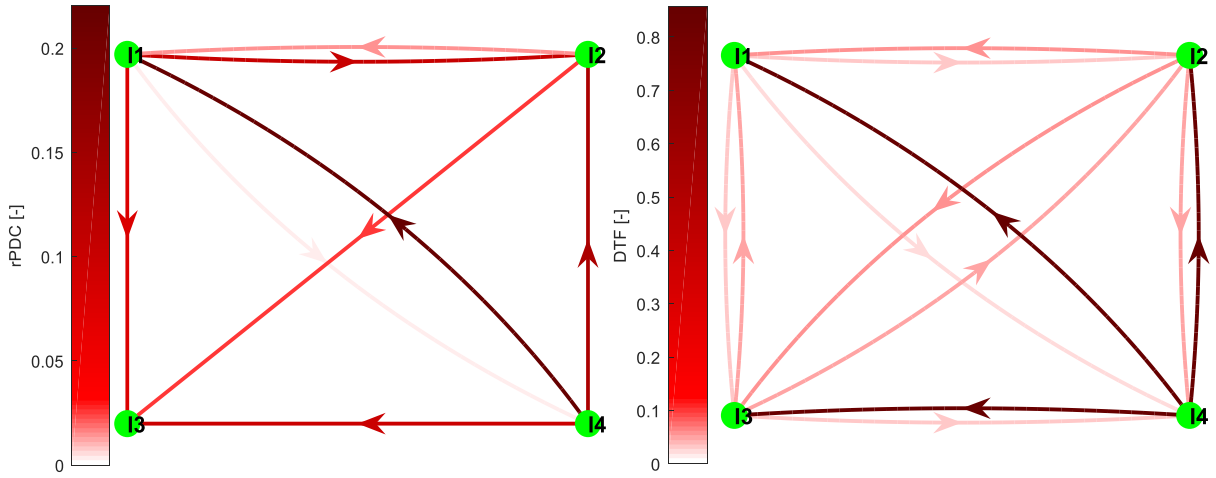

Fig. 116: rPDC (left) and DTF (right) connectivity network graphs between the in-core neutron detectors at the core-bottom axial level due to the vibration of the fuel assembly at the D12 core location.

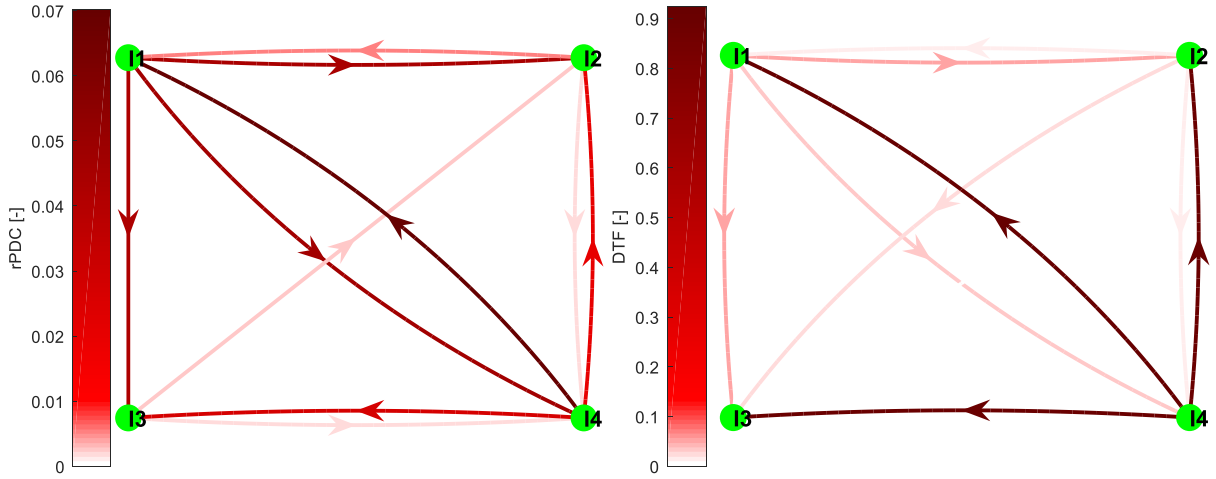

Fig. 117: rPDC (left) and DTF (right) connectivity network graphs between the in-core neutron detectors at the core-top axial level due to the vibration of the fuel assembly at the D12 core location.

The following Fig. 118 shows the connectivity graphs at the core-bottom axial level for the second scenario corresponding to the lateral vibration of $3x3$ cluster of fuel assemblies, located between the in-core instrumentation tubes I2 and I4, at the east side of the core (Fig. 114b). As can be seen, the in-core detectors at the I2 and I4 strings have a clear key role in the analyzed system. However, in this example, it is not straightforward to identify a single root-cause, which is expected, since the vibrating cluster is located equidistantly from the I2 and I4 instrumentation tubes. Consequently, the two detectors closer to the noise source are identified as the ones with a central role. Moreover, similarly to the toy model III in Sec. 6.6.1, a

strong feedback mechanism between the I2 and I4 detectors is observed, indicating that both signals have a common perturbation source, which is however not included in the analyzed model (i.e. the lateral movement of fuel assemblies). Last, the I2 and I4 detectors influence significantly the behavior of the other two detectors, showing that, the information propagates from the east side towards the rest of the core.

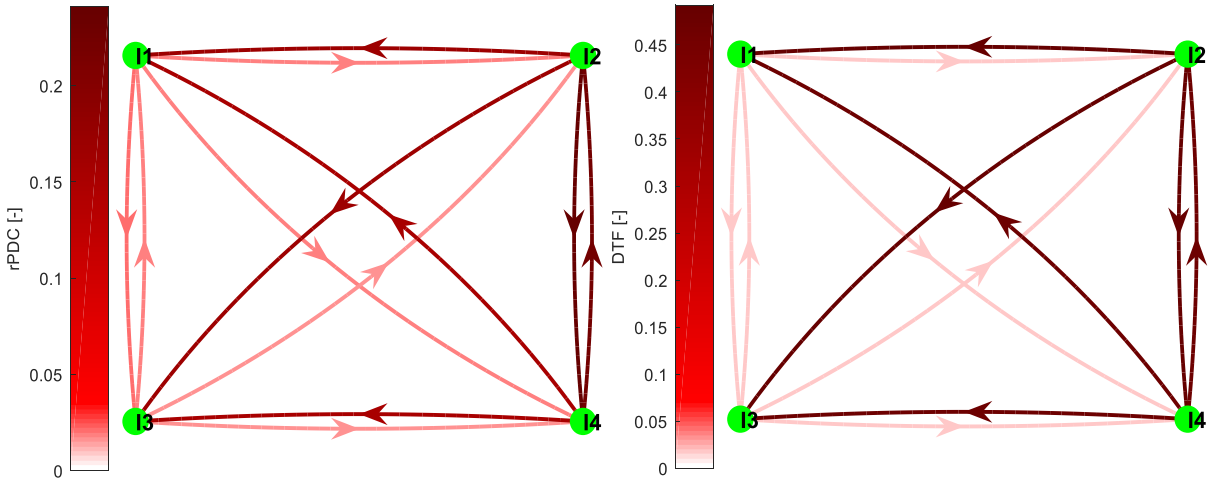

Fig. 118: rPDC (left) and DTF (right) connectivity network graphs between the in-core detectors at the core-bottom level due to the vibration of the $\mathbf{3x3}$ cluster of fuel assemblies at the east-core side.

Fig. 119 presents the connectivity graph results at the core-bottom axial level in terms of rPDC and DTF for the third scenario. In this case, a central cluster of $3x3$ fuel assemblies is modelled to vibrate at $1\ Hz$ (Fig. 114c). Intentionally, the perturbation source is modelled to be equidistant from all four detectors to study the performance of the connectivity analysis method. Both graphs clearly indicate strong interconnections with feedback among all signals. A single root-cause cannot be identified from the given system. This can be explained by the fact that the noise source is not part of the model and all signals are almost equally affected by the perturbation. Consequently, the connectivity analysis methodology reveals its limitation on identifying a single root-cause, even if it can be still possible to infer that the noise source shall be between the four detectors.

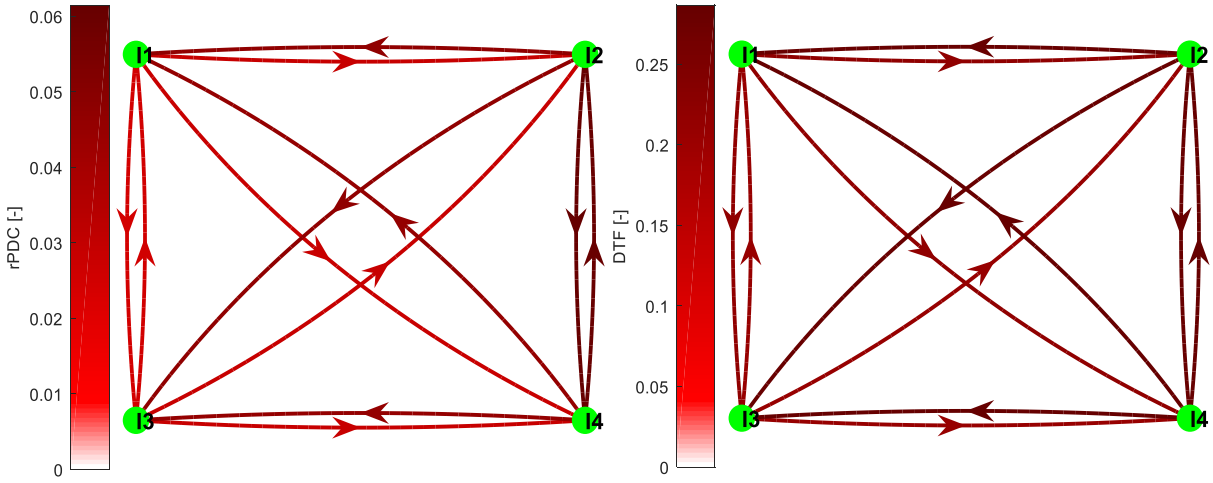

Fig. 119: rPDC (left) and DTF (right) connectivity network graphs between the in-core neutron detectors at the core-bottom axial level due to the vibration of the $\mathbf{3x3}$ central cluster of fuel assemblies.

In the last scenario, the fluctuation of the inlet coolant temperature in the coolant loop 4 is examined (Fig. 114d). Fig. 120 and Fig. 121 present the connectivity graphs in terms of rPDC and DTF between the four

detectors at the core-bottom axial level, and between the three detectors in the instrumentation tube I4 located next to the perturbation source, respectively. In Fig. 120, both connectivity graphs can correctly indicate that the root-cause of this perturbation is in the neighborhood of the I4 detector. The I4 detector strongly drives the behavior of the other three signals, and therefore, this analysis reflects that the information propagates from the south-east side towards the rest of the core. In addition, Fig. 121 focuses on the three in-core detectors (i.e. core-bottom, core-middle, and core-top axial levels), located at the I4 instrumentation string. The selection of the I4 location is justified by the fact that the connectivity analysis indicate that the south-east side of the core is the origin of the disturbance. Clearly, the connectivity analysis shows that there is an information flow from the core-bottom towards the core-top level, which is in agreement with the upward flow of the coolant. Consequently, the cause-and-effect interconnections between the in-core detectors, can indicate the spatial location of the imposed simulated perturbation source.

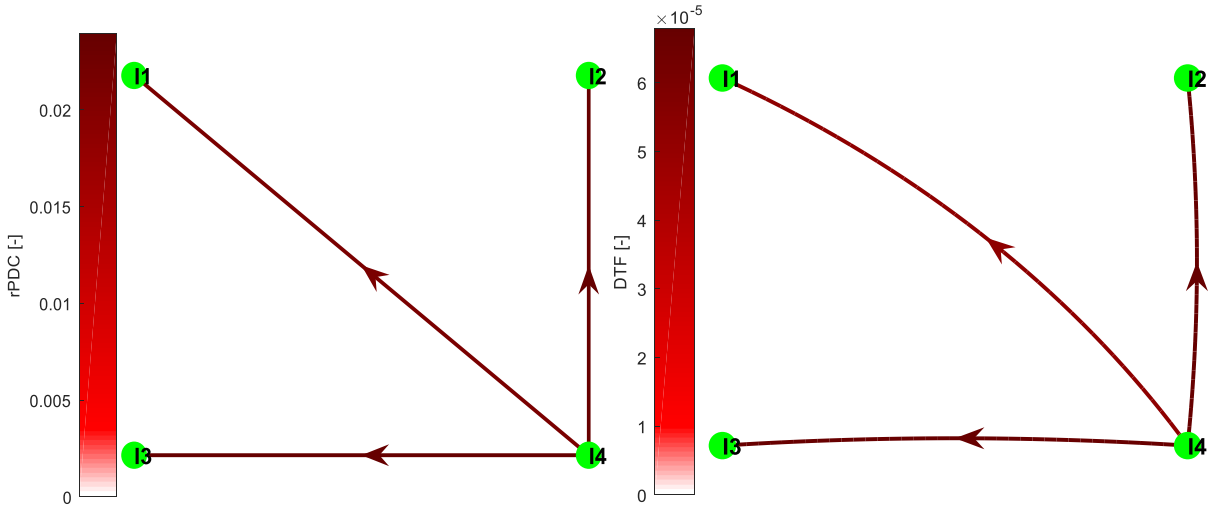

Fig. 120: rPDC (left) and DTF (right) connectivity network graphs between the in-core neutron detectors at the core-bottom axial level due to the inlet coolant temperature fluctuation of coolant loop 4.

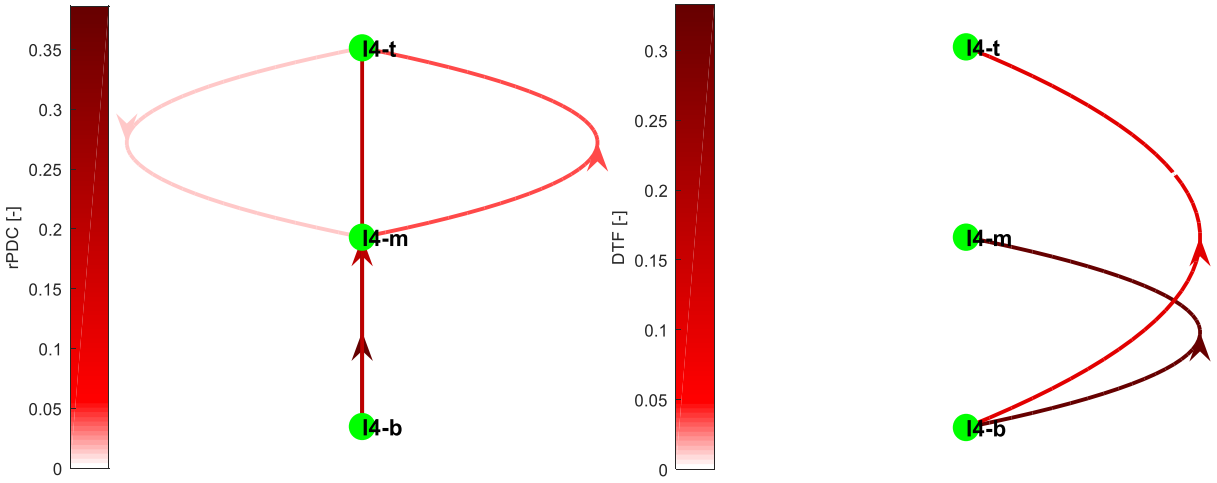

Fig. 121: rPDC (left) and DTF (right) connectivity network graphs between the core-bottom, core-middle, and core-top in-core neutron detectors at the core location I4 due to the inlet coolant temperature fluctuation of coolant loop 4.

6.6.3. Measured nuclear plant data

This last section demonstrates the application of the connectivity analysis methodology on real measured data, recorded from a nuclear reactor. It is recalled that, one of the key goals of this doctoral thesis is the application of advanced signal analysis techniques on nuclear reactor systems for studying the reactor signals interconnectivity behavior during the occurrence of a transient event. By doing so, the understanding of the reactor operation can be enhanced, and the reliable and safe reactor operation during the occurrence of possible malfunctions or disturbances could be enhanced.

The connectivity analysis methodology, introduced and verified in analytical models and simulated nuclear reactor systems in the previous sections, is applied on nuclear reactor data originating from the Swiss KKL BWR. Two available data sets are studied in this section: the *first* corresponds to the start-up of the 24^{th} operational cycle of KKL, with high decay ratios at a frequency of $0.9\ Hz$; and the *second set* was recorded during the generator synchronization stage of the start-up of the 33^{rd} operational cycle of KKL, leading to unexpectedly high decay ratios.

High decay ratios during the start-up of KKL cycle 24

A stability event, with high decay ratios, i.e. close to unity, at a frequency of $0.9\ Hz$, has been recorded at KKL during the start-up of cycle 24. This event has been extensively analyzed at PSI using both traditional signal analysis techniques [6] and the advanced time-series modelling approaches such as CSARMA and STP [8], briefly described in chapter 2. The previous analyses emphasized on studying the relationships between the in-core neutron detector responses, the steam flow (Q_S), and reactor pressure signals. The main conclusion of the previous investigations was that the main contributor to the high decay ratios was caused by a plant system disturbance and not due to any neutronic instability. However, no further estimation or possible indication about the root-cause of this perturbation was able to be given neither in [6] nor [8].

This stability event is studied again in this section, by extending the analysis to further data, including additional signals related to the turbine operation, such as the opening position of the turbine control valves (TCV_A) and the turbine pressure (P_T). Increasing the size of data set enhances the understanding of the connectivity pattern and assists in estimating how the information is propagating within the analyzed system during the occurrence of the stability event. The screening phase of all the available signals indicates that seven signals exhibit a strong spectral peak at the frequency of $0.9\ Hz$. The studied system is, therefore, composed of a neutron detector signal ($APRM$), the inlet core coolant flow (Q_C), the reactor pressure drop (PD_R), the steam flow (Q_S), the jet pump flow (Q_{JP}), the TCV_A, and the P_T. This multi-variate system has been sampled with $8\ Hz$ sampling frequency over $600\ sec$. The signals responses in the time and frequency domains are presented in Fig. 122.

The connectivity analysis methodology is applied on this multi-variate system in order to identify the cause-and-effect interconnections between the analyzed signals. A MVAR model of an order p=5, estimated using the BIC algorithm, is fitted to the measured data set. At a first glance, the connectivity graphs, in Fig. 123, show multiple edges with feedbacks between almost all nodes, especially for rPDC. However, a deeper analysis of the connectivity pattern indicates the importance of the TCV_A signal. First, the rPDC graph (Fig. 123a) indicates the direct directional interconnections between all signals and infers the central role of the opening position of TCV_A. The oscillatory behavior of the TCV_A response at $0.9\ Hz$ clearly influences almost all the other processes. Moreover, the DTF graph (Fig. 123b) highlights more the importance and the central role of the

TCV_A during the stability event, since the information clearly originates from that particular process and eventually propagates throughout the other signals.

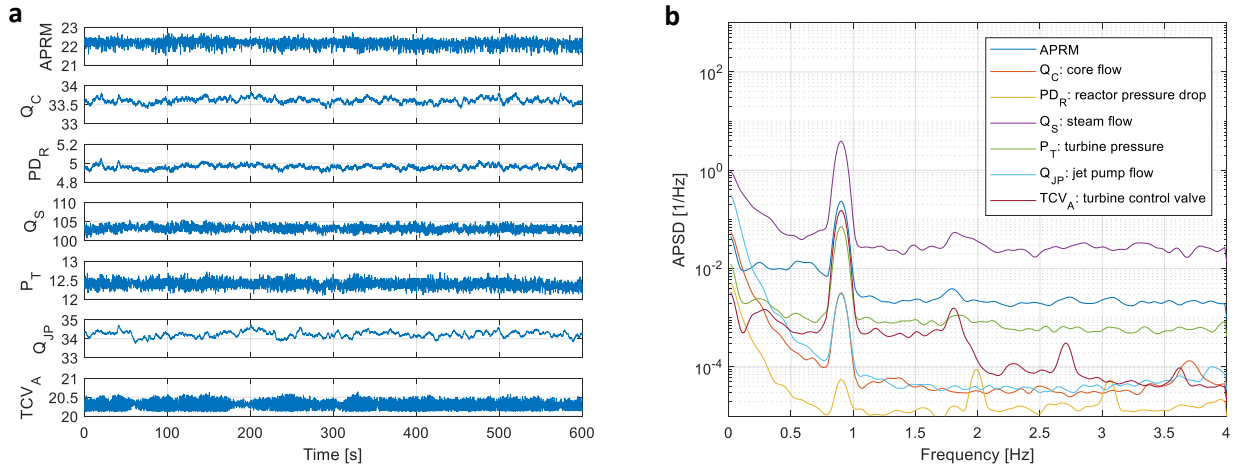

Fig. 122: Nuclear reactor signals during the stability event of KKL cycle 24, in the time (a) and frequency (b) domains.

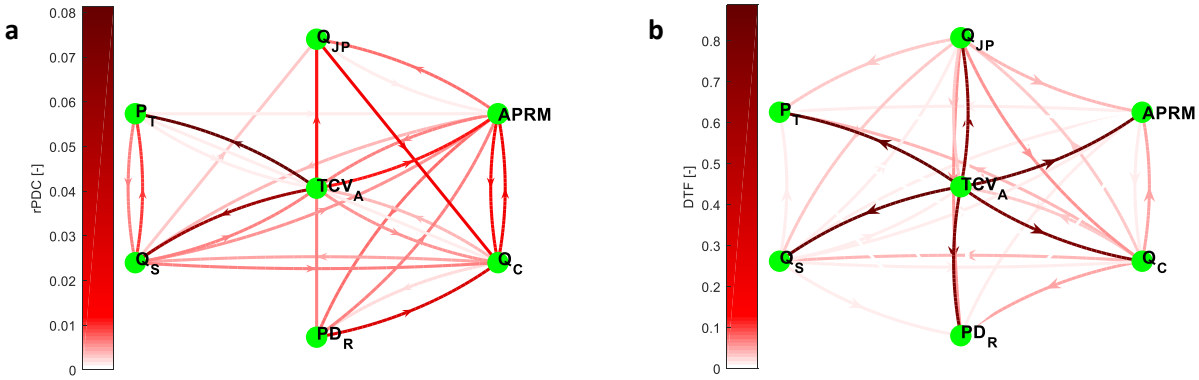

Fig. 123: Connectivity network graphs based on the rPDC (a) and DTF (b) measures for the stability event of KKL cycle 24, at 0.9 Hz.

Clearly, the connectivity graphs based on real data, as the case for the current application, are much more complicated compared to those of the simplified analytical models or simulated systems. Therefore, the interpretation of the structural connectivity pattern might be a challenging task. The connectivity network measures (i.e. nodes degree and strength) can be used as a complementary tool for indicating the signals central roles within the analyzed system. Table 11 shows that, the $APRM$, Q_S, and TCV_A have the highest out-degree values based on the rPDC measure, whereas all signals apart the PD_R and P_T exhibit the highest possible out-degree according to the DTF analysis. Furthermore, both the rPDC and DTF measures show that the TCV_A signal has the highest out-strength values and, therefore, its key role on influencing the behavior of almost all the other signals could be confirmed.

Table 11: Nodes degree and strength based on the rPDC and DTF measures for the stability event of KKL cycle 24 at 0.9 Hz.

		rPDC							DTF						
Measure	**Node**	$APRM$	Q_C	PD_R	Q_S	P_T	Q_{JP}	TCV_A	$APRM$	Q_C	PD_R	Q_S	P_T	Q_{JP}	TCV_A
Node degree	**out**	**5**	4	3	**5**	4	2	**5**	6	6	1	6	0	6	6
	in	6	6	2	4	2	4	4	4	4	5	4	5	5	4
Node strength	**out**	0.04	0.03	0.04	0.03	0.01	0.02	**0.17**	0.09	0.27	0.00	0.10	0.00	0.27	**4.91**
	in	0.05	0.08	0.01	0.07	0.09	0.03	0.02	0.97	0.88	0.92	0.97	1.00	0.79	0.10

High decay ratios during the start-up of KKL cycle 33

The second data set, to be analyzed here, corresponds to operating conditions with low thermal power (18.8%) and low coolant flow rate (33.5 %), during the generator synchronization stage at the start-up of the 33^{rd} operational cycle in KKL. The stability analysis of the in-core detector signals revealed unexpected high decay ratios at very low frequency of 0.27 Hz [139]. However, the reactor is expected to be very stable (i.e. low decay ratios) at such low power and flow operating conditions. Therefore, the connectivity analysis methodology is applied on this data set with the goal to identify what are the causes leading to these high decay ratio values.

First, the plant data have been post-processed using the PSI-TSAR methodology, i.e. the statistical analysis and the screening in the time and frequency domains, which revealed that the steam flow (Q_S), core pressure (P_C), core coolant flow (Q_C), turbine bypass control valve ($TBCV_{NM}$) and average power range monitor ($APRM_A$) are the processes exhibiting distinct oscillatory behavior during this event. The signals were sampled with 8 Hz sampling frequency and were recorded over 100 sec. Fig. 124 shows the time and frequency dependent behavior of the analyzed signals. It is observed that these signals have a strong spectral peak at the frequency of 0.27 Hz. In addition, the opening position of the turbine bypass control valve $TBCV_{NM}$ shows an almost noise-free response (i.e. nearly pure sine wave) during the entire measurement.

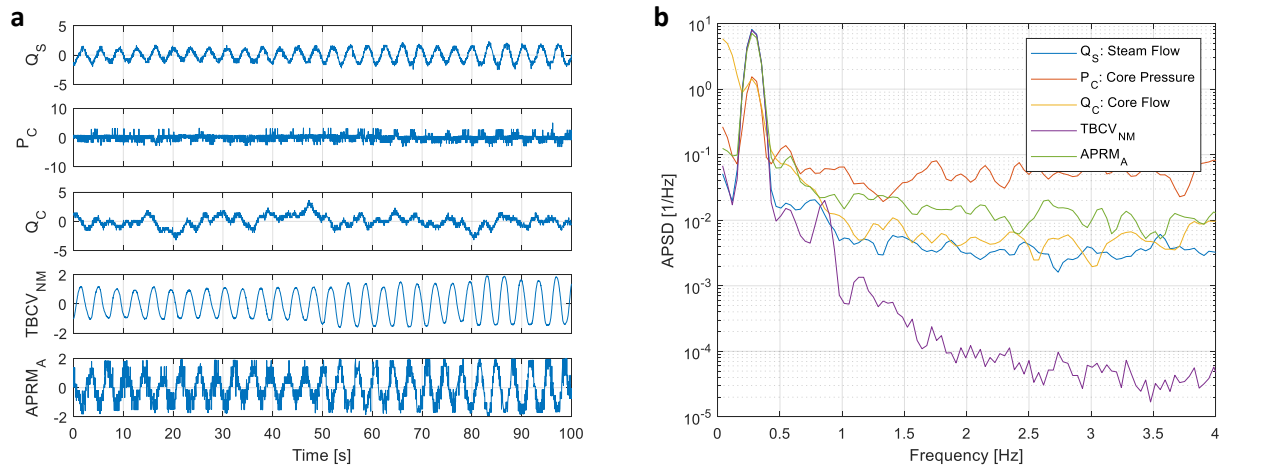

Fig. 124: In-core neutron detector and process signals behavior during the generator synchronization of KKL cycle 33, in the time (a) and frequency (b) domains.

A MVAR model of order p=6, using the BIC algorithm, is fitted to the measured data set, and the connectivity analysis methodology is applied for estimating the causal interactions within this five-variate model. It is observed in the connectivity graphs in Fig. 125 that, the $TBCV_{NM}$ signal has a leading role within the system, in particular, the DTF graph (Fig. 125b) highlights the essential impact of the bypass valve during the synchronization of the generator. The central role of the $TBCV_{NM}$ is explained as follows: The turbine control valves ($TCVs$) are only partially open during the generator synchronization stage, as the steam is damped to the condenser. The opening positions of the $TBCVs$ are adjusted accordingly to the system that controls the steam dome pressure until the generator is fully synchronized. That is why the steam is directed to the $TBCVs$. Consequently, the $TBCVs$ positions are appropriately adjusted to the steam dome pressure, which explains the direct interconnection from P_C to $TBCV_{NM}$ in Fig. 125a. Therefore, the $TBCVs$ have the oscillatory behavior, as presented in Fig. 124a, and influence all the other processes as the connectivity graphs indicate in Fig. 125.

In addition to the connectivity graphs, Table 12 summarizes the connectivity network measures results for the analyzed measurement. The rPDC measure highlights the central behavior that the P_C, $TBCV_{NM}$ and $APRM_A$

have by exhibiting high out-degree values. In addition, the DTF measure indicates that all the observed interconnections are controlled by the opening position of the $TBCV_{NM}$, which has the maximum possible out-degree value. It should be noted that, both the rPDC and the DTF measures demonstrate the high out-strength value of the $TBCV_{NM}$. In a nutshell, results clearly indicate the key role of the turbine bypass valve within the analyzed system during the generator synchronization stage. Clearly, the current analysis illustrate the potential of the connectivity analysis to infer the possible root-causes of the observed disturbances even for highly complex systems like BWRs.

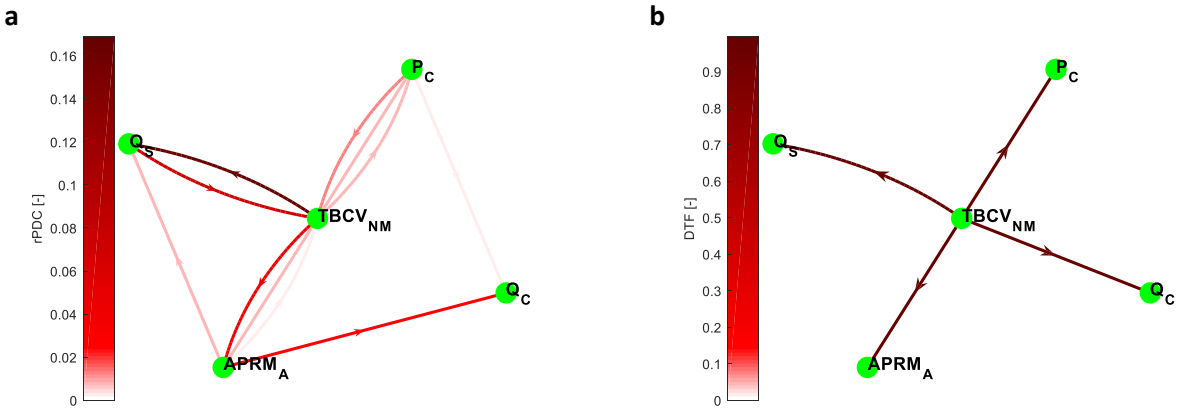

Fig. 125: Connectivity graphs based on the rPDC (a) and DTF (b) measures during the start-up of KKL cycle 33, at 0.27 Hz.

Table 12: Node degree and strength based on the rPDC and DTF measures during the start-up of KKL cycle 33.

		rPDC					DTF				
Measure	**Node**	Q_S	P_C	Q_C	$\boldsymbol{TBCV_{NM}}$	$APRM_A$	Q_S	P_C	Q_C	$\boldsymbol{TBCV_{NM}}$	$APRM_A$
Node degree	**out**	1	3	0	**3**	3	1	1	0	**4**	0
	in	2	1	2	**3**	2	1	1	1	0	1
Node strength	**out**	0.07	0.02	0.00	**0.22**	0.04	0.00	0.00	0.00	**3.98**	0.00
	in	0.18	0.01	0.03	0.09	0.05	1.00	1.00	0.99	0.00	1.00

6.7. Conclusions

In the current chapter the causality analysis techniques have been introduced and applied to many systems, including nuclear reactors applications, which represent a first of its kind, to the author's knowledge. The PSI connectivity analysis methodology utilizes advanced signal processing techniques based on multi-variate autoregressive modelling of a time-series system, and attempts to infer the cause-and-effect relationships between the analyzed signals and, more importantly, to identify the root-cause of a possible observed malfunction or anomaly. The application of causality analysis techniques on nuclear reactor data sets offers a new opportunity to study how the information propagates throughout the reactor components and to understand in depth the interconnectivity patterns of nuclear reactors during the occurrence of transient events. Therefore, gaining better insights of the structural behavior of nuclear processes can provide key information of the reactor functionality and can assist in taking the appropriate actions for the safe and reliable operation of the nuclear reactor.

In this work, it has been attempted to introduce the principles of causality analysis techniques and to highlight its advantages and usefulness, compared to traditional signal processing techniques (e.g. correlation and coherence functions, etc.), which are commonly utilized in nuclear research and industry. The speed and robustness of the causality tools to estimate the signals connectivity patterns has been presented via a series of simplified analytical examples (i.e. toy models), in which pre-defined causal interactions are imposed and the PSI connectivity analysis methodology is assessed with the attempt to identify these interactions correctly. It has been demonstrated that, the rPDC and DTF causality measures are complementary to each other for the precise estimation of the signal interconnectivity relationships and for identifying the root-cause of the imposed perturbation. More interesting, it has been shown that the utilized causality techniques can still be useful even when the analyzed data set is incomplete and does not include all the key involved processes. In this case, the causality estimators are highlighting the signals, which are directly influenced by the missing root-cause as the central source of the perturbation. The engineering judgment of the causality results is therefore crucial for interpreting correctly the causal interactions.

The successful application of the connectivity analysis methodology on numerical examples has allowed to a better understanding of the advantages and limitations of this technique, and it has given confidence for further applications on nuclear reactor systems. First, a BWR system has been modeled with the transient nodal code SIMULATE-3K and a perturbation has been imposed on the feed-water flow. Then, the causality estimators were able to identify the root-cause of the simulated disturbance and to study how the simulated processes interact between each other. In addition, the application of connectivity analysis on simulated perturbations allow the indication of the location of the noise sources. After that, two real plant data sets, originating from the Swiss BWR, KKL, have been studied. Both data sets correspond to measurement showing unexpected high decay ratios, indicating possible core instabilities. With the help of causality analysis it was found that the first event occurred due the turbine control valve opening fluctuations and not induced by the core instability, whereas the second data set indicated that the bypass control valves were driving the reactor system response and the corresponding oscillatory behavior of the neutron flux at the low frequency range. Clearly, it was illustrated that, the connectivity analysis methodology enhances the way how nuclear reactor signals can be analyzed, by improving the understanding of their interconnectivity pattern and the propagation of the information via the reactor processes and components.

It should be noted however that, in order to minimize the risk of identifying erroneous interactions and wrong connectivity patterns, it is substantial to utilize a data set, which is composed of high quality signals. To this aim, the monitoring systems shall have high enough sampling frequency that includes all the spectral components of the involved processes, and more importantly, to simultaneously record as many signals as possible. By doing so, the quality of the data set will be significantly improved, and the probability of identifying the correct causal interactions will be higher.

Chapter 7: Thesis Summary and Conclusions

The key target of the current doctoral research is the improvement and the in-depth understanding of the neutron noise phenomena and their impacts on the dynamic behavior of nuclear reactors. To this aim, a twofold approach is adopted based on the developed tools, which assist in the analysis of the neutron noise behavior. First, a neutron noise modelling methodology using advanced simulation tools is developed in the time-domain, in the framework of this thesis. This approach is one of the first efforts for a systematic modelling of various noise sources in a 3D critical power reactor, and can be utilized for studying the impact of separate as well as combined noise sources on the neutron noise phenomenology. Second, an advanced signal analysis technique, using the so-called causality analysis approach, is developed and applied on simulated and measured reactor data. The causality analysis methodology enhances the comprehension of signals interconnectivity, and could be used to identify the root-cause of a disturbance.

The next paragraphs present in detail the main achievements and the key observations of this research, then Sec. 7.1 *and* Sec. 7.2 *are dedicated to summarize the thesis conclusions and to highlight recommendations for future work, respectively.*

First, an extensive signal analysis of real plant data originating from KKG has been performed using the PSI-TSAR methodology. Plant data have been provided by KKG and they have been analyzed in both the time and the frequency domains. This systematic study revealed the KKG neutron noise characteristics. One the one hand, most of these signatures have been also observed in other KWU pre-Konvoi/Konvoi PWRs. On the other hand, however, this research revealed some particular noise phenomenology, which has never reported in the literature for the same reactor design family, indicating that specific reactor features could influence the associated noise phenomenology signature. The main observations of the KKG signal analysis could be briefly summarized as follows:

- The neutron noise amplitude shows a systematic increase within-a-cycle, as expected, due to the boron concentration decrease along the cycle. In addition, a relative increase of neutron noise level from cycle-to-cycle could also be observed.
- KKG has a particularity of significantly higher neutron noise levels at the core-east side.
- The neutron noise levels tend to be higher at the core-top axial elevation due to a lower moderator density at that part of the core.
- The noise spectrum is characterized by a higher content in the lower frequency range, as expected.
- Spectral peaks at 1.5-2 Hz and 8 Hz could be clearly identified and they could be related to the fuel assembly vibrations and the core barrel motion, respectively.
- The inlet coolant temperature transit time could be estimated based on the phase difference between neutron detectors located at different axial levels.
- Two core-halves could be distinguished in which they exhibit an out-of-phase behavior at about 2 Hz, indicating the presence of a noise source located at the core center.

The identification of the KKG neutron noise characteristics was a crucial part of this thesis. The obtained neutron noise phenomenology was then used as a basis to be reproduced using the advanced transient nodal solver SIMULATE-3K. To this aim, the PSI neutron noise modelling methodology has been developed within this research. The PSI methodology is based on the CMSYS codes, i.e. CASMO/SIMULATE-3/SIMULATE-3K, and allows the modelling of fuel assembly vibrations and the inlet coolant temperature and flow fluctuations. A

stepwise approach has been used to systematically verify and qualify the newly developed methodology, and to demonstrate its capabilities to reliably model the neutron noise. In addition, the systematic study of a large range of simulated perturbation scenarios resulted to a series of valuable observation, summarized as follows:

- The modelling of a fuel assembly vibration (by modifying the nodal cross-sections) affects mainly the adjacent fuel assemblies, located in the direction of the vibration, where the highest neutron noise levels are obtained.
- Higher neutron noise levels were observed at the core-top axial levels, mainly due to the decrease of the moderator density.
- The neutron noise axial distribution is directly affected by the bow shape of a vibrating bundle and by the fuel vibration mode. In other words, highest noise amplitudes are observed at the elevations with the highest axial displacement, e.g. at the core-middle for a C-shape bowed assembly, at the core-top for a first mode (cantilevered mode) vibrating assembly, etc.
- The random fluctuation (uncolored) of the inlet coolant flow and temperature results in a colored spectrum, with a higher content in the low frequency range.
- The inlet coolant temperature fluctuations were observed to have more impact on the neutron noise compared to that due to the inlet coolant flow fluctuations.
- When the three main noise sources (i.e. fuel assembly vibration, and inlet coolant temperature and flow fluctuations) are combined, it is found that, the inlet coolant temperature fluctuation has a leading role in the lower frequency range up to $2\,Hz$, then beyond that range, the fuel assembly vibration effects become more dominant, compared to the other effects.
- The transit time of the transport phenomenon is correlated to the slope of the phase difference between detectors belonging to the same string but located at different axial levels when the inlet coolant temperature fluctuation is modelled.
- The inlet flow perturbations are found to propagate instantaneously across the core, which make the detectors located at different axial levels fully synchronized (in-phase).
- The neutron noise increase trend over the cycles, being observed in KKG for more than a decade, could be qualitatively explained by modelling the realistic loading of the newer fuel design, which is more susceptible to lateral vibrations. However, additional analyses and comparison against measured data have to be performed in a future work for reaching a definite conclusion.

Last, a new supportive diagnostic tool based on the causality analysis principles was developed within this research. The main goal was to develop an in-house methodology for providing in more details the signal connectivity information flow paths within complex systems. This information can be used in root-cause analysis identification and in the early detection of possible malfunction operations. To the author's knowledge, this work is the first systematic attempt in establishing a robust connectivity analysis methodology for nuclear reactor applications. The newly developed PSI connectivity analysis methodology has been applied in a series of simulated and measured datasets. The signals connectivity patterns can be identified based on the most eminent causality measures, namely the rPDC and the DTF measures. The first, provides information about the direct signal interconnections, and the latter, can be used for estimating how the information propagates from a noise source to the rest of the system. The combination of rPDC and DTF causality measures allows the root-cause identification of a perturbation or a system disturbance. The main observations of this analysis are the following:

- The effectiveness and robustness of the new developed methodology has been demonstrated successfully through a series of analytical examples. The signals interconnections in predefined connectivity patterns were able to be correctly identified using the rPDC and DTF causality measures.
- The area of applicability of the PSI connectivity analysis was able to be identified, with the help of numerical examples. In other words, the perturbation root-cause could be accurately identified always when its response is taken into account in the analyzed dataset. In addition, the difficulty to interpret correctly the connectivity patter increases as the signals interconnections become more complex. Therefore, a critical assessment of the connectivity results should be always made based on the analyst knowledge on the system physical mechanisms to avoid erroneous conclusions.
- The utilized causality measures could still provide useful information about the interpretation of the information flow paths and the root-cause of a perturbation even if the analyzed dataset is incomplete. This means that, if an analyzed dataset does not contain all the key signals, in particular the absence of the actual noise source, this could introduce challenges for the root-cause identification. However, despite that, the PSI connectivity analysis methodology demonstrates its capability to indicate the first available signal, which is directly influenced by the missing root-cause, as the driving perturbation in the analyzed model
- The connectivity analysis application on nuclear reactor simulated data, where the perturbation source is known a priori, successfully identifies the perturbation root-cause as well as the information flow path of its propagation within the reactor core.
- The causality analysis of real plant data, related to incidents occurred in some reactor cores, has demonstrated the capability of the developed methodology to identify the key information about the disturbance root-cause, although the engineering judgment of the analyst has to be always considered.

7.1. Main conclusions

Based on the various observed results obtained along this doctoral thesis, the main conclusions could be summarized as follows:

- The PSI neutron noise analysis methodology, PSI-TSAR, was successfully utilized for the identification of the KKG neutron noise characteristics.
- The KKG neutron noise phenomenology has been systematically studied and key neutron noise characteristics were successfully reproduced using the PSI neutron noise modelling methodology.
- The performed analysis confirms the statement that, the strong spectrum at low frequencies is clearly related to the inlet coolant temperature fluctuations.
- The spectral peak at the frequency of $1.8\text{-}2\ Hz$ could be related to the lateral vibration of fuel assemblies, since such vibrations represent the only explanation of the observed out-of-phase relationship between the two halves of the KKG core.
- The neutron noise level increase trend could be explained by the new fuel design introduced in KKG core along more than a decade.
- Few KKG noise characteristics, mainly the higher noise levels at the core-east side, the dip at $6\ Hz$ of the coherence function between detectors at different axial levels, and the low radial coherence values at frequencies above $4\ Hz$, could not be explained. Therefore, further investigations on the neutron noise analysis are highly recommended, as described in more details in the next section.

- CASMO-5 generates nuclear data to be used for downstream 3D full core modelling of fuel assembly vibration. It has been found that, despite the modelling simplifications and assumptions, the generated nuclear data can be accurately used to mimic the lattice lateral displacement.
- SIMULATE-3K was found to be a reliable and robust solver for modelling neutron noise phenomena, even if it is not a dedicated neutron noise solver. Its applicability and robustness was demonstrated via a series of simulated scenarios, ranging from simplified up to more complicated cases.
- A platform for generating neutron noise simulated data using the SIMULATE-3K code in the framework of the CORTEX project was developed. The generated noise data was provided to the CORTEX project partners for further analysis. This collaboration enhanced the utilization of advanced techniques for modelling and analyzing the neutron noise phenomena.
- The PSI connectivity and causality analysis methodology has been developed and successfully applied in nuclear reactor datasets. The current thesis demonstrated that, the developed methodology could be used not only for the identification of the information flow path within the system but also as a valuable supportive tool for the early identification of the root-cause of possible plant anomalies.

7.2. Future work recommendation

The current doctoral thesis is clearly just a first attempt to understand in-depth the complex neutron noise phenomenon through a systematic and comprehensive methodology using advanced simulation techniques. Therefore, to the author's opinion, various improvements and investigations are still needed to understand better many observed characteristics that are still not explained. The following are the main recommendations:

- Signal analysis techniques are strongly dependent on both the quality and quantity of the measured signals. Therefore, more detailed and systematic measuring campaigns at KKG, or a similar KWU pre-Konvoi PWR, at high sampling frequency and in more frequent burnup intervals will provide a better representation of the signals characteristics, and consequently a more detailed understanding of the neutron noise phenomenology. For instance, concerning the causality analysis, measured data sets with broader variety of signals at high sampling frequency, including both neutron detectors and process responses, will improve the understanding of the system behavior and assist in the better estimation of their connectivity patterns.

- In addition to causality analysis activities, the PSI-TSAR can be further enhanced by incorporating advanced machine learning techniques that will be developed in the framework of CORTEX project. To this aim, deep-learning methods based on recurrent neural networks to perform classification and localization of in-core perturbations by unfolding in-core and ex-core neutron detector signals from the reactors can be implemented in the PSI activities. This involves training the deep-learning methods with the "labelled" simulated data first, calculated with known perturbations and obtained prior with the CMSYS codes. In addition, advanced signal analysis methods to detect in-core anomalous patterns from the induced neutron noise can be further improved. As the detector signals are available at few core locations, current techniques, although very promising, are not sufficient as a standalone approach for neutron noise diagnostics. Therefore, in the future, it is aimed to implement these neutron noise identification and characterization strategies in the PSI methodology to achieve a comprehensive model for neutron noise diagnostics.

- The fuel assembly vibration model in SIMULATE-3K is based on nuclear data generated using the CASMO-5 delta gap model. It has been demonstrated that, the currently utilized approach, i.e. delta gap model, needs to improve its accuracy. One straight forward way, is to make possible the use nuclear data generated with the CASMO-5 fuel displacement model for the fuel vibration modelling in SIMULATE-3K.

- The SIMULATE-3K code could be further developed allowing the user to impose a perturbation on selected nodal cross-sections. This technique is followed in the CORE-SIM solver offering a better control of the applied noise sources. In addition to that, a finer radial grid discretization will allow the modelling of local noise sources reflecting more accurate the real phenomena.

- The core barrel vibration and its impact on neutron noise phenomenology has not been modelled in the current thesis. Therefore, it is recommended that such vibration mode should be modeled and analyzed in a similar manner as with the fuel assembly vibration. The core barrel can be modelled to laterally vibrate by modifying appropriately the water gap widths between the outer peripheral bundles and the reflector, using SIMULATE-3K. By doing so, it will be possible to model more accurately the key phenomena affecting the neutron noise behavior, and consequently, the comparison against plant data will be improved.

- The current available fuel assembly vibration model, in SIMULATE-3K, could be applied so far only on PWR cores. Extending the model capabilities to BWR applications would be valuable, since vibrating fuel channels could affect significantly the precision of the in-core neutron detector responses, which are crucial for both the on-line monitoring of the core and the validation of the 3D nodal simulators.

Even if the CMSYS capabilities on neutron noise modelling could not be validated against real plant data in a quantitative manner, it is still possible to compare the SIMULATE-3K results against expected analytical formulation. This can be performed by extracting the point-kinetic component of a system perturbation based on the SIMULATE-3K results, and comparing against the point-kinetic zero-power reactor transfer function of the analyzed core, as presented in [62]. The proposed formulation has been already successfully applied for the verification and validation of many neutron noise solvers in neutron transport models ([62], [80]).

Appendix i: KKG signal analysis (continuation)

The current appendix provides additional noise phenomenology plots based on the KKG data. In particular, the axial phenomenology in terms of coherence and phase difference functions is presented in the following figures. The core-locations C08, G10, N08, and G02 are used as a reference. These plots are supplementary material for the analysis presented in Sec. 2.3.2.2.

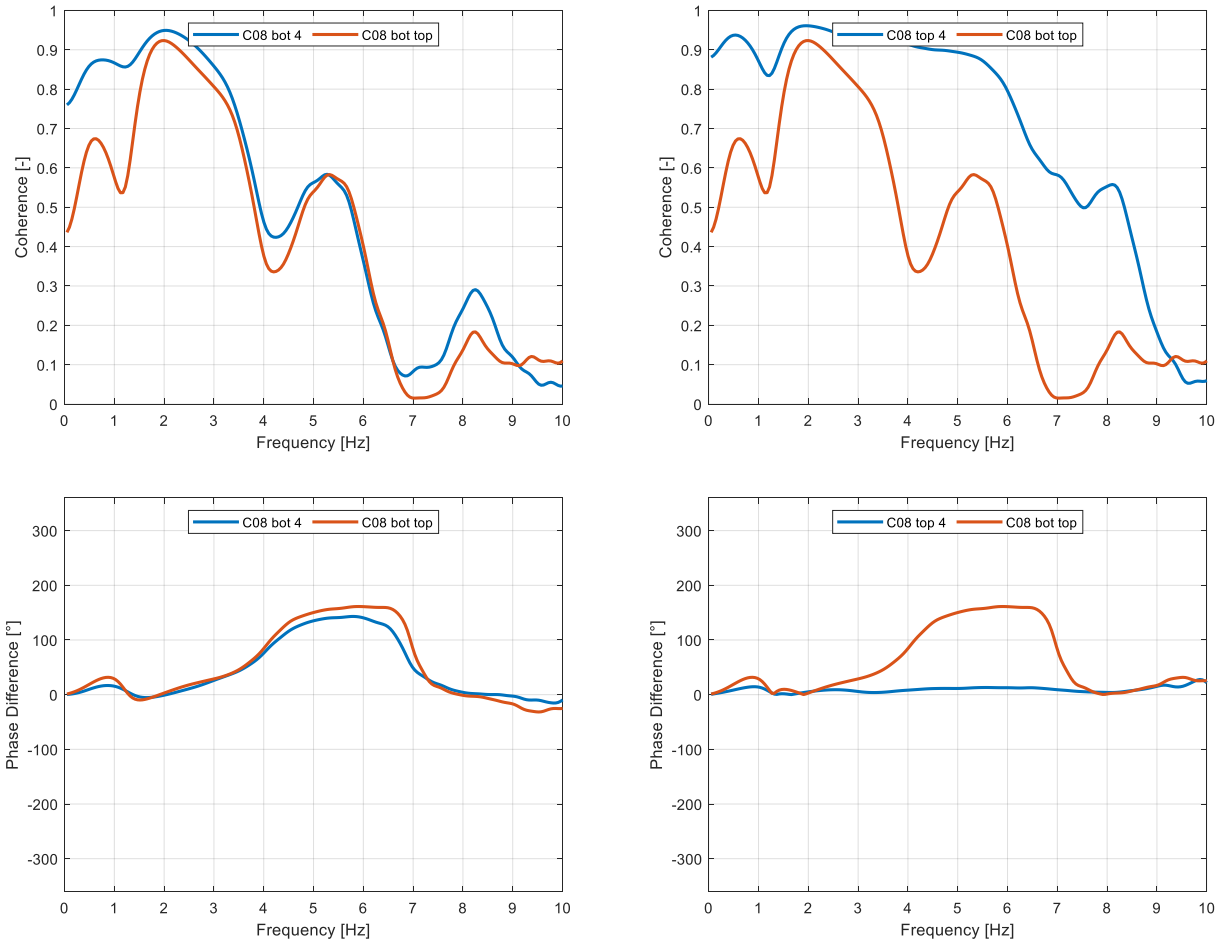

Fig. 126: Coherence (top plots) and phase difference (bottom plots) between measured in-core detector signals at south-core azimuthal location C08 using as reference the core-bottom in-core detector (left plots) and the core-top in-core detector (right plots).

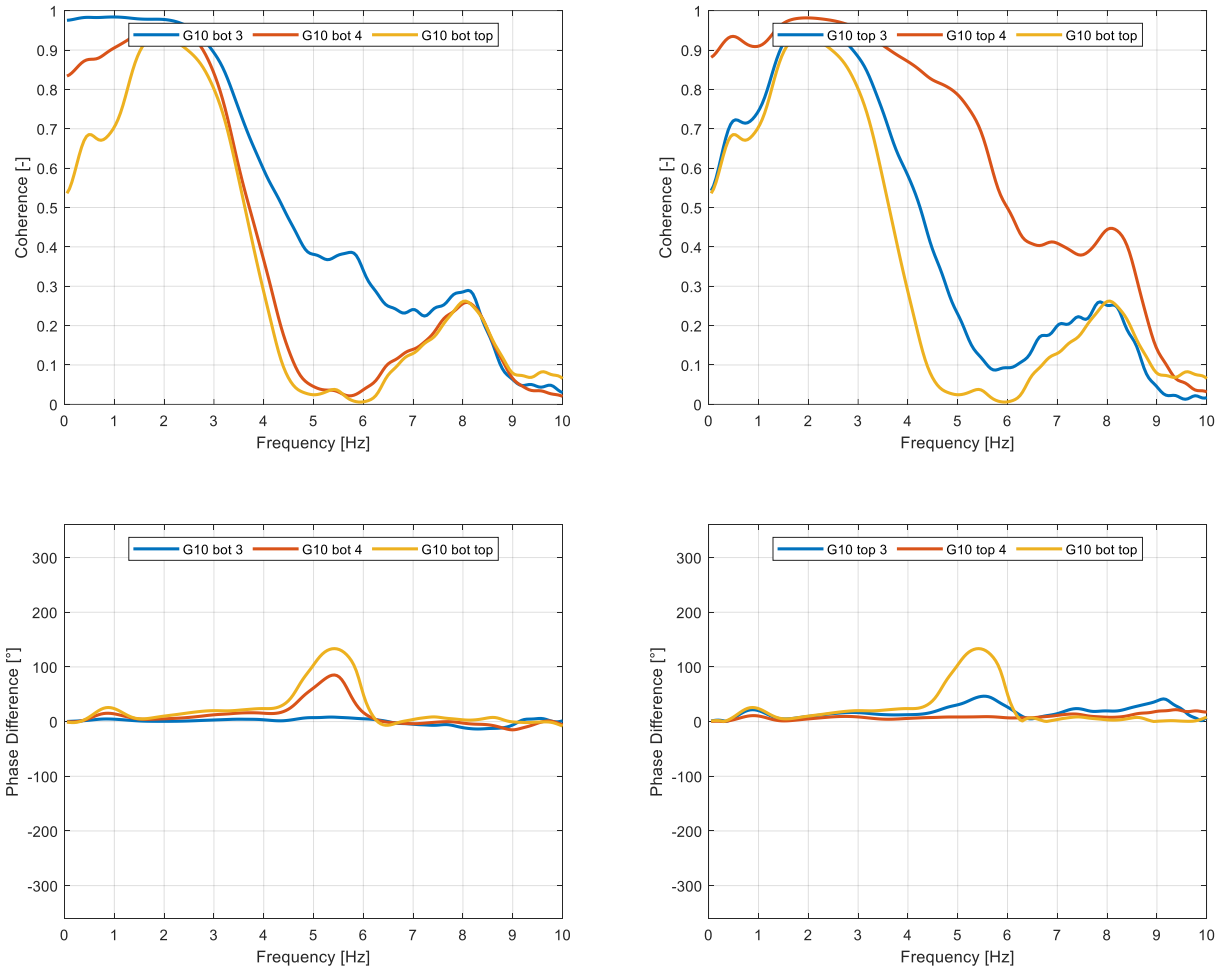

Fig. 127: Coherence (top plots) and phase difference (bottom plots) between measured in-core detector signals at central-core azimuthal location G10 using as reference the core-bottom in-core detector (left plots) and the core-top in-core detector (right plots).

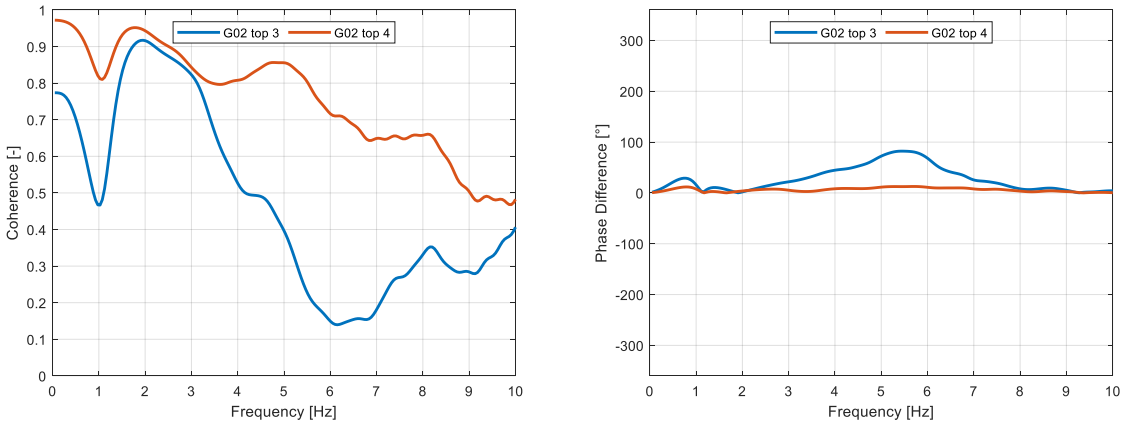

Fig. 128: Coherence (left) and phase difference (right) between measured in-core detector signals at west-core azimuthal location G02 using as reference the core-top in-core detector.

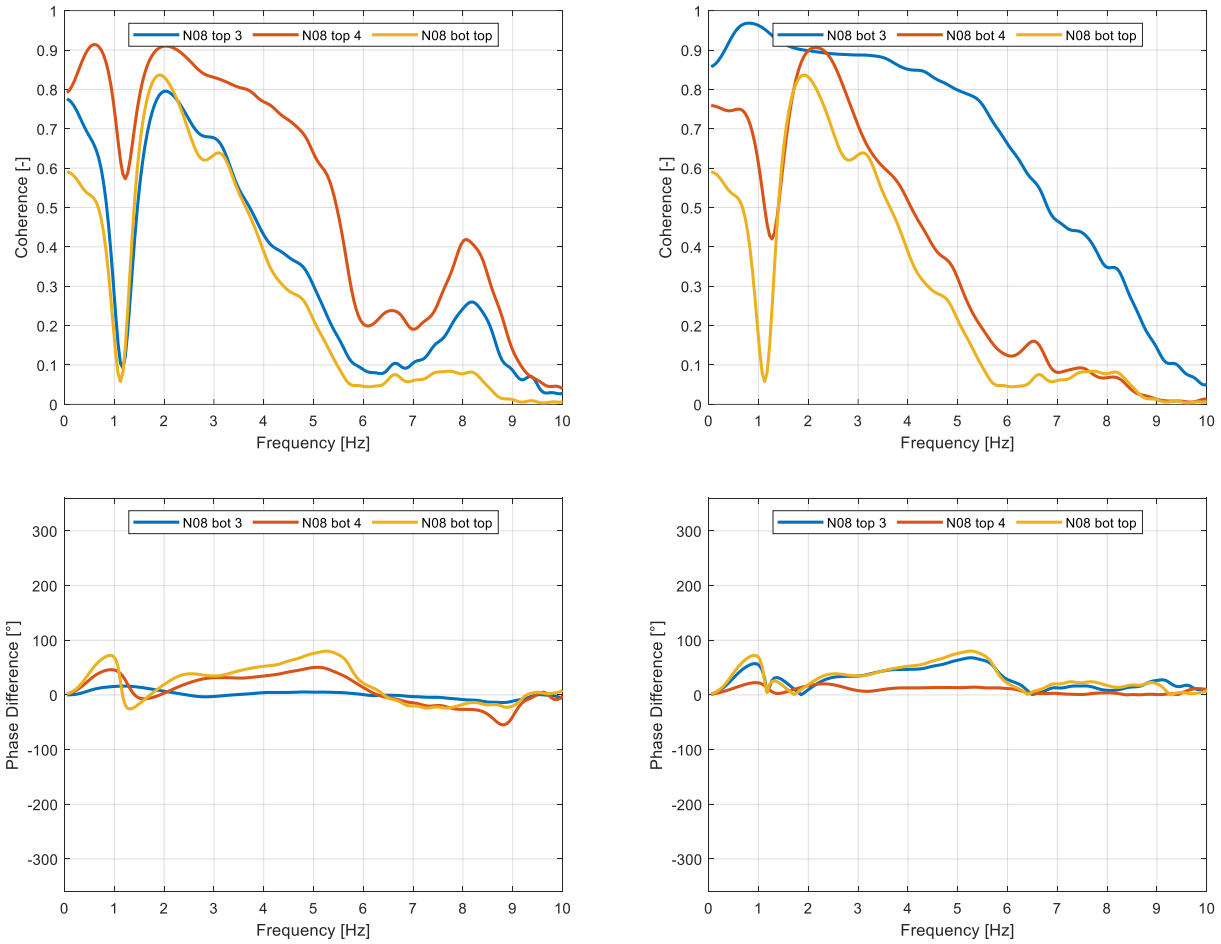

Fig. 129: Coherence (top plots) and phase difference (bottom plots) between measured in-core detector signals at north-core azimuthal location N08 using as reference the core-bottom in-core detector (left plots) and the core-top in-core detector (right plots).

Appendix ii: 2D water gap widths input preparation

The details of the developed MATLAB program for the automatized generation of the full core water gap widths between vibrating fuel assemblies is presented in this appendix. The reader is introduced in the PSI script functionality and capabilities through the following example. Let's assume that the user wants to prepare the SIMULATE-3K input deck for the case of a $3x3$ vibrating cluster at the center of the KKG core. The $3x3$ central cluster corresponds to the fuel bundles, located at the locations $J7$, $J8$, $J9$, $H7$, $H8$, $H9$, $G7$, $G8$, and $G9$, according to the KKG core map in Fig. 7. These nine fuel bundles are going to vibrate with an amplitude of $0.2\ cm$ in both x- and y-directions, following a pure sine-wave function at a nominal frequency of $1\ Hz$. Last, all the selected fuel assemblies will vibrate in a synchronized movement between each other. In other words, exactly the same vibration pattern will be imposed on all nine oscillating bundles, at each time step.

The goal of the PSI automatized tool is to generate the text files *gaps_x_Direction.inc* and *gaps_y_Direction.inc,* which describe the time-dependent water gaps widths between the nine selected bundles and their first neighboring assemblies in the x- and y-directions, respectively. These two text files will be then "called" by the main SIMULATE-3K input file, as presented in Fig. 30. According to the PSI tool, first, the user has to define the main simulation parameters in the MATLAB script (*step 1,* Fig. 130). In the current example, the parameters *TimeStep*, *Duration*, and *VibAmb* of the MATLAB structure *Set* define the simulation time step, its duration, and the maximum vibration amplitude, respectively. These are the only three parameters that require the intervention of the user in the MATLAB script. All the other simulation options are defined by the user using a series of user-friendly graphical user interfaces (GUIs), which appear subsequently on the screen after the script execution.

```
%% Define main simulation parameters
Set.TimeStep=0.01;                      % in [sec] / It is recommended to be the same with the time step as defined in S3K input (card KIN.TIM)
Set.Duration=35;                        % in [sec] / It is recommended to be the same with the time step as defined in S3K input (card KIN.TIM)
Set.Length=Set.Duration/Set.TimeStep;   % Number of data points in the time domain
Set.VibAmp=0.11;                        % Maximum dispacement amplitude of the FAs in [cm]. The FA will vibrate randomly between -VibAmp and +VibAmp

% Define the time domain
t=0:Set.TimeStep:Set.Duration;          % The time domain [s] is recommended to be like the one in the S3K simulation
```

Fig. 130: Initialization of PSI automated MATLAB script for the preparation of the SIMULATE-3K input deck for simulating the lateral vibration of fuel bundles.

In the first GUI, the user has to select whether or not the same vibration characteristics (i.e. amplitude, frequency, type) will be applied on all the selected bundles (Fig. 131a). In this example, it is assumed that, a single vibration pattern will be used, and therefore, the generated time-dependent water gap widths will be imposed identically to all nine selected bundles. Then, a core map of the analyzed reactor appears on the screen and the user selects, by clicking on, those bundles, which will undergo the simulated lateral vibration (*step 2*, Fig. 131b). The third GUI allows the user to select the direction of fuel bundles vibration (i.e. in the x- and/or y-directions; *step 3*, Fig. 131c).

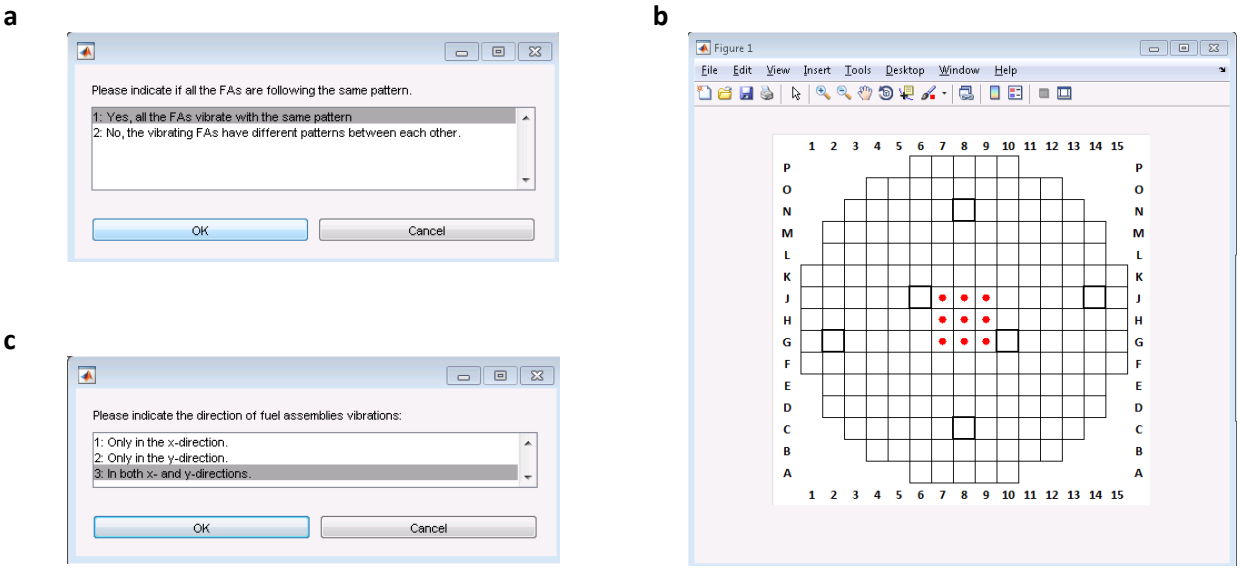

Fig. 131: First three GUIs of the PSI toolbox for the automatized generation of the water gap widths for the SIMULATE-3K input file.

In the last two GUIs (*steps 3* and *4*, Fig. 132), the user selects the type of the vibration mode (i.e. random movement or lateral oscillation following a sinus behavior), the presence or not of synchronized movement between the selected bundles, and the nominal frequency of vibration in the case of sinus type vibration.

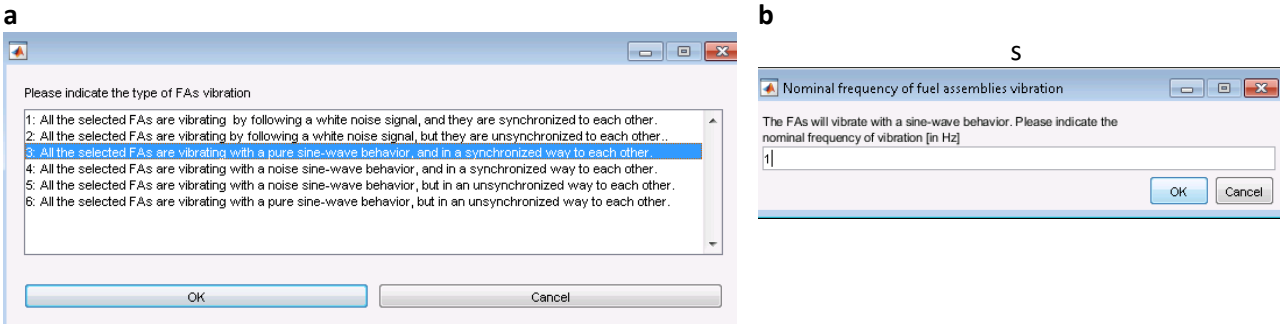

Fig. 132: Selection of vibrational pattern via GUIs in the PSI toolbox for the preparation of the SIMULATE-3K input file.

Based on the user selections of this example, the change of water gap widths between all the vibrated bundles will be estimated according to the basic sinusoid form as a function of time (Eq. 59):

$$\delta gap_x(t) = A \cdot \sin(2\pi f t)$$

$$\delta gap_y(t) = A \cdot \sin(2\pi f t) \qquad \text{Eq. 59}$$

where, A and f are the vibration amplitude and nominal frequency, respectively, defined by the user in the PSI toolbox (i.e. Fig. 130). In the current example, all the fuel bundles are vibrating identically between each other and they follow the same sinus movement in both directions. The evolution of the change of the water gap widths for all the nine bundles of the vibrating central cluster and the first neighboring bundles is presented in Fig. 133, where the plot a shows the time dependent behavior of the change of the water gap widths in both directions, and plot b describes the movement of a single vibrating bundle in space. As can be observed, the sinus oscillation of a fuel bundle with the same vibrational characteristics (i.e. frequency and amplitude) for both directions results in a diagonal movement over its nominal position (Fig. 133b).

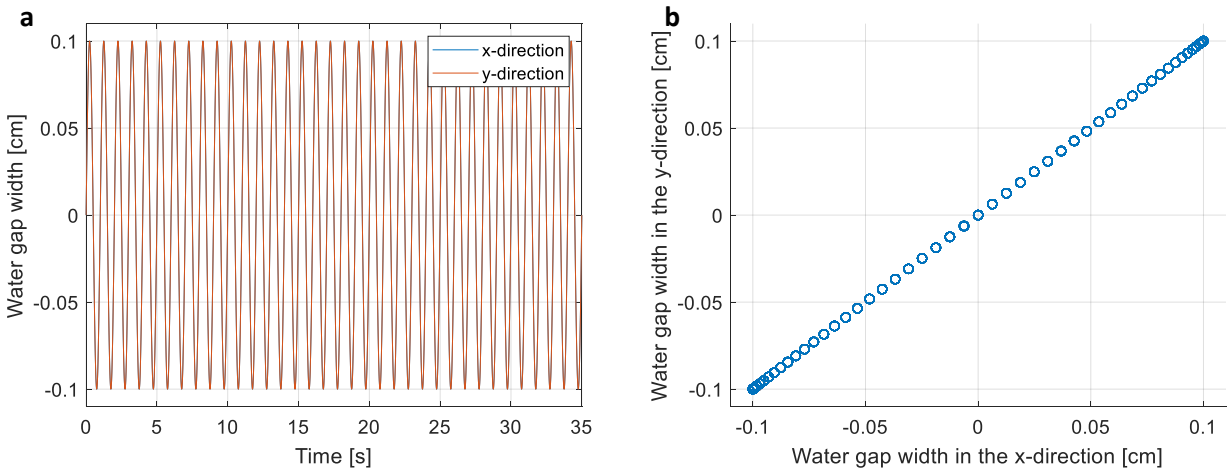

Fig. 133: Evaluated change of the water gap widths in time (plot a) and space (plot b) in the case of a fuel bundle vibration of a sinus behavior with an amplitude of $\mathbf{1}\boldsymbol{mm}$ at a nominal frequency of $\mathbf{1}\ \boldsymbol{Hz}$ in two directions.

Last, the time-dependent description of the change of the water gap widths in both directions for all the selected assemblies is automatically printed out in the text files *gaps_x_Direction.inc* and *gaps_y_Direction.inc*, which are then used in the SIMULATE-3K input file. The top parts of these two text files describe the change of the water gap widths of the nine bundles over the very first time steps of the simulation, as illustrated in Fig. 134.

First, the *KIN.XVL* card (*gaps_x_Direction.inc*, Fig. 134 left plot) shows the change of the water gap widths for the nine bundles in the x-direction. These are modified at every time step, therefore, nine entries per time step are included in the file (i.e. the file has in total $3'501$ x 9 entries). For instance, the central cluster is moving to the east-core side by an increment amount $\delta gap_x(t_2)$=$0.007\ cm$, at the second time step t_2=$0.01\ s$. The first entry of that time step appears in the 11^{th} line of text file and is composed of six numbers; "$0.010\ 7\ 7\ 8\ 0.007\ 0.000$". The first number indicates the time step (i.e. t_2=$0.01\ s$). The second number corresponds to the y-axis coordinate (i.e. core-row j) of the studied bundle, and the third and fourth numbers give the x-axis coordinates (i.e. core gaps columns i and i+1) of the water gaps on both sides of that specific bundle. The first bundle of the vibrating cluster is located at the position $J7$, which corresponds to the J-row of the core (i.e. j=7) and its water gaps are in columns 7 (i.e. i=7 for the gap between $J6$ and $J7$ bundles) and 8 (i.e. i+1=8 for the gap between $J7$ and $J8$ bundles). The last two numbers show that the change of the water gap width between $J6$ and $J7$ bundles is $\delta gap_{7,7}$=$0.007\ cm$, and between $J7$ and $J8$ bundles is $gap_{7,8}$=$0.000\ cm$, at time step t_2=$0.01\ s$. It should be noted that, the latter gap width change is zero since the $3x3$ cluster is laterally moving in a synchronized way, and therefore, the change of the water gap widths in both sides of the central bundles will remain unchanged during the simulation. Consequently, the only change of the water gap widths will be for those bundles, located at the periphery of the vibrating cluster, in the case of the synchronized vibration of a cluster. In other words, the change of the water gap widths between $J6$ and $J7$ (i.e. $gap_{7,7}$), $H6$ and $H7$ (i.e. $gap_{8,7}$), and $G6$ and $G7$ (i.e. $gap_{9,7}$) increases by δgap_x=$0.007\ cm$, and the change of the water gap widths between $J9$ and $J10$ (i.e. $gap_{7,10}$), $H9$ and $H10$ (i.e. $gap_{8,10}$), and $G9$ and $G10$ (i.e. $gap_{9,10}$) decreases by the same value, i.e. δgap_x=-$0.007\ cm$, at time step t_2=$0.01\ s$. The process of the lateral movement of the $3x3$ central cluster from the nominal position, at t_1 = $0.00\ s$, towards a displacement of δgap_x = $0.007\ cm$, at t_2=$0.01\ s$, is illustrated in Fig. 135. The described process is repeated at every time step and the change of the water gap widths are modified according to Eq. 59.

```
'KIN.XVL',   3501,     9,
0.000   7  7  8  0.000  0.000
        7  8  9  0.000  0.000
        7  9 10  0.000 -0.000
        8  7  8  0.000  0.000
        8  8  9  0.000  0.000
        8  9 10  0.000 -0.000
        9  7  8  0.000  0.000
        9  8  9  0.000  0.000
        9  9 10  0.000 -0.000
0.010   7  7  8  0.007  0.000
        7  8  9  0.000  0.000
        7  9 10  0.000 -0.007
        8  7  8  0.007  0.000
        8  8  9  0.000  0.000
        8  9 10  0.000 -0.007
        9  7  8  0.007  0.000
        9  8  9  0.000  0.000
        9  9 10  0.000 -0.007
0.020   7  7  8  0.014  0.000
        7  8  9  0.000  0.000
        7  9 10  0.000 -0.014
        8  7  8  0.014  0.000
        8  8  9  0.000  0.000
        8  9 10  0.000 -0.014
        9  7  8  0.014  0.000
        9  8  9  0.000  0.000
        9  9 10  0.000 -0.014
0.030   7  7  8  0.021  0.000
        7  8  9  0.000  0.000
        7  9 10  0.000 -0.021
        8  7  8  0.021  0.000
        8  8  9  0.000  0.000
        8  9 10  0.000 -0.021
        9  7  8  0.021  0.000
        9  8  9  0.000  0.000
        9  9 10  0.000 -0.021
```

```
'KIN.YVL',   3501,    18,
0.000   7  7  8  0.000  0.000
        8  7  8  0.000  0.000
        7  8  9  0.000  0.000
        8  8  9  0.000  0.000
        7  9 10  0.000  0.000
        8  9 10  0.000  0.000
        8  7  8  0.000  0.000
        9  7  8  0.000  0.000
        8  8  9  0.000  0.000
        9  8  9  0.000  0.000
        8  9 10  0.000  0.000
        9  9 10  0.000  0.000
        9  7  8  0.000  0.000
       10  7  8  0.000  0.000
        9  8  9  0.000  0.000
       10  8  9  0.000  0.000
        9  9 10  0.000  0.000
       10  9 10  0.000  0.000
0.010   7  7  8  0.007  0.007
        8  7  8  0.000  0.000
        7  8  9  0.007  0.007
        8  8  9  0.000  0.000
        7  9 10  0.000  0.000
        8  9 10  0.000  0.000
        8  7  8  0.000  0.000
        9  7  8  0.000  0.000
        8  8  9  0.000  0.000
        9  8  9  0.000  0.000
        8  9 10  0.000  0.000
        9  9 10  0.000  0.000
       10  7  8 -0.007 -0.007
        9  8  9  0.000  0.000
       10  8  9 -0.007 -0.007
        9  9 10  0.000  0.000
       10  9 10 -0.007  0.000
```

Fig. 134: Change of the water gap width sizes in the x- (left) and y-direction (right) of a vibrating $3x3$ central cluster, produced by a MATLAB scripts, to be used by the SIMULATE-3K input deck.

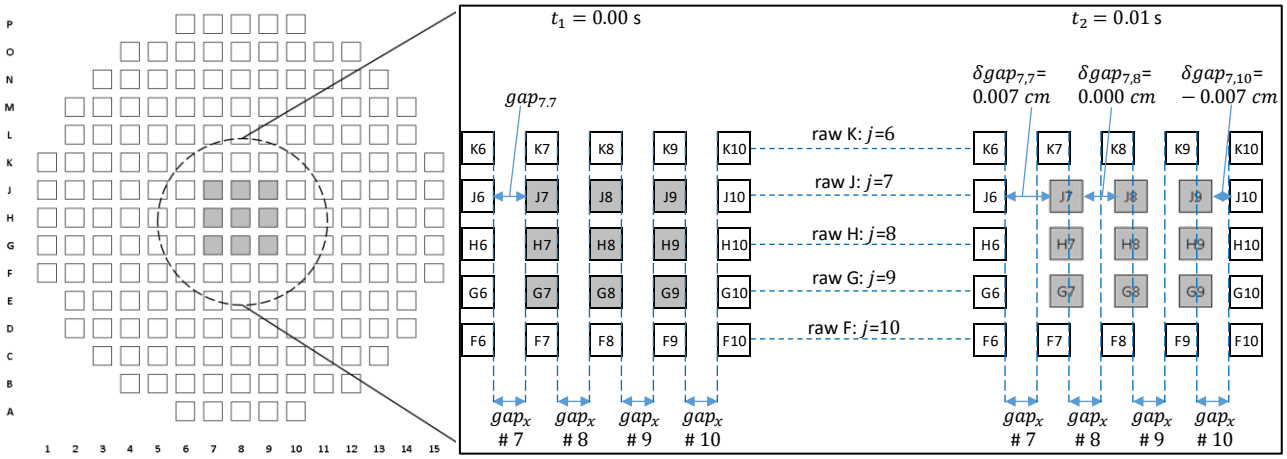

Fig. 135: Left: Location of the vibrating $3x3$ central cluster (grey). Right: Coordinates definition used in *KIN.XVL* input card in SIMULATE-3K accompanied by the change of water gap widths in the x-direction for a displacement of the central cluster by δgap_x=0.007 cm at t_2=0.01 s.

The content of the *KIN.YVL* input card (*gaps_y_Direction.inc*, Fig. 134 right plot), which describes the change of the water gap widths for the nine bundles of the vibrating $3x3$ central cluster in the y-direction, is slightly more complicated compared to the structure of the *KIN.XVL* input card. The *KIN.YVL* card has $3'501$ time steps, similarly to the *KIN.XVL* card. However, the structure of the *KIN.YVL* card requests that the user defines the change of the water gap widths between the selected bundles and their north and south neighbors, accompanied by the change of the water gap widths between the east neighbors of the selected bundles and their corresponding north and south adjacent ones. Due to that, the number of entries of the *KIN.YVL* input card are double compared to those of *KIN.XVL* card. For instance, the analyzed central cluster moves towards the core-north side by an increment amount δ=0.007 cm at the second time-step, t_2=0.01 s, as illustrated in Fig. 136. The first two entries of that time-step appear in the 20^{th} and 21^{st} lines of *KIN.YVL* card and they describe the water gap widths modification of the first vibrating bundle of the central cluster (i.e. bundle at the core location $J7$). The former line is composed of six numbers; "0.010 7 7 8 0.007 0.000". The latter line is composed of five numbers; "8 7 8 -0.007 0.000". Related to the 20^{th} line, the first number corresponds to time step (i.e. t_2=0.01 s), the second number corresponds to the y-axis coordinate (i.e. core gap row j) of the water

gap between the vibrating bundle $J7$ and its north neighbor $K7$, while the third and fourth numbers correspond to the x-axis coordinates (i.e. core-columns i and i+1) of vibrating bundle $J7$ and its east neighbor $J8$, respectively. The first bundle of the vibrating cluster is located at the position $J7$, which is positioned at the 7^{th} column of the KKG core (i.e. i=7), and its east neighbor is $J8$ positioned at the 8^{th} column of the KKG core (i.e. i+1=8). Their water gaps with their north neighbors are at the row 7 (i.e. j=7 for the gap between $K7$ and $J7$ bundles and for the gap between $K8$ and $J8$ bundles). Therefore, the last two numbers of the 20^{th} line show that, the change of the water gap width between $K7$ and $J7$ bundles is $\delta gap_{7,7}$=0.007 cm, and between $K8$ and J8 bundles is $\delta gap_{7,8}$=0.007 cm, at time step t_2=0.01 s. Similarly, the 21^{st} line describes the water gap widths between the $J7$ and $H7$ bundles, and between the $J8$ and $H8$ bundles. It is to note that, these water gap widths remain unchanged (i.e. $\delta gap_{8,7}$=$\delta gap_{8,8}$=0.000 cm), since all nine fuel assemblies vibrate in a synchronized way between each other within the central cluster.

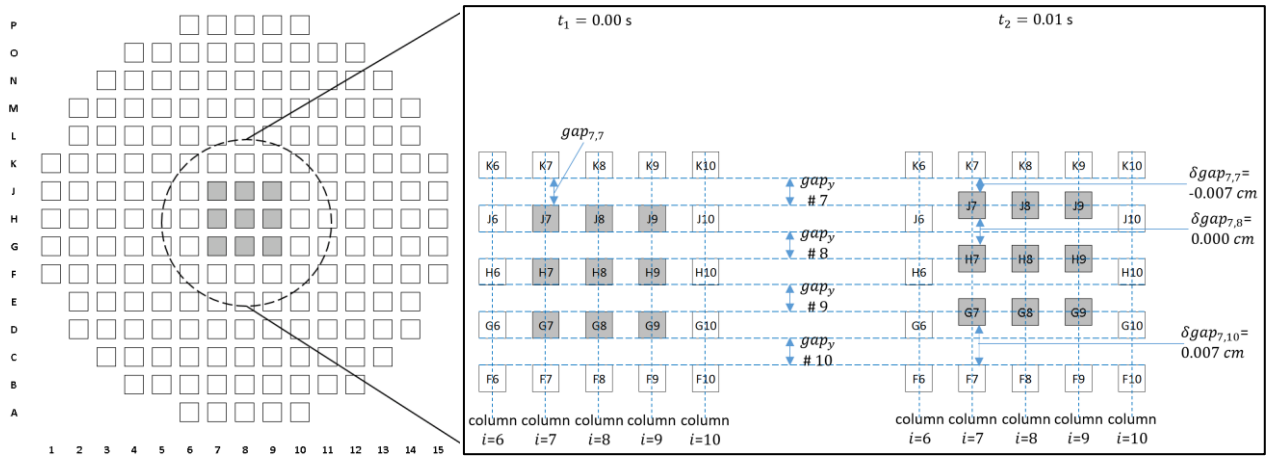

Fig. 136: Left: Location of the vibrating $3x3$ central cluster (grey). Right: Coordinates definition used in *KIN.YVL* input card in SIMULATE-3K accompanied by the change of water gap widths in the y-direction for a displacement of the central cluster by δgap_y=0.007 cm at t_2=0.01 s.

The superposition of the movement in two directions results in a dislocation of the bundle by 0.01 cm towards the core north-east side, which explains the diagonal vibrational pattern, as presented in Fig. 133b. For completeness it is noted that, the user can impose a random movement or a noisy sinusoid movement between the vibrating bundles in the x-y space, alternatively to the simplified oscillation of an assembly, which follows just a pure sine-wave function, as it is shown in the abovementioned example. To do so, the respective option in the GUI of Fig. 132a has to be selected. The change of the water gap widths of a randomly vibrating fuel bundle is based on a random number generator, according to the Eq. 60, whereas the noisy sinusoid movement follows the expressions in Eq. 61.

$$\delta gap_x(t) = A \cdot (2 \cdot rand - 1)$$

$$\delta gap_y(t) = A \cdot (2 \cdot rand - 1)$$

Eq. 60

$$\delta gap_x(t) = A \cdot \sin(2\pi f t + \frac{3}{2} \cdot rand)$$

$$\delta gap_y(t) = A \cdot \sin(2\pi f t + \frac{3}{2} \cdot rand)$$

Eq. 61

On the one hand, the following Fig. 137a shows the time-dependent evolution of the water gap width in the x- and y-directions in the case of a randomly vibrating fuel bundle over its nominal position. In addition, Fig. 137b shows how the randomly vibrating fuel assembly is moving in space as a result of the time-dependent expressions in Eq. 60.

On the other hand, Fig. 138a presents the time-dependent variation of the water gap widths in the x- and y-directions for a fuel bundle, oscillating in a sine-wave function, at a nominal frequency of $1\ Hz$, supplemented by a stochastic pattern. In contrast to the pure sinusoid movement in both directions, which resulted in a diagonal oscillation of the fuel assembly (Fig. 133b), it is observed that the noisy sinusoid movement provides a stochastic character to the bundle movement in x-y space, as presented in Fig. 138b.

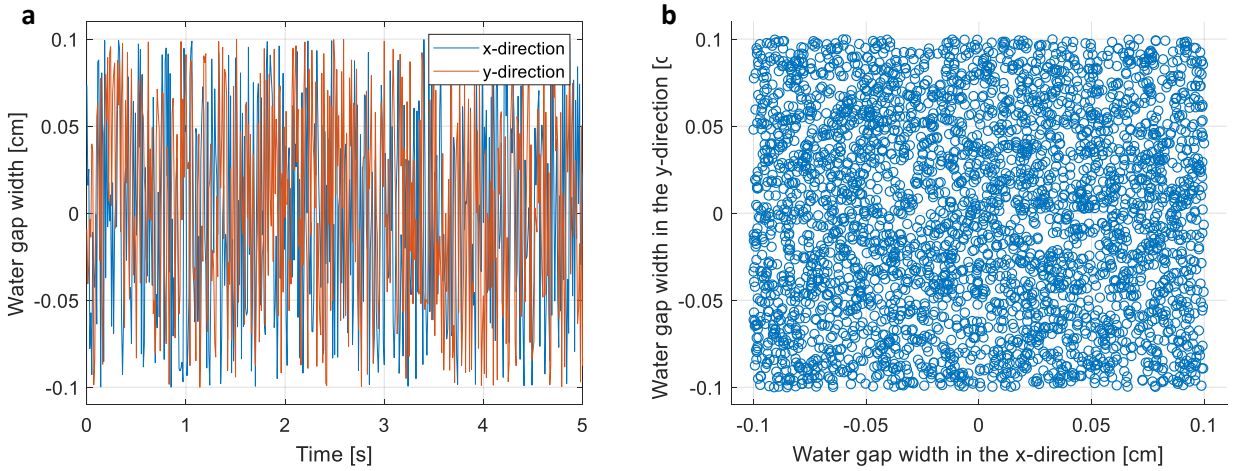

Fig. 137: Evaluated water gap widths in time (plot a) and space (plot b) in the case of a random fuel bundle vibration with an amplitude of $\mathbf{1}\boldsymbol{mm}$.

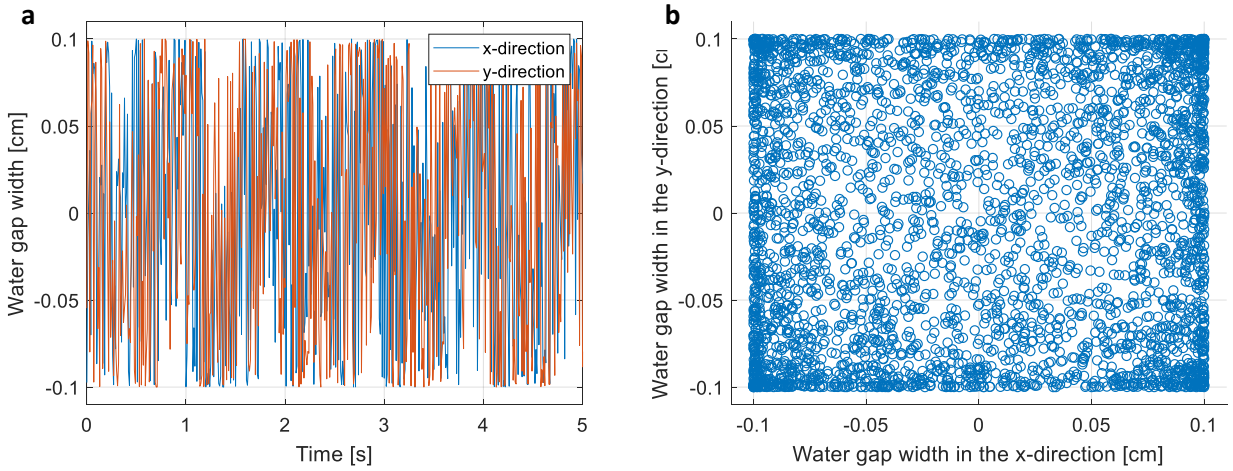

Fig. 138: Evaluated water gap widths in time (plot a) and space (plot b) in the case of a fuel bundle vibration of a noisy sinus behavior with an amplitude of $\mathbf{1}\boldsymbol{mm}$ at a nominal frequency of $\mathbf{1}\ \boldsymbol{Hz}$.

Additionally, the PSI toolbox offers the capability to prepare the SIMULATE-3K input deck to simulate different vibrating fuel assemblies with different vibrational characteristics. This capability is of particular interest when local operating conditions are taken into account. For instance, a heterogeneous turbulent coolant flow pattern at the inlet of the active core can result in different strengths of forces imposed from the coolant on the fuel bundles, and therefore, the fuel assemblies can oscillate with different amplitudes or at various

nominal frequencies depending on their position inside the core. In addition, the fuel assembly vibration can be subject to burnup. It has been already reported in [91] that, the stiffness of the bundles spacers dimples decreases with the burnup increase, and consequently, the burned fuel bundles tend to vibrate with larger amplitudes compared to the fresh ones. These remarks indicate that fuel assemblies with different vibrational characteristics can coexist at the same time during the normal operation of the reactor. This behavior can be modeled using the PSI toolbox by the superposition of multiple vibrational patterns.

To do so, the user has to specify that, multiple, instead of a single, vibrational patterns are going to be analyzed, by selecting the respective option in the first GUI of the PSI toolbox (i.e. Fig. 131a). Then, the user categorizes the vibrating bundles in groups, where each group is characterized by specific vibrational features (i.e. type and amplitude of vibration, nominal frequency of oscillation), defined by the user in a tabulated format, as presented in the bottom image in Fig. 139. For instance, Fig. 139 shows the case in which a total of twelve fuel bundles is selected to vibrate. These bundles are split in three groups, having a color identification (i.e. blue, red, and green), and then the vibrational characteristics of each group are imposed by the user. The PSI toolbox generates the time-dependent changes of the water gap widths in the x- and y-directions following the same process as described before.

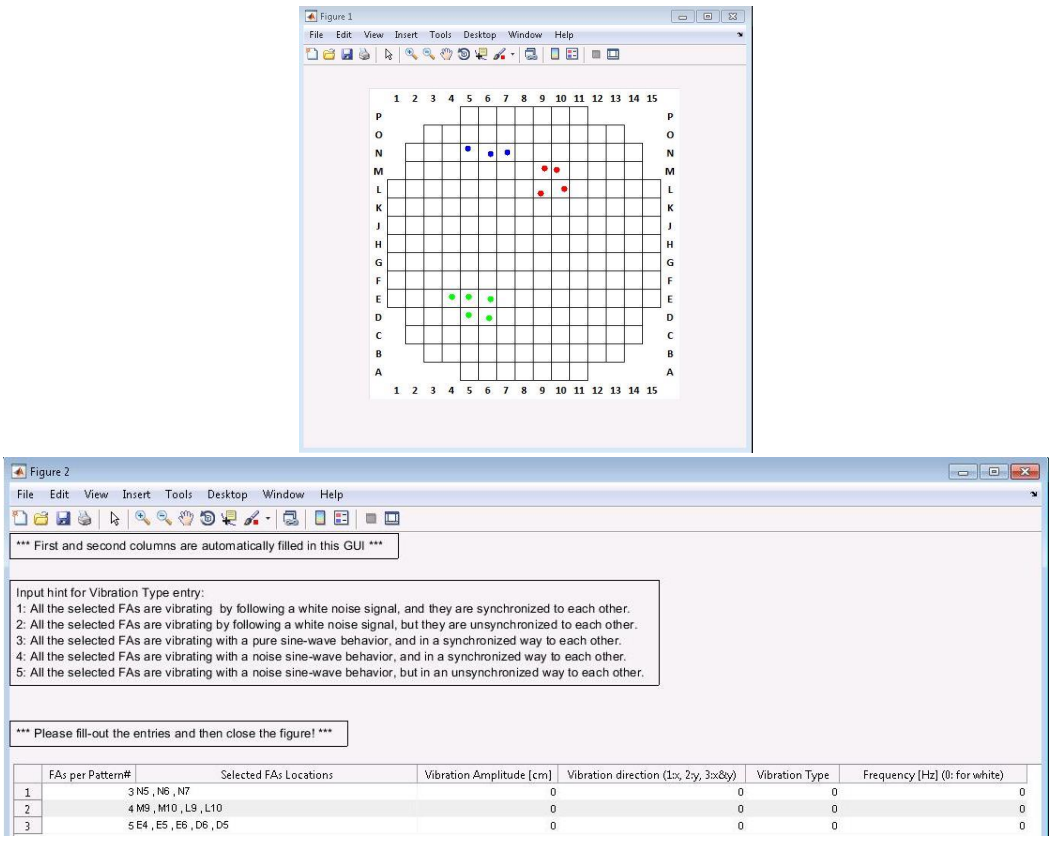

Fig. 139: GUIs of the PSI tool which allow the imposition of multiple vibrating patterns on the selected assemblies.

It should be emphasized that, the PSI toolbox is composed of a series of MATLAB functions, developed in such a way that the user can easily use them and further develop them, if necessary. Many control functions have been implemented in the developed scripts in order to ensure the proper functionality of the PSI toolbox.

Appendix iii: Thermal-hydraulic parameters fluctuation input preparation

The functionality of thermal-hydraulics parameters fluctuation model in SIMULATE-3K is demonstrated using the following example, presented in Fig. 140. In this example, the KKG core with three coolant loops is analyzed, and it is assumed that the inlet coolant temperature in all three cold legs fluctuates, stochastically, with an amplitude of $2°C$ over the mean value of $286.7°C$ $(548°F)$ and with a time step of $100\ ms$. In addition, it is assumed that the inlet coolant temperature fluctuates, stochastically between all three coolant loops (i.e. non-synchronized perturbation). The other thermal-hydraulic parameters (i.e. inlet coolant flow and the boron concentration) are not varied in this example.

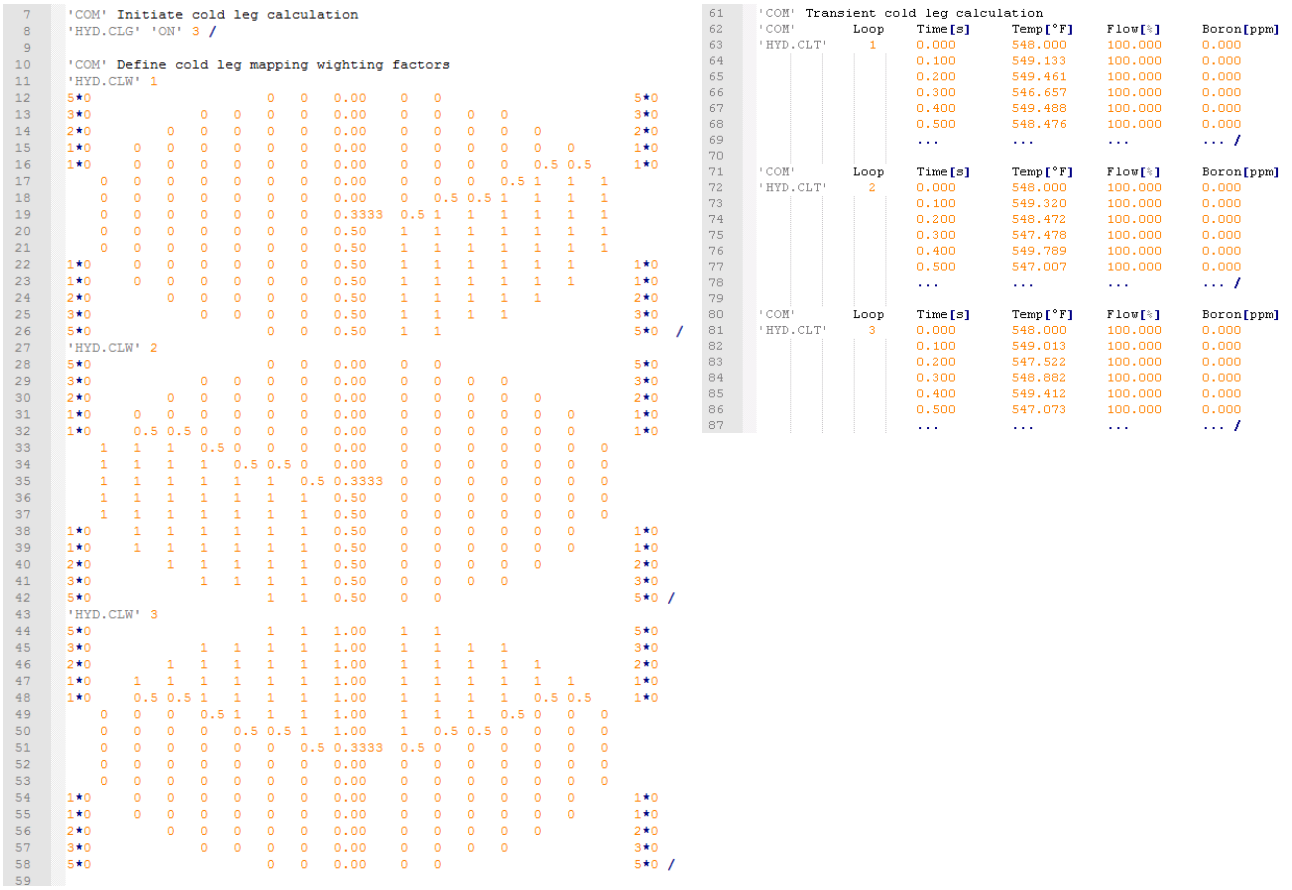

```
'COM' Initiate cold leg calculation
'HYD.CLG' 'ON' 3 /

'COM' Define cold leg mapping wighting factors
'HYD.CLW' 1
5*0                     0   0   0.00    0   0                       5*0
3*0                 0   0   0   0   0.00    0   0   0   0           3*0
2*0             0   0   0   0   0   0   0.00    0   0   0   0   0   2*0
1*0     0   0   0   0   0   0   0   0.00    0   0   0   0   0   0   1*0
1*0     0   0   0   0   0   0   0   0.00    0   0   0   0   0.5 0.5 1*0
    0   0   0   0   0   0   0   0   0.00    0   0   0   0   0.5 1   1
    0   0   0   0   0   0   0   0   0.00    0   0   0.5 0.5 1   1   1
    0   0   0   0   0   0   0   0   0.3333  0.5 1   1   1   1   1   1
    0   0   0   0   0   0   0   0   0.50    1   1   1   1   1   1   1
    0   0   0   0   0   0   0   0   0.50    1   1   1   1   1   1   1
1*0     0   0   0   0   0   0   0   0.50    1   1   1   1   1   1   1*0
1*0     0   0   0   0   0   0   0   0.50    1   1   1   1   1   1   1*0
2*0             0   0   0   0   0   0.50    1   1   1   1   1       2*0
3*0                 0   0   0   0   0.50    1   1   1   1           3*0
5*0                     0   0   0.50    1   1                       5*0 /
'HYD.CLW' 2
5*0                     0   0   0.00    0   0                       5*0
3*0                 0   0   0   0   0.00    0   0   0   0           3*0
2*0             0   0   0   0   0   0   0.00    0   0   0   0   0   2*0
1*0     0   0   0   0   0   0   0   0   0.00    0   0   0   0   0   0   1*0
1*0     0.5 0.5 0   0   0   0   0   0.00    0   0   0   0   0   0   1*0
    1   1   1   0.5 0   0   0   0   0.00    0   0   0   0   0   0   0
    1   1   1   1   0.5 0.5 0   0   0.00    0   0   0   0   0   0   0
    1   1   1   1   1   1   0.5 0.3333  0   0   0   0   0   0   0   0
    1   1   1   1   1   1   1   0.50    0   0   0   0   0   0   0   0
    1   1   1   1   1   1   1   0.50    0   0   0   0   0   0   0   0
1*0     1   1   1   1   1   1   0.50    0   0   0   0   0   0   0   1*0
1*0     1   1   1   1   1   1   0.50    0   0   0   0   0   0   0   1*0
2*0             1   1   1   1   1   0.50    0   0   0   0   0       2*0
3*0                 1   1   1   1   0.50    0   0   0   0           3*0
5*0                     1   1   0.50    0   0                       5*0 /
'HYD.CLW' 3
5*0                     1   1   1.00    1   1                       5*0
3*0                 1   1   1   1   1.00    1   1   1   1           3*0
2*0             1   1   1   1   1   1   1.00    1   1   1   1   1   2*0
1*0     1   1   1   1   1   1   1   1   1.00    1   1   1   1   1   1   1*0
1*0     0.5 0.5 1   1   1   1   1   1.00    1   1   1   1   0.5 0.5 1*0
    0   0   0   0.5 1   1   1   1   1.00    1   1   1   0.5 0   0   0
    0   0   0   0   0.5 0.5 1   1   1.00    1   0.5 0.5 0   0   0   0
    0   0   0   0   0   0   0   0.5 0.3333  0.5 0   0   0   0   0   0
    0   0   0   0   0   0   0   0   0.00    0   0   0   0   0   0   0
    0   0   0   0   0   0   0   0   0.00    0   0   0   0   0   0   0
1*0     0   0   0   0   0   0   0   0.00    0   0   0   0   0   0   1*0
1*0     0   0   0   0   0   0   0   0.00    0   0   0   0   0   0   1*0
2*0             0   0   0   0   0   0.00    0   0   0   0   0       2*0
3*0                 0   0   0   0   0.00    0   0   0   0           3*0
5*0                     0   0   0.00    0   0                       5*0 /

'COM' Transient cold leg calculation
'COM'       Loop    Time[s]     Temp[°F]    Flow[%]     Boron[ppm]
'HYD.CLT'     1     0.000       548.000     100.000     0.000
                    0.100       549.133     100.000     0.000
                    0.200       549.461     100.000     0.000
                    0.300       546.657     100.000     0.000
                    0.400       549.488     100.000     0.000
                    0.500       548.476     100.000     0.000
                    ...         ...         ...         ... /

'COM'       Loop    Time[s]     Temp[°F]    Flow[%]     Boron[ppm]
'HYD.CLT'     2     0.000       548.000     100.000     0.000
                    0.100       549.320     100.000     0.000
                    0.200       548.472     100.000     0.000
                    0.300       547.478     100.000     0.000
                    0.400       549.789     100.000     0.000
                    0.500       547.007     100.000     0.000
                    ...         ...         ...         ... /

'COM'       Loop    Time[s]     Temp[°F]    Flow[%]     Boron[ppm]
'HYD.CLT'     3     0.000       548.000     100.000     0.000
                    0.100       549.013     100.000     0.000
                    0.200       547.522     100.000     0.000
                    0.300       548.882     100.000     0.000
                    0.400       549.412     100.000     0.000
                    0.500       547.073     100.000     0.000
                    ...         ...         ...         ... /
```

Fig. 140: Example of SIMULATE-3K input deck for modeling the random fluctuation of the inlet coolant flow in one of the three coolant loops of a LWR.

This stochastic perturbation scenario is modeled using the SIMULATE-3K input deck as described in Fig. 140. First, the model that controls the dynamic modification of the thermal-hydraulics parameters has to be activated and the number of the coolant loops of the analyzed reactor has to be defined using the input card *HYD.CLG*. Then, the user defines the weighting factors map for each of the coolant loops using the *HYD.CLW* card. These maps indicate the level of influence of the thermal-hydraulic inlet conditions of each fuel assembly based on the coolant properties of each of the three coolant loops. For simplicity, it is assumed that the inlet coolant properties are not homogenized at the active core entrance. Thus, the inlet coolant properties of each fuel assembly will be affected by the coolant properties of the closest cold leg, as depicted in Fig. 7. In other words, the south-east part, the south-west, and the north part of the core are driven by fluctuations of the

thermal-hydraulic parameters in the inlet loop 1, 2, and 3, respectively. Hence, the bundles belonging to the south-east part of the core will depend with a 100% weight on the cold leg 1, and with 0% weight on cold legs 2 and 3. For the sake of simplicity it is assumed that, the bundles located at the virtual boarder between two core-parts (e.g. between the south-east and south-west parts) will be equally depending with a 50% weight on each of the respective cold legs. Accordingly, the central fuel bundle at the location $H8$ will depend with a weight of 33.3% on each one of the three cold legs.

The description of the time-dependent modification of the inlet coolant properties of each cold leg is performed using the input card *HYD.CL*T (i.e. Fig. 140, right part). An automatized script written in the MATLAB environment has been developed in the framework of this thesis in order to simplify and ease the preparation of the SIMULATE-3K input file for the thermal-hydraulic property fluctuation. The following figure, Fig. 141, shows the initialization part of the MATLAB script, in which the user defines the simulation parameters (i.e. coolant loop number and simulation duration) and the initial properties of the coolant at each cold leg. The fluctuation amplitude of each of the three thermal-hydraulic parameters (i.e. inlet coolant temperature, inlet coolant flow, and boron concentration) is then imposed for each coolant loop. Last, the user selects whether or not the fluctuations of the thermal-hydraulic coolant properties are synchronized between the three cold legs.

```
% S3K simulation parameters
LP=3;        % Number of coolant loops (NLOOP in HYD.CLG card of S3K)
S=35;       % Simulation duration in [sec] (TEND in KIN.TIM card of S3K)
N=S*10-1;    % Number of data points
t=S/N:S/N:S; % Time domain

% Initial conditions
Tin=[548 548 548];   % Inlet temperature initial value [in °F]    *** One value per loop
Fin=[100 100 100];   % Flow rated initial value [in %]            *** One value per loop
Bin=[0 0 0];         % Boron concentration initial value [in ppm] *** One value per loop
                         %   *** for compatibility with S3K input please read the boron
                         %       converged value from S3K output first ***

% Perturbation of T/H parameters
Td=[1.8 1.8 1.8];        % Inlet temperature deviation (+/-) from initial value Tin   *** One value per loop
                         %   *** [in °F]  change of 1°C=1.8°F ***
Fd=[0 0 0];            % Inlet flow deviation (+/-) from initial rated value Fin    *** One value per loop
Bd=[0 0 0];            % Boron concentration deviation (+/-) from initial value Bin *** One value per loop
                         %   *** [in ppm]  1-2 ppm is a reasonable value based on plant
                         %                 data from KKG ***

% Synchronized perturbation between all loops
s=0;         % s=1; All LP loops will have the same perturbation
             % s=0; LP loops will have the different perturbation between each other
```

Fig. 141: Setup of the MATLAB script for the automatized preparation of the input card *HYD.CLT* in SIMULATE-3K for the simulation of the stochastic fluctuation of the thermal-hydraulic properties in the cold legs.

The coolant properties ($f_{i,j}$) are modified at every time step using a normally distributed random number generator, based on expression Eq. 62. The index i corresponds to the thermal-hydraulic property (i.e. inlet coolant flow, inlet coolant temperature, or boron concentration) of the respective cold leg j. Moreover, $f_{i,j}(0)$ are the initial coolant properties, and $A_{i,j}$ describe the user defined amplitude of fluctuation of the i^{th} coolant property at the j^{th} coolant loop. The time-dependent stochastic fluctuation of the inlet coolant temperature in the three coolant legs, as described in the current example, is depicted in Fig. 142a. For completeness, the undisturbed behavior of the inlet coolant flow and the boron concentration in all coolant loops, as defined in the MATLAB script (Fig. 141a), is depicted in Fig. 142b.

$$f_{i,j}(t) = f_{i,j}(0) + A_{i,j} \cdot rand \qquad \text{Eq. 62}$$

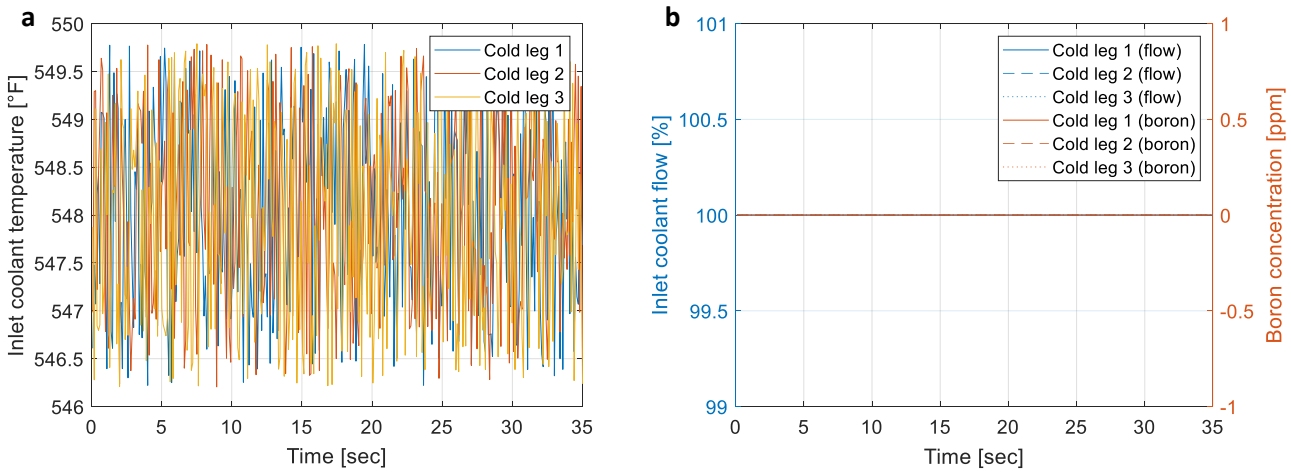

Fig. 142: Time-dependent stochastic fluctuation, in the three cold legs, of: the inlet coolant temperature (plot a); the inlet coolant flow and the boron concentration (plot b).

Following this procedure, the user can easily prepare the SIMULATE-3K input deck for simulating noise sources originating from the coolant thermal-hydraulic properties of the reactor cold legs. The assessment of the impact that the thermal-hydraulic coolant fluctuations have on the neutron noise spatial phenomenology is discussed in *chapter 5*, using a series of simulation scenarios. It is important to note, that this type of noise sources can be simulated, by SIMULATE-3K, in both PWR and BWR systems[33].

[33] It is recalled that, the noise sources due to fuel assembly vibration can be modelled in SIMULATE-3K only for PWR systems.

Bibliography

[1] IAEA, *IAEA Annual Report 2018*. 2018.

[2] J. Thie, *Power reactor noise*. American Nuclear Society, 1981.

[3] A. Dokhane and H. Ferroukhi, “Reactor signal analysis for BWR core stability evaluation - Methodology and application to KKL cycle 19 - PSI Internal Report TM-41-04-16,” 2005.

[4] Marple Lawrence, *Digital spectral analysis with applications*. 1987.

[5] A. Dokhane, H. Ferroukhi, M. A. Zimmermann, and C. Aguirre, “Spatial and model-order based reactor signal analysis methodology for BWR core stability evaluation,” *Ann. Nucl. Energy*, vol. 33, no. 16, pp. 1329–1338, 2006, doi: 10.1016/j.anucene.2006.08.010.

[6] H. Ferroukhi, “Reactor signal analysis of KKL BOC24 data measured on the 22.08.2007 - PSI Internal Report TM-41-08-06,” 2008.

[7] R. Oguma, “Method to evaluate signal transmission paths in dynamic systems and its application to reactor noise analysis,” *Nucl. Sci. Technol.*, vol. 18, no. 11, pp. 835–844, 1981, doi: 10.1080/18811248.1981.9733328.

[8] M. Demeshko, A. Dokhane, T. Washio, H. Ferroukhi, Y. Kawahara, and C. Aguirre, “Application of continuous and structural ARMA modeling for noise analysis of a BWR coupled core and plant instability event,” *Ann. Nucl. Energy*, vol. 75, pp. 645–657, 2015, doi: 10.1016/j.anucene.2014.08.045.

[9] X. Jin, Y. Guo, S. Sarkar, A. Ray, and R. M. Edwards, “Anomaly detection in nuclear power plants via symbolic dynamic filtering,” *IEEE Trans. Nucl. Sci.*, vol. 58, no. 1, pp. 277–288, 2011, doi: 10.1109/TNS.2010.2088138.

[10] F. Calivá *et al.*, “A deep learning approach to anomaly detection innNuclear reactors,” in *Proceedings of the International Joint Conference on Neural Networks*, 2018, doi: 10.1109/IJCNN.2018.8489130.

[11] C. W. J. Granger, “Investigating causal relations by econometric models and cross-spectral methods,” *Econometrica*, vol. 37, no. 3, pp. 424–438, 1969, doi: 10.2307/1912791.

[12] J. Thie, “Core motion monitoring,” *Nucl. Technol.*, vol. 45, 1979, doi: 10.13182/NT79-A32283.

[13] E. D. Courant and P. R. Wallace, “Fluctuations of the number of neutrons in a pile,” *Phys. Rev.*, vol. 72, no. 11, pp. 1038–1048, 1947, doi: 10.1103/PhysRev.72.1038.

[14] M. Seidl, K. Kosowski, U. Schüler, and L. Belblidia, “Review of the historic neutron noise behavior in German KWU built PWRs,” *Prog. Nucl. Energy*, vol. 85, pp. 668–675, 2015, doi: 10.1016/j.pnucene.2015.08.016.

[15] C. Demazière, “CORE SIM : A multi-purpose neutronic tool for research and education,” *Ann. Nucl. Energy*, vol. 38, pp. 2698–2718, 2011, doi: 10.1016/j.anucene.2011.06.010.

[16] C. Demazière, P. Vinai, M. Hursin, S. Kollias, and J. Herb, “Noise-based core monitoring and diagnostics - Overview of the CORTEX project,” in *Physor’18*, 2018.

[17] D. Chionis, A. Dokhane, H. Ferroukhi, G. Girardin, and A. Pautz, “PWR neutron noise phenomenology : Part II – Qualitative comparison against plant data,” in *Physor18*, 2018.

[18] A. Dokhane, D. Chionis, and H. Ferroukhi, “Towards systematic and continuous tracking of neutron and process noise signatures during LWR operation,” in *Physor’18*, 2018.

[19] D. Chionis, “Neutron noise analysis of KKG measured data (cycle 30 to 37) - PSI Internal Report TM-41-14-003 V.0,” 2020.

[20] D. Chionis and A. Dokhane, “ENSI On-Call - Causality analysis of KKL cycle 33 - Start-up measurements from February 2017 - PSI Internal Report AN-41-18-01 V.0,” 2018.

[21] M. Williams, *Random processes in nuclear reactors*. New York: Pergamon Press, 1974.

[22] M. Moore, “The determination of reactor transfer functions from measurements at steady operation,” *Nucl. Sci. Eng.*, vol. 3, no. 4, pp. 387–394, 1958.

[23] N. Pacilio, “Proceedings of NEACPR specialist meeting on reactor noise (SMORN-1),” 1975.

[24] M. Williams, “Proceedings of the second specialists meeting on reactor noise (SMORN-II),” 1977.

[25] M. Williams, “Proceedings of the third specialists meeting on reactor noise (SMORN-III),” 1981.

[26] M. Williams, “Proceedings of the fourth specialists meeting on reactor noise (SMORN-IV),” 1984.

[27] T. Beynon, “Proceedings of the fifth specialists meeting on reactor noise (SMORN-V),” 1987.

[28] R. Kryter and B. Upadhyaya, “A symposium on nuclear reactor surveillance and diagnostics (SMORN-VI),” 1991.

[29] P. Savelli, “A symposium on nuclear reactor surveillance and diagnostics (SMORN-VII),” 1995.

[30] M. Calcagno, F. Cioli, A. Gadola, G. Possa, and G. Vanoli, “Trino nuclear power station in-service monitoring of reactor internals,” in *Non-destructuve testing for reactor core components and pressure vessels*, 1971, pp. 357–382.

[31] J. Dragt and E. Türkcan, “Borssele PWR noise: Measurements, analysis and interpretation,” *Prog. Nucl. Energy*, vol. 1, pp. 293–307, 1977, doi: 10.1016/0149-1970(77)90086-5.

[32] D. N. Fry, R. C. Kryter, and J. C. Robinson, “Analysis of neutron-density oscillations resulting from core barrel motion in a PWR nuclear power plant,” *Ann. Nucl. Energy*, vol. 2, pp. 341–351, 1975, doi: 10.1016/0306-4549(75)90037-7.

[33] D. Wach and R. Sunder, “Improved PWR-neutron noise interprentation based on detailed vibration analysis,” *Prog. Nucl. Energy*, vol. 1, pp. 309–322, 1977, doi: 10.1016/j.pnueene.2005.05.018.

[34] W. Bastl and D. Wach, “Experiences with noise surveillance systems in German LWRs,” *Prog. Nucl. Energy*, vol. 9, pp. 505–516, 1982, doi: 10.1016/0149-1970(82)90070-1.

[35] E. Türkcan, “Review of Borssele PWR noise experiments, analysis and instrumentation,” *Prog. Nucl. Energy*, vol. 9, pp. 437–452, 1982, doi: 10.1016/0149-1970(82)90066-X.

[36] H. Stölben and H.-J. Wehling, “Vibration monitoring of Kraftwerk Union pressurized water reactor - Review, present status, and further development,” *Nucl. Technol.*, vol. 80, pp. 400–411, 1988, doi: 10.13182/NT88-A34064.

[37] N. Pazsit, I., Karlsson, J., Garis, “Some developments in core-barrel vibration diagnostics,” *Ann. Nucl. Energy*, vol. 25, no. 13, pp. 1079–1093, 1998, doi: 10.1016/S0306-4549(98)00012-7.

[38] R. Oguma and E. Türkcan, “Application of an improved multivariable noise analysis method to

investigation of PWR noise; Signal transmission path analysis," *Prog. Nucl. Energy*, vol. 15, pp. 863–873, 1985, doi: 10.1016/0149-1970(85)90120-9.

[39] G. Pór, I. Lux, and L. Meskó, "Comments on practical application of autoregressive signal analysis to PWR NPP noise data," *Prog. Nucl. Energy*, vol. 15, pp. 897–902, 1985, doi: 10.1016/0149-1970(85)90124-6.

[40] O. Glöckler and B. Upadhyaya, "Results and interpretation of multivariate autoregressive analysis applied to the Loft reactor process noise data," *Prog. Nucl. Energy*, vol. 21, pp. 447–456, 1988, doi: 10.1016/0149-1970(88)90062-5.

[41] M. Antonopoulos-Domis, K. Mourtzanos, and G. Por, "Study on reactor system identification with multivariate auto-regressive analysis," *Ann. Nucl. Energy*, vol. 21, no. 11, pp. 667–686, 1994, doi: 10.1016/0306-4549(94)90034-5.

[42] C. Demazière and I. Pázsit, "Development of a method for measuring the moderator temperature coefficient by noise analysis and its experimental verification in Ringhals-2," *Nucl. Sci. Eng.*, vol. 148, pp. 1–29, 2004, doi: 10.13182/NSE04-A2437.

[43] C. Demazière and I. Pazsit, *Power reactor noise*. Gothenburg, Sweden: Chalmers University of Technology, 2008.

[44] D. G. Cacuci, *Handbook of nuclear engineering*. Springer, 2010.

[45] P. Wellch, "The use of fast fourier transform for the estimation of pwer spectra: A method based on time averaging over shoer, modified periodograms," *IEEE Trans. Audio Electroacoust.*, vol. AU-15, no. 2, pp. 70–73, 1967, doi: 10.1109/TAU.1967.1161901.

[46] L. Faes, G. D. Pinna, A. Porta, R. Maestri, and G. Nollo, "Surrogate data analysis for assessing the significance of the coherence function," *IEEE Trans. Biomed. Eng.*, vol. 51, no. 7, pp. 1156–1166, 2004, doi: 10.1109/TBME.2004.827271.

[47] B. Askari and D. Hennig, "High performance time series analysis code (HPTSAC2000)," 2001.

[48] A. Dokhane, "Reactor signal analysis of the KKL cycle 10 stability measurements using the PSI methodology - PSI Internal Report TM-41-04-32," 2005.

[49] A. Dokhane, "Reactor signal analysis of the KKL cycle 13 stability measurements usign the PSI methodology - PSI Internal Report TM-41-04-33."

[50] J. A. Bermejo, C. Montalvo, and A. Ortego, "On the possible effects contributing to neutron noise variations in KWU-PWR reactor : Modelling with S3K," *Prog. Nucl. Energy*, vol. 95, pp. 1–7, 2017, doi: 10.1016/j.pnucene.2016.11.004.

[51] M. Viebach, N. Bernt, C. Lange, D. Hennig, and A. Hurtado, "On the influence of dynamical fuel assembly deflections on the neutron noise level," *Prog. Nucl. Energy*, vol. 104, pp. 32–46, 2018, doi: 10.1016/j.pnucene.2017.08.010.

[52] U. Rohde, M. Seidl, S. Kliem, and Y. Bilodid, "Neutron noise observations in German KWU built PWRs and analyses with the reactor dynamics code DYN3D," *Ann. Nucl. Energy*, vol. 112, pp. 715–734, 2018, doi: 10.1016/j.anucene.2017.10.033.

[53] B. Everittt and A. Skrondal, *The Cambridge dictionary of statistics - 4th edition*. New York (USA): Cambridge University Press, 2010.

[54] C. Sweeney, F., March-Leuba, J., Smith, "Contribution of fuel vibration to ex-core neutron noise during

the first and second fuel cycles of the Sequoyah-1 pressurized water reactor," *Prog. Nucl. Energy*, vol. 15, no. 40, pp. 283–290, 1985, doi: 10.1016/0149-1970(85)90051-4.

[55] I. Pazsit, H. Nylen, and C. Montalvo, "Refined method for surveillance and diagnostics of the core barrel vibration of the Ringhals PWRs," in *Physor'14*, 2014.

[56] D. Chionis, A. Dokhane, L. Belblidia, G. Girardin, H. Ferroukhi, and A. Pautz, "Development and verification of a methodology for neutron noise response to fuel assembly vibrations," *Submitt. to Ann. Nucl. Energy*.

[57] D. Chionis *et al.*, "SIMULATE-3K analyses of neutron noise response to fuel assembly vibrations and thermal-hydraulics parameters fluctuations," in *M&C'17*, 2017.

[58] H. Ferroukhi, K. Hofer, J. Hollard, A. Vasiliev, and M. A. Zimmermann, "Core modelling and analysis of the Swiss nuclear power plants for qualified R&D applications," in *Physor'08*, 2008.

[59] W. Stacey, *Nuclear Reactor Physics*, Second Edi. Weinheim, Germany: Wiley-VCH Verlag GmbH & Co., 2007.

[60] S. Choi, D. Lee, and K. Smith, "Investigation of diffusion coefficient calculation methods for two-step LWR analysis," in *Physor'16*, 2016.

[61] F. Giust, *Appraisal of core analysis methods against zero-power experiments on full-scale BWR fuel assemblies*. 2012.

[62] C. Demazière, V. Dykin, and K. Jareteg, "Development of a point-kinetic verification scheme for nuclear reactor applications," *J. Comput. Phys.*, vol. 339, pp. 396–411, 2017, doi: 10.1016/j.jcp.2017.03.020.

[63] N. Bernt, C. Lange, M. Viebach, D. Hennig, and A. Hurtado, "The influence of full-core deflection to the nodalized cross sections," in *Physor'18*, 2018.

[64] C. Montalvo, I. Pazsit, and H. Nylen, "First evidence of the pivotal motion ('tilting mode') of the core barrel in the Ringhals-4 PWR," in *Physor'16*, 2016.

[65] V. Arzhanov and I. Pázsit, "Diagnostics of core barrel vibrations by in-core and ex-core neutron noise," *Prog. Nucl. Energy*, vol. 43, pp. 151–158, 2003, doi: 10.1016/S0149-1970(03)00023-4.

[66] V. Arzhanov, I. Pázsit, and N. Garis, "Localization of a vibrating control rod pin in pressurized water reactors using the neutron flux and current noise," *Nucl. Technol.*, vol. 131, no. 2, pp. 239–251, 2000, doi: 10.13182/nt00-a3114.

[67] I. Pazsit and O. Glöckler, "BWR Instrument tube vibrations: Interprentation of measurements and simulation," *Ann. Nucl. Energy*, vol. 21, no. 12, pp. 759–786, 1994, doi: https://doi.org/10.1016/0306-4549(94)90024-8.

[68] W. Bastl and V. Bauernfeind, "The estimation of vibration of reactor internals by noise analysis of non-nuclear parameters," *Ann. Nucl. Energy*, vol. 2, pp. 277–285, 1975.

[69] C. Demazière and I. Pázsit, "Numerical tools applied to power reactor noise analysis," *Prog. Nucl. Energy*, vol. 51, no. 1, pp. 67–81, 2009, doi: 10.1016/j.pnucene.2008.01.010.

[70] V. Verma, C. Demazière, P. Vinai, G. Ricciardi, and R. Jacqmin, "Assessment of the neutron noise induced by stationary fuel assembly vibration in a LWR," in *M&C'19*.

[71] A. Mylonakis, P. Vinai, and C. Demazière, "Numerical solution of two-energy-group neutron noise diffusion problems with fine spatial meshes," *Ann. Nucl. Energy*, vol. 140, 2020, doi:

10.1016/j.anucene.2019.107093.

[72] H. Yi, P. Vinai, and C. Demazière, “A discrete ordinates solver with diffusion synthetic acceleration for simulation of 2-D and 2-energy group neutron noise problems,” in *M&C’19*, 2019.

[73] U. Rohde *et al.*, “The reactor dynamics code DYN3D - Models, validation and applications,” *Prog. Nucl. Energy*, vol. 89, pp. 170–190, 2016, doi: 10.1016/j.pnucene.2016.02.013.

[74] M. Viebach, C. Lange, N. Bernt, M. Seidl, D. Hennig, and A. Hurtado, “Simulation of low-frequency PWR neutron flux fluctuations,” *Prog. Nucl. Energy*, vol. 117, 2019, doi: 10.1016/j.pnucene.2019.103039.

[75] A. Zoia, E. Brun, F. Damian, and F. Malvagi, “Monte Carlo methods for reactor period calculations,” *Ann. Nucl. Energy*, vol. 75, pp. 627–634, 2015, doi: 10.1016/j.anucene.2014.09.014.

[76] A. Rouchon, A. Zoia, and R. Sanchez, “A new Monte Carlo method for neutron noise calculations in the frequency domain,” *Ann. Nucl. Energy*, vol. 102, pp. 465–475, 2017, doi: 10.1016/j.anucene.2016.11.035.

[77] C. Diop *et al.*, “TRIPOLI-4: A 3D continuous-energy Monte Carlo transport code,” in *PHYTRA1*, 2007.

[78] A. Rouchon, R. Sanchez, and I. Zmijarevic, “The new 3-D multigroup diffusion neutron noise solver of APOLLO3 and a theoretical discussion of fission-modes noise,” in *M&C’17*, 2017.

[79] N. Olmo-Juan, C. Demazière, T. Barrachina, R. Miró, and G. Verdú, “PARCS vs CORE SIM neutron noise simulations,” *Prog. Nucl. Energy*, vol. 115, pp. 169–180, 2019, doi: 10.1016/j.pnucene.2019.03.041.

[80] A. Vidal-Ferrandiz, A. Carreno, D. Ginestar, C. Demazière, and G. Verdú, “A time and frequency domain analysis of the effect of vibrating fuel assemblies on the neutron noise,” *Ann. Nucl. Energy*, vol. 137, pp. 1–12, 2020, doi: https://doi.org/10.1016/j.anucene.2019.107076.

[81] J. Rhodes, K. Smith, and D. J. Lee, “CASMO-5 development and applications,” in *Physor’06*, 2006.

[82] R. Ferrer, “CASMO-5 methodology manual - SSP Technical Report SSP-08/405, Rev. 4,” 2015.

[83] T. Bahadir, “CMS-LINK user ’s manual - SSP Technical Report SOA-97/04, Rev. 2,” 1999.

[84] J. Cronin, K. Smith, and D. Ver Planck, “SIMULATE-3 methodology - SSP Technical Report SOA-95/18, Rev 0.,” 1995.

[85] G. Grandi, “SIMULATE-3K models & methodology - SSP Technical Report SSP-98/13, Rev. 7,” 2011.

[86] Y. Jo, M. Hursin, D. Lee, H. Ferroukhi, and A. Pautz, “Analysis of simplified BWR full core with serpent-2/simulate-3 hybrid stochastic/deterministic code,” *Ann. Nucl. Energy*, vol. 111, pp. 141–151, 2018, doi: 10.1016/j.anucene.2017.08.061.

[87] T. Bahadir, “CMS assembly bow model - SSP Technical Report SSP-97/34, Rev. 1,” 2010.

[88] J. Rhodes, “CASMO-5 user’s manual - SSP Technical Report SSP-07/431, Rev. 9,” 2015.

[89] Z. Liu, K. S. Smith, and B. Forget, “Cumulative migration method for computing rigorous transport cross sections and diffusion coefficients for LWR lattices with Monte Carlo,” in *Physor’16*, 2016.

[90] J. Stabel-Weinheimer and M. Ren, “Method for preventing fretting damage to fuel rods, nuclear reactor fuel element, device for preventing damange, and spacer in a fuel assembly of a nuclear reactor (US 6888911 B2),” 2005.

[91] A. Billerey, “Evolution of fuel rod support under irratiation impact on the mechancial behaviour of fuel

assemblies [IAEA-TECDOC-1454],” in *Proceeding of a technical meeting on Structural behaviour of fuel assemblies for water cooled reactors*, 2005.

[92] P. Gabrielsson, D. Schrire, E. Suvdantsetseg, and M. Malmberg, “Investigation of the development of fuel assembly bow in Ringhals 3 and 4,” in *Top Fuel*, 2018.

[93] R. Adamson, C. Coleman, and M. Griffiths, “Irradiation growth of zirconium alloys - A critical review,” *Nucl. Mater.*, vol. 521, pp. 167–244, 2019, doi: 10.1016/j.jnucmat.2019.04.021.

[94] V. Verma, D. Chionis, A. Dokhane, and H. Ferroukhi, “Modelling and analysis of fuel assembly vibrational modes in PWRs using SIMULATE-3K,” in *Physor’20*, 2020.

[95] D. Chionis, A. Dokhane, H. Ferroukhi, G. Girardin, and A. Pautz, “PWR neutron noise phenomenology : Part I – Simulation of stochastic phenomena with SIMULATE - 3K,” in *Physor’18*, 2018.

[96] L. A. Torres, D. Chionis, C. Montalvo, A. Dokhane, and A. García-Berrocal, “Neutron noise analysis of simulated mechanical and thermal-hydraulic perturbations in a PWR core,” *Ann. Nucl. Energy*, vol. 126, pp. 242–252, 2019, doi: 10.1016/j.anucene.2018.11.032.

[97] L. A. Torres, D. Chionis, C. Montalvo, A. Dokhane, and A. García-Berrocal, “Neutron noise spectral features of simulated mechanical and thermal-hydraulic perturbations in a PWR core,” in *Physor’20*, 2020.

[98] L. J. Kostić, J. Runkel, and D. Stegemann, “Thermohydraulics surveillance of pressurized water reactors by experimental and theoretical investigations of the low frequency noise field,” *Prog. Nucl. Energy*, vol. 21, pp. 421–430, 1988, doi: 10.1016/0149-1970(88)90060-1.

[99] A. Wanninger, M. Seidel, and R. Macián-Juan, “Development of Computational Methods to Describe The Mechanical Behavior of PWR Fuel Assemblies,” in *Annual Meeting on Nuclear Technology*, 2016.

[100] D. Chionis, A. Dokhane, H. Ferroukhi, and A. Pautz, “On causality analysis of nuclear reactor noise using partial directed coherence,” in *Physor’16*, 2016.

[101] D. Chionis, A. Dokhane, H. Ferroukhi, and A. Pautz, “Application of causality analysis on nuclear reactor systems,” *Chaos*, vol. 29, no. 4, pp. 043126 1–16, 2019, doi: 10.1063/1.5083905.

[102] D. Chionis, A. Dokhane, H. Ferroukhi, and A. Pautz, “Spatial localization of perturbation propagation in LWRs using causality and connectivity analysis,” in *M&C’19*, 2019.

[103] L. Faes and G. Nollo, “Multivariate frequency domain analysis of causal interactions in physiological time series,” in *Biomedical Engineering Trends in Electronics, Communications and Software*, InTech, 2011, pp. 403–428.

[104] K. J. Blinowska and J. Zygierewicz, *Practical biomedical signal analysis*. Taylor & Francis Group, 2012.

[105] A. L. Luis Coito, “Directed functional connectivity in patients with focal epilepsy using high density scalp EEG,” Univeristy of Geneve, Switzerland, 2016.

[106] M. Kamiński and H. Liang, “Causal Influence: Advances in Neurosignal Analysis,” *Crit. Rev. Biomed. Eng.*, vol. 33, no. 4, pp. 347–430, 2005, doi: 10.1615/CritRevBiomedEng.v33.i4.20.

[107] T. Mullen, “Source information flow toolbox (SIFT),” 2010.

[108] H. Lütkepohl, *Introduction to multiple time series analysis*. Berlin, Germany: Springer, 1991.

[109] T. Schneider and A. Neumaier, “Algorithm 808 : AR FIT — A Matlab package for the estimation of

parameters and eigenmodes of multivariate autoregressive models," *ACM Trans. Math. Softw.*, vol. 27, no. 1, pp. 58–65, 2001, doi: 10.1145/382043.382316.

[110] A. Neumaier and T. Schneider, "Estimation of parameters and eigenmodes of multivariate autoregressive models," *ACM Trans. Math. Softw.*, vol. 27, no. 1, pp. 27–57, 2001, doi: 10.1145/382043.382304.

[111] A. Schlögl, "A comparison of multivariate autoregressive estimators," *Signal Processing*, vol. 86, pp. 2426–2429, 2006, doi: 10.1016/j.sigpro.2005.11.007.

[112] K. Blinowska, "Review of the methods of determination of directed connectivity from multichannel data," *Med. Biol. Eng. Comput.*, vol. 49, pp. 521–529, 2011, doi: 10.1007/s11517-011-0739-x.

[113] M. Winterhalder *et al.*, "Comparison of linear signal processing techniques to infer directed interactions in multivariate neural systems," *Signal Processing*, vol. 85, pp. 2137–2160, 2005, doi: 10.1016/j.sigpro.2005.07.011.

[114] S. Cekic, D. Grandjean, and O. Renaud, "Time, frequency, and time-varying Granger-causality measures in neuroscience," *Stat. Med.*, pp. 1–22, 2018, doi: 10.1002/sim.7621.

[115] L. Massaroppe and L. Baccalá, "Causal connectivity via kernel methods : Advances and challenges," in *38th Annual International Conference of the IEEE Engineering in Medicine and Biology Society (EMBC)*, 2016.

[116] L. Sommerlade *et al.*, "Assessing the strength of directed influences among neural signals : An approach to noisy data," *J. Neurosci. Methods*, vol. 239, pp. 47–64, 2015, doi: 10.1016/j.jneumeth.2014.09.007.

[117] M. Rubinov and O. Sporns, "Complex network measures of brain connectivity: Uses and interpretations," *Neuroimage*, vol. 52, pp. 1059–1069, 2010, doi: 10.1016/j.neuroimage.2009.10.003.

[118] H. Elsegai, H. Shiells, M. Thiel, and B. Schelter, "Network inference in the presence of latent confounders: The role of instantaneous causalities," *Neurosci. Methods*, vol. 245, pp. 91–106, 2015, doi: 10.1016/j.jneumeth.2015.02.015.

[119] L. Massaroppe and L. Baccalá, "Detecting nonlinear Granger causality via the kernelization of partial directed coherence," in *60th World Statistics Congress of the International Statistical Institute (ISI2015)*, 2015, pp. 2036–2041.

[120] L. A. Baccalá and K. Sameshima, "Partial directed coherence: a new concept in neural structure determination," *Biol. Cybern.*, vol. 84, no. 6, pp. 463–474, 2001, doi: 10.1007/PL00007990.

[121] B. Schelter, J. Timmer, and M. Eichler, "Assessing the strength of directed influences among neural signals using renormalized partial directed coherence," *Neurosci. Methods*, vol. 179, no. 1, pp. 121–130, 2009, doi: 10.1016/j.jneumeth.2009.01.006.

[122] B. Schelter *et al.*, "Testing for directed influences among neural signals using partial directed coherence," *J. Neurosci. Methods*, vol. 152, pp. 210–219, 2005, doi: 10.1016/j.jneumeth.2005.09.001.

[123] N. Japaridze *et al.*, "Neuronal nnetworks during burst suppression as revealed by source analysis," *PLoS One*, vol. 4, pp. 1–18, 2015, doi: 10.1371/journal.pone.0123807.

[124] B. Crouch, L. Sommerlade, P. Veselcic, G. Riedel, B. Schelter, and B. Platt, "Detection of time- , frequency- and direction-resolved communication within brain networks," *Sci. Rep.*, vol. 8, no. 1825, pp. 1–15, 2018, doi: 10.1038/s41598-018-19707-1.

[125] N. Japaridze *et al.*, "Neuronal networks in West syndrome as revealed by source analysis and

renormalized partial directed coherence," *Brain Topogr.*, vol. 26, pp. 157–170, 2013, doi: 10.1007/s10548-012-0245-y.

[126] B. Marty *et al.*, "Neuromagnetic cerebellar activity entrains to the kinematics of executed finger movements," *The Cerebellum*, 2018, doi: doi.org/10.1007/s12311-018-0943-4.

[127] G. Tirabassi, L. Sommerlade, and C. Masoller, "Inferring directed climatic interactions with renormalized partial directed coherence and directed partial correlation," *Chaos*, vol. 27, 2017, doi: 10.1063/1.4978548.

[128] M. J. Kamiński and K. J. Blinowska, "A new method of the description of the information flow in the brain structures.," *Biol. Cybern.*, vol. 65, no. 3, pp. 203–210, 1991, doi: 10.1007/BF00198091.

[129] L. A. Baccala, D. Y. Takahashi, and K. Sameshima, "Directed transfer function: unified asymptotic theory and some of its implications," *IEEE Trans. Biomed. Eng.*, vol. 63, no. 12, pp. 2450–2460, 2016, doi: 10.1109/TBME.2016.2550199.

[130] R. Kus, M. Kaminski, and K. Blinowska, "Determination of EEG activity propagation : Pair-wise versus multichannel estimate," *IEEE Trans. Biomed. Eng.*, vol. 51, no. 9, pp. 1501–1510, 2004, doi: 10.1109/TBME.2004.827929.

[131] M. Eichler, "On the evaluation of information flow in multivariate systems by the directed transfer function," *Biol. Cybern.*, vol. 94, pp. 469–482, 2006, doi: 10.1007/s00422-006-0062-z.

[132] A. Moharramipour, P. Mostame, G. A. Hossein-Zadeh, J. Wheless, and A. Babajani-Feremi, "Comparison of statistical tests in effective connectivity analysis of ECoG data," *Neurosci. Methods*, vol. 308, pp. 317–329, 2018, doi: 10.1016/j.jneumeth.2018.08.026.

[133] Y. J. Gross Jonathan, *Graph Theory and its Applications*. CRC Press, 1999.

[134] E. Bullmore and O. Sporns, "Complex brain networks: Graph theoretical analysis of structural and functional systems," *Nat. Rev. Neurosci.*, vol. 10, pp. 186–198, 2009, doi: 10.1038/nrn2575.

[135] A. Marshall and F. Verdun, *Fourier transforms in NMR, optical and mass spectrometry*. Elsevier Science Publishers B.V., 1990.

[136] K. Sameshima and L. Baccalá, *Methods in brain connectivity inference through multivariate time series analysis*. CRC Press, 2014.

[137] A. Dokhane, H. Ferroukhi, and A. Pautz, "Validation studies and interpretation of the Oskarshamn-2 1999 stability event with SIMULATE-3K," *Ann. Nucl. Energy*, vol. 96, pp. 344–353, 2016, doi: 10.1016/j.anucene.2016.06.016.

[138] T. Kozlowski and T. J. Downar, "PWR MOX/UO2 Core Transient Benchmark," NEA/OECD, 2007.

[139] A. Dokhane, D. Chionis, and H. Ferroukhi, "ENSI On-Call - Signal analysis of KKL cycle 33 - Start-up measurements from February 2017 - PSI Internal Report AN-41-17-03 V.0," 2015.

[140] F. Jatuff, "Fuel assemblies' dance and neutron music in pressurised water reactors - PSI/NES Colloquium," 2012.

[141] J. Leppänen, M. Pusa, T. Viitanen, V. Valtavirta, and T. Kaltiaisenaho, "The Serpent Monte Carlo code: Status, development and applications in 2013," *Ann. Nucl. Energy*, vol. 82, pp. 142–150, 2015, doi: 10.1016/j.anucene.2014.08.024.

Acronyms and Abbreviations

AIC	Akaike information criterion
APSD	Auto power spectral density
ARMA	Auto-regressive moving average
BIC	Bayesian information criterion
BOC	Beginning of cycle
BWR	Boiling water reactor
Coh	Coherence function
CORTEX	Core monitoring techniques and experimental validation and demonstration (Horizon-2020 European project)
CPSD	Cross power spectral density
CSARMA	Continuous and Structural auto-regressive moving average technique
CV	Coefficient of variation
DGA	Delta gap model in CASMO-5
DTF	Directed transfer function
EFPD	Equivalent full power days
ENSI	Eidgenössisches Nuklearsicherheitsinspektorat (Swiss Federal Nuclear Safety Inspectorate)
EOC	End of cycle
EPFL	École polytechnique fédérale de Lausanne (Swiss federal institute of technology in Lausanne)
FA(s)	Fuel assembly(-ies)
FPE	Final prediction criterion
GUI(s)	Graphical user interface(-s)
HQ	Hannan-Quin criterion
KKG	Kernkraftwerk Gösgen (nuclear power plant Gösgen)
KKL	Kernkraftwerk Leibstadt (nuclear power plant Leibstadt)
KWU	Kraftwerk Union AG (predecessor of SIEMENS AG)
LRS	Laboratory for reactor physics and systems behavior
LRT	Laboratory for reactor physics and thermal-hydraulics
LWR	Light water reactor
MoC	Method of characteristics
MOC	Middle of cycle
MTC	Moderator temperature coefficient
MVAR	Multivariate auto-regression model
NPP(s)	Nuclear power plant(s)
PDC	Partial directed coherence
PSI	Paul Scherrer Institute
PWR	Pressurized water reactor
RPV	Reactor pressure vessel
SIEMENS	SIEMENS Nuclear Power GmbH
SNR	Signal-to-noise ratio
SPND	Self-powered neutron detectors
STARS	Steady-state and transient analysis research for Swiss reactors program
STP	Signal transmission path method
TSAR	Time series analysis methodology for reactors

Curriculum Vitae

Dionysios Chionis

Mechanical-Nuclear Engineer (M.Sc., B.Sc.)

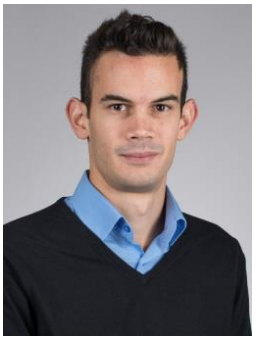

Tel: +41 78 878 73 61
E-Mail: chionis.dionisis@gmail.com
Web: www.linkedin.com/in/dchionis
Address: Wiesenstrasse 30B, 5400 Baden AG, Switzerland
Born: July 18th, 1988
Nationality: Greek
Marital status: Married

Education

2014-2020 **PhD in Nuclear Reactor Physics**
Swiss Federal Institute of Technology in Lausanne (EPFL)
PhD Thesis: "*Development of advanced methodologies for monitoring and modelling of neutron noise in modern LWR cores*"
Advisors: Prof. Andreas Pautz, Dr. Abdelhamid Dokhane, Mr. Hakim Ferroukhi

2012-2014 **M.Sc. in Nuclear Engineering**
Swiss Federal Institute of Technology in Zürich (ETHZ)
Swiss Federal Institute of Technology in Lausanne (EPFL)
Master Thesis: "*Peak cladding temperature prediction and assessment for the Leibstadt NPP using SIMULATE-3K*"
Advisors: Prof. Andreas Pautz, Mr. Kurt Hofer

2006-2011 **Diploma of Mechanical Engineer (B.Sc. & M.Sc.)**
National Technical University of Athens (NTUA), Greece
Diploma Thesis: "*Calculation of true coincidence correction factors using Monte-Carlo simulation techniques*"
Advisors: Prof. Marios Anagnostakis, Dr. Marilia Savva, Dr. Konstantinos Karfopoulos

Professional Experience

04/2018-present ***Nuclear Engineer***
In-core Nuclear Fuel Management – Axpo Power AG, Switzerland
- Safety analyst for the Leibstadt nuclear power plant (KKL).
- Improvement and optimization of simulation processes.
- KKL core design and yearly licensing support.

11/2014-03/2018 ***Doctoral Assistant***
Laboratory of Reactor Physics and Thermal-Hydraulics - Paul Scherrer Institute (PSI), Switzerland
- Development of neutron noise modelling methodology using advanced solvers.
- Development of advanced signal processing techniques for nuclear reactor data.
- Improvement of reactor signal processing techniques.

07-09/2013 ***Mechanical Engineer (intern)***
In-core Nuclear Fuel Management – Axpo Power AG, Switzerland
- Improving the 3D KKL core model using advanced simulation tools.
- KKL transient analysis modelling.

Other Projects

Semester Project "CFD simulations of innovative nuclear fuel designs", ETH Zürich, 2013
This project is part of the international MeAWaT project aiming on performing CFD calculation for new fast reactor fuel geometries.

Semester Project "Analysis of particulate pollutant dispersion in air with the use of Monte-Carlo simulation techniques", NTUA, 2010
This project evaluates the particulate pollutant dispersion over Europe after the Islandic volcano eruption in April 2010 by using probabilistic calculations.

Languages

English		Fluent (C2 level)
German		Intermediate (B2-C1 level)
Greek		Native

List of Journal and Conference Publications

- D. Chionis, A. Dokhane, L. Belblidia, G. Girardin, H. Ferroukhi, A. Pautz, "Development and verification of a methodology for neutron noise response to fuel assembly vibrations", accepted to be published in *Annals of Nuclear Energy*, 2020.
- V. Verma, D. Chionis, A. Dokhane, H. Ferroukhi, "Modelling and analysis of fuel assembly vibrational modes in PWRs using SIMULATE-3K", *Proceedings of the 2020 International Conference on the Reactor Physics* (Physor'20), Cambridge, United Kingdom, 2020.
- L.A Torres, D. Chionis, C. Montalvo, A. Dokhane, A. García-Berrocal, "Neutron noise spectral features of simulated mechanical and thermal-hydraulic perturbations in a PWR core", *Proceedings of the 2020 International Conference on the Reactor Physics* (Physor'20), Cambridge, United Kingdom, 2020.
- D. Chionis, A. Dokhane, H. Ferroukhi, A. Pautz, "Application of causality analysis on nuclear reactor systems", *CHAOS*, **vol. 29**, issue 4, 2019.
- L.A Torres, D. Chionis, C. Montalvo, A. Dokhane, A. García-Berrocal, "Neutron noise analysis of simulated mechanical and thermal-hydraulic perturbations in a PWR core", *Annals of Nuclear Energy*, **vol. 126**, pp. 242-252, 2019.
- D. Chionis, A. Dokhane, H. Ferroukhi, A. Pautz, "Spatial localization of perturbation propagation in LWRs using causality and connectivity analysis", *Proceedings of the 2019 International Conference on Mathematics & Computational methods applied to nuclear science and engineering* (M&C'19), Portland, OR, USA, 2019.
- D. Chionis, A. Dokhane, H. Ferroukhi, A. Pautz, "PWR neutron noise phenomenology: Part I – Simulation of stochastic phenomena with SIMULATE-3K", *Proceedings of the 2018 International Conference on the Reactor Physics* (Physor'18), Cancun, Mexico, 2018.
- D. Chionis, A. Dokhane, H. Ferroukhi, A. Pautz, "PWR neutron noise phenomenology: Part II – Qualitative comparison against plant data", *Proceedings of the 2018 International Conference on the Reactor Physics* (Physor'18), Cancun, Mexico, 2018.
- A. Dokhane, D. Chionis, H. Ferroukhi, "Towards systematic and continuous tracking of neutron and process noise signatures during LWR operation", *Proceedings of the 2018 International Conference on the Reactor Physics* (Physor'18), Cancun, Mexico, 2018.
- F. Ribeiro, D. Chionis, A. Dokhane, A. Mylonakis, C. Demaziere, G. Leontidis, S. Kolias, "Towards a deep unified framework for nuclear reactor perturbation analysis", *Proceedings of the 2018 IEEE Symposium Series on Computational Intelligence* (SSCI), Bengaluru, India, 2018.
- T. Tambouratzis, D. Chionis, A. Dokhane, "General regression neural networks for the concurrent, timely and reliable identification of detector malfunctions and/or nuclear reactor deviations from steady-state operation", *Proceedings of the 2018 IEEE Symposium Series on Computational Intelligence* (SSCI), Bengaluru, India, 2018.

- D. Chionis, A. Dokhane, M. Pecchia, G. Girardin, H. Ferroukhi, A. Pautz, "SIMULATE-3K analyses of neutron noise response to fuel assembly vibrations and thermal-hydraulics fluctuations", *Proceedings of the 2017 International Conference on Mathematics & Computational methods applied to nuclear science and engineering* (M&C'17), Jeju, Korea, 2017.
- D. Chionis, A. Dokhane, H. Ferroukhi, A. Pautz, "On causality analysis of nuclear reactor noise using partial directed coherence", *Proceedings of the 2016 International Conference on the Reactor Physics* (Physor'16), Sun Valley, ID, USA, 2016.
- D. Chionis, K. Hofer, A. Pautz, "Peak Cladding Temperature Prediction and Assessment for the Leibstadt NPP using SIMULATE-3K", *Proceedings of the ANS Student Conference 2015*, College Station, TX, USA, 2015.
- D. Chionis, M. Savva, K. Karfopoulos, M. Anagnostakis, "Determination of True Coincidence Correction Factors using Monte-Carlo Simulation Techniques"
  Nuclear Technology & Radiation Protection, **vol. 29**, pp. 8-13, 2014.

Special Courses Attended

- *Short Courses on Multiphase Flow* – Feb. 2020 (2 weeks duration)
  ETH Zürich, Switzerland
- *Initial Reactor Engineering Training Course* – Sep., Dec. 2019 (5 weeks duration)
  RETAQS Inc. - BWR SNE qualification program, Blue Bell, PN, USA
- *Summer Institute* – June-July 2019 (5 weeks duration)
  World Nuclear University, Bucharest, Romania & Baden, Switzerland
- *Decommissioning of Nuclear Power Plants* – Dec. 2016 (2 weeks duration)
  ETH Zürich, Switzerland
- *Nuclear Energy Management School* – Oct. 2016 (2 weeks duration)
  ICTP/IAEA, Trieste, Italy
- *Energy Regulation* – Sep. 2016 (2 days duration)
  EPF Lausanne, Switzerland
- *Eurotech, Integrated approach to energy systems* – Feb. 2015 (2 weeks duration)
  EPF Lausanne, Switzerland

Awards

- *Best poster & presentation award (3rd/4th PhD student)*
  Nuclear Energy Safety Division PhD Day 2017, PSI, Villigen AG, Switzerland
- *Best student paper award (among 91 PhD participants)*
  ANS PHYSOR Conference 2016, Sun Valley ID, USA
- *Best graduate presentation award (Operations & power technical session)*
  ANS Student Conference 2015, A&M University, College Station TX, USA
- *Best paper award (1st year PhD student)*
  Nuclear Energy Safety Division PhD Day 2015, PSI, Villigen AG, Switzerland